High-precision molecular measurements in an electrostatic fluidic trap



Maria Bespalova

Merton College

University of Oxford

A thesis submitted for the degree of

Doctor of Philosophy

Hilary 2022

This thesis is dedicated to
Stas
whose love, support and encouragement were my fulcrum

Acknowledgements

I would like to express my deepest gratitude to my supervisor Prof. Madhavi Krishnan. I am thankful for all your mentorship, guidance, and support. Thank you for believing in me, even in the moments when I doubted myself. I truly appreciate all the opportunities you provided to me and the lessons I learned throughout my DPhil journey will stay with me forever (unless the misfolded proteins affect my brain activity).

I would like to take the opportunity to thank my viva examiners Prof. Dirk Aarts and Prof. Aleksandra Radenovic. Thank you so much for your helpful comments, suggestions and enjoyable viva.

I am also thankful to all former and current members of Madhavi Krishnan's group, and in particular: Ali, for your kind support, help on all fronts, and wise pieces of advice. Sushanta, for sharing the DPhil journey and life moments with me and your sense of humour. Narain, for simply being a great friend and collaborator. Sven, for all the help, encouragement, and time we spent inside and outside the lab. Katharina, for your support and valuable contribution to the Matlab codes. Rowan, for helping me with the double-helix paper. Gasper, for supervising me during my first trapping experiments. Oleg, for teaching me optics and sharing the adventures in the cleanroom. Francesca and Chris, for your cheerfulness, support, and endless help with the measurements and nanofabrication. I am also incredibly grateful to Gunnar, Lei, Pedro, Pawel, Tim, and Sida. I absolutely enjoyed working with you during all these years. I am also thankful to Jack from the group of Michael Booth and Pablo from Hagan Bayley's group for helping me with HPLC and CD-spectrometry.

My huge gratitude goes to Michael Fritzsche, who developed and fabricated the vacuum chucks which made the double-helix experiments possible. I am also thankful to Aga, a graduate studies administrator. Thank you for your support and for being always optimistic. Thanks to Kim Nixon for the help with moving the lab.

Before moving to Oxford in 2018th, I worked on my DPhil project at the University of Zurich, where I met many great people who positively contributed to both this work and my life. I am thankful to Franzi and Karin for their help with the FCS measurements. Thanks to Fabio Amadei for teaching me PAGE. I am particularly grateful to Roland from the Mechanical Workshop. Thank you for

your infinitive help with building and repairing things inside and outside the lab and infinitive kindness. Thanks to Larissa and Nathalie from HR, who provided me lots of support in organising my stay in Zurich. I am also grateful to all the members of the FIRST lab at ETH.

I would also like to thank my friends Sasha and Irina for their empathy and love. Your support and optimism mean a lot to me, and your encouragement and keen interest gave me lots of inspiration.

I am also infinitely thankful to my mom, dad, and grandma. Thank you for always supporting and believing in me, as well as for tremendous understanding and encouragement during the past few years. Ksusha, my dear sister, thanks for being your cheerful self, you are luminous. I am deeply thankful to Stas, my beloved husband. You have truly changed my life for the better, and it is simply impossible to overestimate your contribution to this work through your care of me from day to day.

Abstract

Measurement of molecular properties at the single-molecule level can reveal valuable information, often hidden in ensemble measurements. In this Thesis, we present a range of novel high-precision molecular measurements in solution enabled by the electrostatic fluidic trapping approach [1][2].

The working principle of an electrostatic fluidic trap relies on the equilibrium thermodynamic repulsion experienced by a charged object confined in a fluid-filled gap between two like-charged surfaces. Geometric tailoring of one of the surfaces by nanostructured surface indentations reduces interaction energy, creating an electrostatic potential well capable of stable trapping of a charged object in solution. The ability of a recently developed escape-time electrometry (ETe) technique to precisely measure the depth of potential well underlies the high-precision measurement of effective electrical charge, q_{eff}, of a trapped molecule [3][4][5][6].

In the original work, upon which this Thesis is based, we first focus on expanding the capabilities of the electrostatic fluidic trapping approach. We demonstrate the ability of stable trapping in a range of solvents of different polarities and present a novel approach for measuring the net surface charge at the solid-liquid interface [7]. We further explore the applicability of charged lipid bilayer systems for single-molecule electrostatic trapping and describe how chemical composition of nanostructured supported lipid bilayers can be measured by means of ETe [8].

We finally demonstrate the ability to use the q_{eff} of a biomolecule in solution to infer key details of its atomic level structure. Performing ETe measurements on A- and B-form (RNA and DNA) double helixes, we achieve a $\sim$ 1Å and $\sim$ 0.1Å precision on the helical radius and rise per basepair, respectively. Moreover, in conjunction with a recently developed theoretical approach to model electrostatics of biomolecules in solution, our examination of structural parameters provides an unprecedented new view of the molecule-solvent interface [9][10].

Contents

List of Symbols and Abbreviations **xi**

1 Introduction **1**
- 1.1 Why study single molecules? . . . 1
- 1.2 Single-molecule measurments in solution . . . 2
- 1.3 Electrostatic fluidic trapping . . . 3
- 1.4 Effective electrical charge . . . 5
- 1.5 Escape-time electrometry: working principle and previous achievements 7
- 1.6 Thesis outline . . . 9

2 State-of-the-art methods for single-molecule trapping in solution **11**
- 2.1 Paper I . . . 12

3 Surface charge measurements in polar and apolar solvents **23**
- 3.1 Other measurement techniques . . . 25
- 3.2 Surface charge measurements in an electrostatic fluidic trap . . . 27
- 3.3 Paper II . . . 28

4 Single-molecule electrostatic trapping using charged lipid bilayers **43**
- 4.1 Surface-confined lipid bilayers . . . 44
- 4.2 Characterisation techniques . . . 45
- 4.3 Paper III . . . 49

5 Molecular and interfacial structural measurements in solution **67**
- 5.1 The effect of ion type . . . 68
- 5.2 Charge-spectrometry in an electrostatic fluidic trap . . . 70
- 5.3 Paper IV . . . 72

6 Conclusions **127**

References **131**

List of Symbols and Abbreviations

$a_{\mathbf{H}}$ . . . . . Hydrated radius

AFM . . . . . Atomic force microscopy

b . . . . . Helical rise per basepair

c . . . . . Concentration

D . . . . . Diffusion coefficient

d . . . . . Pocket depth

ds . . . . . Double-stranded

e . . . . . Elementary charge

ε_0 . . . . . Vacuum permittivity

$\varepsilon_{\mathbf{s}}$ . . . . . Relative permittivity of the solvent

ET*e* . . . . . Escape-time electrometry

Γ . . . . . Surface ionisable groups density

$\Delta F_{\mathbf{el}}$ . . . . . Electrostatic interaction free energy

f . . . . . Fluctuations contribution to the well depth

$2h$ . . . . . Channel height

$K_{\mathbf{a}}$ . . . . . Acid dissociation constant

κ^{-1} . . . . . Debye length

$k_{\mathbf{B}}$ . . . . . Boltzmann's constant

$l_{\mathbf{B}}$ . . . . . Bjerrum length

n . . . . . Number of basepairs

$N_{\mathbf{A}}$ . . . . . Avogadro's number

NMR . . . . . Nuclear magnetic resonance

NR . . . . . Neutron reflectometry

$q_{\mathbf{eff}}$ . . . . . Effective electrical charge

$q_{\mathbf{str}}$ . . . . . Structural charge

r . . . . . Helical radius

$r_{\mathbf{H}}$ . . . . . Hydrodynamic radius

SEM . . . . . Scanning electron microscopy

SLB . . . . . Supported lipid bilayer

ss . . . . . Single-stranded

SUV . . . . . Small unilamellar vesicles

σ . . . . . Surface charge density

T . . . . . Temperature

$t_{\mathbf{esc}}$ . . . . . Average escape time

$t_{\mathbf{r}}$ . . . . . Relaxation time

W . . . . . Well depth

$\phi_{\mathbf{m}}$ . . . . . Midplane potential

$\phi_{\mathbf{s}}$ . . . . . Effective surface potential

List of Publications

This Thesis is based on the work contained in the following research papers:

Measured electrical charge of SiO_2 in polar and nonpolar media
G. Kokot*, M.I. Bespalova*, and M. Krishnan
The Journal of Chemical Physics, 145, (2016), 194701
* Contributed equally

Single-molecule trapping and measurement in solution
M.I. Bespalova, S. Mahanta, and M. Krishnan
Current Opinion in Chemical Biology, 51, (2019), 113-121

Single molecule trapping and measurement in a nanostructured lipid bilayer system
M. Bespalova, R. Öz, F. Westerlund, and M. Krishnan
Langmuir, (2022), Advance online publication

Opto-electrostatic determination of nucleic acid double helix dimensions and the structure of the molecule-solvent interface
M. Bespalova, A. Behjatian, N. Karedla, R. Walker-Gibbons, and M. Krishnan
Macromolecules, 55, (2022), 6200-6210

Additional research paper not included in this Thesis:

Electroviscous effect for a confined nanosphere in solution
A. Behjatian, M. Bespalova, N. Karedla, and M. Krishnan
Physical Review E, 102, (2020), 042607

1 Introduction

Contents

1.1 Why study single molecules? 1
1.2 Single-molecule measurments in solution 2
1.3 Electrostatic fluidic trapping 3
1.4 Effective electrical charge 5
1.5 Escape-time electrometry: working principle and previous achievements 7
1.6 Thesis outline 9

1.1 Why study single molecules?

The last few decades have witnessed a breakneck growth of the field of single-molecule research. New approaches to measuring the properties of matter at a single molecule level have truly revolutionised the characterisation, observation, and studying of biological macromolecules – constituents of life.

In conventional ensemble techniques, the large number of molecules present in an ensemble yields the averaged-out measurement of molecular properties. Thus, sample inhomogeneities as well as the dynamic fluctuations of molecules can be lost in the averaging process. By contrast, single-molecule techniques enable direct measurement of distribution functions of molecular properties. This crucial

difference becomes especially important when studying heterogeneous systems. For example, single-molecule approaches permit detection and measurement of co-existing structures in protein or oligonucleotide samples, while in the ensemble regime rarer structures can be averaged out or swamped by more populated structures. Detection and identification of single molecules are also important for medical diagnostics. For instance, the presence of misfolded proteins in living organisms can serve as evidence of the early stage of various diseases [11].

Single-molecule techniques are also advantageous for studying the systems of many molecules undergoing some time-dependent changes. For example, in order to study the mechanisms of enzymatic reactions in the ensemble regime, an initial synchronisation of all enzyme molecules is required, which is barely possible due to stochastic and uncorrelated structural transitions of individual enzymes. However, synchronisation is not needed for single-molecule methods as the transition sequence of an individual molecule can be observed and studied.

Moreover, some objects of study cannot be present in the number of copies large enough for ensemble measurements. Those include, for example, some components of a cell that are present there in one or a few copies [12][13].

Finally, single-molecule techniques offer a platform to examine the molecular response to external fields and mechanical manipulation. Besides that, by confining a molecule in solution and varying its environment, additional information about molecular interface and dynamics can be extracted. Alternatively, using single molecules as sensitive nanoprobes, information about their nanoenvironment can be obtained [14].

1.2 Single-molecule measurments in solution

As described in the previous section, single-molecule measurements can reveal valuable information about molecular properties and functions. However, single-molecule measurements in solution remain a non-trivial task because of Brownian motion: freely diffusing molecules do not hold still long enough to perform a measurement. Immobilisation does not always provide the best solution for this

problem. For biological macromolecules, for example, a decrease of mobility caused by immobilisation can further affect their conformation, stability, and biological activity [15]. Thus, an ideal single-molecule experiment should be carried out in a molecule's native environment and in absence of any external influences which could also affect the natural molecule's behavior.

In order to satisfy these requirements, trapping approaches for spatial control of molecules have been used. In contrast to immobilization methods, trapping techniques do not restrict the mobility of freely diffusing molecules but confine their motion in space. This work focuses on single-molecule trapping and measurements in an electrostatic fluidic trap invented earlier by Krishnan and collaborators [1][2].

1.3 Electrostatic fluidic trapping

An electrostatic fluidic trap is created in a fluid-filled gap between two like-charged parallel walls that form a slit of height, $2h$ (Figure 1.1a). For trapping a molecule carrying a charge of the same sign as the walls, the distance between the walls is chosen so that $h \sim \kappa^{-1}$. Here, the Debye length, κ^{-1}, characterises the extent of decay of electrostatic interactions, and is $\approx 0.304/\sqrt{c}$ nm for a 1-1 aqueous electrolyte solution of a molar concentration c at 25 °C. This configuration provides a non-zero electrical potential at the midplane of the slit, ϕ_{m}. Due to the overlap of electrical double layers in the slit, a charged molecule placed there experiences an energy minimum at the midplane of the slit. That already confines the molecule's motion in one (z) dimension (Figure 1.1b). Nanoscale structuring of one of the slit surfaces with surface indentations, or "pockets", reduces the repulsive interaction energy between the molecule and the walls, creating an electrostatic potential well or a trap that confines the molecule's motion in all three dimensions (Figure 1.1c). Since the distance between the walls at the pocket locations is much larger than κ^{-1}, a molecule inside the trap inhabits a field-free zone identical to the bulk solution. In order to adjust the depth of the potential well, the ϕ_{m} can be tuned by varying κh. For single-molecule trapping experiments, typical κh values vary from 2.5 to 5, given by $\kappa^{-1} \approx 7 - 13$ nm and $2h \approx 70$ nm.

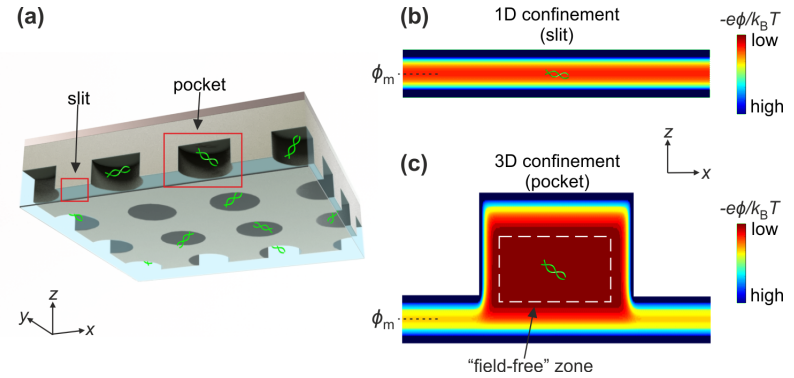


Figure 1.1: Electrostatic fluidic trapping device. **(a)** Schematic illustration of molecules confined in an array of electrostatic fluidic traps. Representative electrostatic potential distributions in the slit and the pocket obtained by solving Eq. (1.1) and (1.2) are shown in panels **(b)** and **(c)**, respectively. The following input parameters were used for the calculations: $2h$=70 nm, pocket depth, d =150 nm, c =1 mM, pH=8, pK_a=7.5, Γ=8e/nm^2.

In the present study, similar to previous work, we used SiO_2 and glass surfaces to construct the trap [1][3][4][5][6]. Both materials have terminal silanol groups, SiOH, which dissociate in contact with water and yield a charged SiO^- group staying on the surface [16]:

$$SiOH \rightleftharpoons SiO^- + H^+$$

In the current study, the SiO_2 walls are modelled as in previous work [3][4][5][6]. Briefly, we use a single pK_a charge regulation model which predicts the response of SiO_2 walls to both pH and ionic strength of the solution. Thus, we use a charge regulation boundary condition:

$$\sigma = \frac{-\Gamma e}{1 + 10^{(\mathrm{p}K_a - \mathrm{pH})} \exp \frac{-e\phi_{s,0}}{k_B T}} \tag{1.1}$$

which describes the surface charge density of SiO_2 walls, σ, as a function of true surface potential, $\phi_{s,0}$ [17]. Equation (1.1) together with the Poisson-Boltzmann (PB) equation,

$$\Delta\psi = \kappa^2 \sinh\psi \tag{1.2}$$

self-consistently determines the non-dimensional electrical potential, $\psi = e\phi/k_B T$. Here, k_B denotes the Boltzmann's constant, T is the temperature, K_a is the acid

dissociation constant of ionisable surface groups (SiOH in this case), Γ is the number density of ionisable surface groups, and e is the elementary charge. We assume Γ=8 e/nm^2 and pK_a=7.5 [16].

An electrostatic fluidic trap not only enables trapping of single molecules in solution but also provides a tool for high-precision measurement of effective electrical charge, q_{eff}, of a trapped molecule. In the next two sections we describe how q_{eff} of a macromolecule is different from its structural charge and describe the principle of escape-time electrometry (ETe) approach.

1.4 Effective electrical charge

At the simplest level, the structural electrical charge, q_{str}, of a molecule in solution at a given pH is a sum of its charged groups and can be estimated using the following equation:

$$q_{\text{str}} = \sum_i \frac{z_i e}{1 + 10^{z_i(\text{pH}-\text{p}K_{\text{a},i})}} \tag{1.3}$$

Here, i denotes each of the ionisable groups, and z_i = +1 or -1 is the charge of each group.

In practice, however, a macromolecule's structural charge in solution can be partially neutralised by two distinct phenomena: charge regulation and charge renormalisation. This leads to a reduced "effective" electrical charge, q_{eff} [9].

Charge regulation phenomenon generally describes how the protonation state of an ionisable group is perturbed by the surrounding molecular environment. The origin of charge regulation mechanism stems from protons that migrate to and from molecule's ionisable sites. For example, for a hypothetical macromolecule immersed in an electrolyte and carrying identical ionisable sites, HA, the dissociation of HA group can be written as

$$\text{HA} \rightleftharpoons \text{H}^+ + \text{A}^-$$

The corresponding thermodynamic equilibrium constant is given by [18]:

$$K_a = \frac{\gamma_{\text{H}^+}\gamma_{\text{A}^-}}{\gamma_{\text{HA}}} \cdot \frac{c_{\text{H}^+}c_{\text{A}^-}}{c_{\text{HA}}} \tag{1.4}$$

Here, c are average concentrations and γ are activity coefficients. Using the relation $\mathrm{pH} = -\log(\gamma_{\mathrm{H}^+} c_{\mathrm{H}^+})$, Eq. (1.4) can be rewritten as:

$$-\log\frac{c_{\mathrm{HA}}}{c_{\mathrm{A}^-}} = \mathrm{pH} - \mathrm{p}K_{\mathrm{a}} + \log\frac{\gamma_{\mathrm{HA}}}{\gamma_{\mathrm{A}^-}} \tag{1.5}$$

where fraction $\frac{c_{\mathrm{HA}}}{c_{\mathrm{A}^-}}$ directly defines the charged state of the group. However, in a densely packed system of charges, activity coefficients take different values than in isolation, due to non-zero surface electrical potential, ϕ_{s}, of a charged macromolecule. At equilibrium, the chemical potential or activity, $a_i = \gamma_i c_i$, must stay constant throughout the medium and if γ changes, so must c. The departure from degree of ionisation of HA group can be described by a factor α, as given by the following equation:

$$\alpha = \frac{1}{1 + 10^{z_i(\mathrm{pH}-\mathrm{p}K_{\mathrm{a}})}\exp(z_i e\phi_{\mathrm{s}}/k_{\mathrm{B}}T)} \tag{1.6}$$

where k_{B} denotes the Boltzmann's constant and T is the temperature [17]. Charge regulation is known to affect densely charged globular macromolecules, e.g., globular proteins, and has little to no effect for strongly charged linear polyelectrolytes, e.g., nucleic acids, in solution [9]. Besides that, charge regulation can take place when a charged macromolecule approaches an alien molecular matter [19].

Charge renormalisation phenomenon refers to strong accumulation of counterions in the vicinity of a charged molecule or colloid. For example, for a highly charged macromolecule, the interaction energy between the molecule and its counterions can be $> k_{\mathrm{B}}T$ in close proximity to the molecular surface. From a far-field prospective, such molecule with its condensed counterionic shell can be considered as one whole which carries $q_{\mathrm{eff}} < q_{\mathrm{str}}$. It was shown that for a linear polyelectrolyte, charge renormalisation takes place if the dimensionless factor, ξ, satisfies [20]:

$$\xi = l_{\mathrm{B}}/L > 1/\nu \tag{1.7}$$

Here L represents a linear charge spacing, ν is the valency of counterions, and $l_{\mathrm{B}} = e^2/(4\pi\varepsilon_0\varepsilon_{\mathrm{s}}k_{\mathrm{B}}T)$ is the Bjerrum length, where $\varepsilon_0\varepsilon_{\mathrm{s}}$ is the electrical permittivity of the medium. Furthermore, factor ξ enables q_{eff} predictions for linear polyelectrolyte

molecules in absence of charge regulation: $q_{\text{eff}} \sim q_{\text{str}} \cdot (\nu\xi)^{-1}$ [21]. For example, for the classic Watson-Crick B-DNA in water at 25 °C, $\xi_{\text{B-DNA}} = 7.14/1.7 = 4.2$. Hereby the effective charge of B-DNA is expected to be roughly $0.24q_{\text{str}}$ or $0.12q_{\text{str}}$ in, for example, aqueous Na^+ or Mg^{2+} environments, respectively. It is also important to note that charge renormalisation is relevant for other molecular geometries as well, such as spheres and planes [22][23].

Both charge renormalisation and charge regulation are defined by molecular geometry thereby providing a link between molecule's effective charge and its structure [9]. We use this relationship in Chapter 5, where we demonstrate the possibility to infer molecular and interfacial structural information by means of high-precision effective electrical charge measurements.

1.5 Escape-time electrometry: working principle and previous achievements

Escape-time electrometry (ETe) is a novel technique enabling high-precision (<1e) molecular q_{eff} measurements in solution [3][4][5][6]. ETe exploits the electrostatic fluidic trap and relies on measuring the average escape time, t_{esc}, spent by a charged molecule in a potential well of the depth, W. For $W > 4k_{\text{B}}T$, the relationship between t_{esc} and W is well described by Kramer's equation:

$$t_{\text{esc}} = t_{\text{r}} \exp\left(\frac{W}{k_{\text{B}}T}\right) \tag{1.8}$$

where t_{r} is a position relaxation time of a molecule that depends on geometric features of the potential well and inversely proportional to the molecule's diffusion coefficient $D = k_{\text{B}}T/6\pi\eta r_{\text{H}}$ [24]. Here η denotes solvent viscosity and r_{H} is the molecule's hydrodynamic radius. In turn, the total well depth, W, is composed of electrostatic free energy of interaction, $\Delta F_{\text{el}} = q_{\text{eff}} \cdot \phi_{\text{m}}$, and a term f accounting for the spatial fluctuations of a molecule [5]. In turn, the electrical midplane potential, ϕ_{m} is well approximated by:

$$\phi_{\text{m}} = 2\phi_{\text{s}} \exp(-\kappa h) \tag{1.9}$$

where ϕ_s represents an effective surface electrical potential [25]. Note that in general ϕ_s is smaller than true surface potential , $\phi_{s,0}$, obtained from Eq. (1.1) and Eq. (1.2) due to non-linearity of the PB equation. We do not know *a priori* the exact value for effective surface potential in a given device unless the calibrator molecule, whose effective electrical charge is accurately known, was measured to define ϕ_s. Thus, W can be written as:

$$W = \Delta F_{el} + f = q_{eff} \cdot \phi_m + f \tag{1.10}$$

The high precision of q_{eff} measurements offered by ET*e* stems from Eq. (1.8) and (1.10), which reveal an exponential dependence of the measurand, t_{esc}, on the measurable, q_{eff}. As shown in the earlier work, the fractional measurement uncertainty on q_{eff} is given by $q_{eff,e} = t_{esc,e}/\Delta F_{el}$, where $t_{esc,e} = 1/\sqrt{N}$ is the fractional measurement uncertainty on t_{esc} and N is the number of registered escape events [3]. For example, $t_{esc,e} = 10\%$ given by $N = 100$ events would result in only $\sim 3\%$ measurement uncertainty on q_{eff} for a typical value of $\Delta F_{el} = 3k_BT$. In this work, however, we use $N \sim 10^3 - 10^4$ events which correspond to $t_{esc,e} \sim 1 - 3\%$ and $q_{eff,e} \sim 0.3 - 1\%$. The experimental details on measuring the value for t_{esc} as well as the algorithm for converting the measured t_{esc} value to q_{eff} are provided in further chapters.

ET*e* has already proven to be a powerful, robust, and versatile tool for studying many different macromolecules: from single dye molecules of molecular weight ~ 1 kDa to big globular proteins, such as the enzyme Gusβ (~ 300 kDa) [3][5]. The ability of ET*e* to distinguish structural and/or compositional differences based on high-precision q_{eff} measurements was demonstrated on single- and double-stranded DNA molecules, Gusβ ($q_{str} \approx 134e$, $q_{eff} = 22e$) and Stm-1 ($q_{str} \approx 103e$, $q_{eff} = 89e$) proteins, point-mutated proteins, and protein/DNA molecules labelled with different dyes [3][6]. Moreover, it was shown that ET*e* is capable of monitoring the q_{eff} fluctuations of a single molecule in real time [3]. Besides q_{eff} measurements, the applicability of the ET*e* approach for measurements of the molecular hydrodynamic radius was demonstrated [4]. Additional studies devoted to improving the

measurement accuracy of ETe by using a calibrator molecule with the accurately known value for q_{eff} were also performed [6].

1.6 Thesis outline

The major goal of this Thesis was to expand the range of possible measurements in an electrostatic fluidic trap, particularly using the ETe approach.

This work has given rise to 4 papers, published in the peer-reviewed journals. The main Chapters (2-5) of the Thesis include these publications along with the brief introductions providing context for the work performed.

In Chapter 2 we present our review paper, *"Single-molecule trapping and measurement in solution"*, which provides an overview of state-of-the-art trapping techniques and molecular measurements enabled by them [26].

The first experimental results are described in our published paper, *"Measured electrical charge of SiO_2 in polar and nonpolar media"*, presented in Chapter 3 [7]. Here, we explore the effect of solvent polarity on the net surface charge of SiO_2, the material of which our trapping devices are fabricated.

In Chapter 4, we present our recently published paper *"Single molecule trapping and measurement in a nanostructured lipid bilayer system"* [8]. Here, we discuss the current limitations of the electrostatic trapping technique and explore the applicability of supported lipid bilayers (SLBs) for single-molecule trapping. Using ETe, we also demonstrate a new approach for measuring the chemical composition of nanostructured SLBs.

Chapter 5 introduces the findings of our paper *"Opto-electrostatic determination of nucleic acid double helix dimensions and the structure of the molecule-solvent interface"* [10]. In this work, we demonstrate a novel experimental approach for molecular and interfacial structural measurements in solution using the ETe technique.

Finally, Chapter 6 describes the main results achieved in this work and outlines the scope of work for future studies.

2

State-of-the-art methods for single-molecule trapping in solution

Contents

2.1 Paper I 12

This Chapter introduces our recently published research paper, *"Single-molecule trapping and measurement in solution"* [26]. The paper presents a review of the state-of-the-art single-molecule confining and trapping approaches used in solution. The single-molecule trapping techniques are classified according to their mechanisms, and their unique capabilities, features, and limitations are discussed. Furthermore, we describe a range of molecular measurements enabled by single-molecule trapping in solution. To conclude, we comment on the trends and perspectives in the field of single-molecule measurements.

2.1 Paper I

Available online at www.sciencedirect.com

ScienceDirect

Current Opinion in Chemical Biology

Single-molecule trapping and measurement in solution

Maria I Bespalova, Sushanta Mahanta and Madhavi Krishnan

Trapping of a single molecule in the fluid phase was realized decades following developments in the gas-phase, because in some ways the solution phase posed a greater challenge. The key issues have since been addressed by several different means; techniques to confine nanometer scale entities in solution now abound and are gaining traction in a variety of single molecule studies. Available methods range from pure physical entrapment of a molecule on the one hand to electrokinetic and optical techniques, and approaches that exploit thermodynamic principles on the other. Some trapping techniques have also opened up new avenues to highly precise, accurate measurements of molecular physical properties in solution.

Address
Physical and Theoretical Chemistry Laboratory, Department of Chemistry, University of Oxford, South Parks Road, Oxford OX1 3QZ, United Kingdom

Corresponding author: Krishnan, Madhavi (madhavi.krishnan@chem.ox.ac.uk)

Current Opinion in Chemical Biology 2019, **51**:113–121

This review comes from a themed issue on **Molecular imaging**

Edited by **Philipp Kukura** and **Sua Myong**

For a complete overview see the Issue and the Editorial

Available online 27th June 2019

https://doi.org/10.1016/j.cbpa.2019.05.013

1367-5931/© 2019 Elsevier Ltd. All rights reserved.

Since the advent of single molecule optical detection in the condensed phase [1,2], imaging and detection of emitters using visible light has become a methodological cornerstone in the quest to measure the properties and understand the dynamics of molecular scale matter in solution. The short timescales associated with free diffusion in solution however generally render molecules in motion invisible above the noise floor of the detector and/or measurement background. Experiments on optically emitting molecules have therefore generally relied on physical attachment of the entity of interest to a surface in order to facilitate long term observation, with immobilization and related methods such as encapsulation, tethering, and confinement using nanostructured surfaces serving as the mainstay of biomolecular imaging experiments [3–5].

Following the cue from the century-old effort in the gas phase, external fields may be used to quell thermal motion and to spatially confine a molecule in solution. However in general, the trade-off between thermal energy and say, the free energy of the field-induced dipole in a macromolecule, turns out highly unfavorable in room temperature solution [6]. In other words, potential wells created by approaches capable of spatially trapping cold atoms at one extreme and micron-scale particles in a warm fluid on the other, are far too shallow in the intermediate regime of the small, weakly polarizable, and warm, invariably encountered when dealing with biomolecular matter in room temperature solution. So novel trapping approaches have had to be developed in order to address the unique challenges posed by the solution phase.

Physical confinement approaches for long term observation of single molecules

Beginning with an early demonstration of elastomeric microfluidics in single molecule experiments, approaches based on the soft elastomer polydimethylsiloxane (PDMS) have continued to provide a robust route to confining single molecules in solution [7,8]. Initial single molecule enzymology experiments in passive femto-liter reaction chambers have given way to approaches that further exploit the soft and reversibly deformable nature of PDMS [9,10]. 'Flexible confinement' has proven a highly useful and novel development in that it permits rapid alternation between bulk-like and confined states, supporting mixing, exchange, and rapid transport of material into and out of the vicinity of the individual molecule of interest, as demonstrated in a recent comprehensive study at the molecular scale [10]. Along similar lines, convex-lens induced confinement and nanotemplating is a simple, versatile approach that uses a lens in near contact with a nanostructured substrate to generate molecular confinement [11–13]. Banterle and Lemke provide an exhaustive review of recent developments in confinement-based approaches for single molecule experiments [14] (Figure 1).

An overview of techniques offering long term observation of molecules in solution would not be complete without reference to the refinement in 3d tracking microscopy that now permits direct observation via particle tracking of a single molecule freely diffusing in solution [15]. Although the approach offers lower molecular throughput than the nanostructure-based techniques, it does directly address and solve the key challenge of long term observation without recourse to any confinement or trapping principle.

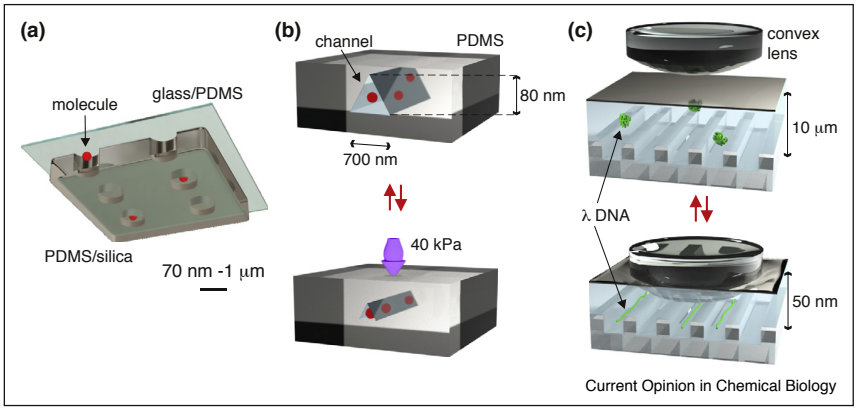
Trapping single molecules in solution

Direct spatial control of single molecules diffusing in solution remained elusive until the invention of the anti-Brownian electrophoretic trap (ABEL trap) a little over a decade ago [16]. The approach furnished single molecule fluorescence-based feedback-control of the position of a molecule in solution using applied electric fields and has been realized in one [17,18•] and two dimensions [16]. Subsequently, other field-based approaches utilizing deterministic AC electrical fields [19,20••], near field optical effects [21,22,23••], and temperature gradients [24•], have demonstrated the ability to directly confine nanoscale matter and large macromolecules in solution. Passive trapping approaches relying on equilibrium thermodynamics rather than field-driven or gradient-driven transport have been further developed, now not only addressing the need for long term observation but importantly enabling new approaches to high precision measurement of molecular properties in solution [25,26••]. Below we briefly discuss state-of-the-art trap-based approaches to molecular control in free solution, their unique capabilities and limitations, and the prospects held out by the most recent developments in this burgeoning field of research (Table 1).

Spatial control based on electrical mobility

Most biological macromolecules carry some net electrical charge, either positive or negative. Motion of a charged molecule in a uniform electrical field in solution arises both from the response of its electrical charge to the local field charge (electrophoresis) as well as from field-driven flows due to possible charge non-neutrality in the surrounding fluid (electro-osmosis). While Earnshaw's theorem forbids the realization of a stable spatial trap for an electrical charge in a static field, time-dependent electric fields — both stochastic and deterministic — can confine charged objects in free space and solution [16,19]. The ABEL trap for example, exploits an electrical feedback-based mechanism requiring continuous monitoring of single molecule fluorescence [27–29] (Figure 2a). An analogous approach using a similar planar electrode configuration is the Paul trap in the fluid phase, with the important distinction that deterministic electrical fields are used in order to attain time-averaged stable confinement, and particle observation is not required [19]. The challenge in scaling down the Paul trap to the molecular level appears to be the high frequencies involved which have concomitant heating effects. Nonetheless it would be a welcome development with important implications for measurement if this trapping principle which has been so successfully deployed in the gas phase were able to deliver promising results for molecular scale matter in solution. Finally, replacing the DC field used in molecular separations with an alternating field applied to an effectively one dimensional nanocapillary, Lesoine *et al.* [18•] have demonstrated a straightforward route to trapping molecules in solution (Figure 2b). The key feature of this approach is that it permits trapping of single molecules without the need for continuous observation, which considerably reduces the photobleaching rate and increases the overall trapping time. Furthermore, the one-dimensional scheme supports parallelization, and may also facilitate feedback-free operation, similar to the aqueous Paul Trap.

Figure 1



Confinement approaches for long term observation of single nanoparticles and molecules. **(a)** Attoliter to femtoliter silica [8] or PDMS [7] chambers. Particles are confined in closed nanoscopic chambers created between a glass surface and PDMS layer, facilitating long term parallel observation of single molecules. **(b)** Size-adjustable elastomeric micro-channels. Compressing a channel with micrometer scale cross-sectional dimensions reduces its dimensions to the order of the point spread function of the optical excitation. This permits visualization of molecules diffusing in one dimension in a wide field fluorescence microscope. Removal of the applied force restores the channel to its original form, thus enabling mixing and transport of molecules and solutes [9]. **(c)** Convex lens induced confinement and nanotemplating utilizes tunable contact between a convex lens and a substrate carrying nanoscale topography to generate reversible spatial confinement of molecules [13].

Table 1

The table presents a comparison of trap-based methods for single molecule confinement and measurement in solution. Parameters noted are: longest reported trapping time for a single molecule in a single trap; the smallest reported trapped molecule and its approximate mass; number of individual molecules that can be trapped in parallel and observed in the same field of view; prospects for simultaneous confinement of more than one molecule in a single trap. Finally we list a key feature of each technique that currently poses a challenge but whose resolution would present a signification future advance

Trapping mechanism		Time	Size	Number	Multimolecular trapping	Future developments
Feedback-based electrokinetic trapping	ABEL	~5 min (eGFP) [49]	Organic fluorophores (1 kDa) [41]	1	No	Scattering detection [50]
	Recycling	>15 s (dsDNA) [18•]	13 bp dsDNA (8.5 kDa) [18•]	1	No	Scattering detection, feedback-free operation
Nano-aperture optical trapping		~3 min (Streptavidin) [23••]	20 b ssDNA (6.5 kDa) [34]	600 [23••]	Yes	Preserving molecular structural integrity
Thermophoretic trapping		>8 min (λ-DNA) [24•]	λ-DNA (~30 M Da) [24•]	1	Yes	Trapping molecules <1 MDa
Geometry-induced trapping	Electrostatic	~30 min (disordered protein, Stm-l) [26••]	Organic fluorophores (1 kDa) [40•]	>4000	Yes	Operation in ionic strengths >10 mM
	Dielectrophoretic	Seconds (immunoglobulin G antibody) [20••]	IgG antibody (~144 kDa) [20••]	~1	Yes	Trapping small molecules (<140 kDa)

Beyond transport arising from net electrical charge, electrical mobility can also arise from a dipolar response in a field gradient, even if the molecule has no intrinsic electrical dipole. Although dielectrophoretic (DEP) forces have been used for concentration and local spatial enrichment of molecules [30] in high field regions, stable spatial trapping of an individual molecule over longer periods appeared harder to achieve. A recent demonstration of DEP concentration in conjunction with nanopore-based conductance sensing highlights some of the issues encountered in attempts to realise DEP trapping in free solution [31]. However reduction in system dimensions to an effectively one dimensional nanochannel elegantly circumvents these challenges and has recently enabled confinement of single macromolecules in regions of low electric field [20••], as discussed in the final section.

Optical control of matter beyond the focused beam trap

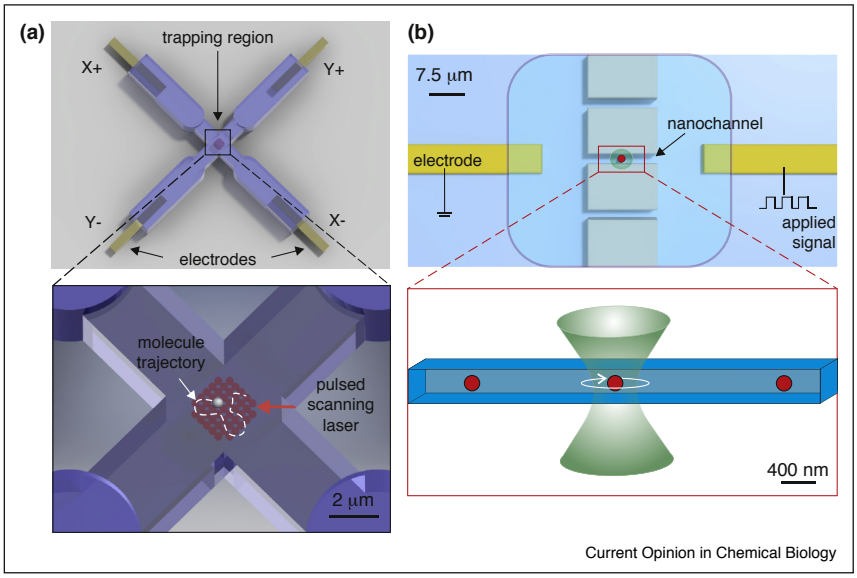
Trapping particles in a focused optical beam in free solution has a rich and long-standing tradition in experimental biophysics [32]. However the depth of the minimum in dipole energy in a free-space optical focus scales with the third power of object size, rendering the optical gradient force alone infeasible at the molecular scale in room temperature solution [6]. Recently, novel optical techniques have been developed that substantially enhance the gradient force, or harness different physical principles in addition, thereby not only permitting trapping of single biomolecules in solution but also enabling new forms of optical measurement on molecules using low optical powers (Figure 3).

The self-induced back action (SIBA) optical trap is a new concept in optical trapping at the nanometer scale [21,22,23••]. The technique exploits conservation of momentum in the transmission of light through a nanoaperture in a metal film. Briefly, the motion of a dielectric object away from the nanoaperture results in a reduction in transmission and hence photon momentum through the aperture. This loss in momentum in turn creates a restoring force on the particle toward the aperture. The method also supports measurements of changes in mass or conformation of a molecule by monitoring the modulation of transmitted light through the aperture.

In contrast to 'nanoparticle-based' plasmonic traps such as bowtie antennae, where resonant excitation produces high local gradients in the electromagnetic field, aperture-based traps do not require a high quality resonance. The nanoaperture approach also benefits from efficient dissipation of thermal energy through the metal film preventing the buildup of high local temperatures [33]. The strong 'back-action force' supports very long molecular residence times in the nanoaperture on the order of several minutes, or even hours [34]. Furthermore the high temporal resolution in monitoring transmission through the aperture could enable high resolution measurement of attributes of molecular states such as 3D conformation [33].

A novel measurement method developed using the SIBA experiment takes advantage of the inherent acoustic vibrational modes of the molecule of interest [35••,36]. Detuning a second laser so that the beat frequency matches that of an acoustic mode of the molecule, a resonant vibrational excitation occurs which causes local

Figure 2



Electrokinetic approaches to single molecule trapping. **(a)** The Anti-Brownian Electrokinetic trap relies on a scanning laser beam and fluorescent feedback from a diffusing single molecule to electrically cancel the effect of Brownian motion and restore the molecule to the center of the trap [16,29]. **(b)** The 'recycling trap' reduces the problem to one dimension using a nanochannel to confine the molecule [18•].

heating. Thermal motion of the molecule is altered which manifests in the fluctuation amplitude of light transmitted through the aperture. The molecule's low frequency vibrational spectrum can be recorded by monitoring thermal motion over a range of beat frequencies. Although the mechanism remains to be fully understood, the observed resonance frequencies match the Raman spectrum of the molecule, opening up new avenues for spectroscopy at the single molecule level. Differences in length and base sequence in single stranded DNA have been detected by this approach with prospects for detection of single base differences [36]. Protein interactions with DNA [37] or smaller molecules [38] have also been probed using this technique.

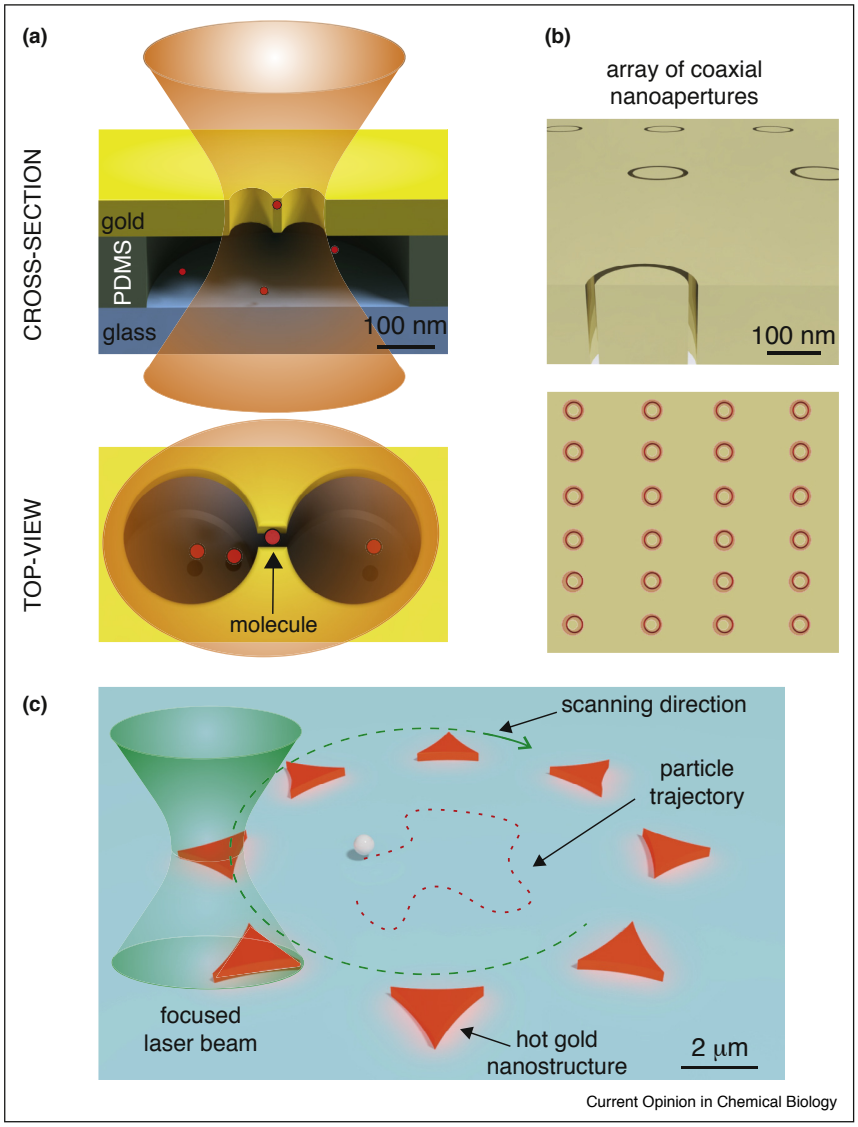
However, since proteins are essentially deformable dielectric objects, early realizations of molecular trapping in double nanohole apertures reported unfolding of trapped proteins [22]. It is likely that this aspect may be addressed through the use of different aperture geometries such as the coaxial nanoaperture [23••] (Figure 3b), in which case this new optical approach could turn into the method of choice for a wide variety of single molecule studies.

Thermophoretic trapping

The Soret effect refers to the motion of molecules and ions in solution in response to a spatial temperature gradient. Molecules travel either up or down a temperature gradient depending on the value of the Soret coefficient, which is about $1\,K^{-1}$ for a large DNA molecule [39]. Although the microscopic details of the process are not yet fully understood, particle motion is attributed to a temperature-induced spatial entropic gradient, entailing contributions from both the screening ions in solution as well interfacial water [39]. A spatial gradient in temperature therefore drives a molecule in solution to a location that minimizes the free energy of the system.

Braun *et al.* recently demonstrated the ability to use optically induced heating of a structured gold film in order to create the necessary spatial temperature profile in solution [24•] (Figure 3c). Large thermophoretically induced potential well depths, $U = S_T\,\Delta T > 10\,kT$ where k is Boltzmann's constant and T is the absolute ambient temperature, can be attained for certain macromolecular species. The requirement of a temperature difference of $\Delta T \sim 10\,K$ to stably confine λ–DNA which has a Soret coefficient, $S_T \sim 1\,K^{-1}$ however suggests that current experiments may have already attained the approximate size-limit of the approach. For example, S_T scaling as $\sqrt{L}$ for double-stranded DNA would imply a lower bound of 1000 bp for thermophoretic trapping of single DNA molecules [24•]. Nonetheless it remains to be seen if variations on the basic theme behind this conceptually novel approach — perhaps involving different ionic species in solution, or combination with other effects — may support operation in the regime of molecular dimensions approaching 1–10 nm.

Figure 3



Trapping based on the optical near-field and thermophoretic trapping. **(a)** Illumination of double nanohole apertures in a metal film confines single molecules in the cusp region between the nanoholes (≥5 mW in the optical focus) [22,23••]. **(b)** High density arrays of coaxial nanoaperture traps can confine molecules using low laser powers, <5 mW [23••]. **(c)** Plasmonic nanostructures heated by a scanning laser beam generate a radial temperature gradient in solution that traps single nano-objects via thermophoresis [51].

Geometry-induced trapping in nanoscale systems

Electrostatic and entropic trapping offer 'field-free' confinement

We recently demonstrated the use of an equilibrium thermodynamic principle that exploited geometry-induced local spatial minimization of free energy to trap single charged molecules in solution [26••]. Molecules confined in solution in a thin gap between like-charged parallel plates experience repulsive interaction energies everywhere in the slit except at locations where one of the slit walls carries a nanoscale surface indentation. At these locations, the slit surfaces are farther away and the repulsive interaction energy between the plates and object is smaller; in fact the free energy of interaction is set to go to zero by design, creating a stable thermodynamic trap for the object of interest. The approach not only permits trapping of single molecules without the application of any external fields, but it also provides sub-diffraction limited spatial confinement and highly parallel trapping of single entities (Figure 4a). Importantly, trapped molecules spend most of their time in a 'field-free' region where the electrical potential is zero, and thermal

equilibrium guarantees that the solution conditions are identical to those in the bulk (Figure 4a). This feature of geometry-induced trapping — using pure electrostatics, and possibly to some extent in the dielectrophoretic version as well (discussed next) — sets it apart from all other molecular trapping approaches where the trap is always a region of significant field.

We have shown that measuring the average residence time of a single molecule in a trap permits molecular electrical properties such as net charge, spatial charge distribution and interior dielectric constant to be measured with high precision, or inferred given additional information such as chemical composition [26••]. Trapped molecules migrating or 'hopping' through a lattice of traps can be followed individually in real time over a period of minutes or hours in order to extract information on slow dynamic molecular processes. Although operation of the electrostatic fluidic trap in its current form is confined to salt concentrations in the low mM range, improvements on this front may be expected in the future through the use of surface functionalization of the slit walls. Importantly, we demonstrated in a recent study that 'entropic enhancement' of geometry-induced trapping free energies could deliver all the advantages of electrostatic trapping while supporting operation in higher ionic strength solution, say 10 mM or higher [40•].

Dielectrophoretic trapping

The concept of geometry-induced modulation of an electrical interaction energy can be extended beyond the monopole electrostatic picture described above to the minimization of dipole energy in a spatially varying electric field. Electrodes in trough regions of a geometrically modulated nanochannel can be used to generate the required electric field gradients (Figure 4b). The frequency-dependent polarization response of an object in an electric field results in the formation of an effective molecular dipole that is either repelled or attracted to regions of high field. At very high field frequencies (~1 GHz) the system response is dominated by permittivities rather than conductivities and low dielectric nanoparticles in water seek field minima. At intermediate frequencies the qualitative response (positive or negative DEP) results from a balance between effective particle and medium conductivities. Using applied fields of about 1 V/μm at frequencies of 10 MHz in nanochannels with constrictions of cross sectional dimension ~70 nm permits confinement of 144 kDa Immunoglobulin G molecules (diameter ca. 10 nm) in solutions of 16 mM ionic strength [20••]. Although the unfavourable third power scaling of dipole energy with molecular size may be offset by scaling down the dimensions of the constriction in this approach [20••], all things considered well depths larger than ~1 kT, where k is Boltzmann's constant, will be challenging to attain for smaller molecules (Figure 4b).

It is worth noting that of the current molecular trapping techniques, the ABEL trap and electrostatic fluidic trap are the only approaches that have demonstrated the ability to confine a single small molecule such as an organic fluorophore in solution [40•,41]. Furthermore although dissociative charging of an ionizable group is not energetically favoured in an apolar medium and electrostatic interactions are expected to be weak compared to water, the long screening length attainable permits the electrostatic fluidic trap to work surprisingly well in organic solvents [42]. This could open up possibilities for single molecule experiments in, for example, polymer chemistry [43].

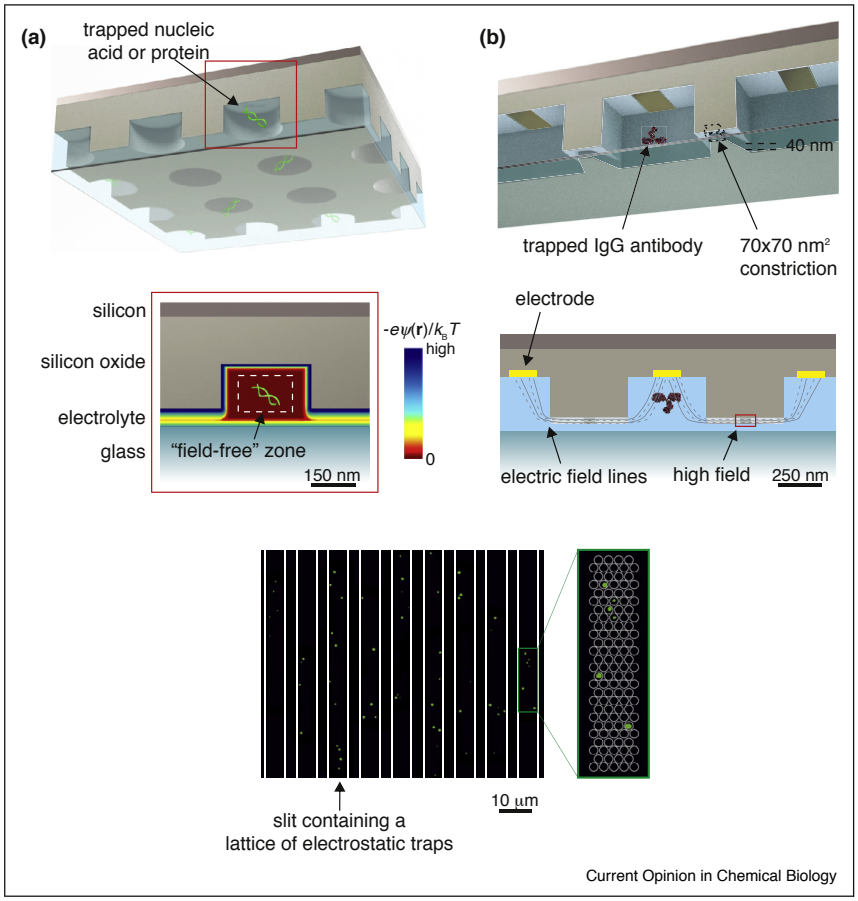
To summarize, realization of a technique that meets every single requirement of non-destructive or non-invasive trapping or confinement of a small molecule that offers long term (continuous observation time ~ seconds or minutes), strong spatial confinement (diffraction limited), in room temperature physiological solution conditions is yet to fully materialize; although most experiments will not require all these criteria to be met. The interesting question is now turning into what single molecule trapping can offer beyond long-term observation in the solution phase.

New science using single molecule traps

The effort to trap single molecules in solution has spawned new measurement techniques in molecular spectroscopy as well as approaches to addressing fundamental questions in molecular transport and the nature of the molecular interface in the fluid phase. For example, the nanoaperture optical trapping measurements have furnished an unanticipated novel way of measuring acoustic vibrational modes of single molecules [33,36]. Traps exploiting transport and thermodynamic principles have opened up the unique possibility of making high precision measurements of transport and physical properties of molecular species, including mixtures, at the single molecule level. Examples of such properties are electrical mobility [44••], translational [44••,45] and rotational diffusion coefficients [29], oligomeric state [44••], conformation [28], photophysical properties of pigment proteins [27,46], binding constants [38,44••], net electrical charge, non-uniform charge distribution, and dielectric constant of the globular interior of, for example, a folded protein [26••]. Furthermore, many of these approaches may enable careful examination of intermolecular interactions by controlling the precise number of molecules in a single trap.

Single molecules serve as highly well defined probes of interaction energies in solution. Relating accurate experimental measurements to the appropriate theory will likely foster a deeper understanding of the underlying phenomenology and the discovery of new effects. For instance, the ability to probe the transport and interactions of a single well-defined entity such as short dsDNA fragment in

Figure 4



Geometry-induced electrical trapping. **(a)** The electrostatic fluidic trap [25,26••,40•]. Schematic representation of the fluidic nanostructure used to generate a lattice of electrostatic traps in solution (upper panel). Spatial electrostatic potential distribution in a single trapping nanostructure. The dashed outline indicates the 'field-free' region in the trap where the electrical potential is zero and solution conditions (e.g. pH and salt concentration) are identical to those in the bulk. The energy scale shown is that of a negative point charge (middle panel). Representative wide field fluorescence microscopy image of single ATTO532 labelled 60bp DNA fragments in a lattice of electrostatic fluidic traps. The image presents a very low density of molecules (ca. 50 in the field of view), but high densities are now routine (Table 1). Locations of traps are indicated by circles and individual nanoslits bearing high-density lattices of traps are demarcated by vertical lines (lowest panel). **(b)** Dielectrophoretic trapping in a nanochannel [20••]. AC fields applied at electrodes in trough regions of a corrugated nanochannel create zones of high electric field at channel constrictions. At high frequencies energy barriers in the high-field zones enable confinement of macromolecules in the troughs. The approach has been used to demonstrate confinement and field driven sorting of large macromolecules. Depicted molecules are not to scale.

solution in a size-dependent manner may shed light on poorly understood phenomena such as the Soret effect and interfacial solvation. Precise measurements of electrical interaction free energies in solution could enhance our understanding of ion-specific effects in solution phase electrostatics, and possibly shed light on the long-standing "like-charge attraction" problem [47,48]. Measurements of electrical mobility at the single molecule level may enable more accurate comparisons and benchmarking against theoretical predictions, not possible previously due to poorer measurement accuracy inherent in ensemble-averaging experimental approaches. Many open questions in soft-matter and liquid state science, specifically in colloid physics, molecular biophysics, interfacial phenomena and electrohydrodynamics, may be addressed by the kind of high precision molecular level measurements enabled by single molecule trapping techniques. These advances may well be accompanied by the development of new ultrasensitive biomolecular detection technologies.

Conflict of interest statement

Nothing declared.

Acknowledgement

We gratefully acknowledge the European Research Council for financial support.

References and recommended reading

Papers of particular interest, published within the period of review, have been highlighted as:

- • of special interest
- •• of outstanding interest

1. Moerner WE, Kador L: **Optical detection and spectroscopy of single molecules in a solid**. *Phys Rev Lett* 1989, **62**:2535-2538.

2. Orrit M, Bernard J: **Single pentacene molecules detected by fluorescence excitation in a p-terphenyl crystal**. *Phys Rev Lett* 1990, **65**:2716-2719.

3. Küchler A, Yoshimoto M, Luginbühl S, Mavelli F, Walde P: **Enzymatic reactions in confined environments**. *Nat Nanotechnol* 2016, **11**:409-420.

4. Haran G: **Surface-tethered lipid vesicles**. In *Encyclopedia of Biophysics.* Edited by Roberts GCK. Berlin Heidelberg: Springer; 2013:2553-2556 http://dx.doi.org/10.1007/978-3-642-16712-6_524.

5. Gorris HH, Walt DR: **Analytical chemistry on the femtoliter scale**. *Angew Chem – Int Ed* 2010, **49**:3880-3895.

6. Ashkin A, Dziedzic JM, Bjorkholm JE, Chu S: **Observation of a single-beam gradient force optical trap for dielectric particles**. *Opt Lett* 1986, **11**:288.

7. Rondelez Y *et al.*: **Microfabricated arrays of femtoliter chambers allow single molecule enzymology**. *Nat Biotechnol* 2005, **23**:361-365.

8. Shon MJ, Cohen AE: **Mass action at the single-molecule level**. *J Am Chem Soc* 2012, **134**:14618-14623.

9. Huh D *et al.*: **Tuneable elastomeric nanochannels for nanofluidic manipulation**. *Nat Mater* 2007, **6**:424-428.

10. Tyagi S *et al.*: **Continuous throughput and long-term observation of single-molecule FRET without immobilization**. *Nat Methods* 2014, **11**:297-300.

11. Leslie SR, Fields AP, Cohen AE: **Convex lens-induced confinement for imaging single molecules**. *Anal Chem* 2010, **82**:6224-6229.

12. Berard DJ *et al.*: **Convex lens-induced nanoscale templating**. *Proc Natl Acad Sci U S A* 2014, **111**:13295-13300.

13. Berard DJ *et al.*: **Formatting and ligating biopolymers using adjustable nanoconfinement**. *Appl Phys Lett* 2016, **109**.

14. Banterle N, Lemke EA: **Nanoscale devices for linkerless long-term single-molecule observation**. *Curr Opin Biotechnol* 2016, **39**:105-112.

15. Liu C *et al.*: **3D single-molecule tracking enables direct hybridization kinetics measurement in solution**. *Nanoscale* 2017, **9**:5664-5670.

16. Cohen AE, Moerner WE: **Method for trapping and manipulating nanoscale objects in solution**. *Appl Phys Lett* 2005, **86**:1-3.

17. Davis LM *et al.*: **Electrokinetic delivery of single fluorescent biomolecules in fluidic nanochannels**. *Proc Biosens* 2008, **7035** 70350A-7035–12.

18. • Lesoine JF, Venkataraman PA, Maloney PC, Dumont ME, Novotny L: **Nanochannel-based single molecule recycling**. *Nano Lett* 2012, **12**:3273-3278.
This paper demonstrates a facile route to confining a single molecule in solution using an alternating electrical field in one dimension.

19. Guan W, Joseph S, Park JH, Krstic PS, Reed MA: **Paul trapping of charged particles in aqueous solution**. *Proc Natl Acad Sci U S A* 2011, **108**:9326-9330.

20. •• Eberle P *et al.*: **Single entity resolution valving of nanoscopic species in liquids**. *Nat Nanotechnol* 2018, **13**:578-582.
The authors demonstrate the use of external electric fields in the electrostatic fluidic trap to confine single immunoglobulin G antibodies.

21. Juan ML, Gordon R, Pang Y, Eftekhari F, Quidant R: **Self-induced back-action optical trapping of dielectric nanoparticles**. *Nat Phys* 2009, **5**:915.

22. Pang Y, Gordon R: **Optical trapping of a single protein**. *Nano Lett* 2012, **12**:402-406.

23. •• Yoo D *et al.*: **Low-power optical trapping of nanoparticles and proteins with resonant coaxial nanoaperture using 10 nm Gap**. *Nano Lett* 2018, **18**:3637-3642.
Nanoaperture trapping takes an important step forward in the paper. The use of coaxial apertures in a metal film permits both low-power and highly parallel trapping of single molecules.

24. • Braun M, Bregulla AP, Günther K, Mertig M, Cichos F: **Single molecules trapped by dynamic inhomogeneous temperature fields**. *Nano Lett* 2015, **15**:5499-5505.
The authors demonstrate the ability to use optically controlled temperature gradients to stably spatially confine λ-DNA in solution.

25. Krishnan M, Mojarad N, Kukura P, Sandoghdar V: **Geometry-induced electrostatic trapping of nanometric objects in a fluid**. *Nature* 2010, **467**:692-695.

26. •• Ruggeri F *et al.*: **Single-molecule electrometry**. *Nat Nanotechnol* 2017, **12**:488.
The work demonstrates the use of the electrostatic fluidic trap to stably confine single molecules and measure their effective charge with sub-elementary charge precision. The molecular species examined range from single-stranded and double-stranded nucleic acids to globular and disordered proteins.

27. Squires AH, Moerner WE: **Direct single-molecule measurements of phycocyanobilin photophysics in monomeric C-phycocyanin**. *Proc Natl Acad Sci U S A* 2017, **114** 201705435.

28. Manger LH *et al.*: **Revealing conformational variants of solution-phase intrinsically disordered tau protein at the single-molecule level**. *Angew Chem Int Ed* 2017, **56**:15584-15588.

29. Yang HY, Moerner WE: **Resolving mixtures in solution by single-molecule rotational diffusivity**. *Nano Lett* 2018, **18**:5279-5287.

30. Clarke RW, Piper JD, Ying L, Klenerman D: **Surface conductivity of biological macromolecules measured by nanopipette dielectrophoresis**. *Phys Rev Lett* 2007, **98** 198102.

31. Freedman KJ *et al.*: **Nanopore sensing at ultra-low concentrations using single-molecule dielectrophoretic trapping**. *Nat Commun* 2016, **7**:1-9.

32. Fazal FM, Block SM: **Optical tweezers study life under tension**. *Nat Photon* 2011, **5**:318-321.

33. Al Balushi AA, Gordon R: **A label-free untethered approach to single-molecule protein binding kinetics**. *Nano Lett* 2014, **14**:5787-5791.

34. Gordon R: **Biosensing with nanoaperture optical tweezers**. *Opt Laser Technol* 2019, **109**:328-335.

35. •• Wheaton S, Gelfand RM, Gordon R: **Probing the Raman-active acoustic vibrations of nanoparticles with extraordinary spectral resolution**. *Nat Photon* 2014, **9**:68.
The authors perform spectroscopy on Raman-active modes of single proteins confined in a nano-aperture trap with three orders of magnitude better spectral resolution that the conventional approach.

36. Kotnala A, Wheaton S, Gordon R: **Playing the notes of DNA with light: extremely high frequency nanomechanical oscillations**. *Nanoscale* 2015, **7**:2295-2300.

37. Kotnala A, Gordon R: **Double nanohole optical tweezers visualize protein p53 suppressing unzipping of single DNA-hairpins**. *Biomed Opt Express* 2014, **5**:1886-1894.

38. Al Balushi AA, Gordon R: **Label-free free-solution single-molecule protein–small molecule interaction observed by double-nanohole plasmonic trapping**. *ACS Photon* 2014, **1**:389-393.

39. Duhr S, Braun D: **Why molecules move along a temperature gradient**. *Proc Natl Acad Sci U S A* 2006, **103**:19678-19682.

40. • Ruggeri F, Krishnan M: **Entropic trapping of a singly charged molecule in solution**. *Nano Lett* 2018, **18**:3773-3779.
This study presents the use of translational entropy to augment the depth of geometry-induced electrostatic potential wells thus enabling trapping of single fluorophores as well as operation in higher ionic strength solution.

41. Fields AP, Cohen AE: **Electrokinetic trapping at the one nanometer limit**. *Proc Natl Acad Sci U S A* 2011, **108**:8937-8942.

42. Kokot G, Bespalova MI, Krishnan M: **Measured electrical charge of SiO_2 in polar and nonpolar media**. *J Chem Phys* 2016, **145**.

43. Easter QT, Blum SA: **Single turnover at molecular polymerization catalysts reveals spatiotemporally resolved reactions**. *Angew Chem* 2017, **129**:13960-13963.

44. •• Wang Q, Moerner WE: **Single-molecule motions enable direct visualization of biomolecular interactions in solution**. *Nat Methods* 2014, **11**:555.
In this study, the ABEL trap is used to simultaneously determine the electrical mobility and diffusing coefficient of single molecules in solution. The technique is applied to analyse heterogenous mixtures of oligomeric proteins and hybridization kinetics of DNA.

45. Ruggeri F, Krishnan M: **Lattice diffusion of a single molecule in solution**. *Phys Rev E* 2017, **96** 62406.

46. Wang Q, Moerner WE: **Dissecting pigment architecture of individual photosynthetic antenna complexes in solution**. *Proc Natl Acad Sci U S A* 2015, **112**:13880-13885.

47. Grier DG: **A surprisingly attractive couple**. *Nature* 1998, **393**:621.

48. Polin M, Grier DG, Han Y: **Colloidal electrostatic interactions near a conducting surface**. *Phys Rev E* 2007, **76**:41406.

49. Hou JH, Venkatachalam V, Cohen AE: **Temporal dynamics of microbial rhodopsin fluorescence reports absolute membrane voltage**. *Biophys J* 2014, **106**:639-648.

50. Squires AH, Lavania AA, Dahlberg PD, Moerner WE: **Interferometric scattering enables flourescence-free electrokinetic trapping of single nanoparticles in free solution**. *Nano Lett* 2019, **19**:4112-4117.

51. Braun M, Cichos F: **Optically controlled thermophoretic trapping of single nano-objects**. *ACS Nano* 2013, **7**:11200-11208.

Statement of Authorship for joint/multi-authored papers for PGR thesis

To appear at the end of each thesis chapter submitted as an article/paper

The statement shall describe the candidate's and co-authors' independent research contributions in the thesis publications. For each publication there should exist a complete statement that is to be filled out and signed by the candidate and supervisor **(only required where there isn't already a statement of contribution within the paper itself).**

Title of Paper	Single-molecule trapping and measurement in solution
Publication Status	☑ Published □ Accepted for Publication □ Submitted for Publication □ Unpublished and unsubmitted work written in a manuscript style
Publication Details	M.I. Bespalova, S. Mahanta, and M. Krishnan Current Opinion in Chemical Biology, 51, (2019), 113-121

Student Confirmation

Student Name:	Maria Bespalova		
Contribution to the Paper	Participated in manuscript preparation		
Signature		Date	20.05.2022

Supervisor Confirmation

By signing the Statement of Authorship, you are certifying that the candidate made a substantial contribution to the publication, and that the description described above is accurate.

Supervisor name and title: Prof. Madhavi Krishnan			
Supervisor comments			
Signature		Date	20.05.2022

This completed form should be included in the thesis, at the end of the relevant chapter.

3

Surface charge measurements in polar and apolar solvents

Contents

3.1 Other measurement techniques 25
3.2 Surface charge measurements in an electrostatic fluidic trap 27
3.3 Paper II 28

The surface electrical charge of a solid material immersed in solution is one of the key parameters characterising the solid-liquid interface. There are few different mechanisms for the origin of surface charge including ionisation or dissociation of surface groups and adsorption or binding of ions from solution onto a surface [27] [28]. Furthermore, it is known that charging behavior in polar, e.g., aqueous, media differs from that in apolar solvents due to a higher electrostatic barrier to ionisation for the latter. That happens because the free energy of the Coulomb interactions, w, between two charges z_1 and z_2 is inversely proportional to dielectric permittivity of the medium, ε_s, which is usually higher for polar solvents [28]: $w = (z_1 z_2 e^2) \,/\, (4\pi\varepsilon_0\varepsilon_\mathrm{s} r)$. Here, z denotes the valence of ions, $\varepsilon_0\varepsilon_\mathrm{s}$ is the electrical permittivity of the medium, e is the elementary charge, and r is the distance between two ions. The distance at which $w = k_\mathrm{B}T$ characterises the length at which

electrostatic interactions are balanced by the thermal energy $k_{\mathrm{B}}T$ and is called the Bjerrum length, l_{B}. In order to prevent charge recombination or neutralisation, the distance between two ions should be larger than l_{B}. In polar solvents, such as water ($\varepsilon_{\mathrm{s}} = 78$), $l_{\mathrm{B}} \approx 0.7$ nm for 1-1 electrolytes and room temperature. Thus, the required charge separation can be easily achieved by formation of a hydration shell around the ions. However, in apolar solvents l_{B} takes much larger values. For example, in bromobenzene ($\varepsilon_{\mathrm{s}} = 5$), $l_{\mathrm{B}} \approx 11$ nm for a monovalent salt solution and room temperature, which makes it more difficult to stabilise the ions. Moreover building a solvation shell is impossible in apolar solvents due to the lack of sufficient dipole moment to facilitate this construction.

These factors, namely the larger Bjerrum length and the lack of sufficient dipole moment for apolar solvent molecules, result in fewer ions existing in a fluid which in turn leads to two or three orders of magnitude smaller surface charge in apolar solvents than in aqueous solutions. Although the surface charge is small in absolute terms in low dielectric media, it can still produce strong effects due to an order of magnitude larger Debye screening lengths, $\kappa^{-1} = \sqrt{\varepsilon_0 \varepsilon_{\mathrm{s}} k_{\mathrm{B}} T / 2 c N_{\mathrm{A}} e^2}$, than those attainable in aqueous solutions. Here N_A is Avogadro's number, and c is the salt concentration.

In both polar and apolar media, surface charge plays a significant role in controlling various properties of both hard and soft matter as well as of micro- and nanofluidic systems. As explained by the Derjaguin-Landau-Verwey-Overbeek (DLVO) theory, the interactions between charged colloidal particles and surfaces in solution occur via a screened electrostatic interaction [29] [30]. In aqueous solutions, this interaction can cause strong mutual repulsions between charged particles, leading to stabilisation of colloidal dispersions and preventing aggregation. This effect enables the use of charged nanoparticles in various applications, e.g., in drug delivery [31]. In apolar media, charging of colloidal particles also plays a crucial role in various applications, including the development of motor oil additives, drug delivery systems, printing toners and electrophoretic inks [32][33][34][35]. Thus,

the ability to know the surface charge of matter suspended in polar and apolar media is of great interest to both fundamental science and industrial purposes.

3.1 Other measurement techniques

A number of different experimental approaches have already been developed for measuring surface charge density, σ, or surface potential, ϕ_s, values in liquid media. Both σ and ϕ_s can be related to each other using the Grahame or Ohshima equations, which are based on Guoy-Chapman theory [36] [37].

A large group of standard measurement techniques is based on electrokinetic characterisation of colloids [38]. A wealth of methods exploiting various phenomena – electrophoretic, electroosmotic, streaming potential, and electroacoustic – have been successfully used to infer zeta potential, ζ, in dispersed nanoparticle systems [38][39][40]. Zeta potential is interpreted as the electrostatic potential at the shear plane separating the stagnant layer which moves together with the particle from the flowing liquid and is generally smaller than surface potential, ϕ_s [38]. Although extrapolating ϕ_s from ζ is a nontrivial task due to uncertainty in the distance between the shear plane and the surface, ζ measurements remain of considerable value establishing a lower limit for ϕ_s [41].

Conductance measurements in nanochannels represent another approach for probing surface charge at low salt concentrations [42][43][44]. This technique relies on the fact that in nanometer-size apertures with overlapped electrical double layers the electrical conductance is governed by surface charge and not by bulk salt concentration. However, establishing a direct correlation between measured conductances and σ values can be complicated and not accurate enough due to various assumptions used for nanochannel conductance modelling [45][46].

Another large group of methods relies on probing static properties of solid-liquid interfaces. One of the methods is potentiometric titration which is commonly used for probing average surface charge density [47]. More direct probing techniques, such as atomic force microscopy (AFM) and surface force apparatus (SFA), have

also been used for determining surface potentials by measuring force-distance curves between a surface and a particle or two surfaces [48][49][50].

Second-order nonlinear optical techniques, such as second harmonic generation (SHG) and sum-frequency generation (SFG), provide another way to characterise charged surfaces in liquid media and solid-liquid interfaces [51][52][53][54]. For example, SHG has proven to be a valuable technique for determining surface charge and surface pK_a values for substrates and particles in aqueous solutions [55][56][57][58]. Recent SHG experiments of Darlington *et al.* are of particular interest to our work [58]. Their study shows that surface SiO_2 groups can exist in three different states with different pK_a values and demonstrate the dependence of SiO_2 surface chemistry on pH history [58].

Apart from the above approaches, surface analysis techniques based on X-rays, such as X-ray reflectivity (XR), resonant anomalous XR (RAXR), and X-ray standing waves (XSW) techniques, have been employed to study the charging behaviour of solid-liquid interfaces [59][60][61][62][63]. For example, a new method for quantifying the value for surface charge density by measuring the maximum coverage of adsorbed counterions was demonstrated in a recent RAXR work [63]. Another novel approach combining X-ray photoelectron spectroscopy (XPS) with a liquid microjet was used for measuring the surface potential of SiO_2 nanoparticles suspended in an aqueous electrolyte [64]. In a later work, the applicability of this method was extended to predicting the structure of Stern layer [65]

While by no means exhaustive, the above list of techniques includes some of very common and well-established methods as well as relatively novel approaches. In our work, we propose another approach to measuring the net surface charge of ionizable surfaces immersed in pure aqueous or organic solvents based on the measurements of electrostatic interaction energies in an electrostatic fluid trap.

3.2 Surface charge measurements in an electrostatic fluidic trap

In the paper presented in this Chapter, *"Measured electrical charge of SiO_2 in polar and nonpolar media"* [7], we demonstrate a new approach for measuring the net electrical surface charge of ionisable surfaces using an electrostatic fluidic trap. Using silicon dioxide (SiO_2) as a test material, we performed the measurements of SiO_2 surface charge in a range of solvents of dielectric constants between 5 and 80. Specifically we used water ($\varepsilon_s = 78$), acetonitrile ($\varepsilon_s = 37$) and ethanol ($\varepsilon_s = 24$), and bromobenzene ($\varepsilon_s = 5$).

Briefly, our experimental approach is based on tracking single SiO_2 nanoparticles confined within electrostatic nanofluidic traps formed by SiO_2 surfaces. Using particles' positions inside the traps, we determined a radial probability density function, $P(r)$, which we further used to define the corresponding measured confining potential $F(r) = -k_B T \ln [P(r)/P_{max}(r)]$. In parallel, we numerically solved the nonlinear Poisson-Boltzmann equation for a given trap geometry using surface charge density, σ, of the SiO_2 surfaces as an input parameter. We further compared the experimentally measured confining potential, $F(r)$, with theoretically calculated free energy profiles to determine the best fit to the measured profile, and consequently the value of surface charge density. We found that the $\sigma(\varepsilon_s)$ dependence revealed in our experiments can be explained by a charge regulation model, which contains a single, physically plausible, tunable parameter.

Our approach for measuring the net surface charge does not require the use of external electric fields and can be applied to particles and solvents of any polarity and composition. Besides that, stable electrostatic trapping observed in low-polar and apolar media, e.g., well depth >50 $k_B T$ in acetonitrile, confirm the presence of significant repulsive forces in low-dielectric media. These results open up a prospective field of single molecule trapping and measurements in organic solvents or solvent mixtures.

3.3 Paper II

The Journal of Chemical Physics

Measured electrical charge of SiO_2 in polar and nonpolar media

Cite as: J. Chem. Phys. **145**, 194701 (2016); https://doi.org/10.1063/1.4967401
Submitted: 01 September 2016 • Accepted: 27 October 2016 • Published Online: 21 November 2016

G. Kokot, M. I. Bespalova and M. Krishnan

COLLECTIONS

This paper was selected as an Editor's Pick

View Online Export Citation CrossMark

ARTICLES YOU MAY BE INTERESTED IN

The charge of glass and silica surfaces
The Journal of Chemical Physics **115**, 6716 (2001); https://doi.org/10.1063/1.1404988

A simple model for electrical charge in globular macromolecules and linear polyelectrolytes in solution
The Journal of Chemical Physics **146**, 205101 (2017); https://doi.org/10.1063/1.4983485

Electrostatic free energy for a confined nanoscale object in a fluid
The Journal of Chemical Physics **138**, 114906 (2013); https://doi.org/10.1063/1.4795087

Lock-in Amplifiers up to 600 MHz
Zurich Instruments
Watch



© 2016 Author(s).

THE JOURNAL OF CHEMICAL PHYSICS **145**, 194701 (2016)

Measured electrical charge of SiO_2 in polar and nonpolar media

G. Kokot,[1,a)] M. I. Bespalova,[1,a)] and M. Krishnan[1,2,b)]
[1]*Department of Chemistry, University of Zurich, Winterthurerstrasse 190, CH 8057 Zurich, Switzerland*
[2]*Department of Physics, University of Zurich, Winterthurerstrasse 190, CH 8057 Zurich, Switzerland*

(Received 1 September 2016; accepted 27 October 2016; published online 15 November 2016)

We present measurements of the net electrical surface charge of silicon dioxide (SiO_2) in contact with solvents of dielectric constants between 5 and 80. Our experimental approach relies on observing the thermal motion of single silica particles confined in an electrostatic fluidic trap created by SiO_2 surfaces. We compare the experimentally measured functional form of the trapping potential with that from free energy calculations and thereby determine the net surface charge in the system. Our findings clearly demonstrate that contrary to popular perception, even in the absence of surfactants, the net electrical charge of ionizable surfaces in contact with apolar solvents can be large enough to lead to significant repulsive forces. A charge regulation model for SiO_2 surfaces with a single tunable parameter explains our measurements. This model may find general applicability in estimating the net charge of ionizable surfaces, given system parameters such as the dissociation or association constants of the ionizable groups and the pH, ionic strength, and dielectric constant of the solvent phase. *Published by AIP Publishing.* [http://dx.doi.org/10.1063/1.4967401]

I. INTRODUCTION

An ionizable chemical group in a solvent dissociates to yield a charged group and a free counterion; for many inorganic oxides in solution, the counterion is a proton. A surface carrying a large number of ionizable groups denoted by a density Γ thus acquires a net charge density, σ in contact with a polar medium, with the balance of electrostatics and entropy determining the magnitude of this net surface charge. Charged colloidal particles and surfaces in solution interact via a screened electrostatic interaction, described by Derjaguin-Landau-Verwey-Overbeek (DLVO) theory[1] and considered largely well understood. In the aqueous phase, mutual repulsions between particles can be strong enough to stabilize dense suspensions of colloidal particles against aggregation, and indeed the principle of charge stabilization is ubiquitous in nature and in industrial formulations.

In low dielectric media, however, the electrostatic self energy of an ion, which depends inversely on the medium's dielectric constant, ε_s, is high, rendering the formation of free ions highly statistically unlikely. Thus, while matter can be expected to be strongly charged in water ($\varepsilon_s \sim 80$), an ionizable surface should carry much less charge in a nonpolar medium with $\varepsilon_s \sim 5$. Although electrostatic interactions in apolar media are indeed weak relative to the aqueous phase,[2–7] the repulsion is often regarded as negligible[8,9] mainly on the basis of solvation energy arguments. Generally efforts are invested in enhancing repulsions in apolar media by the addition of micelle-forming surfactants that stabilize potential-determining ions[2–7,9] or by chemical modification of the surface.[3,4,9] Electrostatic interactions in nonpolar media have been exploited in model systems for atomic crystals[10,11] in chemical formulations[12] and technological applications such as electronic ink.[13,14] Knowledge of the surface charge of ionizable matter suspended in weakly polar or nonpolar media is important not only from a charge stabilization perspective but also from the more fundamental point of view of understanding, quantifying, and delineating the various contributions to the total interaction potential between colloidal particles or surfaces in various intervening media.

Several experimental techniques have been used to estimate the charge of colloidal particles in nonpolar media. In the electrokinetic approach, which is possibly the most widespread, the mobility of a particle an electric field is used as a measure of the electrical potential at the particle surface, namely, the zeta potential. The zeta potential in turn can be related to the electrical charge carried by the particle. The approach has been implemented in various forms on free particles in a DC electric field[4,15,16] or using an alternating field in combination with the particle-position control implemented optically[2,17] or piezoelectrically.[18] Fast detection and long observation times have further enabled the measurement of temporal fluctuations in electrical charge on very weakly charged optically trapped particles in a nonpolar solvent.[17] Techniques that probe the charge of particles by measuring their mutual interactions in an ensemble at equilibrium, in the absence of fields, have also been successfully implemented in nonpolar media containing surfactants.[3,19]

In this study we perform direct measurements of the equilibrium repulsive electrostatic potential of silica surfaces interacting across pure aqueous and organic solvents, namely, water (H_2O, ε_s = 78.3), acetonitrile (MeCN, ε_s = 36.64), ethanol (EtOH, ε_s = 24.3), and bromobenzene (BBr, ε_s = 5.4), with no added surfactants. Our approach to the problem of measuring a particle-surface interaction potential exploits the electrostatic fluidic trap for nano- or micron-scale matter in solution.[20–23] Briefly, the trap relies on the equilibrium thermodynamic

a)G. Kokot and M. I. Bespalova contributed equally to this work.
b)Electronic mail: madhavi.krishnan@uzh.ch

repulsion experienced by a particle confined in a fluid-filled micrometer-scale gap between the like-charged confining parallel plates. Micron-scale structuring of one of the slit surfaces leads to a modulation of the local electrostatic potential, creating a deep thermodynamic potential well for a like-charged entity (Fig. 1). We have previously demonstrated that in conjunction with a straightforward calculation of the trapping free energy, a direct optical measurement of the spatial sampling behavior of a single trapped particle can be used to measure its electrical charge with good precision.[21,23] In the present work, the walls of the slit and the particle are composed of SiO_2. Thus the theoretical model for the electrostatic free energy involves a single unknown parameter, namely, the regulated charge density, σ of the SiO_2 surfaces (slit and particle). Comparing the experimentally measured trapping potential for a single SiO_2 particle with a calculation of the spatial electrostatic interaction free energy where σ is a tunable parameter yields the net charge density of the SiO_2 surfaces in the system. Note that the entropic contribution to the total trap free energy arising from spatial fluctuations of the particle in z is estimated to be small (1%-10%) and therefore neglected in this work. Not only is the modeling of such a measurement more straightforward than, for example, the electrokinetic approach, but also in contrast our method probes the electrostatic interaction at equilibrium, at the single particle level, does not require calibration, and can be ubiquitously applied to particles and solvents of any polarity and composition.

In our measurements we encounter substantial repulsive electrostatic forces between silica surfaces even in a weakly polar solvent such as bromobenzene which was recently used as the intervening medium in an experiment to demonstrate the long range repulsive Casimir force between a gold and the silica surface.[8] Our measurements further permit us to estimate well the charge density of SiO_2 in contact with media of various polarities. Finally we apply a theoretical model that was originally proposed to describe the charge of SiO_2 and glass surfaces in water[24] to our measurements in various solvents. We find that the model captures our measurements of SiO_2 over the entire range of ε_s with the use of a single tunable parameter that contains the pH of the solvent and pK_a, the acid dissociation constant of the SiOH group in the solvent of interest. The results suggest that the model may be generally applied to estimate the electrostatic contribution to force measurements involving ionizable surfaces in the fluid phase.

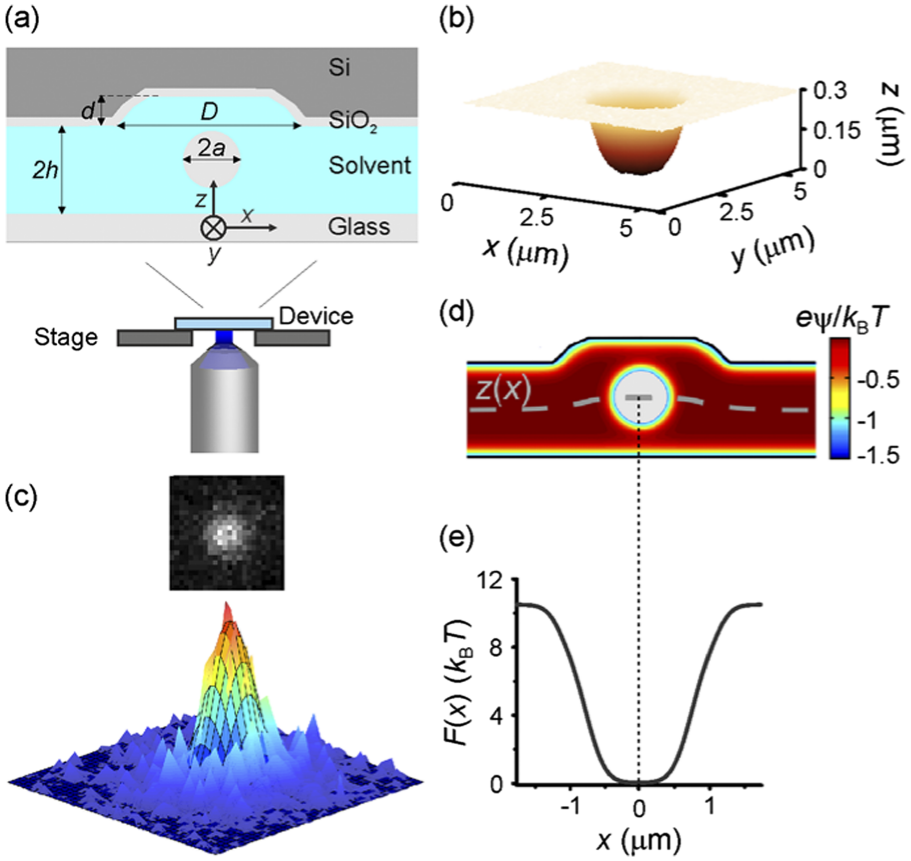


FIG. 1. (a) Schematic illustration of a single negatively charged SiO_2 microsphere of radius a, confined in an electrostatic fluidic trap, imaged using fluorescence microscopy. The cross-sectional view of a single trapping microstructure or pocket displays the relevant geometric parameters, namely, channel depth, $2h$; pocket depth, d; and pocket diameter, D. (b) 3D atomic force microscopy (AFM) image of pocket topography where the color scale spans a height range of 300 nm. (c) Typical fluorescence microscopy image of a single trapped particle (top), where the spatial intensity distribution (colormap, bottom) is fitted with an elliptical 2D Gaussian function (black contours). (d) Spatial electrostatic potential distribution, ψ around a particle in EtOH in a trapping microstructure (D = 2126 nm, $2h$ = 1139 nm, d = 308 nm, a = 325 nm). The dashed curve denotes the contour of minimum axial (z) electrostatic energy of the spherical particle as a function of lateral position, x. (e) Calculated spatial electrostatic free energy profile, $F(x)$ for parameter values in (d) for a particle surface charge density, $\sigma = -0.73 \times 10^{-3}$ e/nm^2.

II. EXPERIMENTAL METHODS

A. Electrostatic fluidic trap fabrication and characterization

The electrostatic fluidic trap devices were fabricated using a combination of photolithography and reactive-ion etching of Si substrates (for experiments in EtOH, MeCN, and H_2O) or wet-etching of glass substrates (for BBr), similar to previous work.[20] For measurements in EtOH, MeCN, and H_2O, the surface microstructures defining the trap locations were generally 300 nm deep and 2-2.2 μm in diameter, while the slit heights, $2h$, were in the range of 950-1150 nm. Surface features etched into Si substrate were coated with ~60 nm SiO_2. For experiments in BBr, however, the large Debye lengths involved (~400 nm) necessitated larger surface features with diameters, D, in the range 3.7-4.1 μm, depth, d ~ 1 μm, and slit height, $2h \sim 4$ μm. Therefore for BBr experiments alone, the surface indentations were wet-etched into the glass substrate using HF as previously described.[20] Surface-microstructured fluidic slits were thus created by a glass surface on one side and a silica surface on the other. The trapping microstructures were characterized by scanning electron microscopy (SEM), profilometry, and atomic force microscopy (AFM); the various geometric parameters of interest such as slit height, pocket diameter, and depth are illustrated in Fig. 1.

B. Solvent conductivity and salt concentration

We performed single particle trapping experiments in bromobenzene, ethanol, acetonitrile (all >99% purity, Sigma Aldrich), and water. Water content of the pure solvents were <1%, <0.1%, and <0.005% for BBr, EtOH, and MeCN, respectively. Solvent conductivities and pH were measured using inoLab Cond 7110 (Xylem Analytics) and LAQUA Twin (Horiba Scientific) conductivity meters, and an Orion Star A215 (ThermoFisher Scientific) pH meter. For experiments in BBr we added tetrabutylammonium chloride (TBAC) salt at a nominal concentration of 8 M. Conductivity measurements however revealed that the fractional dissolution of added salt was only 0.5%, which is in fact in good agreement with previously reported results on ion association constants of large salt ions in solvents of low polarity[25] (see the supplementary material). The final dissolved concentration of ~0.04 M corresponds to a Debye screening length, $\kappa^{-1} = \sqrt{\frac{\varepsilon_s \varepsilon_0 k_B T}{2 N_A c e^2}} = 388$ nm. Here ε_s is the relative permittivity of the solvent, ε_0 is the permittivity of vacuum, N_A is the Avogadro number, c is the concentration of monovalent salt in moles/L, and e is the elementary charge. Due to the extremely low solubility of ions in BBr, we assume that the bulk solvent conductivity value prior to the experiment does indeed accurately reflect the salt concentration during the measurement. For measurements in MeCN and EtOH, our inability to measure low conductivities in the small fluid volumes of the device reservoir necessitated the treatment of c as a fitting parameter in the comparison of the measurements with the calculation. Measurements in H_2O were performed in 1 mM Tris Buffer, pH 8.7, and under an argon atmosphere, necessitated by the requirement of a stable pH, and the fact that the SiO_2 microspheres (diameter 650 ± 30 nm, Corpuscular, Inc.) were supplied in 1 M NaOH. For these experiments, pH and conductivity of the inlet and outlet reservoirs were measured at the end of each experiment using a microconductivity meter. All measured conductivities were converted to concentrations of monovalent salt using standard curves generated by a series of measurements at known salt concentrations (see the supplementary material).

Zeta potential of the silica microspheres were measured in EtOH, MeCN, and H_2O using laser doppler microelectrophoresis (Malvern, Zetasizer Nano ZS90) (Table II).

C. Single particle trapping, spatial potential profile measurements, and net surface charge determination

The fluorescently labeled silica particles were purified by repeated rounds (typically 5) of centrifugation and resuspension in the solvent of interest. The particles were initially loaded into the microslits by capillary flow. After a few minutes, the flow was arrested by loading both inlet and outlet reservoirs with the particle suspension. The device was sealed to prevent evaporation of the solvent during the experiment and allowed to equilibrate for 10 min before commencing with optical measurements. The dynamics of single trapped particles were recorded on time scales of several minutes using a home-built wide-field fluorescence microscopy setup and an electron-multiplying charge-coupled device (EMCCD) camera (Luca, Andor, Inc.). Images were acquired using exposure times of 10 ms, much smaller than the shortest estimated position relaxation time (~0.45 s) of the particle in the potential well.[26] Scatter plots of particle position were generated by fitting a 2D Gaussian function to the intensity profile in each image, as previously described[21] (Figs. 1(c) and 2(c)). Particle positions were thus determined with an average precision of less than 30 nm and then used to generate a radial probability density function, $P(r)$, and the corresponding experimentally measured trapping potential, $F(r) = -k_B T \ln \frac{P(r)}{P_{max}(r)}$ (Figs. 2(b), 2(d), and 3). Measured $P(r)$ for a given trapped particle were verified to be invariant for variable exposure times in the range 6-20 ms, ensuring that there were no exposure-time induced artifacts in the shape of the measured potential.[27] In order to relate the measured potential profiles, $F(r)$ to a net surface charge density in the system, calculations of the position dependent electrostatic free energy were carried out in COMSOL Multiphysics using constant charge boundary conditions as previously described.[22,28] Briefly, we numerically solved the non-linear Poisson-Boltzmann (PB) equation in the geometry shown in Fig. 1(d) and evaluated the electrostatic free energy as a function of particle position. The inputs to the calculation were the geometric parameters for the trapping microstructure, average particle diameter, and the dielectric constant of the solvent. For BBr and H_2O, the measured salt concentration, c of the solvent served as an input parameter, while for EtOH and MeCN, c was a free fitting parameter. Thus σ, and where applicable, c, was varied in the calculation and the best-fit theoretically predicted potentials were determined for each single particle data set. Figures 2 and 3 present experimentally measured confining potentials and the associated

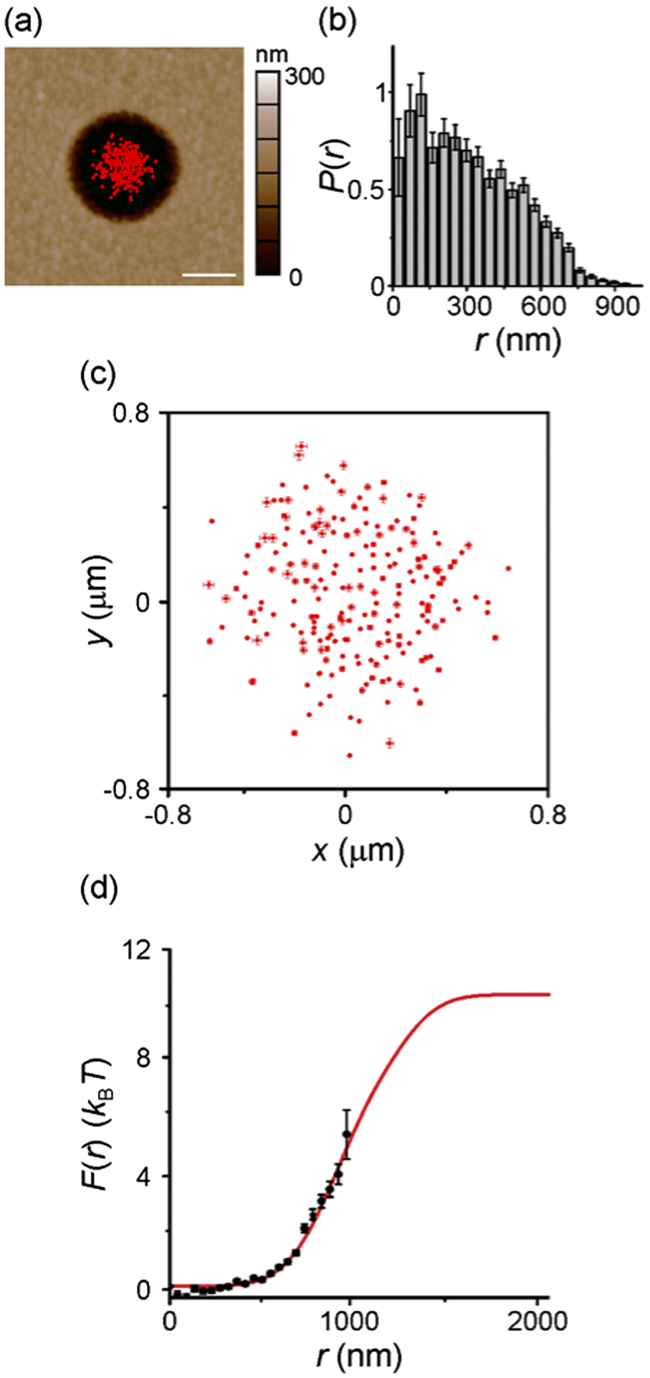


FIG. 2. Measurement of SiO_2 effective surface charge in ethanol. (a) Measured in-plane (x-y) trajectory of a single trapped particle superimposed on the AFM topographic image of the pocket. Each red symbol represents one detected position of the particle. (b) Histogram of the radial probability density, $P(r)$ for the data shown in (a). The displayed distribution was rescaled so that $P_{max}(r) = 1$. (c) The same scatter data as presented in (a) with error bars denoting precisions of localization. (d) Local electrostatic free energy, $F(r)$ (symbols) derived from the experimentally measured $P(r)$ presented in (b), and superimposed on the best-fit calculated potential profile (red line).

best-fit theoretically calculated free energy profiles for the representative single particles in all solvents. The resulting values of σ and κ^{-1} for each solvent together with other relevant system parameters are presented in Table I. We find that σ varies by over 2 orders of magnitude over the range of ε_s tested, with the uncertainty in particle size the dominant contribution to the measurement error (see below).

III. RESULTS AND DISCUSSION

In order to make controlled comparisons over a wide range of solvent polarities, we used the same probe particle sample in all measurements. Furthermore, since we expected a very low surface charge density for experiments in low-polarity solvents, we used a rather large particle size (radius, $a = 325 \pm 15$ nm) compared to our previous work in order to ensure a substantial trap depth of $\sim 10\ k_B T$. By doing so, however, it turned out impossible to achieve uniformly good measurement precision over the 4 order of magnitude range of experimental salt concentrations, necessitated by the range of solvent polarities examined. In water, for example, where κ^{-1} (~20 nm) $\ll a$ (~325 nm), the interaction between the particle and the slit walls, which determines the depth of the trap, resembles a parallel-plate interaction which in turn is exponentially sensitive to κa.[22] The dispersion in particle size thus implies large uncertainties in the value of the measured surface charge density. This uncertainty is further compounded by the non-linearity of the PB equation at the high net surface charge densities necessitated by the high pH ~9 under which the measurement had to be performed. As a result in this work, we are unable to place more than a lower bound on the net charge density of SiO_2 surfaces in water. The EtOH, MeCN, and BBr measurements on the other hand involve smaller values of κa and therefore do not display the same sensitivity of measured surface charge to particle size. The larger Debye lengths in these solvents also yield large well depths even though the net surface charge of the surfaces is relatively low (Table I). The experimental conditions were thus conducive to achieving a reasonable measurement precision of 15%-20% in these solvents.

Furthermore, despite the fact that it was not possible to reliably measure the true conductivity of the microliter solvent reservoirs in the experiments with non-aqueous solvents, the functional form of the measured trapping potential permitted independent determination of the effective screening length in the system as a fit parameter in the EtOH and MeCN measurements. We point out that in BBr, the large Debye lengths that result from weak dissociation of added salt[10,29] resulted in harmonic potential wells for the microstructure geometry used (d ≈ 4 μm) (Fig. 3(c)). Leaving the screening length (salt concentration) as a fit parameter as we did for EtOH and MeCN, it was possible to clearly establish an upper bound on the concentration. However given the dimension of the trapping microstructure, d ≈ 4 μm in the present experiment, it was impossible to establish a lower bound on the concentration in a fitting procedure where the charge density of the system is unknown in addition. Although experiments and theory involving high ion concentrations in apolar media suggest that the formation of Bjerrum pairs can greatly inflate the Debye length,[30,31] at the low concentrations of added TBAC ($\sim 10^{-5}$M) in our experiment, the measurement is well within the regime where the screening length should be correctly estimated by the conductivity-based measurement of free ions.[31] So for BBr we used the measured salt concentration

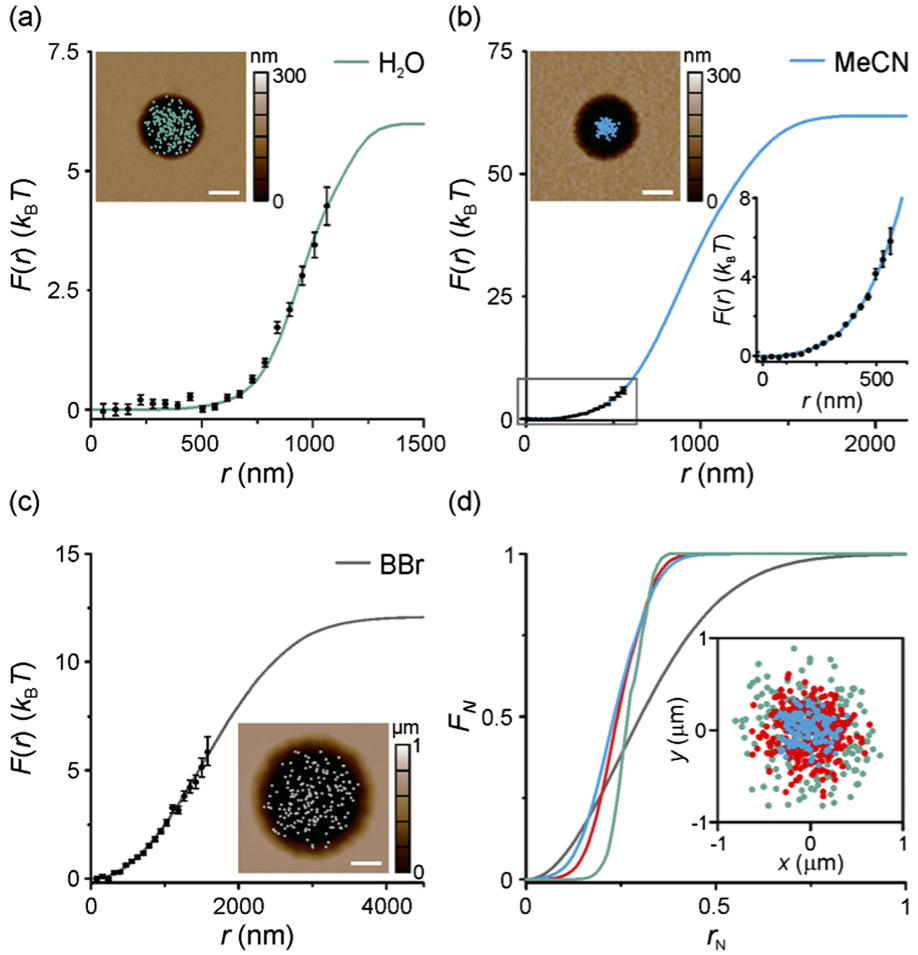


FIG. 3. Experimentally measured (symbols) and calculated (lines) spatial electrostatic free energy profiles, $F(r)$ for a single trapped particle in water (a), acetonitrile (b), and bromobenzene (c). The insets display scatter plots of particle positions overlaid on AFM images of the pockets. Scale bars represent 1 μm. (d) Normalized $F(r)$ values, F_N plotted against the normalized pocket radius, r_N for water (green), acetonitrile (blue), ethanol (red), and bromobenzene (gray). The inset represents spatial scatter plots for single particles in water (green), acetonitrile (blue), and ethanol (red), trapped by the pockets of diameter, D = 2120 ± 80 nm. The plot emphasizes the influence of the Debye length on the degree of confinement of the particle.

as an input parameter to determine σ from the experimentally measured $F(r)$.

A. Comparing experimental measurements with a charge regulation model for the net surface charge of SiO_2

We now compare our experimental measurements with a simple theoretical model for the net surface charge that takes into consideration the dielectric constant, salt concentration, and pH of the solvent. For low surface potentials, the linear regime of the Poisson–Boltzmann equation yields the following relationship between the surface charge and surface potential, $\sigma = \varepsilon_s \kappa \psi_s$. Assuming the surface potential, ψ_s remains constant and we thus expect

$$\sigma \propto \sqrt{\varepsilon_s} \tag{1}$$

at the simplest level of approximation. In practice, however, the relationship between surface charge, surface potential, and system parameters such as κ and ε_s is more accurately described by the following two equations:[32]

TABLE I. Experimentally measured and theoretically estimated parameters for experiments in water (H_2O), acetonitrile (MeCN), ethanol (EtOH), and bromobenzene (BBr). Uncertainties on σ represent standard deviations from 9 to 12 single particle measurements in each solvent, including contributions from uncertainties on particle radius, a and salt concentration, c

		Experimental quantities					Theoretical parameters	
Solvent	ε_s	c, μM	pH	κ^{-1}	p_{fit}	$-\sigma$, 10^{-3} e/nm^2	b	p_{est}
H_2O	78.3	245 ± 9	8.7	19.6 ± 0.3	–	~90	0	-1.2
MeCN	36.64	3.8 ± 0.4	6.1	106 ± 6	3.35	0.8 ± 0.1	1.44	2.84
EtOH	24.3	6.5 ± 0.5	7.3	66 ± 3	3.3	0.9 ± 0.2	2.8	3.0
BBr	5.4	0.040 ± 0.002	-	388 ± 13	1.9	0.35 ± 0.06	17.2	~1.5 to 3.0

$$\psi_s(\sigma) = \frac{k_B T}{e} \ln\left(\frac{-\sigma}{e\Gamma + \sigma}\right) + p\frac{k_B T \ln 10}{e}, \quad (2)$$

$$\sigma(\psi_s) = \frac{2\varepsilon_s \varepsilon_0 \kappa k_B T}{e} \sinh\left(\frac{e\psi_s}{2k_B T}\right), \quad (3)$$

where $p = pK_a - pH$, and we take $\Gamma = 8\ nm^{-2}$ as the density of ionizable surface sites and ignore the Stern layer capacitance.[24] A previous study[33] uses what is essentially a $1 - pK_a$ model for the silica surface, neglects the contribution of the Stern layer, and demonstrates good agreement with potentiometric measurements of surface charge.[34] Note that $\sigma = -e\Gamma_{SiO^-}$ and $\Gamma = \Gamma_{SiO^-} + \Gamma_{SiOH}$.

Equation (2) captures the dependence of the net surface charge, σ on the proton concentration at the surface, which in turn depends on the pH of the bulk electrolyte and the surface potential, ψ_s. Equation (3) is the Grahame equation which comes from integrating the charge density in the diffuse double layer and setting it equal in magnitude to the net surface charge in order to satisfy the requirement of electroneutrality in the system.

The above system of equations contains a single parameter $p = pK_a - pH$, where $pK_{a,w} = 7.5$ denotes the acid dissociation constant of the ionizable surface SiOH groups in water.[24] Although the values of pH and pK_a are readily available for water, they can be difficult to directly measure in apolar media. We therefore treat p as a tunable parameter in applying the model to the solvents EtOH, MeCN, and BBr.

Solving Equations (2) and (3) for various values of p, we note the dependence $\frac{\sigma}{\sqrt{c}} \sim \varepsilon_s^{0.28}$, which is weaker than the square root dependence of (1) (solid line in Fig. 4(a)). However the model also reveals that the surface potential ψ_s itself depends weakly on the solvent dielectric constant as $\psi_s \sim \varepsilon_s^{-0.18}$ (solid line in Fig. 4(b)) which accounts rather well for the net $\sim \varepsilon_s^{0.28}$ dependence of σ at a given salt concentration, c.

Table I lists the measured values of σ and the corresponding best fit values of p, denoted by p_{fit}. We find that the experimental measurements for all the non-aqueous media are captured for p = 1.9-3.35 and now proceed to examine the physical relevance of the obtained values.

We begin by estimating $pK_{a,s}$ in each apolar medium starting from the value in water, $pK_{a,w}$. We assume that the electrostatic contribution from the Born solvation energy, b of a proton in a medium of dielectric constant ε_s is the dominant contribution to the shift in acid dissociation constant relative to water, $\Delta pK_{a,s} = pK_{a,s} - pK_{a,w}$.

Thus we have

$$\Delta pK_{a,s} \cong b = \frac{l_{b,w}}{4.606 a_{H^+}}\left(\frac{\varepsilon_w}{\varepsilon_s} - 1\right), \quad (4)$$

where $l_{b,w} = \frac{e^2}{4\pi\varepsilon_w\varepsilon_0 k_B T} = 0.714$ nm is the Bjerrum length in water at 25 °C, $a_{H^+} = 0.122$ nm is the radius of the hydronium ion,[35] and $\varepsilon_w = 78.3$ is the dielectric constant of water. In EtOH, for example, the estimated shift $\Delta pK_{a,s} = 2.8$ implies that the pK_a of the SiOH group would be expected to lie around 10.3. Measurements of the pH of pure ethanol yield a value of 7.3 (see the supplementary material), placing p_{est}, the theoretically estimated value of p at 3.0. This suggests that our experimentally obtained fit value, $p_{fit} = 3.3$ is indeed plausible.

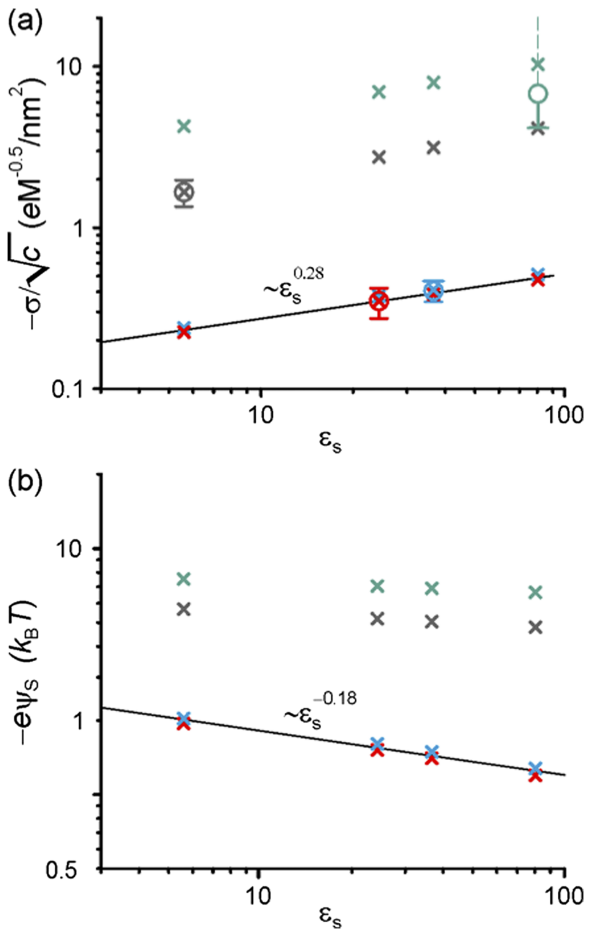


FIG. 4. (a) Theoretical dependence of $\frac{\sigma}{\sqrt{c}}$ on the solvent dielectric constant, ε_s calculated from the charge regulation model given by Equations (2) and (3) (colored crosses). Colors denote calculations of $\frac{\sigma}{\sqrt{c}}$ performed over the entire range of ε_s using specific combinations of the salt concentration, c and the corresponding best-fit p value (see Table I) for the relevant experimental measurement. Experimental measurements are denoted by open circular symbols at the relevant value of ε_s. The solid line represents $\frac{\sigma}{\sqrt{c}} \sim \varepsilon_s^{0.28}$ dependence. (b) Theoretical dependence of the SiO_2 surface potential, ψ_s on ε_s corresponding to the calculations in (a). Solid line denotes $\psi_s \sim \varepsilon_s^{-0.18}$ dependence.

Similarly for acetonitrile, taking the experimentally inferred background conductivity of 0.3 μM of monovalent ions as an order of magnitude estimate of the free proton concentration points to $pH_{MeCN} = 6.5$, which is in fact reasonably close to our measured value of $pH_{MeCN} = 6.1$ (the supplementary material). $\Delta pK_{a,s} = 1.44$ estimated using Eq. (4) and $pH_{MeCN} = 6.1$ together imply an independently determined value of $p_{est} = 2.84$, which again compares reasonably well with the experimentally obtained $p_{fit} = 3.35$.

In BBr, the background solvent conductivity is too small to be directly measured (<0.005 μS/cm) and so we cannot estimate the pH independently. However we note that the measured pH of EtOH and MeCN roughly points to the relation pH_s-$pH_w \sim b$. Here the effective pH of pure water, pH_w is around 5.5-6 owing to the dissolution of CO_2 from the atmosphere[36] and pH_s is the pH of the solvent under consideration. Since it may be reasonable to assume that pH_s and the acid dissociation constant $pK_{a,s}$ of the surface ionizable groups in the solvent respond to a first approximation in a similar way

TABLE II. Comparison of our measured surface charge, σ with that obtained from electrophoretic mobility measurements. ζ—measured zeta potential; σ_{zeta}—the corresponding surface charge density; ψ_s—surface potential corresponding to σ

Solvent	$-\zeta$, (mV)	$-\sigma_{zeta}$, $10^{-3}e/nm^2$	$-\psi_s$, mV	$-\sigma$, $10^{-3}e/nm^2$
H_2O	71 ± 15	22 ± 7 (23 ± 8)	140	~90
MeCN	36 ± 27	0.7 ± 0.6 (1.0 ± 0.9)	38 ± 4	0.8 ± 0.1
EtOH	44 ± 13	1.0 ± 0.4 (1.2 ± 0.4)	39 ± 6	0.9 ± 0.2

to ε_s, taking water ($p \sim 2$) as the reference state, the measurement for BBr might also be expected to be captured by a value of $p \sim 1.5$ to 3. In fact we find good agreement between the measured net charge density of SiO_2 and the value predicted by the charge regulation model for p = 1.9.

Finally, for experiments in water at pH 8.7, we find that the experimentally estimated σ is in order of magnitude agreement with the model prediction for p = −1.2. Overall our study shows that the pK_a of the ionizable groups and pH of the solvent phase play a strong role in determining the net electrical charge of an ionizable surface in media of various polarities. Interestingly we find that although BBr has a dielectric constant ≃7 times smaller than that of MeCN, at -0.35×10^{-3} e/nm^2 the net charge density of SiO_2 in BBr is smaller than that in MeCN by not much more than a factor of 2. The same value is however around an order of magnitude smaller than the measured surface charge of mica in contact with nonpolar solvents containing surfactants.[6]

To conclude, Table II presents measured zeta potentials, ζ, for silica microspheres, and surface charge density values, σ_{zeta} calculated using Equation (3), where $\psi_s = \zeta$. The values in parentheses include the curvature correction due to finite κa.[24] Comparing these values with those obtained using our approach, it is interesting to note that in the linear regime, $e|\psi_s| \sim k_BT$ ($|\psi_s| \sim 25$ mV), which holds for EtOH and MeCN, both methods agree well. But in water where surfaces are strongly charged and non-linearities become important, our approach is able to capture the theoretical prediction, where the corresponding mobility-based value significantly underestimates both surface charge and surface potential.

IV. CONCLUSION

We have demonstrated the use of an electrostatic fluidic trap to directly measure the net surface charge density of ionizable surfaces over a wide range of solvent polarity. The experimental approach is highly versatile, can be applied to solvents of any polarity and composition, makes use of any optically detectable probe particle, and does not involve the use of external electric fields. We find that the measurements can be captured by a charge regulation model containing a single tunable parameter whose value was found physically plausible in all cases. The charge regulation model we tested captures our measurements over a wide range of polarities tested and may find general applicability in estimating the magnitude of net surface charge and electrostatic interactions in experiments in apolar media. Furthermore our technique may be thought of as a form of optical force microscopy with the crucial advantage that it replaces the relatively challenging measurement of a highly calibration-sensitive axial particle-surface interaction potential[37] with a direct measurement based on calibration-free, in-plane spatial information on particle position. Probing an equilibrium interaction at the single particle level, the method also successfully sidesteps concerns on pair-wise additivity of interparticle potentials that often arise in measurements of long-ranged interactions in particle ensembles.

SUPPLEMENTARY MATERIAL

See supplementary material for conductivity-concentration calibration curves, SiO_2 microsphere size distribution measurements, and pH measurements for EtOH and MeCN.

ACKNOWLEDGMENTS

We gratefully acknowledge the Swiss National Science Foundation and University of Zurich for financial support. Nanofabrication was carried out at FIRST Center for Micro- and Nanoscience, ETH Zurich.

[1] E. Verwey and J. T. G. Overbeek, *Theory of the Stability of Lyophobic Colloids* (Elsevier Publishing Company, 1948).
[2] G. S. Roberts, T. A. Wood, W. J. Frith, and P. Bartlett, "Direct measurement of the effective charge in nonpolar suspensions by optical tracking of single particles," J. Chem. Phys. **126**, 194503 (2007).
[3] S. K. Sainis, V. Germain, C. O. Mejean, and E. R. Dufresne, "Electrostatic interactions of colloidal particles in nonpolar solvents: Role of surface chemistry and charge control agents," Langmuir **24**, 1160–1164 (2008).
[4] P. G. Smith, M. N. Patel, J. Kim, T. E. Milner, and K. P. Johnston, "Effect of surface hydrophilicity on charging mechanism of colloids in low-permittivity solvents," J. Phys. Chem. C **111**, 840–848 (2007).
[5] C. E. McNamee, Y. Tsujii, and M. Matsumoto, "Interaction forces between two silica surfaces in an apolar solvent containing an anionic surfactant," Langmuir **20**, 1791–1798 (2004).
[6] W. H. Briscoe and R. G. Horn, "Direct measurement of surface forces due to charging of solids immersed in a nonpolar liquid," Langmuir **18**, 3945–3956 (2002).
[7] F. Strubbe, F. Beunis, and K. Neyts, "Determination of the effective charge of individual colloidal particles," J. Colloid Interface Sci. **301**, 302–309 (2006).
[8] J. N. Munday, F. Capasso, and V. A. Parsegian, "Measured long-range repulsive Casimir-Lifshitz forces," Nature **457**, 170–173 (2009).
[9] J. Ge, L. He, J. Goebl, and Y. Yin, "Assembly of magnetically tunable photonic crystals in nonpolar solvents," J. Am. Chem. Soc. **131**, 3484–3486 (2009).
[10] M. E. Leunissen, C. G. Christova, A.-P. Hynninen, C. P. Royall, A. I. Campbell, A. Imhof, M. Dijkstra, R. Van Roij, and A. Van Blaaderen, "Ionic colloidal crystals of oppositely charged particles," Nature **437**, 235–240 (2005).
[11] P. Bartlett and A. I. Campbell, "Three-dimensional binary superlattices of oppositely charged colloids," Phys. Rev. Lett. **95**, 128302 (2005).
[12] R. J. Pugh, T. Matsunaga, and F. M. Fowkes, "The dispersibility and stability of carbon-black in media of low dielectric-constant. 1. Electrostatic and steric contributions to colloidal stability," Colloids Surf. **7**, 183–207 (1983).
[13] B. Comiskey, J. Albert, H. Yoshizawa, and J. Jacobson, "An electrophoretic ink for all-printed reflective electronic displays," Nature **394**, 253–255 (1998).
[14] Y. Chen, J. Au, P. Kazlas, A. Ritenour, H. Gates, and M. McCreary, "Electronic paper: Flexible active-matrix electronic ink display," Nature **423**, 136 (2003).
[15] R. Kornbrekke, I. Morrison, and T. Oja, "Electrophoretic mobility measurements in low conductivity media," Langmuir **8**, 1211–1217 (1992).
[16] J. F. Miller, K. Schtzel, and B. Vincent, "The determination of very small electrophoretic mobilities in polar and nonpolar colloidal dispersions using phase analysis light scattering," J. Colloid Interface Sci. **143**, 532–554 (1991).

[17]F. Beunis, F. Strubbe, K. Neyts, and D. Petrov, "Beyond Millikan: The dynamics of charging events on individual colloidal particles," Phys. Rev. Lett. **108**, 016101(2012).
[18]A. T. Prez and E. Lemaire, "Measuring the electrophoretic mobility of concentrated suspensions in nonaqueous media," J. Colloid Interface Sci. **279**, 259–265 (2004).
[19]M. F. Hsu, E. R. Dufresne, and D. A. Weitz, "Charge stabilization in nonpolar solvents," Langmuir **21**, 4881–4887 (2005).
[20]M. Krishnan, N. Mojarad, P. Kukura, and V. Sandoghdar, "Geometry-induced electrostatic trapping of nanometric objects in a fluid," Nature **467**, 692–695 (2010).
[21]N. Mojarad and M. Krishnan, "Measuring the size and charge of single nanoscale objects in solution using an electrostatic fluidic trap," Nat. Nanotechnol. **7**, 448–452 (2012).
[22]M. Krishnan, "Electrostatic free energy for a confined nanoscale object in a fluid," J. Chem. Phys. **138**, 114906 (2013).
[23]N. Mojarad, V. Sandoghdar, and M. Krishnan, "Measuring three-dimensional interaction potentials using optical interference," Opt. Express **21**, 9377–9389 (2013).
[24]S. H. Behrens and D. G. Grier, "The charge of glass and silica surfaces," J. Chem. Phys. **115**, 6716–6721 (2001).
[25]R. J. LeSuer, C. Buttolph, and W. E. Geiger, "Comparison of the conductivity properties of the tetrabutylammonium salt of tetrakis(pentafluorophenyl)borate anion with those of traditional supporting electrolyte anions in nonaqueous solvents," Anal. Chem. **76**, 6395–6401 (2004).
[26]W. P. Wong and K. Halvorsen, "The effect of integration time on fluctuation measurements: Calibrating an optical trap in the presence of motion blur," Opt. Express **14**, 12517–12531 (2006).
[27]W. P. Wong and K. Halvorsen, "Beyond the frame rate: Measuring high-frequency fluctuations with light-intensity modulation," Opt. Lett. **34**, 277–279 (2009).
[28]J. T. G. Overbeek, "The role of energy and entropy in the electrical double-layer," Colloids Surf. **51**, 61–75 (1990).
[29]M. E. Leunissen, J. Zwanikken, R. Van Roij, P. M. Chaikin, and A. Van Blaaderen, "Ion partitioning at the oilwater interface as a source of tunable electrostatic effects in emulsions with colloids," Phys. Chem. Chem. Phys. **9**, 6405–6414 (2007).
[30]C. P. Royall, M. E. Leunissen, and A. van Blaaderen, "A new colloidal model system to study long-range interactions quantitatively in real space," J. Phys.: Condens. Matter **15**, S3581–S3596 (2003).
[31]J. Zwanikken and R. Van Roij, "Inflation of the screening length induced by Bjerrum pairs," J. Phys.: Condens. Matter **21**, 424102 (2009).
[32]T. Hiemstra, W. H. Riemsdijk, and G. H. van and Bolt, "Multisite proton adsorption modeling at the solid/solution interface of (hydr) oxides: A new approach," J. Colloid Interface Sci. **133**, 91–104(1989).
[33]M. Barisik, S. Atalay, A. Beskok, and S. Qian, "Size dependent surface charge properties of silica nanoparticles," J. Phys. Chem. C **118**, 1836–1842 (2014).
[34]M. Kobayashi, F. Juillerat, P. Galletto, and M. Borkovec, "Aggregation and charging of colloidal silica particles: Effect of particle size," Langmuir **21**, 5761–5769 (2005).
[35]J. T. Rubino and W. S. Berryhill, "Effects of solvent polarity on the acid dissociation-constants of benzoic-acids," J. Pharm. Sci. **75**, 182–186 (1986).
[36]J. D. Hem, *Study and Interpretation of the Chemical Characteristics of Natural Water* (U.S. Geological Survey, 1985).
[37]D. C. Prieve, "Measurement of colloidal forces with tirm," Adv. Colloid Interface Sci. **82**, 93–125 (1999).

Supplementary Material
Measured electrical charge of SiO_2 in polar and nonpolar media

G. Kokot,[1,a)] M. I. Bespalova,[1,a)] and M. Krishnan[1,2,b)]

[a)]Equal contribution

[b)]Electronic mail: madhavi.krishnan@uzh.ch

1) *Department of Chemistry, Winterthurerstrasse 190, University of Zurich, CH 8057 Zurich, Switzerland.*

2) *Department of Physics, Winterthurerstrasse 190, University of Zurich, CH 8057 Zurich, Switzerland.*

A. Calibration curves showing the relationship between measured solution conductivity, γ and salt concentration, c^* which is determined based on the amount of added salt, for water (H_2O), acetonitrile (MeCN), ethanol (EtOH), and bromobenzene (BBr)

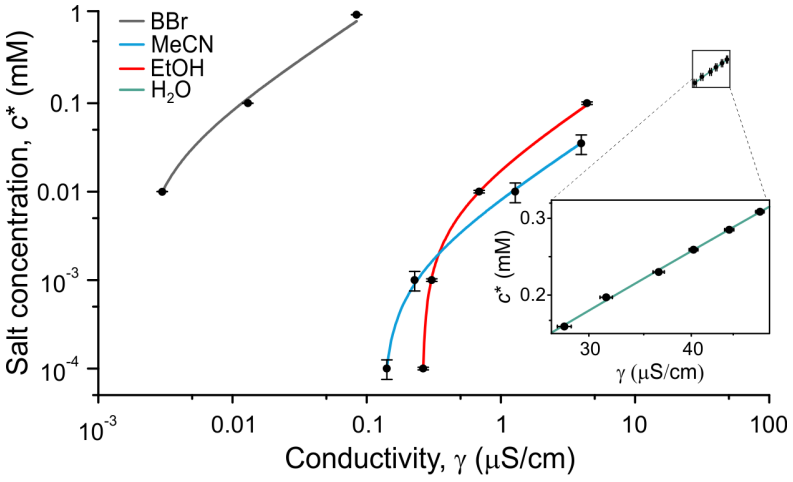


FIG. S1. Calibration curves displaying the relationship between c^* and the measured electrical conductivity, γ. Solid lines represent linear fits of the form $c^*=A\gamma + B$ for H_2O (green), MeCN (blue), EtOH (red), and BBr (gray).

The concentration versus conductivity curves for various solvents were generated as follows: for H_2O, EtOH and MeCN we measured conductivity values of standard solutions of known salt (NaCl) concentration based on the amount of added salt in a given volume of solvent. The coefficients A in the linear fit function were found to agree very closely with the theoretically expected values $\frac{6\pi\eta a_\mathrm{h}}{e^2 N_\mathrm{A}}$ where a_h is average radius of the ions Na^+ and Cl^-, $a_\mathrm{h} = \frac{a_{\mathrm{Na}^+} + a_{\mathrm{Cl}^-}}{2}$, η the viscosity of the solvent, N_A the Avogadro number, and e the elementary electric charge.

For BBr, however we found that the best fit value of A was more than two orders of magnitude higher than that expected based on the radius of the TBAC ion[1]. We attributed this observation to the poor solubility of salt in apolar solvents (see text) and concluded that $\sim 0.5\%$ of the added salt was actually dissolved. Thus the calibration curve enables a conversion of the measured conductivity to true salt concentration, c, where c=0.005c^* in the case of BBr. For all other solvents c=c^*.

B. Determination of the size distribution of the SiO_2 microspheres by scanning electron microscopy (SEM)

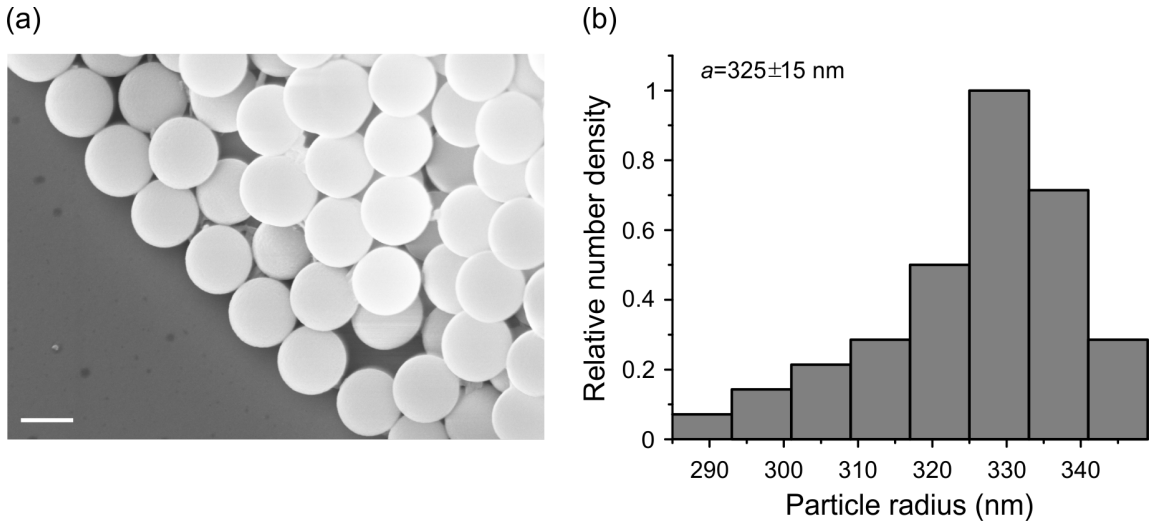


FIG. S2. (a) Scanning electron micrograph of SiO_2 particles. Scale bar represents 500 nm. (b) Experimentally obtained histogram of particle radii, denoting the average measured radius, $a = 325 \pm 15$ nm.

C. Estimating the pH for ethanol and acetonitrile

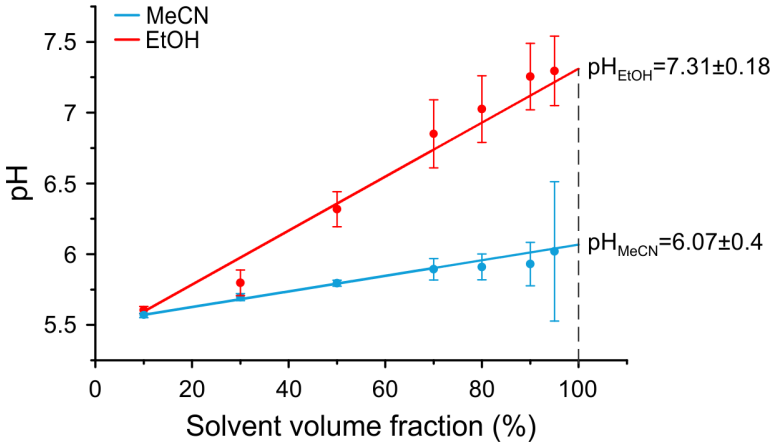


FIG. S3. pH of acetonitrile-water and ethanol-water mixtures were measured using a combination pH microelectrode. Solid lines represent best linear fits of the measured pH values vs. solvent volume fraction. Extrapolating solvent volume fraction to 100% yields an estimated pH for the pure solvent.

REFERENCES

[1]W. L. Masterton, D. Bolocofsky, and T. P. Lee, "Ionic radii from scaled particle theory of the salt effect," The Journal of Physical Chemistry **75**, 2809–2815 (1971).

Statement of Authorship for joint/multi-authored papers for PGR thesis

To appear at the end of each thesis chapter submitted as an article/paper

The statement shall describe the candidate's and co-authors' independent research contributions in the thesis publications. For each publication there should exist a complete statement that is to be filled out and signed by the candidate and supervisor **(only required where there isn't already a statement of contribution within the paper itself).**

Title of Paper	Measured electrical charge of SiO2 in polar and nonpolar media
Publication Status	☑ Published □ Accepted for Publication □ Submitted for Publication □ Unpublished and unsubmitted work written in a manuscript style
Publication Details	G. Kokot*, M. I. Bespalova*, and M. Krishnan The Journal of Chemical Physics, 145, (2016), 194701 * Contributed equally

Student Confirmation

Student Name:	Maria Bespalova		
Contribution to the Paper	Performed measurements in water, ethanol and acetonitrile, analysed all the measurements, participated in manuscript preparation.		
Signature		Date	20.05.2022

Supervisor Confirmation

By signing the Statement of Authorship, you are certifying that the candidate made a substantial contribution to the publication, and that the description described above is accurate.

Supervisor name and title: Prof. Madhavi Krishnan		
Supervisor comments		
Signature		Date 20.05.2022

This completed form should be included in the thesis, at the end of the relevant chapter.

4

Single-molecule electrostatic trapping using charged lipid bilayers

Contents

4.1 Surface-confined lipid bilayers 44
4.2 Characterisation techniques 45
4.3 Paper III 49

Due to relatively high value of the average p$K_a \approx 7$ for SiO_2, all the single-molecule trapping experiments were carried at pH 9 and NaCl salt concentration ≈ 1 mM in previous work [3][4][5][6]. As we have shown in the previous Chapter, surface charge density of SiO_2 is $\approx -0.1\ e/\text{nm}^2$ at these conditions. That enables stable trapping for tens of milliseconds even for short DNA fragments (e.q., 10 bases single-stranded DNA with $q_{\text{eff}} \approx -8e$) [3]. However, this set of conditions, namely relatively high pH and low salt concentration, is not optimal for a range of biomolecules, such as single-stranded RNA and some proteins which tend to degrade and lose their biological activity in alkaline solutions [66][67]. The above limitations prompted us to search for alternative materials for the surfaces of nanoslits of electrostatic trapping devices. Inspired by other works, such as Ref. [68] and [69], we tested the applicability of charged supported lipid bilayers (SLBs) for electrostatic

fluidic trapping. We also used the escape-time electrometry approach to characterise the composition and temporal stability of SLBs in our nanofluidic system.

This Chapter is organised as follows: we first give a brief overview of different surface-confined lipid bilayer systems and approaches for their preparation. We further discuss the currently existing techniques used for SLBs characterisation and present our recently published work *"Single molecule trapping and measurement in a nanostructured lipid bilayer system"* [8]. The paper describes the applicability of lipid bilayer systems for single-molecule electrostatic trapping and provides a new approach to measuring the chemical composition and temporal stability of SLBs formed in nanoslits.

4.1 Surface-confined lipid bilayers

A lipid bilayer is a membrane composed of two layers of lipid molecules packed so that their hydrophobic tails point towards each other while their hydrophilic heads point outward and are exposed to bulk solution. Phospholipids are the most abundant membrane lipids. They are composed of a glycerol molecule substituted by one polar group and one or two hydrophobic tails. These tails are usually fatty acids, and the polar group can be choline (phosphatidylcholine), glycerol (phosphatidylglycerol), serine (phosphatidylserine), ethanolamine (phosphatidylethanolamine), or inositol (phosphatidylinositol).

Following the pioneering work of McConnell in 1984, different models of surface-confined lipid bilayers have garnered considerable interest owing to their ability to imitate native cell membranes and relevance in various biotechnological applications [70][71][72][73]. Examples of the most widespread surface-confined lipid bilayer systems include supported lipid bilayers (SLBs), freely suspended lipid bilayers, polymer-cushioned lipid bilayers, and tethered lipid bilayers (Figure 4.1) [74][75][76][77][78][79][80][79].

To date, there are multiple methods used to create SLBs and other surface-confined lipid bilayers, including Langmuir-type approaches, self-assembly of spin-coated lipids upon hydration, and vesicle fusion (Figure 4.2, see the figure legend for

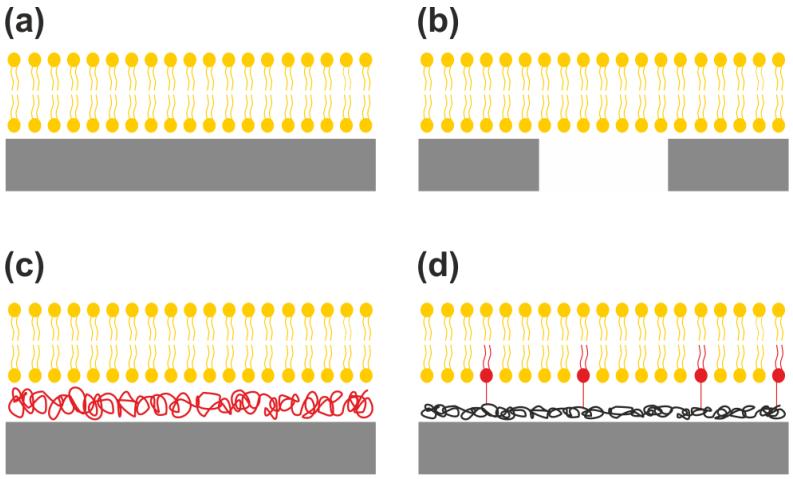


Figure 4.1: Different types of surface-confined lipid bilayer systems. **(a)** Supported lipid bilayer (SLB). **(b)** Freely suspended lipid bilayer. **(c)** Polymer-cushioned lipid bilayer. Here lipid bilayer rests on or near a soft hydrated polymer or polyelectrolyte film (red). **(d)** Tethered lipid bilayer. Here some lipids in the proximal leaflet of a lipid bilayer (red) are chemically linked to a surface, often via a spacer layer (black).

details) [81][82][83][84]. In the work presented in this Chapter we focused on vesicle fusion approach because of its simplicity and applicability in nanostructured systems.

4.2 Characterisation techniques

Chemical composition, physical properties and temporal stability are the key characteristics defining the range of lipid bilayers applicability for nano- and biotechnology approaches. Currently, a variety of methods exist for characterising the properties and formation of surface-confined lipid bilayer systems. The most widespread are Atomic Force Microscopy (AFM), Quartz Crystal Microbalance with Dissipation Monitoring (QCM-D), and Neutron Reflectometry (NR).

In AFM, 3D images of surfaces can be generated by probing a surface with a sharp tip mounted at the end of a cantilever. As the tip is scanned over the sample in a raster pattern, a feedback loop controls the interactions between the tip and the surface. In contact mode, a feedback loop maintains the deflection of the cantilever, and consequently the applied force, constant during the scanning process. In tapping mode, which is employed for soft biological samples including lipid bilayer membranes, a tip at the end of an oscillating cantilever touches the

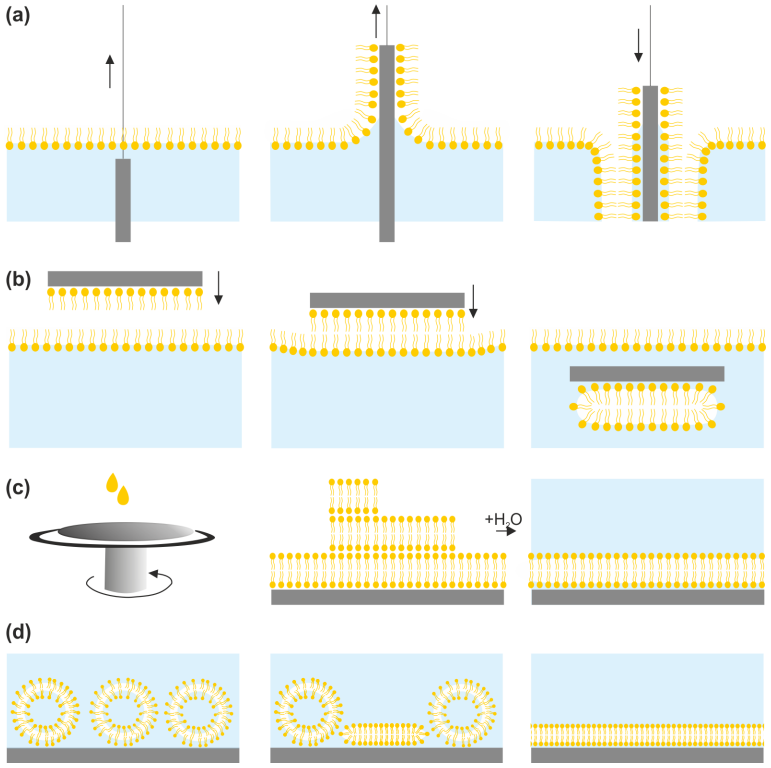


Figure 4.2: Techniques for preparation of solid-confined lipid bilayers. **(a)** In Langmuir–Blodgett approach, one or few lipid layers are deposited from the air-water interface to a solid support. **(b)** In Langmuir–Schaefer approach, a lipid monolayer is deposited from the air-water interface to a solid-supported lipid monolayer. **(c)** In spin coating technique, a lipid solution in a volatile solvent is pipetted onto a clean substrate which is further accelerated to rotation to remove the solvent leaving a stack of multiple lipid bilayers. Excess lipid bilayers are removed by a fluid jet leaving a single lipid bilayer on the substrate. **(d)** In vesicle fusion technique, lipid vesicles settle down on a surface, rupture and coalesce into a lipid bilayer.

surface only at the bottom of its oscillations, and a feedback loop maintains a constant oscillation amplitude. Both constant force in contact mode and constant amplitude in tapping mode are achieved by adjusting the tip-sample distance by moving the tip in the z-direction. These normal movements of the tip relative to the surface provide information on surface topography. By now, AFM has been successfully performed to explore the mechanical properties, domain formation and lipid phase transitions in SLBs, and to study the interaction of proteins or peptides with lipid bilayers [85][86][87][88][89][90].

The Quartz Crystal Microbalance (QCM) is an ultrasensitive mass balance which relies on measuring the resonance frequency of a piezoelectric quartz crystal.

The mechanical oscillation of the crystal, sandwiched between two metal electrodes, is excited by applying an alternating electric potential. The resonance frequency of mechanical oscillation is a function of the crystal mass and affected by a small amount of sample applied to the sensor (electrode) surface. The QCM-D technique provides additional information about the viscoelasticity of the sample by measuring the dissipation of the oscillation. Soft materials, such as lipid bilayer systems, cannot follow the oscillation without being deformed which leads to damping the oscillations and high dissipation. Tracking the changes in frequency and dissipation gives insights into the structural state of the sample in a real time. The QCM(-D) approach has been successfully used for studying the process of SLB-formation [91][92][93].

Another powerful technique used for SLB characterisation is Neutron Reflectometry (NR). Here, a well collimated beam of neutrons hits the surface of a sample at a certain incident angle. Further, the beam is partially reflected from the surface in respect with a scattering length density, SLD. Here, SLD is a product of a material's density and neutron scattering lengths, describing the strength and the character of neutron interactions with the atomic nuclei of the sample. Varying the incident angle or the wavelength of the neutron beam, the specular reflectivity of the sample is measured, providing insight into the chemical composition, thickness and structure of the sample at the molecular level. Moreover, NR-reflectometry is also capable of studying buried interfaces which are not easily accessible by other techniques. By now, NR-reflectometry approach has been successfully used for studying structures, compositions and functions of artificial and biological lipid bilayer membranes and their components[94][95][96].

In addition to the methods described above, optical techniques, such as ellipsometry or approaches based on fluorescence or interferometric scattering (iSCAT) microscopy, also occupy an important niche in studying the formation mechanisms, physical properties and chemical composition of surface-confined lipid bilayers [97][98][99][100].

However, despite the variety of different techniques, it remains challenging to study the nanostructured lipid bilayers, e.g., lipid bilayers formed in microfluidic

devices. In our paper *"Single molecule trapping and measurement in a nanostructured lipid bilayer system"*, we demonstrate a new approach to directly measure the surface potential, chemical composition and temporal stability of nanostructured lipid bilayers. Our approach is highly versatile, non-destructive and does not involve any external electric fields. In this work, we used negatively charged lipid bilayers, however the identical principles may be employed for characterisation of positively charged lipid membranes as well.

4.3 Paper III

LANGMUIR

pubs.acs.org/Langmuir Article

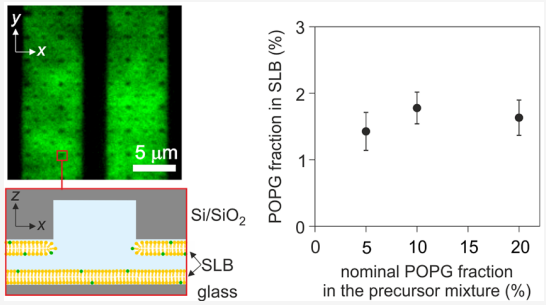
Single-Molecule Trapping and Measurement in a Nanostructured Lipid Bilayer System

Maria Bespalova, Robin Öz, Fredrik Westerlund, and Madhavi Krishnan*

Cite This: https://doi.org/10.1021/acs.langmuir.2c02203 Read Online

ACCESS | Metrics & More | Article Recommendations | Supporting Information

ABSTRACT: The repulsive electrostatic force between a biomolecule and a like-charged surface can be geometrically tailored to create spatial traps for charged molecules in solution. Using a parallel-plate system composed of silicon dioxide surfaces, we recently demonstrated single-molecule trapping and high precision molecular charge measurements in a nanostructured free energy landscape. Here we show that surfaces coated with charged lipid bilayers provide a system with tunable surface properties for molecular electrometry experiments. Working with molecular species whose effective charge and geometry are well-defined, we demonstrate the ability to quantitatively probe the electrical charge density of a supported lipid bilayer. Our findings indicate that the fraction of charged lipids in nanoslit lipid bilayers can be significantly different from that in the precursor lipid mixtures used to generate them. We also explore the temporal stability of bilayer properties in nanofluidic systems. Beyond their relevance in molecular measurement, such experimental systems offer the opportunity to examine lipid bilayer formation and wetting dynamics on nanostructured surfaces.



Downloaded via UNIV OF OXFORD on November 4, 2022 at 11:27:41 (UTC).
See https://pubs.acs.org/sharingguidelines for options on how to legitimately share published articles.

INTRODUCTION

Supported lipid bilayers (SLBs) are self-assembled two-dimensional thin-film coatings composed of a single phospholipid bilayer resting on or near a solid support.[1] The ability of SLB systems to mimic native cell membranes has been successfully employed in fundamental biophysical studies for several decades.[2,3] Specifically, SLB systems serve as a useful tool for studying cell adhesion and repulsion, peptide−cell interactions, cell−surface interactions, and membrane properties in general.[4−12] Given their unique properties, such as biological inertness, amphiphilicity, and ability to serve as matrixes for surface immobilization, SLBs have found applications in biosensors, drug delivery, and medical diagnostics.[13−15] Furthermore, ongoing advances in microfluidics, biosensor design, and micro- and nanofabrication have opened up new application avenues for nanostructured SLBs.[16−18] Owing to their antifouling properties and the diversity in lipid species chemistry, SLBs have been used to modulate surface properties at the nanoscopic level.[19−24] In this work, we explore the relevance of lipid bilayer coatings for electrostatic trapping of single molecules in solution. Such coatings are advantageous in that they offer tunability of both the sign and magnitude of the surface electrical charge in device-based systems where surface interactions play a strong role.[25]

Our experimental approach exploits the electrostatic fluidic trap described in detail in previous work.[26−29] The electrostatic fluidic trap relies on the equilibrium thermodynamic repulsion experienced by an electrically charged object confined in a fluid-filled gap between two like-charged parallel plates that form a slit. Geometric tailoring of one of the parallel plates with nanoscale surface indentations, or "pockets", leads to a local interaction energy minimum, creating a stable thermodynamic spatial trap for a charged object in solution (Figure 1a,b).

In our previous work, the walls of the nanoslits were composed of glass and silicon dioxide. Both materials acquire a negative charge in aqueous solutions due to dissociation of terminal silanol groups: $SiOH \rightleftharpoons SiO^- + H^+$ (ref 30). Although silicon dioxide is an established material for microfluidic and nanofluidic device fabrication, its surface properties can pose restrictions on experimental conditions used for electrostatic trapping.[31] Surface silanol groups are known to exist in states with different values of acid dissociation constants, pK_a, ranging from 2.3 to 10.7 with an average of ≈7 (refs 32, 33). Moreover silicon dioxide surface chemistry even displays strong dependence on treatment history.[32] Due to the relatively high value of the average pK_a we performed all previous single-molecule trapping experiments at pH 9 to ensure that the surface carried substantial

Received: August 15, 2022
Revised: October 15, 2022

© XXXX The Authors. Published by American Chemical Society

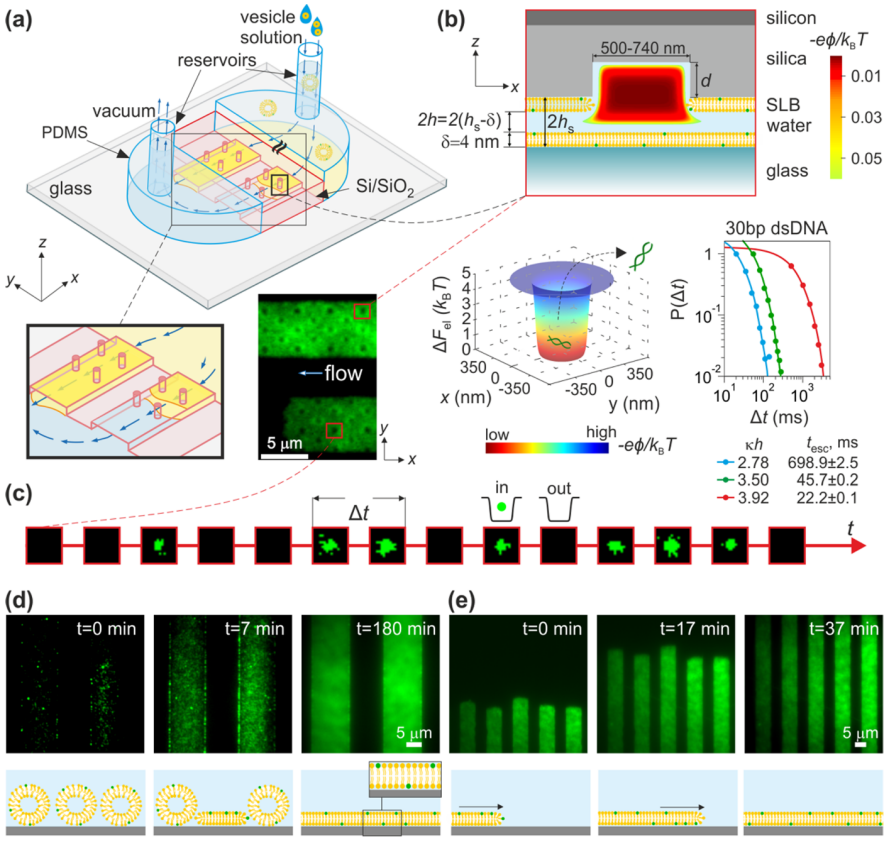


Figure 1. (a) Schematic illustration of a single-molecule trapping device consisting of a parallel array of nanoslits whose surfaces are passivated with SLBs (yellow). Bottom left: illustration of SLBs spreading in the nanoslits carrying surface indentations, or "pockets", on the top surface. The dimensions are not to scale. Bottom right: wide-field fluorescence image of SLBs spreading in the nanostructured region of two nanoslits (top view). (b) Cross section of a single trapping nanostructure or pocket depicting the spatial distribution of electrical potential in the nanostructured region. Nanostructured features were ≈160 nm deep and either ≈500 or 740 nm in diameter. The SLBs coating the nanoslit surfaces contain POPG/POPC (yellow) and a small fraction of fluorescent Rhodamine-DHPE (green). Bottom left: calculated spatial distribution of minimum axial electrostatic free energy, ΔF_{el}. Bottom right: Probability density distribution, $P(\Delta t)$, of measured escape times, Δt, plotted on log−log scale for measurements on 30bp dsDNA in nanostructured POPG/POPC SLB system at three different values of dimensionless slit depth, κh, and fitted to the expression $P(\Delta t) \propto \exp(-\Delta t/t_{esc})/t_{esc}$. (c) A series of snapshots in a trap displays the duration of a single recorded escape time, Δt, for fluorescently labeled single molecules entering and leaving a single trap location. Note that although we use fluorescently labeled lipids to visualize SLB formation as shown in (a), (d) and (e), the SLB is bleached to eliminate the fluorescent background signal in single-molecule measurements. This gives rise to a bright signal from the molecule visible against a dark device background. (d) Top: wide-field fluorescence images of SLB formation in ≈10 μm wide slits recorded over 3 h while flushing the SUV suspension containing nominally 20% of POPG at pH 9 and c = 100 mM. Bottom: schematic representation of SLB formation by vesicle rupture and fusion at the surface. (e) Top: wide-field fluorescence images of SLBs in ≈5 μm wide slits created by "steady-migration", recorded within 37 min while flushing the SUV suspension nominally containing 20% of POPG at pH 3.5 and c = 100 mM. Bottom: schematic representation of SLB migrating steadily in the direction of the flow indicated by the arrow.

charge density (≈−0.1 e /nm^2) (ref 34). Doing so permitted stable electrostatic trapping ranging from tens of milliseconds for single organic fluorophore molecules carrying a single elementary charge to tens of minutes for highly charged proteins such as Stml-1 ($q_{eff} \approx -89\ e$).[35,38] However, high pH may not prove optimal for measurements on some biomolecular species, e.g., single-stranded RNA, which tends to degrade in alkaline solutions.[36]

In this study, we demonstrate electrostatic trapping and effective charge measurements on single molecules in nanostructured slit systems whose surfaces are passivated using SLBs carrying net electrical charge. Electrostatic free energies associated with the molecule−surface interaction are inferred from experimentally measured potential-well depths in the molecular trapping process as described in detail in previous work and recapitulated briefly in the following section.[35,37−40] In earlier studies, we worked with silicon dioxide surfaces and used measured free energies inferred for charged molecular species in order to infer their effective charge, q_{eff} (refs 35, 37−41). In this study, we use double stranded DNA molecules of known effective charge in order to infer the surface electrical properties of supported lipid bilayers. We report measurements of the surface electrical potential and net charge density as a function of lipid bilayer composition. Since the phosphodiester group in phospholipids is highly acidic in nature ($pK_a \leq 3.5$), the use of SLBs should support trapping of negatively charged molecules in aqueous solutions where pH ≥ 4. Using the escape-time electrometry (ETe) approach, we also explore the possibility of tuning surface charge by varying the fraction of charged lipids in SLBs and measuring the depth of the potential well of the corresponding electrostatic trap.

Brief Description of the Electrostatic Fluidic Trap and the ET*e* Measurement Principle. We optically visualize and measure the strength of electrostatic repulsions between a

https://doi.org/10.1021/acs.langmuir.2c02203
Langmuir XXXX, XXX, XXX−XXX

charged molecule and like-charged probe surfaces in solution using the recently developed ET*e* approach, which relies on wide-field optical microscopy.[35,37−41] ET*e* measures the reduction in system free energy associated with transferring a charged molecule from a gap between like-charged parallel plates into a local nanostructured indentation region in the gap. This "trap" region is zone of weak axial confinement where the molecule-plate repulsion is negligible compared to the parallel-plate region[26] (Figure 1a,b). Typically, an array of such electrostatic fluidic traps is created using periodic nanostructured indentations in one surface of a parallel plate slit composed of silica surfaces separated by a gap of height $2h \approx 75$ nm. We introduce an aqueous suspension of the molecular species of interest, labeled with exactly 2 fluorescent ATTO 532 dye molecules, at a concentration of 50−100 pM into a system with multiple parallel lattices of traps (Figure 1a). In this work, we report on measurements performed on double stranded DNA molecules in nanoslits whose silicon oxide/glass walls are passivated with supported lipid bilayers of various lipid compositions.

The ET*e* technique measures the average time, t_{esc}, taken by a molecular species to escape from an electrostatic fluidic trap of typical depth, W (Figure 1b,c). Imaging the escape dynamics of trapped single molecules in a lattice of traps enables us to extract individual molecular escape events of duration, Δt, in each trap (Figure 1c). Fitting the probability density distribution, $P(\Delta t)$, of measured escape times, Δt, to the expression of the form $P(\Delta t) \propto \exp(-\Delta t/t_{esc})/t_{esc}$ permits us to extract the value of the average escape time, t_{esc}. In this work, we typically have $N \sim 10^3-10^4$ escape events. Since escape times are exponentially distributed, the fractional measurement uncertainty on t_{esc}, given by $t_{esc,e} = 1/\sqrt{N}$, is about 1−3% (ref 35). For $W > 4k_BT$, the relationship between t_{esc} and W is well described by Kramer's relation:

$$t_{esc} = t_r \exp(W/k_BT) \quad (1)$$

where t_r represents a position relaxation time of the molecule.[42] In order to convert measured t_{esc} values to the depth of the underlying potential well, W, we perform Brownian Dynamics simulations of the escape process in a lattice of traps.[37] As we have shown in our previous work, $W = \Delta F_{el} + f$ is composed of two parts: the electrostatic interaction free energy, ΔF_{el}, and an entropic contribution to positional fluctuations of the molecule, f (ref 38). We determine the entropic contribution as previously described and extract ΔF_{el} for each measurement. In turn, we have also shown that $\Delta F_{el} = q_{eff}\,\phi_m$, where q_{eff} is the effective charge of the molecule in solution and ϕ_m denotes the electrical potential at the midplane of the slit.[43] Further, ϕ_m can be well approximated using the linear superposition formula:

$$\phi_m = 2\phi_s \exp(-\kappa h) \quad (2)$$

where ϕ_s is an effective surface potential, and κh is a dimensionless slit depth, where $\kappa^{-1} \cong 0.304/\sqrt{c}$ denotes the Debye length for a monovalent salt solution of a concentration, c (in M), and $h = h_s - \delta$. Here $2h_s$ is the slit height measured by AFM and $\delta = 4$ nm is the thickness of a single lipid bilayer (Figure 1b) determined by small angle neutron and X-ray scattering data and inferred from molecular dynamics simulations.[44−49] Since the true height of the slit is not known to within a few nanometers, the results will not be affected from the same level of uncertainty on the lipid bilayer thickness. Equation 2 is based on a superposition approximation using the linearized Poisson−Boltzmann (PB) equation. Equation 2 is in excellent agreement with the results of the full nonlinear PB equation (NLPB) far away from the slit walls and has been used extensively in previous work.[35,37−41] Disparities between the electrical potential profile calculated using the NLPB equation and that given by the linear superposition approximation are only apparent in the region within a few nanometers of the slit surfaces. Because this region is rarely sampled by a like-charged molecule, the linear superposition approximation shown in eq 2 is sufficiently accurate. Note that ϕ_s can equal the "true surface potential", say $\phi_{s,0}$, in the regime of very small values, $|e\phi_{s,0}| \ll 25$ mV.

As reflected in eq 1, the measurand t_{esc} depends exponentially on the effective charge of the molecule, q_{eff}. As shown in our previous work, the fractional measurement uncertainty on q_{eff} is given by $t_{esc,e}/\Delta F_{el}$ (ref 35.). Thus, 1−3% uncertainty on t_{esc} would result in ≈0.3−1% measurement uncertainty in q_{eff}. In this study, we work with dsDNA and fluorescent dye molecules whose effective electrical charge values are known both from calculations and extensive investigations in silicon dioxide-based systems in previous work.[35,37,38,40,43] Therefore, the only unknown quantity in these experiments is the effective surface potential, ϕ_s, of the SLBs coating the slit surfaces.

EXPERIMENTAL SECTION

Fabrication of Nanofluidic Trapping Devices. The devices were fabricated using Silicon/Silicon dioxide and glass substrates as previously described.[26,35,37−39] Briefly, the device fabrication procedure consisted of deep-UV lithography to pattern the nanoslit regions and electron beam lithography in order to define nanostructured trap regions or "pockets". In each case, lithography was followed by reactive-ion etching to etch both the slit and pocket features into the silicon dioxide substrate surface. The dimensions of the channels and pockets were measured using scanning electron microscopy (SEM), atomic force microscopy (AFM), and profilometry. We used nanoslits of height $2h_s = 71-78$ nm and width of ≈5 and ≈10 μm, and pockets of depths $d \approx 160$ and ≈290 nm and radii, $r \approx 250$, ≈ 300, and ≈370 nm. (Figure 1b).

Vesicle Preparation. Vesicles were prepared by the thin-film hydration method followed by extrusion. We used 1-palmitoyl-2-oleoyl-glycero-3-phosphocholine (POPC) and sodium salt of 1-palmitoyl-2-oleoyl-*sn*-glycero-3-phospho-(1′-rac-glycerol) (POPG) dissolved in chloroform (Avanti Polar Lipids). Fluorescently labeled lipid N-(Lissamine rhodamine B sulfonyl)-1,2-dihexadecanoyl-*sn*-glycero-3-phosphoethanolamine, triethylammonium salt (Rhodamine-DHPE) (Biotium, Inc.) was dissolved in chloroform to a final concentration of 5 mg/mL.

In order to optimize the lipid bilayer coating procedure in our nanostructured fluidic slit system, we prepared the precursor lipid mixtures by mixing POPC, POPG, and Rhodamine-DHPE lipids in a ratio of 79:20:1 mol % respectively (Figure 1d,e). For ET*e* measurements, lipids in precursor lipid mixtures were mixed in the following ratios: 95:5, 90:10, and 80:20% of POPC:POPG with 10−6% Rhodamine-DHPE. Note that we used a very low concentration of labeled lipids in bilayers prepared for ET*e* measurements. This permits bilayer formation to be observed and confirmed while ensuring that bilayer fluorescence can be completely bleached prior to single-molecule measurements. Precursor lipid mixtures contained 10 mg of lipids in total.

Once the precursor lipid mixtures were prepared, chloroform was evaporated with a stream of nitrogen followed by vacuum desiccation for at least 4 h. Multilamellar vesicles (MLVs) were prepared by lipid thin-film rehydration in lipid buffer (10 mM Tris-HCl pH 8, 10 mM Boric acid, 0.225 mM EDTA, 100 mM NaCl) to a final lipid concentration of 1 mg/mL and vortexing for at least 5 min afterward.

https://doi.org/10.1021/acs.langmuir.2c02203
Langmuir XXXX, XXX, XXX−XXX

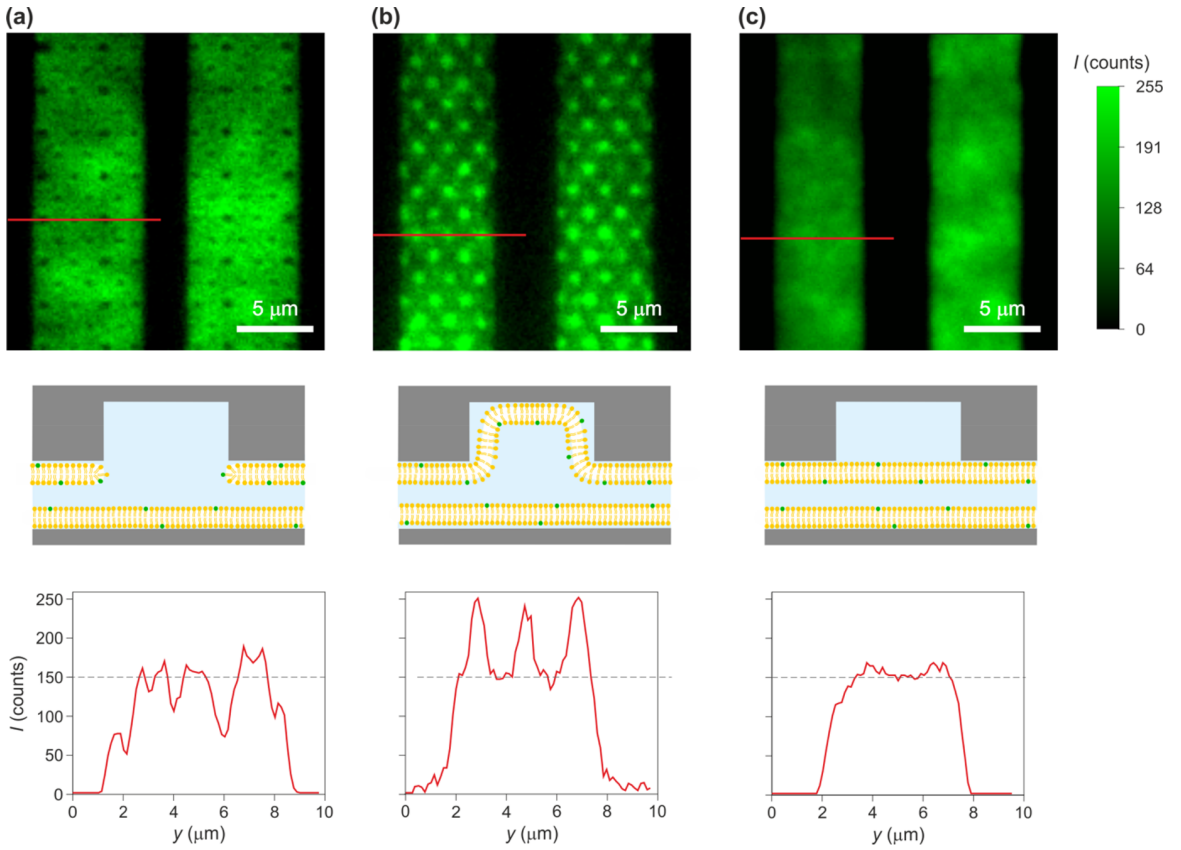


Figure 2. Various modes of surface coverage of SLBs in nanostructured silicon dioxide slits. Top panels depict the wide-field fluorescence images of passivated slits upon the completion of SLB formation when using SUV suspensions with (a) pH 3.5, c = 100 mM (See Supporting Movie), (b) pH = 3.5, c = 2 M, and (c) pH = 9, c = 100 mM. Central panels illustrate possible SLB coverage scenarios in a single pocket region for each of the illustrated fluorescence images: the SLB (a) circumvents the pocket, (b) coats the pocket, and (c) caps the pocket (illustration not to scale). Bottom panels depict intensity profiles plotted along the red lines drawn on top of the corresponding wide-field fluorescence images. Gray dashed line indicates I = 150 counts and shows that intensity level at the planar regions of the slits is relatively constant across the three scenarios.

The MLVs were further extruded using Avanti Mini Extruder (Avanti Polar Lipids). To prepare small unilamellar vesicles (SUVs), we subsequently extruded MLVs 21 times through a 50 nm pore-size pore membrane and 31 times through a 30 nm membrane. We further diluted freshly extruded SUV suspensions with lipid buffer to a final concentration of 250 μg/mL, titrated with HCl to the desired pH value, and we used the suspension immediately for coating of nanoslits.

Supported Lipid Bilayer (SLB) Formation. In order to form the SLB on nanoslit surfaces, we used a microfluidic setup illustrated in Figure 1a. Prior to loading the SUV suspension, the slits were flushed with lipid buffer (10 mM Tris-HCl pH 8, 10 mM Boric acid, 0.225 mM EDTA, 100 mM NaCl) for 15−20 min using pressure driven flow. The extruded vesicle suspension was then flushed through the slits for at least 12 h. Visualization of SLB formation was achieved by fluorescence excitation of Rhodamine-DHPE. Once the lipid bilayer coated the slits entirely, the flow was arrested and plain lipid buffer was flushed into the nanoslits in both flow directions to remove any debris and intact vesicles from the slits. Upon completion of the SLB formation, the fluidity and continuity of the lipid bilayer was confirmed using fluorescence recovery after photobleaching (FRAP).

Purification of DNA Samples. All DNA fragments were purchased from IBA Lifesciences (Germany) with a single ATTO 532 dye molecule coupled to both 5′ termini. The oligomers were purified with RP-HPLC using a Reprosil-Pur 200 C18 AQ column (Dr. Maisch, Germany) and elution with a gradient of acetonitrile in an aqueous 0.1 M triethylammonium acetate solution.

Imaging. Optical measurements were performed using widefield fluorescence imaging. Fluorescence excitation was achieved by illuminating Rhodamine-DHPE (for observing the SLBs) or ATTO 532-labeled DNA and ATTO 542 dye molecules (in escape time electrometry measurements) with a 532 nm DPSS laser (MGL_III-532_100 mW, PhotonTec, Berlin) that was focused at the back aperture of a 60×, NA = 1.35 oil immersion objective (Olympus, U.K.). Images were acquired using a sCMOS camera (Prime95B, Photometrics).

ET*e* Measurements. Prior to ET*e* measurements, the slits were flushed with 1 mM NaCl aqueous solution for at least 30 min. Then the flow was arrested, and the system was allowed to equilibrate for 20−30 min before loading the molecular species of interest. Prior to molecular loading for escape-time measurements, the fluorescent signal due to the Rhodamine-DHPE in the bilayers coating the slit surfaces was bleached in the entire measurement region. Images of molecular motion in the trap arrays were then acquired over a period of about 10−20 min per sample.

RESULTS AND DISCUSSION

In order to construct a nanostructured SLB system, we used a microfluidic setup illustrated in Figure 1a. We first created a suspension of small unilamellar vesicles (SUVs) containing zwitter-ionic lipid 1-palmitoyl-2-oleoyl-glycero-3-phosphocholine (POPC), negatively charged lipid sodium salt of 1-palmitoyl-2-oleoyl-*sn*-glycero-3-phospho-(1′-rac-glycerol) (POPG), and a small amount (≤1 mol %) of Rhodamine-DHPE by extrusion of a multilamellar lipid vesicle suspension through polycarbonate membranes with a 30 nm pore diameter (Experimental Section). Inclusion of fluorescently

https://doi.org/10.1021/acs.langmuir.2c02203
Langmuir XXXX, XXX, XXX−XXX

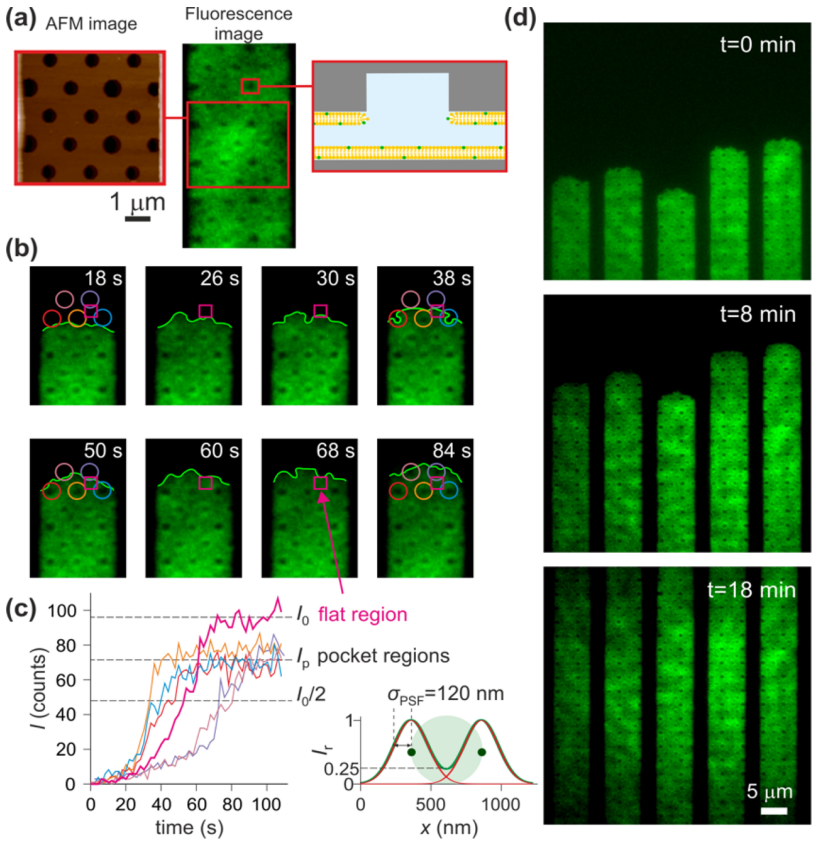


Figure 3. Steadily migrating SLBs circumvent nanostructured surface features. (a) AFM image of the nanostructured slit surface with circular "pocket" indentations (left). Wide-field fluorescence image of the pocket region upon the completion of SLB formation (middle). Here, we used the device with ≈160 nm deep pockets of two different radii, $r \approx 250$ and ≈370 nm. Schematic representation of a cross section through the center of a single pocket where the lipid bilayer coats the slits but circumvents the surface feature (right). (b) Wide-field fluorescence images of progressing SLB sequentially recorded in a ≈ 5 μm wide slit while flushing the SUV suspension nominally containing 20% of POPG with pH 3.5 and c = 100 mM. Colored circles indicate the pocket regions traversed by the lipid bilayer during the recording, and the square displays a flat region of the slit in between two neighboring pockets (See Supporting Movie). (c) Temporal evolution of fluorescence intensity signal, I, in the pockets and flat regions during traversal of the SLB across the slit as shown in (b) (left). I_0 and I_p denote the average intensities in the flat region and pocket regions upon the completion of the SLB formation, respectively. Sketch of optical point spread functions (PSFs) for two fluorescent Rhodamine-DHPE molecules located on the circumference of the surface nanostructure in an SLB coated slit (green circle) (right). For σ_{PSF}= 120 nm and a pocket radius of 250 nm the fluorescence signal intensity in the center of the pocket is ≈25% of the peak intensity at the location of each molecule due to lateral overlap of the PSFs from the two diametrically opposite molecules on the pocket circumference. (d) Wide-field fluorescence images sequentially recorded within 18 min of the SLBs in ≈5 μm wide slits while flushing the SUV suspension nominally containing 20% of POPG with pH 3.5 and c = 100 mM at a typical speed of ≈80 μm/s.

labeled lipid Rhodamine-DHPE in the lipid mixture enabled visualization of the SLB formation process (Figures 1d,e, 2, and 3). We loaded POPG/POPC SUVs in the inlet reservoir of the system and flushed the suspension through nanoslits of height $2h_s \approx 75$ nm using pressure driven flow at a typical speed of 80 μm/s. We found that loading larger vesicles, prepared by extrusion through polycarbonate membranes with larger pore diameters (≥50 nm), led to clogging of the nanoslits.

Mechanisms of Spreading of Supported Lipid Bilayers on Nanostructured Surfaces in a Fluidic Slit. We observed two different mechanisms of SLB formation in our nanoslits depending on the pH and ionic strength of the SUV suspension loaded into the slits (Figure 1d,e). Figure 1d presents a scenario in which vesicles entered the slits, settled down on the surface, and ruptured within an hour, forming discrete patches of lipid bilayer. Subsequently, these bilayer patches coalesced into a continuous lipid bilayer, ultimately coating the slits entirely. We observed this mechanism of lipid bilayer formation for SUV suspensions with pH ≥ 8 and NaCl concentration, c = 100 mM, in ≈5 and ≈10 μm wide nanoslits. In contrast, Figure 1e, depicts a different, steady-migration mechanism of SLBs formation in the direction of fluid flow through the nanoslits. This mechanism was observed when using SUV suspensions of pH 3.5 and c = 100 mM−2 M in ≈5 μm wide nanoslits. We found that the latter set of conditions, i.e., pH 3.5 and c = 100 mM−2 M, provided more reproducible SLB behavior in our experiments. When using SUV suspensions with higher pH values in ≈5 μm wide slits, we did occasionally observe steady migration behavior with a progressing SLB front as in Figure 1e. However, under no experimental conditions did we observe the steady-migration mechanism of SLB formation in ≈10 μm wide nanoslits. For all measurements presented in this work, we therefore used ≈5 μm wide nanoslits and the steady-migration SLB formation procedure depicted in Figure 1e.

We further examined the steady-migration mechanism of SLB formation in regions of the fluidic slit carrying

https://doi.org/10.1021/acs.langmuir.2c02203
Langmuir XXXX, XXX, XXX−XXX

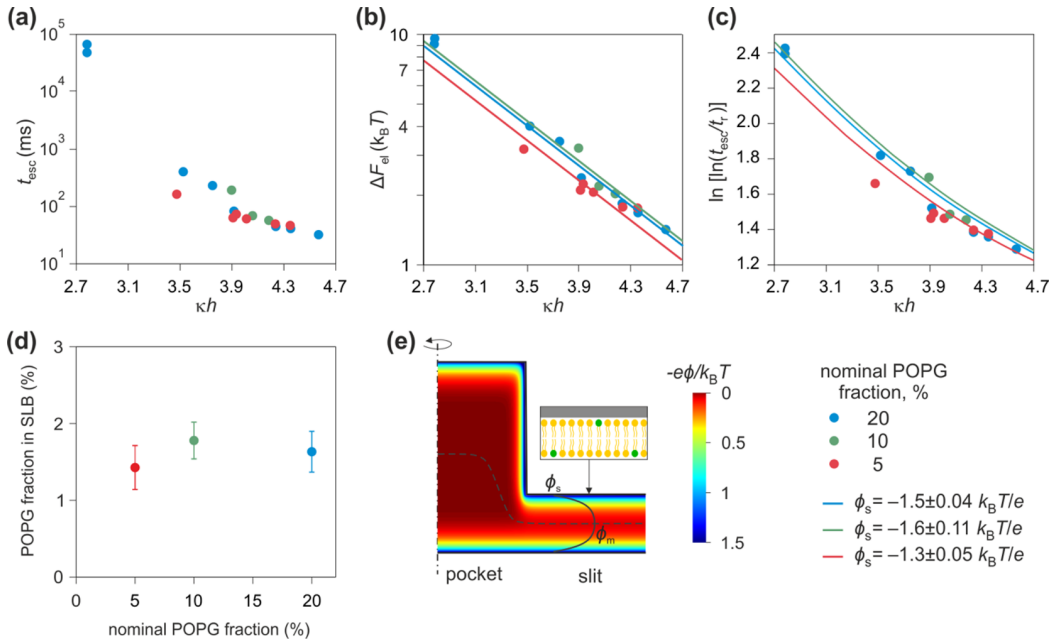


Figure 4. Trapping 60bp dsDNA (q_{eff} = −44.8 e) molecules in SLB systems nominally containing 5% (red), 10% (green), and 20% (blue) of POPG. The three experiments with nominally different SLBs were performed sequentially in the same trapping device. (a) Dependence of measured escape times, t_{esc}, on dimensionless slit height, κh. (b) Measured values (symbols) for electrostatic free energy ΔF_{el} fitted to eq 3 with a single fit parameter, ϕ_s, the effective surface electrical potential of the SLB. We obtained ϕ_s = −1.3 ± 0.05 k_BT/e (−33 ± 1 mV), −1.6 ± 0.11 k_BT/e (−41 ± 3 mV), and −1.5 ± 0.04 k_BT/e (−39 ± 1 mV) for SLBs nominally containing 5, 10, and 20% of POPG respectively. (c) Comparison of measured (symbols) and calculated (solid lines) values for ln[ln(t_{esc}/t_r)] reveals good agreement over the whole range of κh. Calculated ln[ln(t_{esc}/t_r)] values were obtained using eq 4 where ϕ_s values were taken from ΔF_{el} vs κh fits in (b). (d) Comparison of relative POPG fraction in the obtained SLBs with that in the precursor lipid mixtures reveals the absence of a strong correlation. We infer 1−2% charged lipid in the SLBs with nominal POPG fractions of 5−20%. (e) Representative calculation of electrostatic potential in the slit obtained by solving the Poisson−Boltzmann equation for a given device geometry; solution conditions ($2h$ = 68.4 nm, pH 5.85 and c = 1.10 mM) and surface charge density given by eq 5 with the number density of POPG phosphate groups Γ = 0.021 nm^{-2}.

nanostructured surface indentations (Figures 2 and 3). It has been previously demonstrated that the spreading behavior of lipid bilayers over a surface with nanostructured indentations depends on the size of the vesicles as well as on the pH and salt concentration of the bulk solution.[20,50,51] Inspired by these observations, we probed the influence of both pH and ionic strength of a SUV suspension on the spreading behavior of negatively charged SLBs in our nanostructured silicon dioxide slits. For these experiments, we used devices with nanostructure indentations of depth ≈160 nm and with two different radii, r ≈ 250 and ≈370 nm. We probed different SUV suspensions in a range of pH from 3.5 to 9 and NaCl concentrations, c, in a range from 100 mM to 2 M. Figure 2 illustrates three scenarios observed once the lipid bilayer front had traversed a slit surface with an array of nanostructured indentations. When using POPG/POPC SUV suspensions (containing nominally 5−20 mol % of POPG) with c = 100 mM and pH 3.5, we observed a ≈25% decrease of fluorescence signal at the pocket locations, I_p, compared to the intensity, I_0, at the feature-free flat surface region, i.e., I_p/I_0 ≈ 0.75 (Figures 2a (top) and 3). Note that the fluorescence signal in the feature-free region of the slit in our experiment contains contributions from both the top and bottom surfaces and that nanostructured pocket features that disrupt the continuity of the bilayer are only present on one surface of the slit. A naive estimate of the intensity in an uncoated pocket region would therefore suggest I_p/I_0 ≈0.5. However, since the nanostructure radii, r, in our devices are in the range of 250−370 nm, which is comparable to the width of the optical point spread function (PSF) (σPSF= 120 nm in our system), we expect the fluorescence signal in the center of the pocket regions to also contain contributions from the fluorescent lipid bilayer at the circumference of the structure (as illustrated in Figure 3c). Thus, the ratio I_p/I_0 ≈ 0.75 < 1 likely points to a scenario where the lipid bilayer circumvents the pockets as illustrated in Figures 2a (central) and 3a (see Supporting Movie).

Further, using SUV suspensions containing higher NaCl concentrations in the range c = 200 mM-2 M and pH 3.5, we occasionally observed a ≈70% higher fluorescence intensity at the pocket locations in comparison to the featureless region, i.e., I_p/I_0 ≈ 1.7 (Figure 2b, top). As discussed in ref 20, a ratio of I_p/I_0 ≈ 1.7 > 1 likely reflects a scenario where the lipid bilayer follows the contour of the pockets as illustrated in Figure 2b (central). The enhanced intensity at the pocket locations may be simply explained by the fact that pocket diameter (500 and 740 nm) is on the order of the wavelength of light. When the vertically oriented pocket walls are conformally coated with a fluorescent bilayer, the number of fluorescent emitters per unit area projected on to the 2D image plane is much higher than in the planar regions. This gives rise to bright looking pocket regions. Note that in an idealized situation of infinite spatial resolution in imaging, the pockets would appear to have bright rings surrounding central lower intensity disc regions with similar intensity to the flat slit regions. We further found that it was challenging to obtain controllable and reproducible results under these conditions with the SLB occasionally circumventing the pocket nano-

https://doi.org/10.1021/acs.langmuir.2c02203
Langmuir XXXX, XXX, XXX−XXX

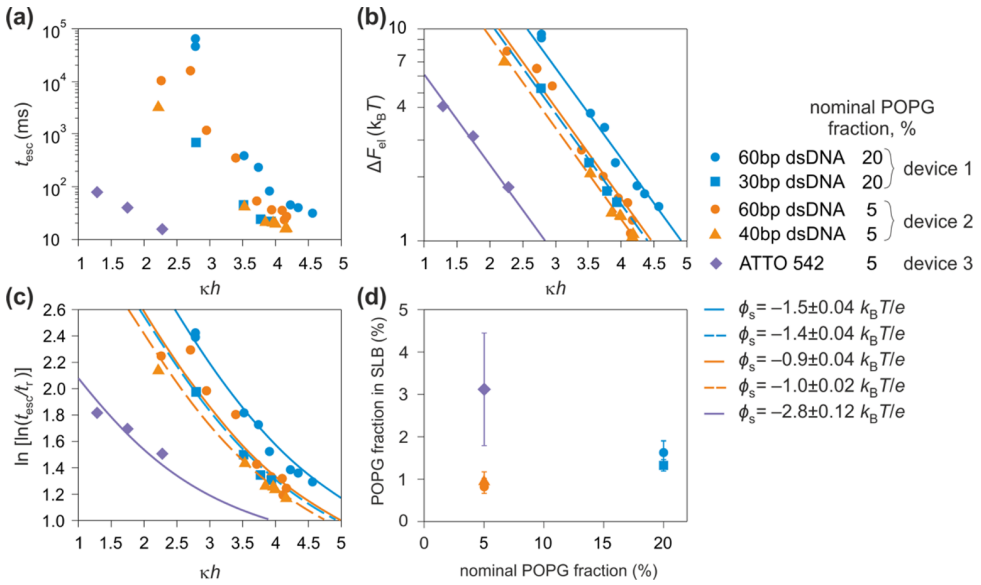


Figure 5. Trapping 60bp dsDNA (q_{eff} = −44.8 *e*, circles), 40bp dsDNA (q_{eff} = −33.8 *e*, triangles), 30bp dsDNA (q_{eff} = −28.1 *e*, squares), ATTO 542 (q_{eff} = −3.0 *e*, diamonds) molecules in three different nanoslit SLB devices. Data are provided for measurements on SLBs nominally containing 20% of POPG (blue symbols and lines; device 1), and 5% of POPG in different devices (orange and violet symbols and lines; devices 2 and 3). (a) Dependence of measured escape times, t_{esc}, on κh. (b) Measured values (symbols) for electrostatic free energy ΔF_{el} fitted to the eq 3 with a single fit parameter, ϕ_s. We obtained ϕ_s = −1.5 ± 0.04 k_BT/e (−39 ± 1 mV) and −1.4 ± 0.04 k_BT/e (−36 ± 1 mV) for 60bp (solid blue line) and 30bp dsDNA (dashed blue line) in the SLB system nominally containing 20% of POPG (device 1). For measurements with nominal 5% of POPG we obtain −0.9 ± 0.04 k_BT/e (−23 ± 1 mV) and −1 ± 0.02 k_BT/e (−26 ± 0.05 mV) for 60bp (solid orange line) and 40bp dsDNA (dashed orange line; device 2) and −2.8 ± 0.12 k_BT/e (−72 ± 3 mV) for ATTO 542 (violet solid line; device 3). (c) Comparison of measured (symbols) and calculated (solid lines) values for ln[ln(t_{esc}/t_r)] reveals good agreement over the whole range of κh. Calculated ln[ln(t_{esc}/t_r)] values were obtained using eq 4 where ϕ_s values were taken from ΔF_{el} vs κh fits in (b). (d) Comparison of relative POPG fraction in the SLBs with that in the precursor lipid mixtures indicates ≈1−3% negatively charged lipids in the SLBs with nominal POPG fractions of 5 and 20%.

structures, as observed in solutions of *c* = 100 mM NaCl described previously.

Finally, Figure 2c depicts a scenario observed for SLBs formed in a solution with pH 9 and *c* = 100 mM. Here we found no optical evidence of the presence of nanoscale surface topography upon completion of SLB spreading, with the fluorescence intensities in the pocket and flat regions displaying no obvious spatial disparities. This suggests that under these conditions the SLB simply traverses a nanostructured pocket, neither circumventing it nor coating its surface, but rather capping the indentation as shown in Figure 2c (central). Previous studies have reported this regime of coating behavior under experimental conditions similar to our study, i.e., pH 9 and *c* = 100 mM (ref 20). Note that the level of background intensity at the planar regions of the slits remains roughly constant across the three scenarios, notwithstanding some amount of spatial nonuniformity in the fluorescence signal from the SLBs, the exact origin of which remains unclear (Figure 2, bottom).

Overall, we observed slightly different SLB spreading behavior than that described in previous work involving feature diameters 3−4 times smaller than in this study.[20] In previous studies, lipid bilayers were found to conformally coat the pocket surfaces at pH 8, whereas our experiments reveal such behavior only occasionally in solutions with pH 3.5 and in the presence of up to 2 M NaCl. It is evident that a low solution pH and strong electrostatic screening favor the formation of conformal SLB coatings on like-charged nanostructured surfaces. It is also clear that increased electrostatic repulsion between the bilayer and silicon dioxide surface at higher pH can introduce interesting modes of wetting behavior when a moving bilayer encounters a surface defect presented by a nanostructured indentation. Since electrostatic interactions play a strong role in the spreading behavior of a charged SLB on a silicon dioxide surface, the process is not only strongly affected by pH and ionic strength of the SUV suspension but can also be highly dependent on sample-surface properties.

For all trapping experiments, described further in this work, we passivated our nanoslit surfaces using the approach depicted in Figures 2a and 3 (see Supporting Movie). Since ET*e* measurements rely on recording the emitted fluorescence signal from trapped fluorophore-labeled molecules, we reduced the fraction of labeled lipids, Rhodamine-DHPE, in the precursor lipid mixtures down to 10^{-6}%. A low concentration of labeled lipids supported the observation of the moving front of the SLB and enabled us to verify the continuity of the SLB upon completion of bilayer formation. Prior to every ET*e* measurement, we bleached the fluorescence signal from Rhodamine-DHPE in order to eliminate any bilayer fluorescence in the observation of trapped single molecules in solution. All trapping experiments described below were performed in nonbuffered aqueous solutions (pH 5−6) containing ≈1 mM NaCl.

Using ET*e* to Probe the Effect of Charge Content in SLBs on Molecule−Surface Electrostatic Interactions. In order to probe the ability to tune the surface charge density using SLB composition, we performed a series of ET*e* measurements using devices passivated with SLBs derived from SUVs of various lipid compositions (Figures 4 and 5). We investigated three different lipid compositions with nominal POPG content (as determined by the mixing ratio

https://doi.org/10.1021/acs.langmuir.2c02203
Langmuir XXXX, XXX, XXX−XXX

of POPG and POPC in the precursor lipid mixtures) of 5, 10, and 20 mol %. In the first series of experiments, we performed measurements of escape-time, t_{esc}, for the same molecular species, namely 60bp dsDNA end-labeled with two ATTO 532 dye molecules (Figure 4a). We used the same trapping device sequentially passivated with lipid bilayers containing nominally different relative fractions of POPG. Prior to every new passivation procedure, we removed the previous SLB using a 10% solution of the surfactant sodium dodecyl sulfate (SDS). Doing so permitted us to compare SLBs of various composition keeping slit geometry identical. Interestingly, we obtained similar escape time values for all of the probed lipid bilayer compositions (Figure 4a). Since the value of t_{esc} for a given molecule at a particular κh value is a function of effective surface electrical potential, ϕ_s, alone, the observation indicates that all probed SLBs had similar surface electrical properties as relevant for long-ranged electrostatic interactions.

In order to quantify the values of ϕ_s in each experiment and to infer the corresponding percentage of negative POPG lipids in the SLBs, we first converted the measured escape time values, t_{esc}, to electrostatic interaction free energies, ΔF_{el}, as described in our previous work.[35] We then plotted the inferred values ΔF_{el} values vs κh and fitted the data to the following equation:

$$\Delta F_{el} = 2q_{eff}\cdot\phi_s\cdot\exp(-\kappa h) \quad (3)$$

with a single fit parameter, ϕ_s. Here we use eq 2 and the relation $\Delta F_{el} = q_{eff}\,\phi_m$, established in previous experimental and theoretical work.[35,43] Furthermore, we use the calculated effective electrical charge, $q_{eff} = -44.8\ e$, for labeled 60bp dsDNA which has been verified in previous measurements.[35,37−40] κ and h are in turn known from conductivity measurements of salt concentration in the measurement solution and from AFM measurements of slit height, respectively. Measurements of escape times of 60bp dsDNA in nanostructured SLBs thus yielded ϕ_s values in a range from $-1.3\ k_BT/e$ (−33 mV) to $-1.6\ k_BT/e$ (−41 mV) for nominal POPG fractions from 5 to 20% (Figure 4b). We did not observe strong correlation between the measured surface potentials and the percentage of negative lipid content in the precursor lipid mixtures. Moreover, the inferred values of ϕ_s are about a factor of 2 smaller than the corresponding values of $\phi_s = -2.7\ k_BT/e$ (−69 mV) and $-3.4\ k_BT/e$ (−87 mV) calculated using the Poisson−Boltzmann electrostatics model for SLBs nominally containing 5 and 20% of POPG respectively, at pH 5.8 and $c = 1.2$ mM as described later.

Next, in order to further characterize the reproducibility of the coating procedure as well as the stability and longevity of the SLB coatings in our work, we performed similar measurements and analysis, as described above, for few different molecular species in three different lipid bilayer-passivated devices (Figures 5a,b). Specifically, we used: (1) 60bp and 30bp dsDNA, (2) 60bp and 40bp dsDNA, and (3) ATTO 542 dye molecules in devices passivated with lipid bilayers nominally containing either 5 or 20% of POPG (Figure 5). Similar to 60bp dsDNA, both the 30bp and 40bp dsDNA molecular species were labeled with two ATTO 532 dyes, and the q_{eff} values for all dsDNA molecules were taken from the measurements and calculations performed as described in earlier work.[40,43] In particular, we used the values $-28.1\ e$, $-33.8\ e$, and $-44.8\ e$ for 30bp, 40bp, and 60bp dsDNA, respectively.[40] The value of q_{eff} for ATTO 542 was assumed to be equal to its structural charge, which is $-3\ e$. Fitting the measured ΔF_{el} vs κh data to eq 3, we obtained similar fit values for ϕ_s for both pairs of molecules measured in the same devices, as expected (Figure 5b, devices 1 and 2). Specifically, t_{esc} measurements on 60bp and 30bp dsDNA molecules in SLB structures with nominally 20% of POPG yielded values of $\phi_s = -1.5 \pm 0.04\ k_BT/e$ (−39 ± 1 mV) and $-1.4 \pm 0.04\ k_BT/e$ (−36 ± 1 mV), and t_{esc} measurements on 60bp and 40bp dsDNA molecules in SLB structures with nominally 5% of POPG yielded $\phi_s = -0.9 \pm 0.04\ k_BT/e$ (−23 ± 1 mV) and $-1.0 \pm 0.02\ k_BT/e$ (−26 ± 0.5 mV), respectively (Figure 5b, devices 1 and 2). Good agreement of ϕ_s values obtained for different molecules in the same system shows that a precise measurement of t_{esc} for one calibrator molecule, i.e., a molecule with the known value for q_{eff}, is sufficient to accurately determine ϕ_s, which may then be applied to the determination of q_{eff} for a test molecular species of unknown effective charge. Interestingly, our experiments on 60bp dsDNA, measured in two different SLB nanoslit devices, composed of SLBs containing nominally identical POPG fraction of 5%, revealed escape times with disparities of around 50% under the same measurement conditions, characterized by the value of the system size parameter κh (Figure S1). These t_{esc} values measured in two different devices correspond to inferred surface electrical potential values of $\phi_s = -1.3 \pm 0.05\ k_BT/e$ (−33 ± 1 mV) and $-0.9 \pm 0.04\ k_BT/e$ (−23 ± 1 mV) for two nominally identical SLBs (Supporting Section 1, Figures 4b and 5b, device 2). Approximately 15−25% of the observed disparity in t_{esc} values, and consequently ≈6−12% in ϕ_s values, could however stem from small inaccuracies in the estimate of the relevant κh value (Supporting Section 1). We attribute the residual discrepancy in escape times for the same molecular species to ≈30% difference in the surface charge density of the SLBs in the two experiments. Importantly, using ATTO 542 as a probe molecule, we did note a higher magnitude of surface potential, $\phi_s = -2.8\ k_BT/e$ (−72 mV) for measurements under similar experimental conditions in a third device coated with 5% POPG. This value suggests a percentage of POPG in the bilayer closer to the nominal value of 5% (Figure 5d). Assuming the nature of the probe molecule has no impact on the measured interaction, our findings suggest that SLBs prepared from precursor lipid mixtures of identical compositions can differ in content of negative POPG lipids and therefore display variable surface electrical potentials. Our observations emphasize the necessity for a calibration measurement to determine ϕ_s for an SLB system, with the composition variabilities from one SLB device to the next likely arising from interactions between the solid silicon dioxide support and lipid vesicles which is not highly controllable.

We then investigated the temporal stability of SLB surface properties by performing repeated measurements of t_{esc} on the same molecular species at similar κh values over more than 24 h (Supporting Section 2). The absence of significant variation in measured escape times indicates that obtained bilayers are stable in composition for at least 24 h. Thus, despite possible compositional variability of SLBs from one device to the next, we establish that the electrostatic properties of SLBs, probed using electrostatic trap performance in a nanostructured SLB system, display high temporal stability in a given measurement device.

Further, in order to compare the dependence of t_{esc} on κh measured experimentally, with that predicted by Kramer's relation given by eq 1, we plotted the experimentally measured and theoretically predicted values for $\ln[\ln(t_{esc}/t_r)]$ vs κh

https://doi.org/10.1021/acs.langmuir.2c02203
Langmuir XXXX, XXX, XXX−XXX

(Figures 4c and 5c). Combining eq 1 with the relation for $W = \Delta F_{el} + f = q_{eff}\,\phi_m + f$, we obtained the following expression for theoretically predicted $\ln[\ln(t_{esc}/t_r)]$ values:

$$\ln[\ln(t_{esc}/t_r)] = \ln[2q_{eff}\cdot\phi_s\cdot\exp(-\kappa h) + f] \quad (4)$$

The trend observed for $\ln[\ln(t_{esc}/t_r)]$ vs κh is not linear due to the presence of the f term on the right-hand side (RHS) of the equation. In order to calculate the RHS of eq 4, we used the ϕ_s values obtained from ΔF_{el} vs κh fits (Figures 4b and 5b) and q_{eff} values for molecules taken from calculations.[43] Note that f is a fluctuation free energy that depends on device geometry and can be calculated for a given set of experimental conditions as previously described.[38] To estimate the experimental $\ln[\ln(t_{esc}/t_r)]$ values, we used the measured t_{esc} values (Figures 4a and 5a) and an estimate for the position relaxation time of the molecule given by $t_r \approx L^2/4D$. Here $L\approx$ 450 nm is an effective diffusion length within the trap, estimated from BD trajectory simulations, $D = k_BT/6\pi\eta r_H$ is the diffusion coefficient, where η denotes water viscosity, and r_H is the hydrodynamic radius of the object. For instance, for 60bp dsDNA, we obtained $t_r \approx 1$ ms using $r_H = 4.51$ nm measured using fluorescence correlation spectroscopy (FCS), as described in our previous work.[35,40] We observe good agreement between calculated and measured $\ln[\ln(t_{esc}/t_r)]$ values over the whole range of tested κh values.

Inferring the Charge Content of SLBs in Nanoslits from ET*e* Measurements. Finally, we outline the theoretical model used to relate values of effective surface electrical potential, ϕ_s, inferred from experiment to a percentage of negatively charged POPG lipids in the SLBs (Figures 4d and 5d). We modeled the lipid bilayer surfaces in our system using a single pK_a charge regulation model to describe the electrical charge density of the surface as a function of salt concentration, pH and number density of ionizable groups, Γ.[35,37,52]

$$\sigma_s = \frac{-\Gamma e}{1 + 10^{(pK_a - pH)}\exp\left(\frac{-e\phi_{s,0}}{k_BT}\right)} \quad (5)$$

where K_a is acid dissociation constant of the phosphate groups in POPG, and we assume pK_a = 3.5 (refs 52−54). Equation 5 serves as a boundary condition for the Poisson−Boltzmann (PB) equation, $\Delta\psi = \kappa^2 \sinh\psi$, describing the spatial distribution of the dimensionless electrostatic potential, $\psi = \frac{e\phi}{k_BT}$, in the system. The PB equation was solved for a range of input values for Γ in eq 5 yielding corresponding values of the true surface potential, $\phi_{s,0}$ (Figure 4e). As mentioned previously $\phi_{s,0}$ is generally larger than the effective surface potential, ϕ_s, accessible in our experiments. For example, values of $\phi_s = -2.7\ k_BT/e$ (−69 mV) and $-3.4\ k_BT/e$ (−87 mV) expected for 5% and 20% POPG correspond to $\phi_{s,0}$ values of $-3.2\ k_BT/e$ (−82 mV) and $-5\ k_BT/e$ (−129 mV), respectively. Our inferred values of ϕ_s enable us to infer a surface density of POPG phosphate groups, Γ, in the SLBs in the experiments. Using the literature value for POPG lipid area, S_{POPG}= 0.7 nm^2, we converted the obtained Γ values to percentage of POPG lipids in the SLB, w (ref 47). Figures 4d and 5d show the dependence of the inferred value of w on percentage of POPG in the corresponding precursor lipid mixture. In general, we observe a range of about 1−3% charged lipids in the SLBs with nominal POPG fractions of 5−20% in all our experiments. Moreover, measurements with two different molecules in the same SLB-coated device confirm that w is relatively independent of the type of probe molecule. Specifically, measurements on 40bp and 60bp dsDNA in the same SLB structure with a nominal concentration of 5% POPG yielded values of $w = 1.0 \pm 0.2\%$ and $0.8 \pm 0.2\%$, and measurements on 30bp and 60bp dsDNA in 20% POPG SLBs yielded $w = 1.3 \pm 0.1\%$ and $1.6 \pm 0.3\%$, respectively (Figures 5d, devices 1 and 2).

Thus, contrary to intuitive expectations, we did not observe a strong correlation of POPG content in the probed SLBs with that in the lipid mixtures used for vesicle preparation. For all compositions studied, the nanoslit SLBs displayed a lower fraction of POPG compared to nominal POPG content (as determined by the mixing ratio of POPC and POPG in the precursor lipid mixture). The significant disparity in lipid compositions of SLBs compared to the precursor lipid mixtures has in fact been repeatedly reported in previous work.[55−62] Possible origins for this effect may lie in specific interactions between the lipid bilayer and solid support, surface-induced impeded lipid mobility, intermembrane repulsion between neighboring charged lipid head groups, as well as heterogeneity in lipid vesicle suspensions.[57,62] Similar observations have been previously reported (ref 62) by Gilbile et al., who measured surface electrical potentials for SLBs using the surface force apparatus (SFA) in a solution of low salt concentration (0.5 mM $NaNO_3$, pH 5.7). Surface potential measurements in that study suggested the presence of ≈1% of anionic charged dimyristoylphosphatidylglycerol (DMPG) lipids in lipid bilayers prepared using precursor lipid mixtures containing 10 and 20% of DMPG.[62] These experiments using macroscopic surfaces strongly echo our own observations involving molecular scale probes of the electrostatic interaction in solution.

One possible explanation for the observed paucity of POPG in the SLBs in our experiments could be related to the fact that lipid vesicles, prepared by extrusion through 30 nm pore filters, are likely highly heterogeneous in size and lipid composition. Previous characterization of extruded vesicles by electron microscopy and dynamic light scattering have shown that extrusion of multilamellar lipid vesicles (MLV) through 30 nm pores results in an average vesicle size of ≈60 nm in diameter with standard deviation of ≈20 nm (refs 63, 64). It is also known that small vesicles (≈ 50 nm in diameter) can have a high degree of heterogeneity, i.e., up to 10-fold variation in relative lipid composition, at the single vesicle level.[65] It is thus possible that the SLBs in our nanoslits form from a fraction of SUVs that contain comparatively low amounts of negatively charged POPG lipids. Moreover it is likely that electrostatic repulsion between negative SUVs and silicon dioxide surfaces—though small at pH 3.5 and salt concentration 100 mM—may play a further role in "electrostatic sieving" of the SLB forming vesicles, presenting a slightly lower energy barrier to entry into the nanoslits for vesicles with a smaller relative fraction of POPG. Furthermore, in a nanoscale system where the Debye length, κ^{-1}, is comparable to a critical system dimension (in this case, the gap between two facing, charged bilayers, h), the system could minimize its electrical free energy by a gradual change in composition occurring by diffusive draining of charged lipids out of the narrow parallel-plate slit region. The observed depletion of negatively charged POPG in the obtained SLBs could thus arise from (1) lower POPG content in the vesicles entering the nanoslits and/or forming the nanoslit SLB and (2) redistribution/drainage of charged lipids in the SLB out of the nanoslit region.

https://doi.org/10.1021/acs.langmuir.2c02203
Langmuir XXXX, XXX, XXX−XXX

CONCLUSIONS

In conclusion, we have characterized the electrical properties of charged lipid bilayers in a nanofluidic system. We have demonstrated the use of lipid bilayer surface coatings formed by vesicle fusion for stable electrostatic trapping of charged molecules in solution. The highly acidic phosphate group of POPG supports strong electrostatic interactions in non-buffered aqueous solutions (pH 5−6). Although we have focused on negatively charged molecules and surfaces in this work, the same principles may be applied to generate positively charged lipid bilayers in order to trap positively charged molecules in solution. Whereas the charge composition of SLBs was found to vary significantly between devices, we found that SLBs displayed good temporal stability in surface electrical properties over a period of 24 h within a given device. The results of this study carry broad implications for the use of charged lipid bilayers as surface coatings in a variety of experiments and measurement situations in nanoscience and nanotechnology.

ASSOCIATED CONTENT

Supporting Information

The Supporting Information is available free of charge at https://pubs.acs.org/doi/10.1021/acs.langmuir.2c02203.

Additional experimental details and discussion of the temporal stability of electrostatic trapping and device longevity in a nanostructured SLB system, device-to-device variation of lipid bilayer-coated devices, list of symbols and abbreviations (PDF)

Supporting movie displaying SLBs circumventing the pocket structures (AVI)

AUTHOR INFORMATION

Corresponding Author

Madhavi Krishnan − *Physical and Theoretical Chemistry Laboratory, Department of Chemistry, University of Oxford, Oxford OX1 3QZ, United Kingdom; The Kavli Institute for Nanoscience Discovery, Oxford OX1 3QU, United Kingdom;* orcid.org/0000-0003-1274-7155; Email: madhavi.krishnan@chem.ox.ac.uk

Authors

Maria Bespalova − *Physical and Theoretical Chemistry Laboratory, Department of Chemistry, University of Oxford, Oxford OX1 3QZ, United Kingdom*

Robin Öz − *Department of Biology and Biological Engineering, Chalmers University of Technology, 412 96 Gothenburg, Sweden*

Fredrik Westerlund − *Department of Biology and Biological Engineering, Chalmers University of Technology, 412 96 Gothenburg, Sweden;* orcid.org/0000-0002-4767-4868

Complete contact information is available at: https://pubs.acs.org/10.1021/acs.langmuir.2c02203

Author Contributions

M.B. performed the experiments and analyzed the data. R.Ö. and F.W. provided expertise on lipid bilayer passivation of nanoslits. M.K. designed and supervised the research. M.B. and M.K. wrote the manuscript.

Funding

M.K. acknowledges the European Union's Horizon 2020 research and innovation program (grant agreement no. 724180). F.W. acknowledges funding from the European Research Council, in the form of an ERC consolidator grant (nanoDNArepair, no. 866238) and the Swedish Research Council (2020-03400).

Notes

The authors declare no competing financial interest.

REFERENCES

(1) Tamm, L. K.; McConnell, H. M. Supported phospholipid-bilayers. *Biophys. J.* **1985**, *47* (1), 105−113.

(2) Chan, Y. H. M.; Boxer, S. G. Model membrane systems and their applications. *Curr. Opin. Chem. Biol.* **2007**, *11* (6), 581−587.

(3) Reimhult, E.; Baumann, M. K.; Kaufmann, S.; Kumar, K.; Spycher, P. R. Advances in nanopatterned and nanostructured supported lipid membranes and their applications. *Biotechnology and Genetic Engineering Reviews* **2010**, *27* (1), 185−216.

(4) Richter, R. P.; Hock, K. K.; Burkhartsmeyer, J.; Boehm, H.; Bingen, P.; Wang, G. L.; Steinmetz, N. F.; Evans, D. J.; Spatz, J. P. Membrane-grafted hyaluronan films: A well-defined model system of glycoconjugate cell coats. *J. Am. Chem. Soc.* **2007**, *129* (17), 5306−5307.

(5) McConnell, H. M.; Watts, T. H.; Weis, R. M.; Brian, A. A. Supported planar membranes in studies of cell-cell recognition in the immune system. *Biochimica Et Biophysica Acta* **1986**, *864* (1), 95−106.

(6) Sengupta, K.; Schilling, J.; Marx, S.; Fischer, M.; Bacher, A.; Sackmann, E. Mimicking tissue surfaces by supported membrane coupled ultrathin layer of hyaluronic acid. *Langmuir* **2003**, *19* (5), 1775−1781.

(7) Hammond, K.; Ryadnov, M. G.; Hoogenboom, B. W. Atomic force microscopy to elucidate how peptides disrupt membranes. *Biochimica Et Biophysica Acta-Biomembranes* **2021**, *1863* (1), 183447.

(8) Nguyen, K. T.; Le Clair, S. V.; Ye, S. J.; Chen, Z. Molecular Interactions between Magainin 2 and Model Membranes in Situ. *J. Phys. Chem. B* **2009**, *113* (36), 12358−12363.

(9) Kilic, A.; Kok, F. N. Peptide-functionalized supported lipid bilayers to construct cell membrane mimicking interfaces. *Colloids and Surfaces B-Biointerfaces* **2019**, *176*, 18−26.

(10) Choi, S. E.; Greben, K.; Wordenweber, R.; Offenhausser, A. Positively charged supported lipid bilayer formation on gold surfaces for neuronal cell culture. *Biointerphases* **2016**, *11* (2), 021003.

(11) Milhiet, P. E.; Vie, V.; Giocondi, M. C.; Le Grimellec, C. AFM characterization of model rafts in supported bilayers. *Single Molecules* **2001**, *2* (2), 109−112.

(12) Dabkowska, A. P.; Niman, C. S.; Piret, G.; Persson, H.; Wacklin, H. P.; Linke, H.; Prinz, C. N.; Nylander, T. Fluid and Highly Curved Model Membranes on Vertical Nanowire Arrays. *Nano Lett.* **2014**, *14* (8), 4286−4292.

(13) Reimhult, E.; Kumar, K. Membrane biosensor platforms using nano- and microporous supports. *Trends Biotechnol.* **2008**, *26* (2), 82−89.

(14) Li, J.; Wang, X. L.; Zhang, T.; Wang, C. L.; Huang, Z. J.; Luo, X.; Deng, Y. H. A review on phospholipids and their main applications in drug delivery systems. *Asian Journal of Pharmaceutical Sciences* **2015**, *10* (2), 81−98.

(15) Sut, T. N.; Yoon, B. K.; Jeon, W. Y.; Jackman, J. A.; Cho, N. J. Supported lipid bilayer coatings: Fabrication, bioconjugation, and diagnostic applications. *Applied Materials Today* **2021**, *25*, 101183.

(16) Mashaghi, S.; Jadidi, T.; Koenderink, G.; Mashaghi, A. Lipid Nanotechnology. *International Journal of Molecular Sciences* **2013**, *14* (2), 4242−4282.

(17) Ando, K.; Tanabe, M.; Morigaki, K. Nanometric Gap Structure with a Fluid Lipid Bilayer for the Selective Transport and Detection of Biological Molecules. *Langmuir* **2016**, *32* (31), 7958−7964.

(18) Kazoe, Y.; Mawatari, K.; Li, L. X.; Emon, H.; Miyawaki, N.; Chinen, H.; Morikawa, K.; Yoshizaki, A.; Dittrich, P. S.; Kitamori, T. Lipid Bilayer-Modified Nanofluidic Channels of Sizes with Hundreds of Nanometers for Characterization of Confined Water and

Molecular/Ion Transport. *J. Phys. Chem. Lett.* **2020**, *11* (14), 5756−5762.
(19) Roiter, Y.; Ornatska, M.; Rammohan, A. R.; Balakrishnan, J.; Heine, D. R.; Minko, S. Interaction of Lipid Membrane with Nanostructured Surfaces. *Langmuir* **2009**, *25* (11), 6287−6299.
(20) Jonsson, P.; Jonsson, M. P.; Hook, F. Sealing of Submicrometer Wells by a Shear-Driven Lipid Bilayer. *Nano Lett.* **2010**, *10* (5), 1900−1906.
(21) Ang, P. K.; Jaiswal, M.; Lim, C. H. Y. X.; Wang, Y.; Sankaran, J.; Li, A.; Lim, C. T.; Wohland, T.; Barbaros, O.; Loh, K. P. A Bioelectronic Platform Using a Graphene-Lipid Bilayer Interface. *ACS Nano* **2010**, *4* (12), 7387−7394.
(22) Persson, F.; Fritzsche, J.; Mir, K. U.; Modesti, M.; Westerlund, F.; Tegenfeldt, J. O. Lipid-Based Passivation in Nanofluidics. *Nano Lett.* **2012**, *12* (5), 2260−2265.
(23) Vafaei, S.; Tabaei, S. R.; Cho, N. J. Optimizing the Performance of Supported Lipid Bilayers as Cell Culture Platforms Based on Extracellular Matrix Functionalization. *Acs Omega* **2017**, *2* (6), 2395−2404.
(24) Clapis, J. R.; Fan, M. Q. J.; Kovarik, M. L. Supported bilayer membranes for reducing cell adhesion in microfluidic devices. *Analytical Methods* **2021**, *13* (12), 1535−1540.
(25) Gomez, E. W.; Clack, N. G.; Wu, H. J.; Groves, J. T. Like-charge interactions between colloidal particles are asymmetric with respect to sign. *Soft Matter* **2009**, *5* (9), 1931−1936.
(26) Krishnan, M.; Mojarad, N.; Kukura, P.; Sandoghdar, V. Geometry-induced electrostatic trapping of nanometric objects in a fluid. *Nature* **2010**, *467* (7316), 692−695.
(27) Mojarad, N.; Krishnan, M. Measuring the size and charge of single nanoscale objects in solution using an electrostatic fluidic trap. *Nat. Nanotechnol.* **2012**, *7* (7), 448−452.
(28) Celebrano, M.; Rosman, C.; Sonnichsen, C.; Krishnan, M. Angular Trapping of Anisometric Nano-Objects in a Fluid. *Nano Lett.* **2012**, *12* (11), 5791−5796.
(29) Myers, C. J.; Celebrano, M.; Krishnan, M. Information storage and retrieval in a single levitating colloidal particle. *Nat. Nanotechnol.* **2015**, *10* (10), 886−891.
(30) Iler, R. K.*The Chemistry of Silica: Solubility, Polymerization, Colloid and Surface Properties, and Biochemistry*; John Wiley and Sons: New York: 1979.
(31) Voldman, J.; Gray, M. L.; Schmidt, M. A. Microfabrication in biology and medicine. *Annu. Rev. Biomed. Eng.* **1999**, *1*, 401−425.
(32) Darlington, A. M.; Gibbs-Davis, J. M. Bimodal or Trimodal? The Influence of Starting pH on Site Identity and Distribution at the Low Salt Aqueous/Silica Interface. *J. Phys. Chem. C* **2015**, *119* (29), 16560−16567.
(33) Macias-Romero, C.; Nahalka, I.; Okur, H. I.; Roke, S. Optical imaging of surface chemistry and dynamics in confinement. *Science* **2017**, *357* (6353), 784−787.
(34) Kokot, G.; Bespalova, M. I.; Krishnan, M. Measured electrical charge of SiO2 in polar and nonpolar media. *J. Chem. Phys.* **2016**, *145* (19), 194701.
(35) Ruggeri, F.; Zosel, F.; Mutter, N.; Rozycka, M.; Wojtas, M.; Ozyhar, A.; Schuler, B.; Krishnan, M. Single-molecule electrometry. *Nat. Nanotechnol.* **2017**, *12* (5), 488−495.
(36) Oivanen, M.; Kuusela, S.; Lonnberg, H. Kinetics and mechanisms for the cleavage and isomerization of the phosphodiester bonds of RNA by Bronsted acids and bases. *Chem. Rev.* **1998**, *98* (3), 961−990.
(37) Ruggeri, F.; Krishnan, M. Lattice diffusion of a single molecule in solution. *Phys. Rev. E* **2017**, *96* (6), 062406.
(38) Ruggeri, F.; Krishnan, M. Entropic Trapping of a Singly Charged Molecule in Solution. *Nano Lett.* **2018**, *18* (6), 3773−3779.
(39) Ruggeri, F.; Krishnan, M. Spectrally resolved single-molecule electrometry. *J. Chem. Phys.* **2018**, *148* (12), 123307.
(40) Bespalova, M.; Behjatian, A.; Karedla, N.; Walker-Gibbons, R.; Krishnan, M. Opto-Electrostatic Determination of Nucleic Acid Double-Helix Dimensions and the Structure of the Molecule-Solvent Interface. *Macromolecules* **2022**, *55* (14), 6200−6210.
(41) Kloes, G.; Bennett, T. J. D.; Chapet-Batlle, A.; Behjatian, A.; Turberfield, A. J.; Krishnan, M. Far-Field Electrostatic Signatures of Macromolecular 3D Conformation. *Nano Lett.* **2022**, *22* (19), 7834−7840.
(42) Kramers, H. A. Brownian motion in a field of force and the diffusion model of chemical reactions. *Physica* **1940**, *7*, 284−304.
(43) Krishnan, M. A simple model for electrical charge in globular macromolecules and linear polyelectrolytes in solution. *J. Chem. Phys.* **2017**, *146* (20), 205101.
(44) Kucerka, N.; Nieh, M. P.; Katsaras, J. Fluid phase lipid areas and bilayer thicknesses of commonly used phosphatidylcholines as a function of temperature. *Biochimica Et Biophysica Acta-Biomembranes* **2011**, *1808* (11), 2761−2771.
(45) Pan, J. J.; Heberle, F. A.; Tristram-Nagle, S.; Szymanski, M.; Koepfinger, M.; Katsaras, J.; Kucerka, N. Molecular structures of fluid phase phosphatidylglycerol bilayers as determined by small angle neutron and X-ray scattering. *Biochimica Et Biophysica Acta-Biomembranes* **2012**, *1818* (9), 2135−2148.
(46) Pan, J. J.; Marquardt, D.; Heberle, F. A.; Kucerka, N.; Katsaras, J. Revisiting the bilayer structures of fluid phase phosphatidylglycerol lipids: Accounting for exchangeable hydrogens. *Biochimica Et Biophysica Acta-Biomembranes* **2014**, *1838* (11), 2966−2969.
(47) Kucerka, N.; Holland, B. W.; Gray, C. G.; Tomberli, B.; Katsaras, J. Scattering Density Profile Model of POPG Bilayers As Determined by Molecular Dynamics Simulations and Small-Angle Neutron and X-ray Scattering Experiments. *J. Phys. Chem. B* **2012**, *116* (1), 232−239.
(48) Rog, T.; Murzyn, K.; Pasenkiewicz-Gierula, M. Molecular dynamics simulations of charged and neutral lipid bilayers: treatment of electrostatic interactions. *Acta Biochimica Polonica* **2003**, *50* (3), 789−798.
(49) Dickey, A.; Faller, R. Examining the contributions of lipid shape and headgroup charge on bilayer behavior. *Biophys. J.* **2008**, *95* (6), 2636−2646.
(50) Zeng, S. S.; Li, S. Y.; Utterstrom, J.; Wen, C. Y.; Selegard, R.; Zhang, S. L.; Aili, D.; Zhang, Z. Mechanism and Kinetics of Lipid Bilayer Formation in Solid-State Nanopores. *Langmuir* **2020**, *36* (6), 1446−1453.
(51) Kumar, K.; Isa, L.; Egner, A.; Schmidt, R.; Textor, M.; Reimhult, E. Formation of Nanopore-Spanning Lipid Bilayers through Liposome Fusion. *Langmuir* **2011**, *27* (17), 10920−10928.
(52) Ninham, B. W.; Parsegian, V. A. Electrostatic potential between surfaces bearing ionizable groups in ionic equilibrium with physiologic saline solution. *J. Theor. Biol.* **1971**, *31* (3), 405−428.
(53) Marsh, D.*Handbook of Lipid Bilayers*; CRC Press, 1990.
(54) Kubincova, A.; Hunenberger, P. H.; Krishnan, M. Interfacial solvation can explain attraction between like-charged objects in aqueous solution. *J. Chem. Phys.* **2020**, *152* (10), 104713.
(55) Akesson, A.; Lind, T.; Ehrlich, N.; Stamou, D.; Wacklin, H.; Cardenas, M. Composition and structure of mixed phospholipid supported bilayers formed by POPC and DPPC. *Soft Matter* **2012**, *8* (20), 5658−5665.
(56) Wacklin, H. P. Composition and Asymmetry in Supported Membranes Formed by Vesicle Fusion. *Langmuir* **2011**, *27* (12), 7698−7707.
(57) Lind, T. K.; Cardenas, M. Understanding the formation of supported lipid bilayers via vesicle fusion-A case that exemplifies the need for the complementary method approach (Review). *Biointerphases* **2016**, *11* (2), 020801.
(58) Lin, W. C.; Blanchette, C. D.; Ratto, T. V.; Longo, M. L. Lipid asymmetry in DLPC/DSPC-supported lipid bilayers: A combined AFM and fluorescence microscopy study. *Biophys. J.* **2006**, *90* (1), 228−237.
(59) Rossetti, F. F.; Textor, M.; Reviakine, I. Asymmetric distribution of phosphatidyl serine in supported phospholipid bilayers on titanium dioxide. *Langmuir* **2006**, *22* (8), 3467−3473.
(60) Richter, R. P.; Maury, N.; Brisson, A. R. On the effect of the solid support on the interleaflet distribution of lipids in supported lipid bilayers. *Langmuir* **2005**, *21* (1), 299−304.

https://doi.org/10.1021/acs.langmuir.2c02203
Langmuir XXXX, XXX, XXX−XXX

(61) Tabaei, S. R.; Vafaei, S.; Cho, N. J. Fabrication of charged membranes by the solvent-assisted lipid bilayer (SALB) formation method on SiO2 and Al2O3. *Phys. Chem. Chem. Phys.* **2015**, *17* (17), 11546−11552.
(62) Gilbile, D.; Docto, D.; Kingi, D. T.; Kurniawan, J.; Monahan, D.; Tang, A.; Kuhl, T. L. How Well Can You Tailor the Charge of Lipid Vesicles? *Langmuir* **2019**, *35* (48), 15960−15969.
(63) Mayer, L. D.; Hope, M. J.; Cullis, P. R. Vesicles of variable sizes produced by a rapid extrusion procedure. *Biochimica Et Biophysica Acta* **1986**, *858* (1), 161−168.
(64) Scott, H. L.; Skinkle, A.; Kelley, E. G.; Waxham, M. N.; Levental, I.; Heberle, F. A. On the Mechanism of Bilayer Separation by Extrusion, or Why Your LUVs Are Not Really Unilamellar. *Biophys. J.* **2019**, *117* (8), 1381−1386.
(65) Larsen, J.; Hatzakis, N. S.; Stamou, D. Observation of Inhomogeneity in the Lipid Composition of Individual Nanoscale Liposomes. *J. Am. Chem. Soc.* **2011**, *133* (28), 10685−10687.

https://doi.org/10.1021/acs.langmuir.2c02203
Langmuir XXXX, XXX, XXX−XXX

Single-Molecule Trapping and Measurement in a Nanostructured Lipid Bilayer System

Supporting Information

Maria Bespalova[1], *Robin Öz*[2], *Fredrik Westerlund*[2] *& Madhavi Krishnan*[1,3]*

[1]Physical and Theoretical Chemistry Laboratory, Department of Chemistry, University of Oxford, South Parks Road, Oxford OX1 3QZ, United Kingdom

[2]Department of Biology and Biological Engineering, Chalmers University of Technology, Gothenburg, Sweden

[3]The Kavli Institute for Nanoscience Discovery, Sherrington Road, Oxford OX1 3QU, United Kingdom

Section 1. Exploring the dependence of device-to-device variation on SLB composition

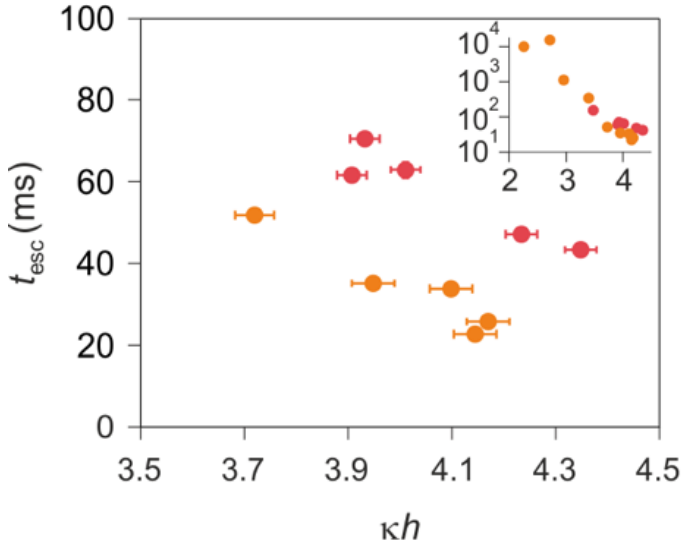


Figure S1. Escape time measurements on 60bp dsDNA molecular species in SLB nanostructures formed in two different devices (depicted with red and orange colors). Both SLB nanostructures contain nominally identical relative POPG fraction of 5%. The errors on t_{esc} ($< 2.5\%$) are smaller than the data symbols.

In order to explore the dependence of device-to-device variation on SLB composition we performed t_{esc} measurements for the same molecular species, i.e., 60bp dsDNA, in two different devices coated with bilayers under nominally identical conditions. The SLBs were prepared from precursor lipid mixture containing identical relative POPG fraction of 5%. Although we followed the same passivation and measurement procedures, we found that the obtained t_{esc} values varied within up to ≈50% under the same measurement conditions, characterized by the value of the system size parameter κh (Figure S1). Here κ^{-1} denotes the Debye length and $h = h_{\mathrm{s}} - 4$ (Figure 1b)[1]. However it is also possible that part of the observed discrepancy could stem from slightly inaccurate κh estimation for one or both cases. As we have shown in our previous work, one of the main contributions to the measurement error arises from the uncertainty on the slit height, $2h_{\mathrm{s}}$, measured by AFM[2,3]. For instance, in the case depicted in Figure S1 over- or underestimation of $2h_{\mathrm{s}}$ by 1-2 nm for the dataset shown with red or orange color respectively would explain 15-25% of observed t_{esc} discrepancy. Taking this into consideration it is unlikely that the observed difference in performance between the two devices arises solely from the properties of the SLBs.

Section 2. Probing the temporal stability of electrostatic trapping and device longevity in a nanostructured SLB system

In order to probe the stability of SLB coatings, and consequently their applicability for reproducible and stable electrostatic trapping, we performed repeated t_{esc} measurements for 40bp and 60bp dsDNA molecular species within 24-48 hours in the same SLB nanostructure. Figure S2 depicts up to ≈5% discrepancy in measured t_{esc} values for 40bp dsDNA and ≈23% discrepancy for 60bp dsDNA. In the latter case the larger discrepancy can be explained by slightly different κh values that cannot always be tightly controlled due to slight salt concentration drifts that are possible during a given measurement. From the perspective of ϕ_{s} measurements however, a 23% departure in measured escape time would correspond to a ≈6%

error on measured ϕ_s value for 60bp dsDNA ($q_{eff} = -44.8\ e$), since the fractional error on ϕ_s when q_{eff} is known (or equivalently on q_{eff} when ϕ_s is known) is expected to be $\approx t_{esc,e} k_B T / \Delta F_{el}$ (Ref. 2, 4, 5). Here $t_{esc,e}$ is the fractional measurement error on t_{esc} and $\Delta F_{el} = q_{eff}\phi_m = 3.8\ k_B T$ in this case. For the measurements on 40bp dsDNA ($q_{eff} = -33.8\ e$), a 5% departure in measured t_{esc} and an inferred value of $\Delta F_{el} = 3.5\ k_B T$ would correspond to a ≈1.4% error on measured ϕ_s, which is relatively small.

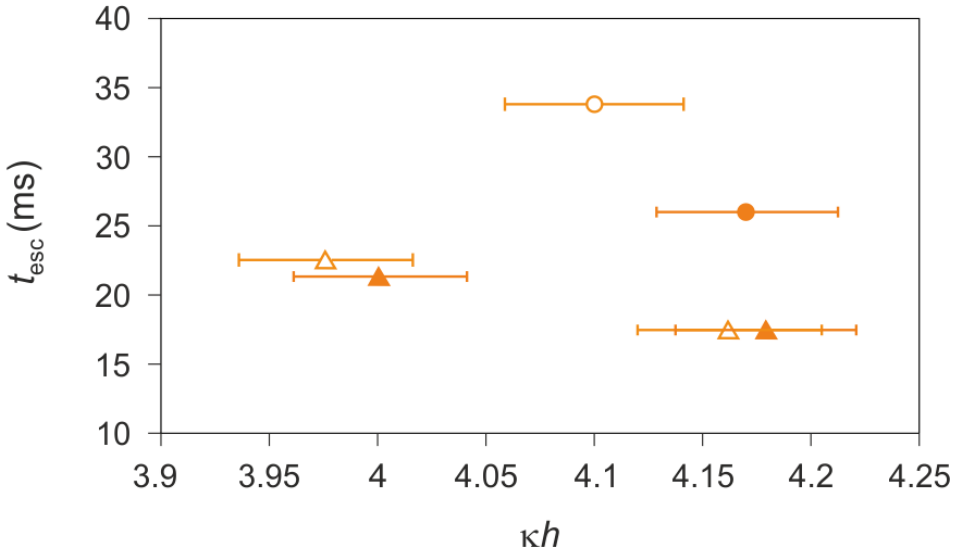


Figure S2. Repeated t_{esc} measurements using 40bp dsDNA (triangles) and 60bp dsDNA (circles) molecular species in the same SLB nanostructure device. Open symbols represent the values for t_{esc} obtained in 24-48 hours after the initial measurements depicted with filled symbols. The errors on t_{esc} ($< 1\%$) are smaller than the data symbols.

Supporting Movie

The video displays SLBs traversing neighboring ≈5 μm wide slits and circumventing the nanostructured circular indentations of radii, r≈250 and ≈370 nm, while flushing a solution of SUVs at pH 3.7 and containing c =100 mM NaCl, prepared from 20% of POPG. The sampling rate in the experiment was 0.4 Hz. The video is sped up by a factor 25.

List of symbols and abbreviations

AFM	Atomic force microscopy
bp	Basepair
c	Salt concentration
d	Depth of the pocket structure
ds	Double stranded
D	Diffusion coefficient
δ	Thickness of a single lipid bilayer
ETe	Escape-time electrometry
e	Elementary unit charge
f	Fluctuation free energy
ΔF_{el}	Electrostatic interaction free energy
Γ	Number density of ionizable groups
$2h_{\mathrm{s}}$	Slit height measured by AFM
$2h$	Effective height of a slit (=$2h_{\mathrm{s}} - 2\delta$)
I_0	Intensity at the feature-free flat surface region of a slit
I_{p}	Intensity at the pocket locations
K_{A}	Acid dissociation constant
κ^{-1}	Debye length
k_{B}	Boltzmann's constant
MLV	Multilamellar vesicles
N	Number of recorded escape events
N_{A}	Avogadro's number
η	Solvent viscosity
POPC	1-palmitoyl-2-oleoyl-glycero-3-phosphocholine
POPG	1-palmitoyl-2-oleoyl-sn-glycero-3-phospho-(1'-rac-glycerol) (sodium salt)
q_{eff}	Effective electrical charge
r_{H}	Hydrodynamic radius
SLB	Supported lipid bilayer
SUV	Small unilamellar vesicles
σ_s	Electrical charge density of the surface
T	Temperature
Δt	Duration of an individual molecular escape event
t_{esc}	Average escape time of the molecule
t_{r}	Position relaxation time of the trapped molecule
W	Depth of the trap or potential well
x_{e}	Error on parameter x
ϕ_{m}	Electrical potential at the slit mid-plane
ϕ_{s}	Effective surface electrical potential
$\phi_{\mathrm{s,0}}$	True surface electrical potential

References

1. Rog, T.; Murzyn, K.; Pasenkiewicz-Gierula, M., Molecular dynamics simulations of charged and neutral lipid bilayers: treatment of electrostatic interactions. *Acta Biochimica Polonica* **2003,** *50* (3), 789-798.
2. Ruggeri, F.; Zosel, F.; Mutter, N.; Rozycka, M.; Wojtas, M.; Ozyhar, A.; Schuler, B.; Krishnan, M., Single-molecule electrometry. *Nature Nanotechnology* **2017,** *12* (5), 488-495.
3. Ruggeri, F.; Krishnan, M., Spectrally resolved single-molecule electrometry. *Journal of Chemical Physics* **2018,** *148* (12), 123307.
4. Ruggeri, F.; Krishnan, M., Lattice diffusion of a single molecule in solution. *Physical Review E* **2017,** *96* (6), 062406.
5. Ruggeri, F.; Krishnan, M., Entropic Trapping of a Singly Charged Molecule in Solution. *Nano Letters* **2018,** *18* (6), 3773-3779.

5

Molecular and interfacial structural measurements in solution

Contents

5.1 The effect of ion type 68
5.2 Charge-spectrometry in an electrostatic fluidic trap . 70
5.3 Paper IV 72

In this Chapter, we present our recently published paper, *"Opto-electrostatic determination of nucleic acid double helix dimensions and the structure of the molecule-solvent interface"* [10]. This work describes a new experimental approach to molecular and interfacial structural measurements in the fluid phase based on the escape-time electrometry (ETe) technique. This study was inspired by recent experimental and theoretical work performed earlier in Krishnan group. Specifically, Ruggeri *et al.* have demonstrated the possibility of high-precision ($<1e$) effective electrical charge, q_{eff}, measurements using ETe [3][4][5][6]. The ability to distinguish the molecules with minor structural and/or compositional differences based on the measured values for q_{eff} was shown on the double- and single-stranded DNA molecular species, point-mutated proteins and protein/DNA molecules labelled with different dyes. Furthermore, a theoretical approach to model electrostatics of biomolecules in

solution was presented by Ref. [9] which provides a method to calculate the values for q_{eff} for linear polyelectrolyte molecules, such as DNA and RNA.

In the present work, we aimed to directly determine the structural parameters of double-helix nucleic acid molecules, comparing their experimentally measured and theoretically calculated values for q_{eff}. Specifically, we used short ($\leq$60 basepairs) B-DNA and A-RNA fragments, modelling them as uniformly charged rigid cylinders of different radii and lengths. In brief, comparing the experimentally measured q_{eff} values with that from theoretical calculations, where helical radius, r, and rise per basepair, b, were used as input parameters, we extracted r and b with 1 and 0.1 Å precision, respectively. Besides that, in order to examine the impact of counterions (Li^+, Na^+, Rb^+, and Cs^+) on molecular electrostatics, we repeated q_{eff} measurements in LiCl, NaCl, RbCl, and CsCl aqueous solutions. While we did not observe any dependence of measured b values on the size of counterions, interestingly, the inferred value for r increased with an increase in the hydrated counterion radius, a_{H}, indicating its strong correlation with the thickness of the "Stern layer". Moreover, the extrapolation of our results to the limiting case of $a_{\text{H}} = 0$ provides an approximation for the thickness of the Stern layer, which qualitatively matches a single layer of hydrated water molecules. We discuss our measurements and conclusions in more detail in the paper at the end of this Chapter. The rest of the Chapter is organised as follows: In section 5.1, we focus on the influence of counterions on processes and properties of biological macromolecules. Further, in section 5.2, we describe how else the relationship between effective electrical charge and structure of a biological macromolecule can be used.

5.1 The effect of ion type

Lots of biochemical properties and processes in electrolyte solutions are known to be dependent not only on the ionic strength of solution but also on the type of ion. Hofmeister and co-workers were the first who studied the effect of the ion type on protein precipitation systematically [101]. Since then, the effect of ion type was observed in regulation of many other biochemical processes, such as enzyme activity,

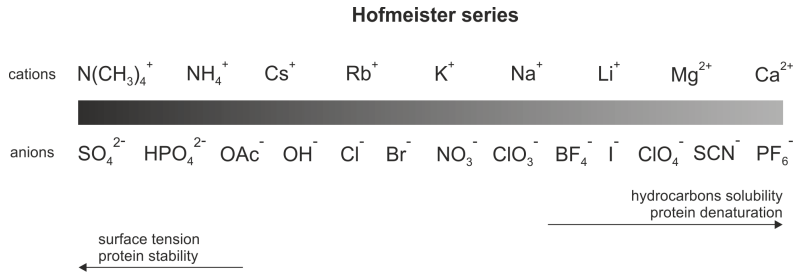


Figure 5.1: Typical ordering of cations and anions in standard direct Hofmeister series based on precipitation studies of negatively charged proteins [110].

protein stability and crystallisation, protein-protein interactions, stabilisation of DNA conformations, and even bacterial growth [102][103][104][105][106][107][108]. In most cases, the influence of cation and anions on biochemical processes follows the ranking of the so-called Hofmeister series (Figure 5.1). However, depending on molecular surface properties, such as sign of the surface charge or surface hydrophobicity, temperature, salt concentration, pH and buffer, the ordering of the ions within the series can be slightly altered or even reversed [109].

Although specific ion effects, also called as Hoffmeister effects, are ubiquitous, the molecular-level mechanisms of these effects are still a matter of debate. It was originally believed that changes in bulk water structure caused by the ions' ability to make or break hydrogen bonds (kosmotropic and chaotropic behavior) are central to the Hofmeister series [111]. Later, however, a negligible impact of ions on the water structure beyond the first hydration shell was demonstrated [112][113]. Moreover, a variety of experimental and computational studies have shown that the origin of specific ion effects most likely stems from the interactions happening at the molecule-solvent interface, such as direct molecule-ions interactions and ions interactions with the molecule's hydration shell [114][115][116][117][118]. Thus, knowing the local arrangement of interfacial ions around a charged molecule holds great interest for understanding the origins of Hoffmeister effects. However, the amount of information on the structure of solid-liquid, and particularly molecule-solvent, interface remains very limited [65]. In our paper, we demonstrate the approach for extracting structural information about molecule-solvent interface using ET*e*. In

conjunction with molecular structural modelling, our measurements furnish a view of the hydration shell and interfacial counterions at a molecular surface.

5.2 Charge-spectrometry in an electrostatic fluidic trap

The unprecedented sensitivity of ET*e* to the value of q_{eff} of a molecule, combined with the ability to predict quantitively accurate values of q_{eff} for a molecule of a given geometry, establishes a powerful platform for probing molecular structural parameters based on q_{eff} measurements [9]. The interconnection between the structure of a molecule and its effective electrical charge can be further exploited for studying heterogeneous molecular systems, which remains a non-trivial task.

This section proposes a new *charge-spectrometry* approach that we started developing in our group. The purpose of charge spectrometry is to detect and identify different kinds of molecules or coexisting structures/conformations of chemically similar molecular species in solution based on the charge values of individual molecules. The first little steps not described in our paper were already done toward this goal. We performed a series of preliminary measurements on individual single-stranded (ss) DNA and RNA molecules of effectively identical sequences, with uracil (U) replacing thymine (T) in ssRNA, as shown in Figure 5.2. In contrast to ssDNA, where stable secondary structure formation is not typical, ssRNA is well known to form stable and varied secondary structures. For the chosen sequence, the formation of at least 17 secondary structures with the values for Gibbs free energy of formation $> 14k_{\text{B}}T$ is expected for ssRNA. While our preliminary measurements yielded a unimodal distribution of q_{eff} values for individual ssDNA molecules, interestingly, they revealed a multimodal distribution of q_{eff} values for the equivalent ssRNA species, likely indicating a variety of folded states.

In conjunction with a theoretical model of molecular electrostatics, these q_{eff} measurements could be further related to the groups of ssRNA secondary structures in solution. The same principle can be used for studying any other

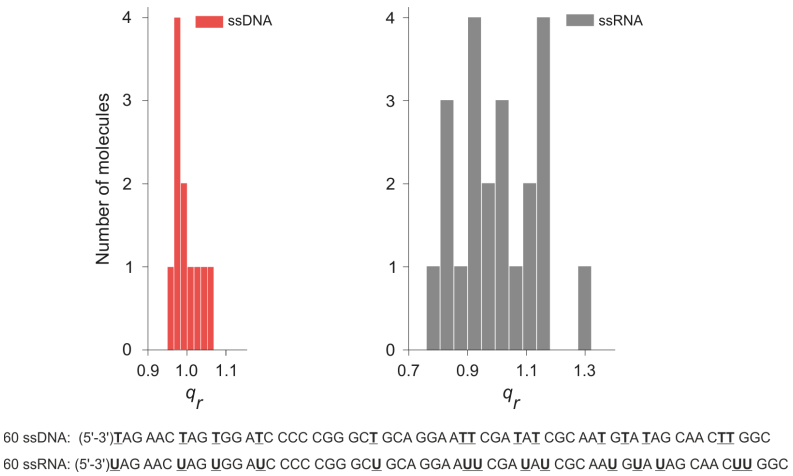


Figure 5.2: Measured distributions of $q_\mathrm{r} = q_\mathrm{eff}/q_\mathrm{mean}$ values for 11 single ssDNA and 22 single ssRNA molecules of provided sequences. Measurements on ssDNA species yielded a unimodal distribution of q_r values (left), while ssRNA measuremenets revealed a multimodal q_r distribution (right), which is likely an evidence of coexisting secondary structures.

mixture of chemically similar yet conformationally/structurally different molecular states in solution.

5.3 Paper IV

Macromolecules

pubs.acs.org/Macromolecules

Article

Opto-Electrostatic Determination of Nucleic Acid Double-Helix Dimensions and the Structure of the Molecule−Solvent Interface

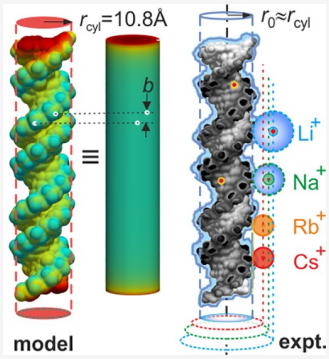
Maria Bespalova, Ali Behjatian, Narain Karedla, Rowan Walker-Gibbons, and Madhavi Krishnan*

Cite This: *Macromolecules* 2022, 55, 6200−6210

Read Online

ACCESS | Metrics & More | Article Recommendations | Supporting Information

ABSTRACT: A DNA molecule is highly electrically charged in solution. The electrical potential at the molecular surface is known to vary strongly with the local geometry of the double helix and plays a pivotal role in DNA−protein interactions. Further out from the molecular surface, the electrical field propagating into the surrounding electrolyte bears fingerprints of the three-dimensional arrangement of the charged atoms in the molecule. However, precise extraction of the structural information encoded in the electrostatic "far field" has remained experimentally challenging. Here, we report an optical microscopy-based approach that detects the field distribution surrounding a charged molecule in solution, revealing geometric features such as the radius and the average rise per basepair of the double helix with up to sub-Angstrom precision, comparable with traditional molecular structure determination techniques like X-ray crystallography and nuclear magnetic resonance. Moreover, measurement of the helical radius furnishes an unprecedented view of both hydration and the arrangement of cations at the molecule−solvent interface. We demonstrate that a probe in the electrostatic far field delivers structural and chemical information on macromolecules, opening up a new dimension in the study of charged molecules and interfaces in solution.



Downloaded via UNIV OF OXFORD on October 27, 2022 at 20:32:41 (UTC).
See https://pubs.acs.org/sharingguidelines for options on how to legitimately share published articles.

Nucleic acids play a central role in biological function. Investigation of the structure of nucleic acids has had a long and compelling history and continues to have far-reaching impact in fields ranging from molecular biology, genetics and disease, to nanotechnology. A range of powerful techniques such as X-ray crystallography, nuclear magnetic resonance (NMR), atomic force microscopy (AFM), small-angle X-ray scattering (SAXS), Forster resonance energy transfer, and optical trapping have generated an unprecedented structural view of DNA, covering all length scales from the atomic to the macroscopic polymer contour level.[1−8] The structural properties and function of this biopolymer in solution are strongly governed not only by steric and mechanical aspects but also by electrostatic considerations, as it is among the most highly charged linear polymers known.[9,10] Indeed, electrical mobility measurements provided an early demonstration of the link between nucleic acid electrostatics and double helix geometry and molecular topology.[11] More recently, magnetic tweezers and SAXS have been used to infer molecular properties of nucleic acids via the measurement of an intra- or intermolecular interaction potential.[12,13] Furthermore, anomalous SAXS and atomic emission spectroscopy (AES) have probed the properties of the counterion atmosphere enveloping nucleic acid molecules,[14,15] while X-ray photoelectron spectroscopy (XPS) has shed light on the interface between a charged nanoparticle and the surrounding electrolyte.[16] To our knowledge, the ability to glean structural information on a diffusing macromolecule and its interface with the electrolyte through precise measurement of the electrical repulsion due to the molecule has not been demonstrated.

EXPERIMENTAL APPROACH

We optically visualize and measure the strength of electrostatic repulsions between a charged molecule and like-charged probe surfaces in solution using wide-field fluorescence microscopy and the recently developed escape time electrometry (ET*e*) approach.[17] In contrast to scanning probe techniques where a nanoscale entity is placed in near contact with a stationary object of interest, our experiment involves a pair of flat, featureless probe surfaces placed in the "far field" of a diffusing charged molecular species in solution. We qualitatively define the electrostatic "far field" as the region in the electrolyte at a distance greater than a Debye length, κ^{-1}, from the object. Here, $\kappa^{-1} \approx 0.304/\sqrt{c}$ nm is a length scale governing the decay of electrostatic interactions in aqueous solution at temperature T = 298 K, where the salt concentration in solution, $c \approx 1-1.5$ mM in this work, implies $\kappa^{-1} \approx 8$ nm. ET*e* measures the reduction in system free energy associated with transferring a charged molecule from a gap between like-charged parallel plates into a nanostructured "trap" region of very weak confinement where the molecule−plate repulsion is negligible[18] (Figure 1a,b). The system is at thermodynamic

Received: April 1, 2022
Revised: June 6, 2022
Published: July 1, 2022



ACS Publications

© 2022 The Authors. Published by American Chemical Society

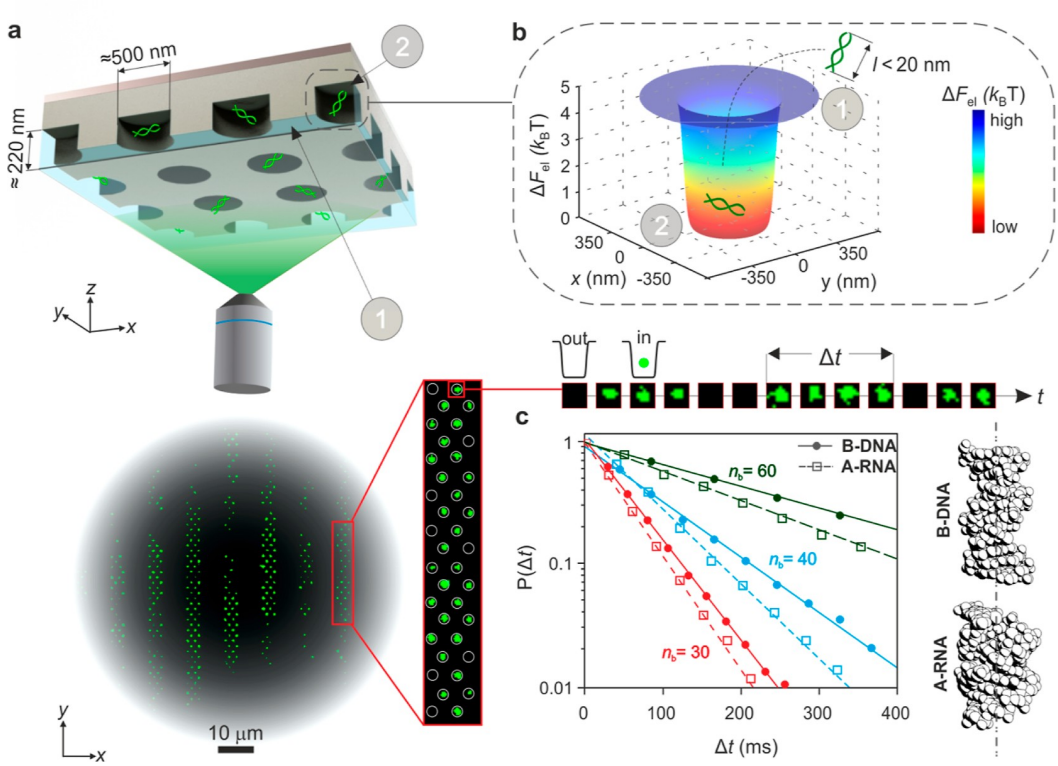


Figure 1. High-precision ET*e* measurements on nucleic acid fragments. (a) Schematic representation (not-to-scale) of fluorescently labeled nucleic acid molecules confined in an array of electrostatic fluidic traps and imaged using wide-field optical microscopy (top). Maximum intensity projection of 500 fluorescence images of parallel arrays of ≈700 traps imaged for 20 s (bottom). (b) Calculated spatial distribution of minimum axial electrostatic free energy, ΔF_{el}, in a representative trap (top). Labels "1" and "2" denote locations of the molecule outside and inside the potential well, respectively, and refer to spatial locations in the trapping nanostructure depicted in the device schematic in (a). A time course of optical images in a single trap (bottom) displays the duration of a single recorded residence event of duration, Δt. (c) Probability density distributions, $P(\Delta t)$, of escape times, Δt, for $N = 10^4$ escape events for measurements on double-stranded B-DNA (solid lines) and A-RNA (dashed lines) in 1.23 mM LiCl for fragment length n_b = 30 (red), 40 (blue), and 60 (green) basepairs fitted to the expression $P(\Delta t) \propto (1/t_{esc})\exp(-\Delta t/t_{esc})$. In order to enable comparison across different molecular species, $P(\Delta t)$ data series are rescaled such that the maximum value is 1. Average escape times, t_{esc}, and measured effective charge values, q_m, are as follows: $t_{esc,30B}$ = 52.2 ± 0.3 ms ($q_{m,30B}$ = −25.28 ± 0.07*e*), $t_{esc,40B}$ 93.9 ± 0.4 ms ($q_{m,40B}$ = −30.46 ± 0.06*e*), and $t_{esc,60B}$= 242.5 ± 1.1 ms ($q_{m,60B}$ = −40.71 ± 0.07*e*) for B-DNA and $t_{esc,30A}$= 46.3 ± 0.2 ms (−23.86 ± 0.04*e*), $t_{esc,40A}$= 70.4 ± 0.8 ms (−28.35 ± 0.13*e*), and $t_{esc,60A}$= 192.5 ± 0.6 ms (−37.26 ± 0.04*e*) for A-RNA. B-DNA systematically displays 10−20% longer escape times and higher magnitudes of effective charge than A-RNA. Space filling structures of B-DNA and A-RNA reproduced with permission from ref 3 (right).

equilibrium, and there are no externally applied fields. We create an array of such electrostatic fluidic traps using periodic nanostructured indentations in one surface of a parallel plate slit composed of silica surfaces separated by a gap of typical height, $2h$ = 75 nm. We introduce nucleic acid molecules at a concentration of 50−100 pM labeled with exactly two fluorescent dye molecules of ATTO 532, suspended in 1 mM Tris buffer and ≈1.2 mM monovalent salt solution, pH 9, into a system with multiple parallel lattices of traps (Figure 1a). Alkaline pH in the experiment ensures that the weakly acidic SiO_2 walls of our nanoslit system are strongly charged.[19] A low (mM) concentration of monovalent salt, in turn, ensures that the electrostatic interactions between a charged molecule and the walls of the slit are sufficiently strong and long-ranged, yielding long-lived trap states of ≈50−200 ms duration. Analytical characterization of the molecular species in the study using, for example, circular dichroism spectroscopy verifies that the solution conditions in our measurement conditions do not perturb the molecules' structural integrity (see Supporting Information Figure S2).

Imaging the escape dynamics of trapped single molecules permits us to identify individual molecular residence events of duration Δt in each trap. Photobleaching of the fluorescent dyes and any potential impact thereof on the measurement have been carefully explored in previous work.[17] Because molecular residence times in the trap are much shorter than dye photobleaching times, we expect dye photophysics and photochemistry not to influence the accuracy of our measured escape times. Overdamped escape of an object from a potential well can be treated as a Poisson process with residence times that are exponentially distributed.[20] Fits of the measured probability density function of residence times, $P(\Delta t)$, to an exponential function of the form $P(\Delta t) \propto \exp(-\Delta t/t_{esc})/t_{esc}$ permit us to extract precise measurements of the molecular species' average time to escape, t_{esc} (Figure 1b,c). The average escape time, in turn, is expected to depend exponentially on well depth, according to the relation $t_{esc} \propto \exp(W/k_BT)$,[20] permitting us to relate measured t_{esc} values to the depth of the trap, W, in the regime of $W > 4k_BT$. In practice, we use Brownian dynamics (BD) simulations of the escape process in order to accurately convert measurements of t_{esc} to the well depth, W, as described previously[17,21,22] (Supporting Information Section S2).

In our BD simulations, we treat molecules as effective spheres of a radius equal to the measured hydrodynamic radius of the molecule. The hydrodynamic radius, r_H, of each molecular species was measured using fluorescence correlation spectroscopy as described in the Supporting Information (Supplementary Methods). The use of an effective hydrodynamic radius, which ignores the anisotropic diffusive behavior of non-spherical objects, is valid when the translational diffusive length scale of interest, l_s, is much larger than the length of

https://doi.org/10.1021/acs.macromol.2c00657
Macromolecules 2022, 55, 6200−6210

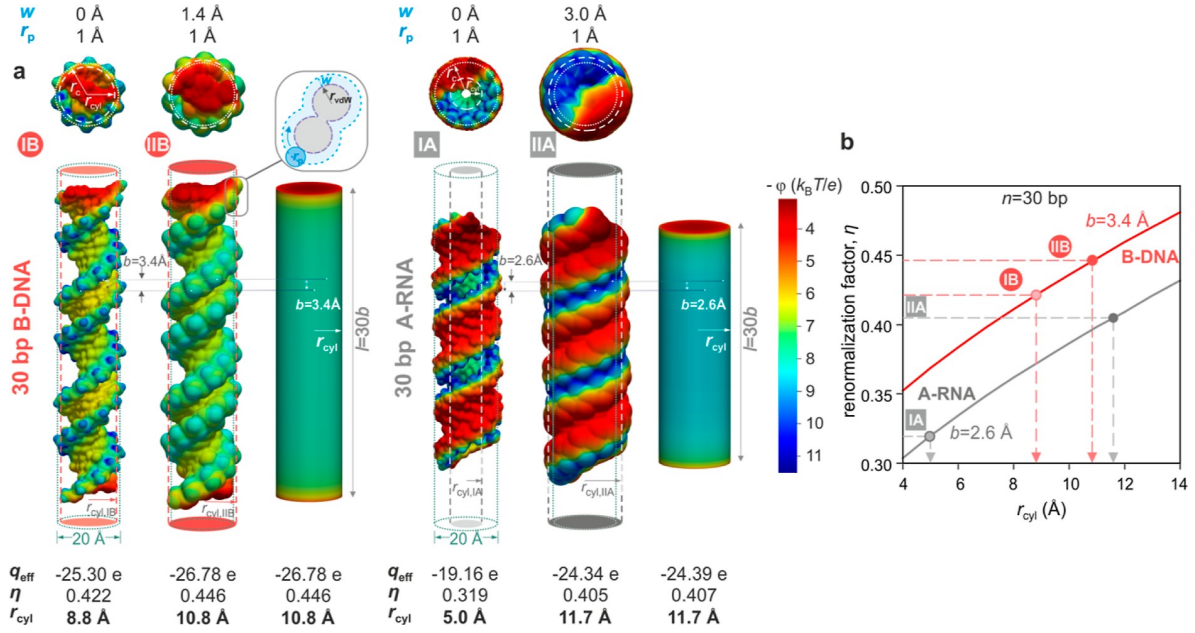


Figure 2. Modeling the double helix as a smooth charged cylinder of finite length. (a) Distributions of surface electrostatic potential, ϕ, for two molecular models of a 30 bp fragment of B-DNA (IB and IIB—left) and A-RNA (IA and IIA—right) generated based on atomic coordinates with rolling probe radius (r_p = 1 Å) and solvent accessible surface (w) parameter values as listed and pictured (inset) alongside axial projections of the molecular models (top panel). Surface potential distributions for corresponding smooth charged cylinders equivalent to models IIB and IIA carrying a total charge $q_{str} = q_{NA} = -60e$ with radii, $r_{cyl,IIB}$= 10.8 Å and $r_{cyl,IIA}$= 11.7 Å, respectively, and length 30b Å in each case. The radius of the equivalent cylinder, r_{cyl} (dashed lines), may be compared with a nominal double-helical radius r_c = 10 Å (dotted lines). (b) Calculated trends for the renormalization factor, $\eta = q_{eff}/q_{str}$, for cylinders of radius r_{cyl} and length 30b Å, with nominal values of b = 3.4 Å for B-DNA (red line) and 2.6 Å for A-RNA (gray line). η values for the four molecular models can be related to those for smooth cylinders and correspond to $r_{cyl,IB}$= 8.8 Å(effective vdW surface), $r_{cyl,IIB}$= 10.8 Å (effective SAS), $r_{cyl,IA}$= 5 Å (vdWS), and $r_{cyl,IIA}$= 11.7 Å (SAS), two of which are depicted in (a). Panels are reproduced from ref 48, with the permission of AIP Publishing.

the molecule, l, or in other words, when the ratio of rotational and translational diffusive timescales $D_t/(l_s^2 D_r) \ll 1$. For a rigid cylinder of length l, this ratio is approximately l^2/l_s^2 (see ref 23). The relevant length scale for translational diffusion, l_s, in an ETe measurement corresponds to the radius of a nanostructured pocket which is typically 250−300 nm. Given the contour length of a 60 bp B-DNA (l ≈ 20 nm), which is the longest fragment considered here, we have $l^2/l_s^2 \approx 0.01 \ll 1$, which ensures that the translational diffusion of an anisometric object may be treated as equivalent to that of an effective sphere for large displacements. It is worth noting that we ignore inertial effects in our BD simulations on the grounds that the momentum relaxation time of the molecule is very small.[24] Although inertial BD simulations of large supercoiled DNA plasmids (∼1000 bp) have shown that mass can have some effects on conformation transition rates in equilibrium, they do also demonstrate that the translational diffusion coefficient of these molecules is accurately captured by conventional BD simulations.[24,25] Thus, for short nucleic acid fragments, which are expected to behave like rigid rods, BD simulations in the overdamped regime are expected to provide an accurate description of our escape time problem.

The highly non-linear dependence of the measurand (escape time, t_{esc}) on the measurable (well depth, W) facilitates precise interaction energy measurements. Observation of a large number of escape events, $N \approx 10^4$, reduces the fractional statistical uncertainty in the determination of W to about 0.1%.[22] Importantly, the dominant contribution to the trap depth, W, is the electrostatic free energy of interaction, ΔF_{el}, which has robust theoretical underpinnings in the Poisson−Boltzmann (PB) framework for solution phase electrostatics as discussed further later.[26−28] Correction of a contribution from axial spatial fluctuations to the total free energy, W, permits us to determine ΔF_{el} with high precision, as described further in Supporting Information, Section S2. We have previously shown that ΔF_{el} may be regarded in terms of the product of the effective charge of the molecule in solution, q_{eff}, and the electrical potential, ϕ_m, at the midplane of the slit, such that $\Delta F_{el} = q_{eff}\phi_m$.[29,30] If ϕ_m is accurately known, the measurable in our experiment is the effective charge, q_{eff}, of the molecular species under the experimental conditions. Note that our values of q_{eff} for charged spheres and cylinders are comparable to those encountered in other charge renormalization theories.[30−32] Furthermore, our interaction-energy-based definition of q_{eff} (i.e., $\Delta F_{el} = q_{eff}\phi_m$) is identical to that in Kjellander's dressed ion theory.[33−36]

The principle behind the present study may be summarized as follows: Accurate measurements of the electrostatic free energy, ΔF_{el}, permit us to measure the effective charge, q_{eff}, of three different lengths of a nucleic acid species (e.g., A- or B-form helix in this work). Theoretically expected effective charge values may also be calculated using the PB theoretical framework for each length of the fragment, as described previously (see Supporting Information Section S7).[30] As described further below, calculations show that q_{eff} depends strongly on geometrical dimensions of the molecular species of interest, for example, the rise per basepair, b, and helical radius, r. The precise functional form of this dependence is itself a function of the length of each fragment, as shown in Figures 3a and S4a. Thus, we have three independent theoretical relationships relating effective charge with molecular geometry for the fragment lengths under consideration. Since the effective charge of the molecular conformation under study (e.g., either the A-form or the B-form helix) may be described by a *common pair* of underlying geometric parameters (e.g., rise per basepair, b, and helical radius, r), a comparison of the measured effective charge values with the theoretically expected values for the three lengths of the double helix permits us to extract estimates of the two geometric properties of interest (described in detail in Supporting

https://doi.org/10.1021/acs.macromol.2c00657
Macromolecules 2022, 55, 6200−6210

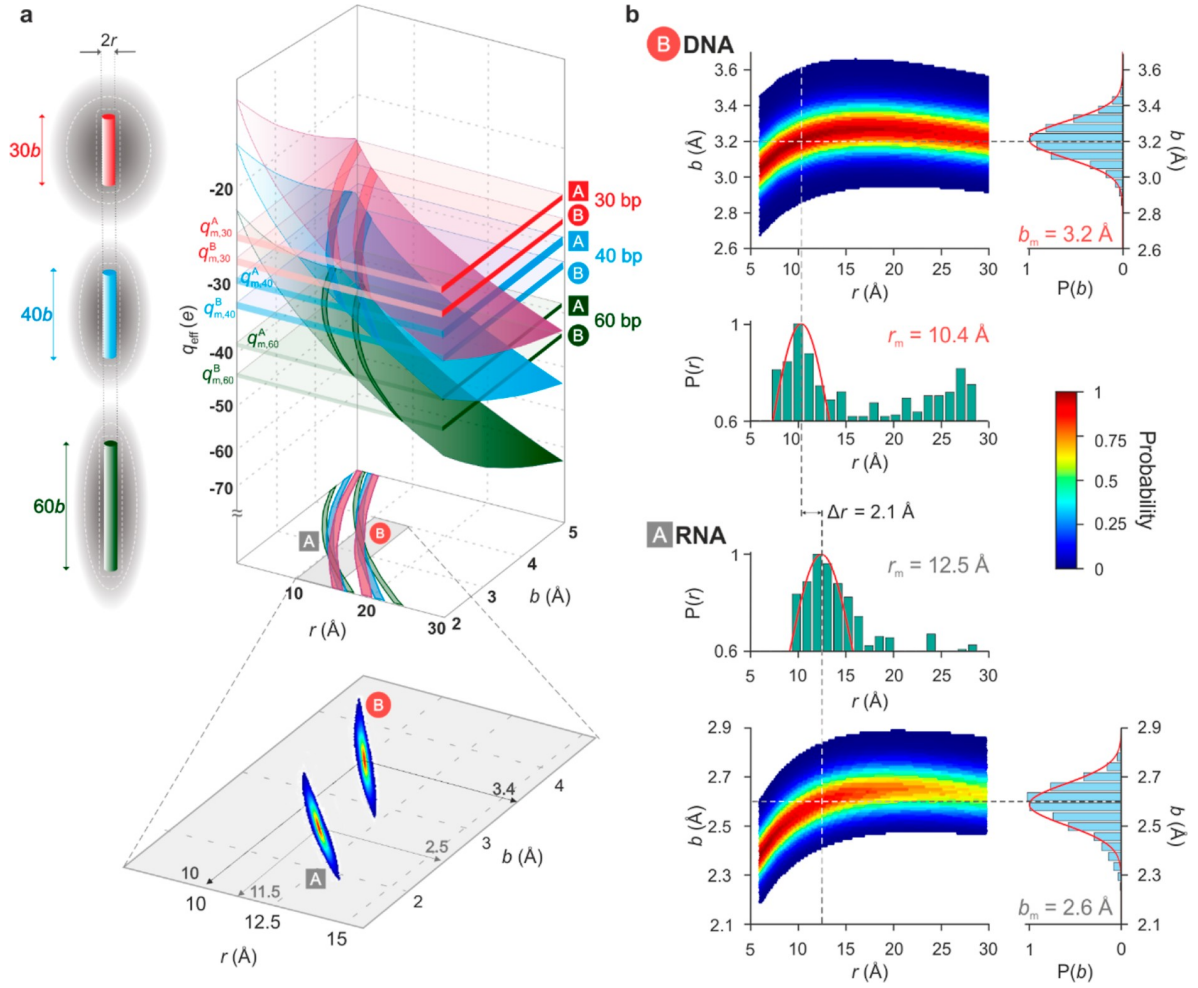


Figure 3. Measuring the helical rise per basepair and radius of the double helix. (a) Principle behind the measurement of the helical rise per basepair, b, and radius, r, of the double helix, for an ideal experiment, free of systematic measurement uncertainty (i.e., $f_M = 1$). Schematic representations of three lengths of a double-stranded nucleic acid species surrounded by a cloud of screening counterions (left). A measured value $q_m \pm q_{m,e}$ for each molecular species of length n bp, in conjunction with the corresponding calculated 2D function (colored surface) for the effective charge, $q_{eff,n} = Q_n(b, r)$, generates a curve of possible solutions in b and r. Intersection of three such curves for n = 30, 40, and 60 bp yields a probability-weighted manifold of solutions from which measured values, b_m and r_m, for the rise and radius, respectively, of each helix form can be obtained. (b) Measured b–r probability manifolds for B-DNA (top) and A-RNA (bottom) for an experiment performed in 1.2 mM CsCl. Since $f_M \neq 1$ in experiments, measured b–r manifolds are broader than those in the ideal case depicted in (a) yielding $b_{m,B}$= 3.2 Å and $r_{m,B}$= 10.4 Å and $b_{m,A}$= 2.6 Å and $r_{m,A}$= 12.5 Å for B-DNA and A-RNA, respectively.

Information, Section S4). The third parameter we extract from the analysis characterizes the measurement device. We find that measurements of the helical radius in electrolytes containing cations of different radii further permit us to make inferences on the structure of the molecular interface with the electrolyte.

For a highly charged molecule in solution, it has been shown that $q_{eff} = \eta q_{str}$, where η is a molecular geometry-dependent charge renormalization factor.[30−32,37,38] q_{str} denotes the net electrical charge in the molecular structure and stems from the sum of charge carried by the ionized structural groups and bound ions from the electrolyte. A highly acidic molecule like DNA, n basepairs in length and carrying a chemical modification at both 5′-end phosphates, has a structural charge $q_{str} = q_{NA} = -2ne$ at pH 7 and higher (see Supporting Information, Section S3.2). Here, e is the elementary charge and q_{NA} is the amount of charge due to the backbone phosphate groups on the molecule which are all fully ionized in our experiments. However, if a number of positively charged counterions, δ, associate with the molecule, for example, via energetic interactions beyond the purely Coulombic that are already accounted for within the PB model, then $q_{str} = q_{NA} - \delta e = f_{ion} q_{NA} e$, where $f_{ion} = (q_{NA} - \delta e)/q_{NA}$ is an inverse ion affinity parameter which tends to zero as $\delta e \rightarrow q_{NA}$.

To a first approximation, a periodic linear charged structure such as a short fragment of a double-stranded nucleic acid may be viewed as a smooth, charged cylinder of finite length.[39,40] Here, η depends on the charge density of the polyelectrolyte and therefore on the axial base spacing, b, and the radius of the polyelectrolyte backbone, r. Considering a short stretch of a nucleic acid whose contour length, $l = nb$, is of the order of the Debye length, η further depends on l.[17,41,42] Upon approximating a short stretch of DNA (≤60 bp) by a rigid cylinder of radius r and length l, we thus have $q_{eff} = \eta q_{str} = Q(n, b, r)$ which can be calculated for a range of b and r values using the PB framework (Figures 2 and 3).[29,30] Finally, for a given molecular geometry and structural charge, η is essentially independent of ion affinity for $f_{ion} > 0.7$. Although η does exhibit some dependence on the salt concentration, c, this variation is negligible over the small range in experimental uncertainty in c in a given measurement.[30,31]

https://doi.org/10.1021/acs.macromol.2c00657
Macromolecules 2022, 55, 6200−6210

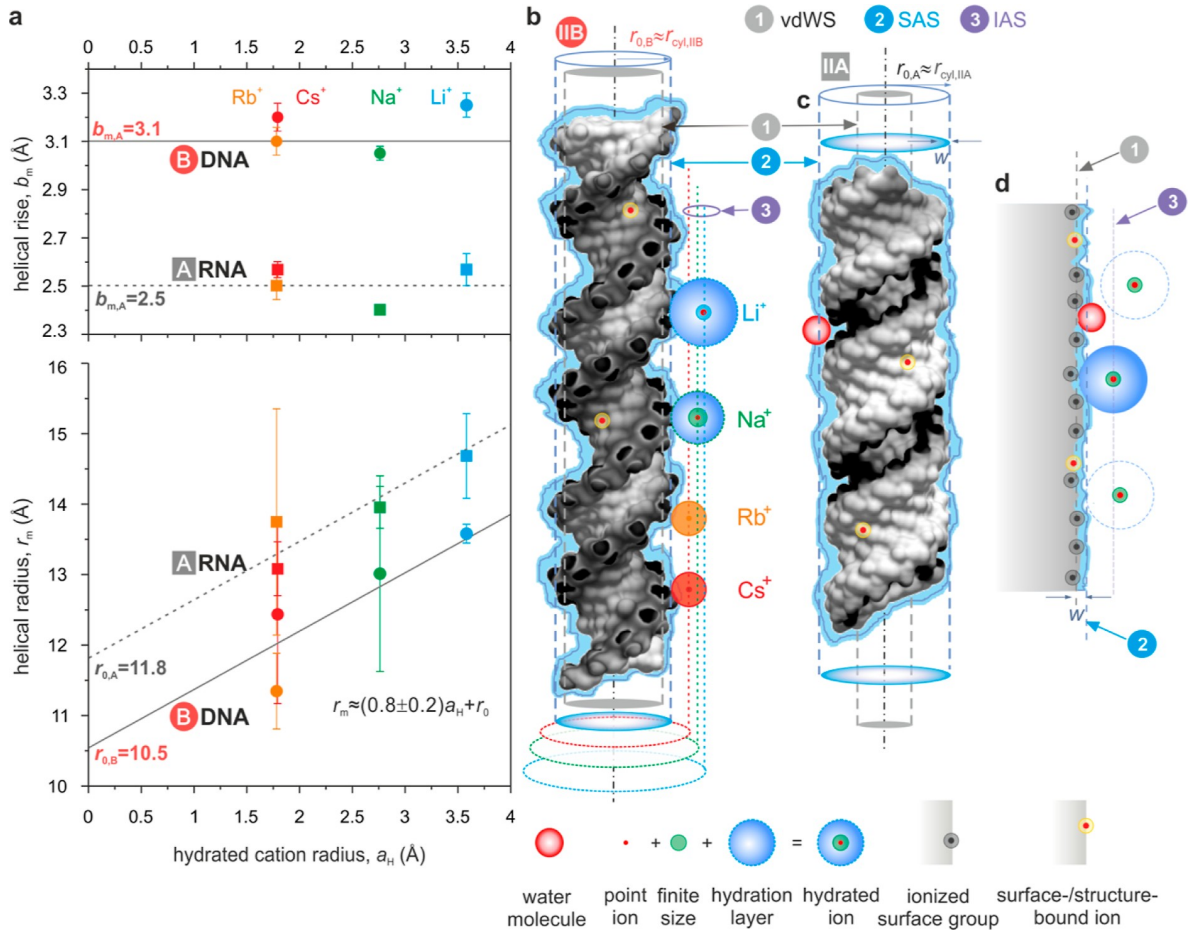


Figure 4. Inferring the structure of the molecule−electrolyte interface. (a) Measured helical rise per basepair, b_m (top), and radius, r_m (bottom), as a function of the hydrated cation radius, a_H. Error bars denote s.e.m. Rise per basepair values show no significant variation with a_H and yield average values of $b_{0,B}$= 3.1 ± 0.1 Å and $b_{0,B}$= 2.5 ± 0.1 Å. Helical radius data were fit with a function of the form $r_{m,A \text{ or } B} = ka_H + r_{0,A \text{ or } B}$, yielding $r_{0,B}$= 10.5 ± 0.6 Å and $r_{0,A}$= 11.8 ± 0.6 Å. The slope, k = 0.8 ± 0.2, is a shared fit parameter in both relationships. (b) Cylinder of radius $r_{0,B}$= 10.5 Å ≈ $r_{cyl,\ IIB}$ (blue dashed cylinder) depicting that the effective cylinder in model-IIB of B-DNA is superimposed for comparison on the vdW molecular surface in model-IB (gray dashed cylinder). k = 0.8 ± 0.2 suggests that the distance of the closest approach of screening cations to the molecular surface is directly related to the radius of the hydrated cation species, a_H. The resulting effective "ion accessible surface" (IAS) is the distance from the molecular axis beyond which the point-ion description of the electrolyte may be invoked (red, green, and blue dotted lines). The molecular structure may carry bound ions (yellow spheres) whose charge is included in q_{str}. (c) For A-RNA, model-IIA which includes a SAS of thickness w = 3 Å meets the condition $r_{cyl,IIA} \approx r_{0,A} \approx$ 12 Å (blue dashed cylinder). (d) Extrapolating the inferred structure of the molecule−electrolyte interface in (b) to a view of a macroscopic interface in solution where w < 3 Å.

In view of the grooved molecular surface of double-stranded nucleic acids and the helicoid distribution of charge on the molecular backbone, we first test the quality of the smooth cylinder electrostatic model for DNA in the context of our experiment (Figure 2). We calculate ΔF_{el} and therefore determine q_{eff} values for molecular models of the full 3D structure of 30 bp B-DNA and A-RNA molecules constructed using the 3DNA platform (Supporting Information Section S7).[43] We then determine q_{eff} values for smooth cylinders of variable radii, r, and the same axial rise per basepair, b, as the molecular helices. Cylinders of radius r_{cyl} whose q_{eff} values are identical to those of the molecular helices within computational error (estimated at <0.1%) are termed equivalent cylinders. Physically, this means that the computed electrostatic free energy difference between the "free" and "trapped" states (states1 and 2 in Fig. 1b respectively)of the molecular helix, ΔF_{el}, is indistinguishable from that due to a smooth cylinder of radius r_{cyl}. Importantly, a domain decomposition of the free energy in the system demonstrates that the electrostatic well depth of the trap, ΔF_{el}, stems in nearly equal proportions from the "near field" (the region within about 2 nm) of both the molecule and the slit surfaces[48]. Note that high-resolution structural studies have shown that the double helix can have local structural variability, for example, sequence-dependent and thermally induced variation of the rise per basepair along the molecular contour, which is not captured in the uniformly charged cylinder model.[44−47] Our approach measures an averaged interaction response from the molecule. Whereas thermal variations are expected to average out in the measurement, local sequence-dependent variations will be interpreted in terms of an *average* rise per basepair parameter characterizing the molecule. Therefore, for the current work, we assume that a coarse-grained model that treats the double helix as a uniformly charged cylinder provides a sufficient description of the measurement. Although mapping of the molecular problem on to that of a uniform cylinder can be highly informative, future work could directly compare electrometry measurements with expectations for molecular structural models.

We considered two molecular models each for B-DNA and A-RNA, with all molecular surfaces generated using rolling probe radii, r_p = 1 Å. Models-IA and -IB were generated using reference van der Waals

https://doi.org/10.1021/acs.macromol.2c00657
Macromolecules 2022, 55, 6200−6210

(vdW) values for all atoms, while models-II A and -IIB entail atomic radii that are all w = 3 Å and w = 1.4 Å larger than the vdW values, respectively (Figure 2a). While model-I is expected to capture the vdW surface (vdWS) of the molecule, a larger atomic radius in model-II is expected to mimic a "solvent accessible surface" (SAS) which defines the distance of closest approach of the center of a water molecule to the macromolecular structure. For B-DNA, we find that models-I and -II yield equivalent electrostatic cylinder radii, $r_{cyl,IB} \approx$ 9 Å and $r_{cyl,IIB} \approx$ 11 Å, respectively, which are in remarkable agreement with the nominal outer helical radius, $r_c \approx$ 10 Å, inferred from molecular crystal structures (Figure 2b).[28] Interestingly, for A-RNA, the r_{cyl} values for the two structures considered are rather different: $r_{cyl,IA} \approx$ 5 Å and $r_{cyl,IIA} \approx$ 12 Å, suggesting that an experimental measurement with sufficient accuracy may be able to distinguish between the two models, shedding light on molecular interfacial structural detail in an electrolyte (Supporting Information Section S7). The modeling procedure has been described in detail previously[48] and is summarized in Supporting Information Section S7.

Precise measurements (uncertainty<1%) of q_{eff} on three nucleic acid fragments of different lengths may be compared with calculated q_{eff} values for charged cylinders in order to extract measures of three unknown quantities of interest (Figure 3a). Two of these three unknowns describe geometric properties of the underlying molecular structure, namely, the radius of the helix, r, and the axial helical rise per basepair, b. The third unknown relates to experimental measurement conditions and the associated uncertainty. Experiments generally contain parameters that need to be well controlled, or accounted for, in order to foster accurate measurements. We account for uncertainties in various experimental quantities through the use of two correction terms: one is a multiplicative factor, f_M, and the other is an additive quantity, f_A, such that the measured effective charge for each fragment of size n bases is given by $q_{m,n} = f_M(q_{eff,n} + f_A)$. The correction factor, $f_M = f_{ion}^R f_\phi$, accounts for effects that influence the measured effective charge in a multiplicative fashion and is, in turn, composed of two terms. f_ϕ reflects a property of the measurement apparatus and involves the overall uncertainty in the midplane electrical potential, ϕ_m, in the slit. ϕ_m directly relates to the effective surface potential of the silica surfaces, ϕ_s, via the relation $\phi_m = 2\phi_s \exp(-\kappa h)$, and we use a nominal value of $\phi_s = -2.8 k_B T/e$ for our experimental conditions as noted in previous work.[21] Examples of factors that contribute to variations in f_ϕ include the finite accuracy of the order of $h_e \approx$ 1 nm in the height of the slit, the particular value of the surface charge density on the confining walls, the salt concentration, and possible ionic species effects on ϕ_s. f_{ion}^R, in turn, represents a relative "inverse affinity" of cations for the nucleic acid molecule, measured with respect to Na^+ ions, such that $f_{Na}^R = 1$. Finally, f_A is an additive term, the main contribution to which is $q_{dye} \approx -0.5e$, the effective charge of the fluorescent label covalently coupled to both 5′-phosphates of the double helix, which is determined by measurement (see Supporting Information, Section S3).

We constructed 30, 60, and 40 bp fragments of dsDNA and dsRNA and measured the effective charge for each molecular species. We then compared the measured effective charge values, q_m, with the corresponding calculated values, q_{eff}, for cylinders with linear charge spacing corresponding to rise per basepair values, b, ranging from 2 to 5 Å and the radius, r, in the range of 6−30 Å. In principle, simultaneously solving the three known relationships for $q_{eff,n} = Q_n(b, r)$ with $q_{eff,n} = q_{m,n} - f_A$ for the three fragments should yield values for the unknowns b and r when $f_M = 1$ (Figure 3a). However, in general, $f_M \neq 1$, and the measurement data, which are of the form $q_m \pm q_{m,e}$, are not single-valued but rather carry Gaussian-distributed uncertainties of width $q_{m,e}$ about the mean value, q_m. Thus, we have three functions of the form $q_m \pm 3q_{m,e} = f_M(q_{eff} + f_A)$. Pairwise division of these three equations eliminates f_M and results in two functions that may be numerically solved to yield a probability-weighted manifold of solutions in b and r (Figure 3b). We determine the most probable measured values b_m and r_m using an algorithm developed based on simulated input data. f_M is then determined self-consistently by substitution into one of the three equations for q_{eff} (Supporting Information Figure S4 and Section S4).

RESULTS

We measured the radius, r, and axial rise per basepair, b, for dsDNA and dsRNA in solution containing alkali metal chlorides LiCl, NaCl, RbCl, and CsCl. Although the bare cationic radius decreases in the order Cs → Li, in an electrolyte, hydrated ionic radii increase with decreasing ionic radius due to favorable interactions between the ionic core and the surrounding polarizable water molecules (Figure 4). We found that our measured rise per basepair values for B-DNA and A-RNA are essentially insensitive to the nature of the cation in solution, and we obtained rise values averaged over all measurements of $b_{m,B}$= 3.1 ± 0.1 Å and $b_{m,A}$= 2.5 ± 0.1 Å for B-form and A-form helices, respectively (Figure 4a, top). These measurements compare well with values from crystallography and NMR.[2,3,5,45,49]

In contrast to the response of the helical rise to the cationic species in solution, we found that the inferred helical radii tended to increase in the order Cs → Li (Figure 4a, bottom). We further systematically found that $r_{m,A} > r_{m,B}$ with an average difference in helical radii between A and B forms of about 1−2 Å. Using values for hydrated ionic radii, a_H, determined from ionic mobilities and slip hydrodynamic boundary conditions, and plotting measured helical radii, r_m, against a_H, revealed a linear relationship between the two quantities.[50] Extrapolating the measured r_m values to a_H = 0 yielded values for r_0 that may be thought to represent the measured radii of equivalent cylinders in a hypothetical electrolyte containing point ions (Figure 4a). We obtained $r_{0,B}$= 10.5 ± 0.6 Å and $r_{0,A}$= 11.8 ± 0.6 Å for B-DNA and A-RNA, respectively (Figure 4a). Atomic models of B-DNA and A-RNA display axial radii of gyration of ≈6.7 and ≈7.8 Å and have helical radii of ≈8 and ≈9.5 Å based on the main backbone carbon atoms, respectively (Supporting Information Figure S10a). Thus, in addition to the average axial charge separation, our measurement is sensitive to the radial arrangement of atoms in the double helix. The latter appears to contribute to an effective electrical molecular surface topography, the geometry of which can be sensed even by a probe in the electrostatic far field, according to our measurements (Figure 2a and Supporting Information Figure S10b).[10] Figure S9 further examines the influence of various literature estimates of hydrated cationic radii on the inferred trends in r_m.

Our measured r_0 values may be thought to reflect a hypothetical experimental scenario involving point ions in solution (Supporting Information Section S7.5). We therefore expect these values to be amenable to direct comparison with the quantity r_{cyl} computed for the molecular models. We find that $r_{0,B}$= 10.5 ± 0.6 Å is comparable to $r_{cyl,IIB}$= 10.8 Å obtained for model-II of B-DNA that incorporates a SAS region of width w = 1.4 Å (Figures 4b and 2a). For A-RNA, we obtain agreement between the measured value of $r_{0,B}$= 11.8 ± 0.6 Å and a molecular model constructed using w = 3 Å, yielding $r_{cyl,IIA}$= 11.7 Å, as reflected in model II-A. Taken together, the measurements and the molecular electrostatic

https://doi.org/10.1021/acs.macromol.2c00657
Macromolecules 2022, 55, 6200−6210

models for both B-DNA and A-RNA would point to the presence of a hydration layer of thickness $1 \lesssim w \lesssim 3$ Å. This is in general agreement with the value of 1.4 ± 0.6 Å reported in a study using XPS of the Stern layer at the silica−water interface.[16,51] Furthermore, the large disparity between the measured r_m value for A-RNA and the r_{cyl} value calculated for model-IA would appear to strongly preclude a molecular electrostatic model that neglects hydration at the molecular interface. A combination of the "hollow spine" along the A-RNA molecular axis, the deep and narrow major groove, and the closer packing of charged atoms in general would appear to render a measurement of the electrostatic free energy of A-RNA a more sensitive probe of interfacial structural detail and the finite size of ions in solution compared to B-DNA.[52,53] Finally, our inferred slope for the r_m versus a_H relationship, $k = 0.8 \pm 0.2 \approx 1$, suggests that the radius of the effective cylindrical molecular surface contour in solution is enlarged by an amount that correlates with the radius of the hydrated cation (Figure 4c). Thus, in our picture, the thickness of the "Stern layer" at the molecular interface has a strong contribution from the size of the counterion in the electrolyte (Figure 4c,d).

Importantly, we find that a PB model of the electrostatics in conjunction with a geometric modification of the object—a slight inflation of the cylindrical radius in this case—is sufficient to model measured free energies in an experimental system with finite-sized ions.[42] A comparison between all-atom molecular dynamics (MD) simulations and a PB model of nucleic acids reveals that the latter is capable of capturing many features evident in MD simulations, for example, integrated spatial free energy density profiles which are central to our work. However, it has also been pointed out that detailed agreement between a PB model and MD simulations, for example, at the level of spatial ionic densities in the major groove of A-RNA, will likely require a suitably modified PB theory.[53,54] In future, a modified PB model for a charged cylinder of a fixed radius, which self-consistently accounts for hydration and finite ion-size effects, is likely to provide a common underlying framework to explain the results for both A- and B-form helices.[55] Such a model will likely furnish more refined estimates of the interfacial parameters of interest, for example, w, k, and a_H.

To conclude the study, we focus on f_M, a parameter describing the experimental apparatus, determined in the measurement alongside b_m and r_m. Like r_m, we found that f_M displayed a systematic dependence on the cationic species in solution. For measurements that hold fixed all other experimental parameters, such as the slit height and salt concentration, any cation species-dependent variation in $f_M = f^R_{ion} f_\phi$ is expected to stem from either, or both, of the two interfacial sources: (1) cation-specific surface potential dependence of the silica surfaces, reflected in f_ϕ and/or (2) non-electrostatic cation interactions with the double helix captured by a relative ion binding affinity factor, given by f^R_{ion}. Our measured f_M values for various cationic species relative to those for the Na^+ ion yielded on average $f_{M,Li}/f_{M,Na} \approx 1.1$, $f_{M,Cs}/f_{M,Na} \approx 0.9$, and $f_{M,Rb}/f_{M,Na} \approx 0.9$ (where $f_{M,Na} \cong 1$), and the affinity factors lie in the order Li > Na > Rb ≈ Cs (Supporting Information Figure S8). These values prove to be close to the "Hofmeister series"-dependent zeta (ζ) potentials reported for silica surfaces in alkali metal chloride solutions of concentration 10^{-3} M to 1 M, where $\frac{\zeta_{Li}}{\zeta_{Na}} = 1.1 \pm 0.1$ and $\frac{\zeta_{Cs}}{\zeta_{Na}} = 0.8 \pm 0.1$ (Supporting Information Figure S8b).[56,57] Assuming that the reported trend for the ζ-potential reflects the behavior of the effective surface electrical potential, ϕ_s, in our experiments, our measured trends for f_M would suggest that most of the observed ion-dependent variation in q_m stems from the variation of surface potential of silica, captured by f_ϕ. Our estimate of $0.9 \lesssim f^R_{Li} \lesssim 1$ would therefore point to a 10% reduction in $|q_{NA}|$, at the most, due to binding of Li^+ cations to the molecule, that is, $0 \lesssim \delta_{Li} e \lesssim 0.1|q_{NA}|$. Therefore, at present, we do not obtain evidence of relative cation affinity values, f^R_{ion}, that depart substantially from 1. To compare these observations with other techniques, Na^{23} NMR reports little significant sodium binding to DNA, with dissociation constants on the order of several molar.[58] MD studies find that while monovalent cations do reside in the major and minor grooves of DNA, there is little preferential long-lived binding of monovalent cations (e.g., Li^+ compared to Na^+).[59] However, AES reports weak affinities for Li^+ cations corresponding to an amount of bound charge of ≈5−10% of $|q_{NA}|$, and transport measurements report decreased electrical mobility of DNA in the presence of Li^+ cations.[14,60,61] Our observation of an absence of substantial variation in relative affinity of alkali metal cations, and a possible weak affinity of Li^+ for the double helix, is thus in broad agreement with previous observations.

DISCUSSION

It is important to note that although it may in principle be possible to evaluate electrostatic interaction free energies, ΔF_{el}, using molecular simulations such as Monte Carlo (MC) or MD methods,[53,62,63] these techniques are computationally resource-intensive as the system size increases. Statistical simulation approaches such as MC require an exhaustive sampling of the configuration space in order to provide reliable results with acceptable accuracy.[64] On the other hand, PB theory ignores correlations between ions but is nonetheless expected to provide satisfactory theoretical description of experiments involving monovalent salts in solution which is typical for ET*e* measurements. The PB approximation relies on the basic assumption that the potential of mean force for each ion type is equivalent to the mean electrostatic potential.[42,65] This assumption neglects all higher-order ion correlations which manifest both through a long-range coulombic interaction and a short-range volume-excluded effect.[42] These correlations are particularly important at high concentrations and in the presence of multivalent ions in solution.[66−68] Nevertheless, comparison of PB ion densities with MC simulations involving finite-sized ions[69,70] reveals unexpectedly good agreement, despite the fact that PB theory is typically thought of as a "point-ion" description of the problem.[42] Although the reason for this behavior has not been fully understood, it might be attributed to fortuitous error cancellation within the PB approximation.[42]

Furthermore, in recent years, several attempts have been made to incorporate missing additional physics into the standard PB model by introducing different forms of modified PB equation.[68,71−73] Although these modified PB models provide results that compare well with MC/MD simulations, their application to situations involving monovalent ions and dilute solutions does not lead to results which are significantly different from those of standard PB theory. Thus, in general, the PB approximation gives a satisfactory description for long-range electrostatic interactions of DNA molecules in

https://doi.org/10.1021/acs.macromol.2c00657
Macromolecules 2022, 55, 6200−6210

monovalent electrolytes, which is also in agreement with MC simulations and hypernetted chain approximations.[67] The fact that our measurements of the rise per basepair and radius of two classes of the double helix are so close to values known from high-resolution structural biology techniques, such as X-ray crystallography and NMR, may be viewed as evidence of the validity and applicability of the combined experimental and modeling approach described here.

In conclusion, although molecular simulations are gaining dramatically in sophistication and power, field theoretical descriptions of these systems remain important due to the high computational cost of problems involving explicit atoms in a many-body problem. We demonstrate that precise measurements of interaction free energies readily distinguish between structurally or conformationally distinct states of a molecular species. Viewed through the lens of the standing theoretical model for electrostatics, such measurements also provide information on molecular and interfacial structure. Although the approach does not furnish single-atom locations, it is capable of delivering more coarse-grained molecular structural information at high resolution, which could prove useful in analyzing molecular species that are challenging to crystallize or to isotope-label for NMR. Our findings further provide estimates of geometric parameters that describe the far-field properties and interactions of a polyelectrolyte in solution, for example, the effective molecular radius, the SAS, and the radii of ions at an interface. With the surface electrical characteristics of the system (given by f_M) determined with high accuracy, we expect that in future, molecular electrometry measurements will be capable of yielding similar information on a molecular species using fewer independent measurements. For example, it may be possible to use our approach to directly measure sequence-dependent differences in the rise per basepair between different oligonucleotide species.[74] Furthermore, given the sensitivity of the method to small differences in 3D conformation, for example, in helical geometry as shown in this work, it is likely that molecular electrometry will provide sensitive detection of more complex 3D conformational states and structural features such as loops and bubbles in molecules. Besides, the method is not limited to the study of rod-like molecules but can be readily extended to longer nucleic acids, as long as the measurements are then compared with free energies calculated for relevant molecular structural models.[53] Although the present work relies on optical observation of about 1 zmol of a species, label-free optical detection could foster such measurements at the level of one molecule in solution, enabling analysis of biomolecular conformational or structural heterogeneity at the highest sensitivity.[75] Finally, since ions and water tend to be disordered, they generally evade detection by high-resolution structural methods. Thus, beyond the structural properties of the molecule, our study furnishes a parameter-free, atomic-level view of the contact region between a molecule and the electrolyte phase (Figure 4b,c), reporting directly on the structure of the "Stern layer" at the liquid−solid interface in solution (Figure 4d).

MATERIALS AND METHODS

ETe Experimental Procedure: The Measurement of Molecular Escape Time, t_{esc}. Devices for ETe measurements were fabricated using silicon/silicon dioxide and glass substrates as previously described.[18] Nanofabricated fluidic slits and nanostructured pocket regions were extensively characterized by scanning electron microscopy (SEM), AFM, and profilometry. We used nanoslits of height $2h$ = 71−77 nm and a width of about 5 μm and pockets of depth d = 140−160 nm and radii of either 250 or 300 nm. Nanoslits were loaded with a suspension of the molecular species of interest at a concentration of 50−70 pM using pressure-driven flow for about 1 min. The flow was then stopped, and the inlet and outlet reservoirs were filled with the same suspension and sealed to prevent evaporation. The system was allowed to equilibrate for 5−10 min and maintained in an argon atmosphere during the whole measurement.

The salt concentration in the electrolyte was monitored before and after the measurement by measuring solution conductivity with a microconductivity meter (Laquatwin, Horiba Scientific, Japan). The conductivity meter was calibrated for each salt species: LiCl, NaCl, RbCl, and CsCl (Supporting Information Figure S2d). Solution pH was measured before and after the measurement using a micro-pH electrode (InLab, Mettler Toledo, UK) and pH meter (Orion Star A215, Thermo Scientific, UK).

Optical measurements were performed using wide-field fluorescence imaging. Fluorescence excitation was achieved by illuminating the labeled molecules with a 532 nm DPSS laser (MGL_III-532_100 mW, PhotonTec, Berlin) that was focused at the back aperture of a 60×, NA = 1.35 oil immersion objective (Olympus, UK). Images were acquired using an sCMOS camera (Prime95B, Photometrics). Time-lapse videos were recorded using an exposure time t_{exp}= 5 ms and a variable lag time between exposures, t_{lag}. The sampling frequency is the inverse of t_{cycle}, where $t_{cycle} = t_{exp} + t_{lag}$ is a factor 2−4 smaller than the average escape time, t_{esc}, for the molecular species of interest. Typical cycle times were in the range of 40−65 ms for 60 bp DNA/RNA, 25−40 ms for 40 bp DNA/RNA, and 15−25 ms for 30 bp DNA/RNA. Therefore, typical imaging frequencies were around 15−25 Hz for 60 bp DNA/RNA, 25−40 Hz for 40 bp DNA/RNA, and 40−67 Hz for 30 bp DNA/RNA.

Fluorescence images of molecular trapping were analyzed as described previously.[17] Briefly, regions of interest (ROIs) centered on the locations of the individual traps were identified in an automated fashion. Intensity time traces for ROIs were analyzed using threshold intensity values to identify durations of trapping events, and the extracted residence times were pooled to construct escape time histograms (Supporting Information Figure S1a). Operating in the rapid escape regime, corresponding to average molecular residence times of $\Delta t \approx$20−350 ms, we were able to acquire $\approx 10^4$ escape events within a total imaging time of 10−20 min for each molecular species of interest. Fitting the probability density of Δt values with an exponential function of the form $P(\Delta t) \propto \frac{1}{t_{esc}} \exp \frac{-\Delta t}{t_{esc}}$ yields the value of average escape time, t_{esc}, in any given measurement with an uncertainty of ≈1% (Supporting Information Figure S1a).

Purification and Characterization of DNA and RNA Samples. All nucleic acid fragments were purchased from IBA Lifesciences (Germany) with a single ATTO 532 dye molecule coupled to either one 5′ end or both 5′ termini (Supporting Information Figure S2a). The oligomers were purified with reversed-phase high-performance liquid chromatography using a Reprosil-Pur 200 C18 AQ column (Dr. Maisch, Germany) and elution with a gradient of acetonitrile in an aqueous 0.1 M triethylammonium acetate solution at a flow rate of 5 mL/min. The integrity of DNA and RNA fragments was examined with 20% polyacrylamide native gel electrophoresis (Supporting Information Figure S2c), and the helical structures (A-form for dsRNA and B-form for dsDNA) were confirmed by acquiring circular dichroism (CD) spectra using a CD spectrometer (Chirascan, Applied Photophysics, UK). Nucleic acid samples in CD spectrometry measurements contained 1 mM NaCl and 1−1.3 mM Tris, similar to the electrometry measurements. CD spectra with a data resolution of 0.5 nm per point were recorded three times for each fragment and averaged (Supporting Information Figure S2b).

https://doi.org/10.1021/acs.macromol.2c00657
Macromolecules 2022, 55, 6200−6210

■ ASSOCIATED CONTENT

Supporting Information

The Supporting Information is available free of charge at https://pubs.acs.org/doi/10.1021/acs.macromol.2c00657.

Considerations influencing the choice of NA fragments for the study; Converting measured escape times, t_{esc}, to measured molecular effective charge, q_m; Accounting for experimental inaccuracies; Inferring values of r, b and f_M from measurements of effective charge; Dependence of the inferred r_m vs. a_H relationship on the assumed values of a_H; Comparing the inferred radii of two forms of the double helix; Electrostatic modeling and free energy calculations for B-DNA and A-RNA (PDF)

■ AUTHOR INFORMATION

Corresponding Author

Madhavi Krishnan − *Physical and Theoretical Chemistry Laboratory, Department of Chemistry, University of Oxford, Oxford OX1 3QZ, U.K.;* orcid.org/0000-0003-1274-7155; Email: madhavi.krishnan@chem.ox.ac.uk

Authors

Maria Bespalova − *Physical and Theoretical Chemistry Laboratory, Department of Chemistry, University of Oxford, Oxford OX1 3QZ, U.K.*

Ali Behjatian − *Physical and Theoretical Chemistry Laboratory, Department of Chemistry, University of Oxford, Oxford OX1 3QZ, U.K.*

Narain Karedla − *Physical and Theoretical Chemistry Laboratory, Department of Chemistry, University of Oxford, Oxford OX1 3QZ, U.K.*

Rowan Walker-Gibbons − *Physical and Theoretical Chemistry Laboratory, Department of Chemistry, University of Oxford, Oxford OX1 3QZ, U.K.;* orcid.org/0000-0002-0524-9839

Complete contact information is available at: https://pubs.acs.org/10.1021/acs.macromol.2c00657

Author Contributions

M.B. and N.K. performed experiments and analyzed the data. A.B. and R.W.-G. performed molecular modeling. M.B., A.B., and R.W.-G. participated in manuscript preparation. M.K. designed and supervised the project and wrote the manuscript.

Notes

The authors declare no competing financial interest.

■ ACKNOWLEDGMENTS

This project has received funding from the European Research Council (ERC) under the European Union's Horizon 2020 research and innovation programme (grant agreement no. 724180) and from the Alexander von Humboldt Foundation.

■ REFERENCES

(1) Watson, J. D.; Crick, F. H. C. Molecular structure of nucleic acids; a structure for deoxyribose nucleic acid. *Nature* **1953**, *171*, 737−738.

(2) Wing, R.; Drew, H.; Takano, T.; Broka, C.; Tanaka, S.; Itakura, K.; Dickerson, R. E. Crystal structure analysis of a complete turn of B-DNA. *Nature* **1980**, *287*, 755−758.

(3) Dickerson, R. E.; Drew, H. R.; Conner, B. N.; Wing, R. M.; Fratini, A. V.; Kopka, M. L. The anatomy of A-, B-, and Z-DNA. *Science* **1982**, *216*, 475−485.

(4) Bustamante, C.; Marko, J. F.; Siggia, E. D.; Smith, S. Entropic elasticity of lambda-phage DNA. *Science* **1994**, *265*, 1599−1600.

(5) Tjandra, N.; Tate, S.-i.; Ono, A.; Kainosho, M.; Bax, A. The NMR structure of a DNA dodecamer in an aqueous dilute liquid crystalline phase. *J. Am. Chem. Soc.* **2000**, *122*, 6190−6200.

(6) Woźniak, A. K.; Schröder, G. F.; Grubmüller, H.; Seidel, C. A. M.; Oesterhelt, F. Single-molecule FRET measures bends and kinks in DNA. *Proc. Natl. Acad. Sci. U.S.A.* **2008**, *105*, 18337−18342.

(7) Chen, H.; Meisburger, S. P.; Pabit, S. A.; Sutton, J. L.; Webb, W. W.; Pollack, L. Ionic strength-dependent persistence lengths of single-stranded RNA and DNA. *Proc. Natl. Acad. Sci. U.S.A.* **2012**, *109*, 799−804.

(8) Heenan, P. R.; Perkins, T. T. Imaging DNA Equilibrated onto Mica in Liquid Using Biochemically Relevant Deposition Conditions. *ACS Nano* **2019**, *13*, 4220−4229.

(9) Rybenkov, V. V.; Cozzarelli, N. R.; Vologodskii, A. V. Probability of DNA knotting and the effective diameter of the DNA double helix. *Proc. Natl. Acad. Sci. U.S.A.* **1993**, *90*, 5307−5311.

(10) Rohs, R.; West, S. M.; Sosinsky, A.; Liu, P.; Mann, R. S.; Honig, B. The role of DNA shape in protein-DNA recognition. *Nature* **2009**, *461*, 1248−1253.

(11) Wang, J. C. Helical repeat of DNA in solution. *Proc. Natl. Acad. Sci. U.S.A.* **1979**, *76*, 200−203.

(12) Maffeo, C.; Schöpflin, R.; Brutzer, H.; Stehr, R.; Aksimentiev, A.; Wedemann, G.; Seidel, R. DNA-DNA interactions in tight supercoils are described by a small effective charge density. *Phys. Rev. Lett.* **2010**, *105*, 158101.

(13) Qiu, X.; Kwok, L. W.; Park, H. Y.; Lamb, J. S.; Andresen, K.; Pollack, L. Measuring inter-DNA potentials in solution. *Phys. Rev. Lett.* **2006**, *96*, 138101.

(14) Bai, Y.; Greenfeld, M.; Travers, K. J.; Chu, V. B.; Lipfert, J.; Doniach, S.; Herschlag, D. Quantitative and comprehensive decomposition of the ion atmosphere around nucleic acids. *J. Am. Chem. Soc.* **2007**, *129*, 14981−14988.

(15) Andresen, K.; Das, R.; Park, H. Y.; Smith, H.; Kwok, L. W.; Lamb, J. S.; Kirkland, E. J.; Herschlag, D.; Finkelstein, K. D.; Pollack, L. Spatial distribution of competing ions around DNA in solution. *Phys. Rev. Lett.* **2004**, *93*, 248103.

(16) Brown, M. A.; Abbas, Z.; Kleibert, A.; Green, R. G.; Goel, A.; May, S.; Squires, T. M. Determination of Surface Potential and Electrical Double-Layer Structure at the Aqueous Electrolyte-Nanoparticle Interface. *Phys. Rev. X* **2016**, *6*, 011007.

(17) Ruggeri, F.; Zosel, F.; Mutter, N.; Różycka, M.; Wojtas, M.; Ożyhar, A.; Schuler, B.; Krishnan, M. Single-molecule electrometry. *Nat. Nanotechnol.* **2017**, *12*, 488−495.

(18) Krishnan, M.; Mojarad, N.; Kukura, P.; Sandoghdar, V. Geometry-induced electrostatic trapping of nanometric objects in a fluid. *Nature* **2010**, *467*, 692−695.

(19) Behrens, S. H.; Grier, D. G. The charge of glass and silica surfaces. *J. Chem. Phys.* **2001**, *115*, 6716−6721.

(20) Kramers, H. A. Brownian motion in a field of force and the diffusion model of chemical reactions. *Physica* **1940**, *7*, 284−304.

(21) Ruggeri, F.; Krishnan, M. Lattice diffusion of a single molecule in solution. *Phys. Rev. E* **2017**, *96*, 062406.

(22) Ruggeri, F.; Krishnan, M. Entropic Trapping of a Singly Charged Molecule in Solution. *Nano Lett.* **2018**, *18*, 3773−3779.

(23) Doi, M.; Edwards, S. F. *The Theory of Polymer Dynamics*; Clarendon Press, 1986.

(24) Schlick, T. Molecular Dynamics: Further Topics. *Molecular Modeling and Simulation: an Interdisciplinary Guide*, 2nd ed.; Springer, 2010; Vol. *21*, pp 463−517.

(25) Beard, D. A.; Schlick, T. Inertial stochastic dynamics. II. Influence of inertia on slow kinetic processes of supercoiled DNA. *J. Chem. Phys.* **2000**, *112*, 7323−7338.

(26) Theodoor, J.; Overbeek, G. The role of energy and entropy in the electrical double layer. *Colloids Surf.* **1990**, *51*, 61−75.

(27) Sharp, K. A.; Honig, B. Calculating total electrostatic energies with the nonlinear Poisson-Boltzmann equation. *J. Phys. Chem.* **1990**, *94*, 7684−7692.

(28) Jayaram, B.; Sharp, K. A.; Honig, B. The electrostatic potential of B-DNA. *Biopolymers* **1989**, *28*, 975−993.
(29) Krishnan, M. Electrostatic free energy for a confined nanoscale object in a fluid. *J. Chem. Phys.* **2013**, *138*, 114906.
(30) Krishnan, M. A simple model for electrical charge in globular macromolecules and linear polyelectrolytes in solution. *J. Chem. Phys.* **2017**, *146*, 205101.
(31) Netz, R. R.; Orland, H. Variational charge renormalization in charged systems. *Eur. Phys. J. E: Soft Matter Biol. Phys.* **2003**, *11*, 301−311.
(32) Aubouy, M.; Trizac, E.; Bocquet, L. r. Effective charge versus bare charge: an analytical estimate for colloids in the infinite dilution limit. *J. Phys. A: Math. Gen.* **2003**, *36*, 5835−5840.
(33) Kjellander, R.; Ulander, J. Effective ionic charges, permittivity and screening length: dressed ion theory applied to 1 : 2 electrolyte solutions. *Mol. Phys.* **1998**, *95*, 495−505.
(34) Kjellander, R. A multiple decay-length extension of the Debye-Huckel theory: to achieve high accuracy also for concentrated solutions and explain under-screening in dilute symmetric electrolytes. *Phys. Chem. Chem. Phys.* **2020**, *22*, 23952−23985.
(35) Ramirez, R.; Kjellander, R. Dressed molecule theory for liquids and solutions: An exact charge renormalization formalism for molecules with arbitrary charge distributions. *J. Chem. Phys.* **2003**, *119*, 11380−11395.
(36) Ramirez, R.; Kjellander, R. Effective multipoles and Yukawa electrostatics in dressed molecule theory. *J. Chem. Phys.* **2006**, *125*, 144110.
(37) Manning, G. S. Limiting laws and counterion condensation in polyelectrolyte solutions. I. Colligative properties. *J. Chem. Phys.* **1969**, *51*, 924−933.
(38) Manning, G. S. Electrostatic free energies of spheres, cylinders, and planes in counterion condensation theory with some applications. *Macromolecules* **2007**, *40*, 8071−8081.
(39) Schellman, J. A.; Stigter, D. Electrical double layer, zeta potential, and electrophoretic charge of double-stranded DNA. *Biopolymers* **1977**, *16*, 1415−1434.
(40) Vologodskii, A.; Cozzarelli, N. Modeling of long-range electrostatic interactions in DNA. *Biopolymers* **1995**, *35*, 289−296.
(41) Manning, G. S.; Mohanty, U. Counterion condensation on ionic oligomers. *Physica A* **1997**, *247*, 196−204.
(42) Anderson, C. F.; Record, M. T. Ion Distributions Around DNA and Other Cylindrical Polyions: Theoretical Descriptions and Physical Implications. *Annu. Rev. Biophys. Biophys. Chem.* **1990**, *19*, 423−463.
(43) Lu, X.-J.; Olson, W. K. 3DNA: a versatile, integrated software system for the analysis, rebuilding and visualization of three-dimensional nucleic-acid structures. *Nat. Protoc.* **2008**, *3*, 1213−1227.
(44) Kornyshev, A. A.; Lee, D. J.; Leikin, S.; Wynveen, A. Structure and interactions of biological helices. *Rev. Mod. Phys.* **2007**, *79*, 943−996.
(45) Wynveen, A.; Lee, D. J.; Kornyshev, A. A.; Leikin, S. Helical coherence of DNA in crystals and solution. *Nucleic Acids Res.* **2008**, *36*, 5540−5551.
(46) Kornyshev, A. A.; Lee, D. J.; Wynveen, A.; Leikin, S. Signatures of DNA flexibility, interactions and sequence-related structural variations in classical X-ray diffraction patterns. *Nucleic Acids Res.* **2011**, *39*, 7289−7299.
(47) Dickerson, R. E.; Klug, A. Base sequence and helical structure variation byin B-DNA and A-DNA. *J. Mol. Biol.* **1983**, *166*, 419−441.
(48) Behjatian, A.; Krishnan, M. Electrostatic free energies carry structural information on nucleic acid molecules in solution. *J. Chem. Phys.* **2022**, *156*, 134201.
(49) Verdaguer, N.; Aymamí, J.; Fernández-Forner, D.; Fita, I.; Coll, M.; Huynh-Dinh, T.; Igolen, J.; Subirana, J. A. Molecular structure of a complete turn of A-DNA. *J. Mol. Biol.* **1991**, *221*, 623−635.
(50) Pau, P. C. F.; Berg, J. O.; McMillan, W. G. Application of Stokes' law to ions in aqueous solution. *J. Phys. Chem.* **1990**, *94*, 2671−2679.
(51) Stern, O. The theory of the electrolytic double layer. *Z. Elektrochem. Angew. Phys. Chem.* **1924**, *30*, 508−516.
(52) Pabit, S. A.; Qiu, X.; Lamb, J. S.; Li, L.; Meisburger, S. P.; Pollack, L. Both helix topology and counterion distribution contribute to the more effective charge screening in dsRNA compared with dsDNA. *Nucleic Acids Res.* **2009**, *37*, 3887−3896.
(53) Chen, A. A.; Marucho, M.; Baker, N. A.; Pappu, R. V. Simulations of RNA interactions with monovalent ions. *Methods Enzymol.* **2009**, *469*, 411−432.
(54) Borukhov, I.; Andelman, D.; Orland, H. Steric effects in electrolytes: A modified Poisson-Boltzmann equation. *Phys. Rev. Lett.* **1997**, *79*, 435−438.
(55) Brown, M. A.; Bossa, G. V.; May, S. Emergence of a Stern Layer from the Incorporation of Hydration Interactions into the Gouy-Chapman Model of the Electrical Double Layer. *Langmuir* **2015**, *31*, 11477−11483.
(56) Franks, G. V. Zeta potentials and yield stresses of silica suspensions in concentrated monovalent electrolytes: Isoelectric point shift and additional attraction. *J. Colloid Interface Sci.* **2002**, *249*, 44−51.
(57) Beloqui Redondo, A.; Jordan, I.; Ziazadeh, I.; Kleibert, A.; Giorgi, J. B.; Wörner, H. J.; May, S.; Abbas, Z.; Brown, M. A. Nanoparticle-Induced Charge Redistribution of the Air-Water Interface. *J. Phys. Chem. C* **2015**, *119*, 2661−2668.
(58) Denisov, V. P.; Halle, B. Sequence-specific binding of counterions to B-DNA. *Proc. Natl. Acad. Sci. U.S.A.* **2000**, *97*, 629−633.
(59) Yoo, J.; Aksimentiev, A. Competitive binding of cations to duplex DNA revealed through molecular dynamics simulations. *J. Phys. Chem. B* **2012**, *116*, 12946−12954.
(60) Stellwagen, E.; Dong, Q.; Stellwagen, N. C. Monovalent cations affect the free solution mobility of DNA by perturbing the hydrogen-bonded structure of water. *Biopolymers* **2005**, *78*, 62−68.
(61) Kowalczyk, S. W.; Wells, D. B.; Aksimentiev, A.; Dekker, C. Slowing down DNA translocation through a nanopore in lithium chloride. *Nano Lett.* **2012**, *12*, 1038−1044.
(62) Mills, P.; Anderson, C. F.; Record, M. T. Grand Canonical Monte-Carlo Calculations of Thermodynamic Coefficients for a Primitive Model of DNA Salt-Solutions. *J. Phys. Chem.* **1986**, *90*, 6541−6548.
(63) Olmsted, M. C.; Anderson, C. F.; Record, M. T. Monte Carlo description of oligoelectrolyte properties of DNA oligomers: range of the end effect and the approach of molecular and thermodynamic properties to the polyelectrolyte limits. *Proc. Natl. Acad. Sci. U.S.A.* **1989**, *86*, 7766−7770.
(64) Schlick, T. Monte Carlo Techniques. *Molecular Modeling and Simulation: An Interdisciplinary Guide*, 2nd ed.; Springer, 2010; Vol. *21*, pp 385−423.
(65) Kjellander, R. *Statistical Mechanics of Liquids and Solutions: Intermolecular Forces, Structure and Surface Interactions*; CRC Press, 2020; Vol. *I*.
(66) Gavryushov, S.; Zielenkiewicz, P. Electrostatics of a DNA-like polyelectrolyte: Effects of solvent dielectric saturation and polarization of ion hydration shells. *J. Phys. Chem. B* **1999**, *103*, 5860−5868.
(67) Gavryushov, S. Electrostatics of B-DNA in NaCl and CaCl2 solutions: Ion size, interionic correlation, and solvent dielectric saturation effects. *J. Phys. Chem. B* **2008**, *112*, 8955−8965.
(68) Gavryushov, S. Dielectric saturation of the ion hydration shell and interaction between two double helices of DNA in mono- and multivalent electrolyte solutions: Foundations of the epsilon-modified Poisson-Boltzmann theory. *J. Phys. Chem. B* **2007**, *111*, 5264−5276.
(69) Bret, M. L.; Zimm, B. H. Monte-Carlo determination of the distribution of ions about a cylindrical poly-electrolyte. *Biopolymers* **1984**, *23*, 271−285.
(70) Mills, P.; Anderson, C. F.; Record, M. T. Monte-Carlo studies of counterion DNA interactions - comparison of the radial-distribution of counterions with predictions of other poly-electrolyte theories. *J. Phys. Chem.* **1985**, *89*, 3984−3994.

https://doi.org/10.1021/acs.macromol.2c00657
Macromolecules 2022, 55, 6200−6210

(71) Antypov, D.; Barbosa, M. C.; Holm, C. Incorporation of excluded-volume correlations into Poisson-Boltzmann theory. *Phys. Rev. E* **2005**, *71*, 061106.
(72) Ben-Yaakov, D.; Andelman, D.; Podgornik, R.; Harries, D. Ion-specific hydration effects: Extending the Poisson-Boltzmann theory. *Curr. Opin. Colloid Interface Sci.* **2011**, *16*, 542−550.
(73) Gongadze, E.; van Rienen, U.; Kralj-Iglič, V.; Iglič, A. Spatial variation of permittivity of an electrolyte solution in contact with a charged metal surface: a mini review. *Comput. Methods Biomech. Biomed. Eng.* **2013**, *16*, 463−480.
(74) Peck, L. J.; Wang, J. C. Sequence dependence of the helical repeat of DNA in solution. *Nature* **1981**, *292*, 375−378.
(75) Li, Y.; Struwe, W. B.; Kukura, P. Single molecule mass photometry of nucleic acids. *Nucleic Acids Res.* **2020**, *48*, No. e97.

Recommended by ACS

Far-Field Electrostatic Signatures of Macromolecular 3D Conformation
Gunnar Kloes, Madhavi Krishnan, *et al.*
SEPTEMBER 20, 2022
NANO LETTERS
READ

RNA Captures More Cations than DNA: Insights from Molecular Dynamics Simulations
Sergio Cruz-León and Nadine Schwierz
OCTOBER 19, 2022
THE JOURNAL OF PHYSICAL CHEMISTRY B
READ

High-Force Application by a Nanoscale DNA Force Spectrometer
Michael Darcy, Michael G. Poirier, *et al.*
APRIL 06, 2022
ACS NANO
READ

Potential-Dependent Adhesion Forces between dsDNA and Electroactive Surfaces
Jingru Shao, Tao Ye, *et al.*
SEPTEMBER 23, 2022
LANGMUIR
READ

Get More Suggestions >

https://doi.org/10.1021/acs.macromol.2c00657
Macromolecules 2022, 55, 6200−6210

Supplementary Information for

Opto-electrostatic determination of nucleic acid double helix dimensions and the structure of the molecule-solvent interface

*Maria Bespalova, Ali Behjatian, Narain Karedla, Rowan Walker-Gibbons & Madhavi Krishnan**

Physical and Theoretical Chemistry Laboratory, Department of Chemistry, University of Oxford,

South Parks Road, Oxford OX1 3QZ, United Kingdom

Table of Contents

Supplementary Methods....2
Supplementary Discussion....3
S1. Considerations influencing the choice of NA fragments for the study....3
S2. Converting measured escape times, t_{esc}, to measured molecular effective charge, q_m....3
S3. Accounting for experimental inaccuracies....6
S4. Inferring the values of r, b and f_M from measurements of effective charge....11
S5. Dependence of the inferred r_m vs. a_H relationship on the assumed values of a_H....16
S6. Comparing the radii of two forms of the double helix....18
S7. Electrostatic modeling and free energy calculations for B-DNA and A-RNA....18
List of important variables and parameters....24
Fig. S1. Converting t_{esc} to q_m....25
Fig. S2. Characterization of B-DNA and A-RNA samples....26
Fig. S3. Measuring the hydrodynamic uncertainty, f_H....28
Fig. S4. Principle behind the measurement of b and r....29
Fig. S5. Influence of small perturbations of q_{dye} on r_m and b_m for $\ln f_H = 0.007$....31
Fig. S6. Influence of small perturbations of q_{dye} on r_m and b_m for $\ln f_H = 0.013$....33
Fig. S7. Example measured b-r probability manifolds for B-DNA and A-RNA....35
Fig. S8. The influence of ionic species on the value of f_M....36
Fig. S9. Dependence of the inferred r_m vs. a_H relationship on the assumed values a_H....37
Fig. S10. Electrostatic modeling for B-DNA and A-RNA....38
Table S1. Experimental details on all r and b measurements....40
References....42

Supplementary Methods

Fluorescence correlation spectroscopy (FCS) to determine molecular hydrodynamic radii, r_{H}

An important part of our data analysis involves Brownian Dynamics simulations which in turn require molecular hydrodynamic radii, r_{H}, values as inputs (described briefly in Sections 2 and 2.1 and extensively in previous work)[1, 2]. Molecular hydrodynamic radii were measured using single-focus FCS under solution conditions identical to the ET*e* measurements (1.2 mM NaCl, 1 mM Tris pH 9), with the addition of 0.01% Tween-20. FCS measurements were performed using a MicroTime 200 confocal single-molecule instrument (PicoQuant, Berlin, Germany). A 532 nm continuous-wave laser (LaserBoxx LBX-532-50-COL-PP; Oxxius) provided fluorescence excitation. Fluorescence emission was separated from the excitation light using a triple-band mirror (zt405/530/630rpc; Chroma, Irvine, CA), collected through a 100 μm pinhole, split according to polarization, and directed onto two detectors following filtering through a long-pass filter (532 LP Edge Basic, Chroma).

The fluorescence intensity cross-correlation for the two detectors was fit with an FCS correlation function, $G(\tau)$, that takes into account translational diffusion and triplet blinking in order to determine the diffusion time of a molecular species of interest, τ_{D}, through the confocal volume:

$$G(\tau) = 1 + \frac{1}{N}\left(1 + \frac{\tau}{\tau_{\mathrm{D}}}\right)^{-1}\left(1 + s^2\frac{\tau}{\tau_{\mathrm{D}}}\right)^{-1/2}\left(1 + c_{\mathrm{T}}\exp\left[-\frac{\tau}{\tau_{\mathrm{T}}}\right]\right) \quad \text{(S1)}$$

Here N is the average number of labeled molecules in the confocal volume, $s = 1/6$ denotes the ratio of the lateral to the axial radii of the confocal volume, τ_{T} is the average lifetime of a triplet state, and c_{T} is the fraction of labeled molecules that are in the triplet state in the confocal volume.

In order to estimate the value for τ_{T}, we first performed FCS measurements on the intrinsically disordered activator for thyroid hormone and retinoid receptors ACTR labeled with ATTO 532 dye, as well as on free ATTO 532 dye molecules[3]. The value for r_{H} for ACTR was obtained from the literature and is equal to 2.3 nm[4]. The value for r_{H} for ATTO 532 dye was estimated from an independent Dual-focus Fluorescence Correlation Spectroscopy (2fFCS) measurement, as described in our previous work, and is equal to 0.61 nm[1]. Using the value for τ_{T} = 6 µs, we obtained $\tau_{\mathrm{D,ACTR}}/\tau_{\mathrm{D,ATTO\ 532}} = 3.78$ which agrees well with the expected ratio of radii, $r_{\mathrm{H,ACTR}}/r_{\mathrm{H,ATTO\ 532}} = 3.77$. Setting τ_{T} = 6 µs we fit the measured correlation data to equation (S1) in order to determine a value for τ_{D} for each nucleic acid species. In order to relate these diffusion times through the optical focus to molecular radii we use a value for the hydrodynamic radius of 60 dsDNA, $r_{\mathrm{H,60dsDNA}} = 4.55$ nm, previously measured using two-focus FCS[1]. Specifically, we use the relation $r_{\mathrm{H},i} = \tau_{\mathrm{D},i} \cdot r_{\mathrm{H,60dsDNA}}/\tau_{\mathrm{D,60dsDNA}}$ in order to determine the unknown $r_{\mathrm{H},i}$ value of the test species from the measured $\tau_{\mathrm{D},i}$ value. Further, we performed linear fits of the data for r_{H} vs *n*, the number of basepairs, for B-DNA and A-RNA (Fig. S3a, solid lines). For the Brownian Dynamics (BD) simulations, described in section S2.1, we used the fit values for r_{H} for each molecular species, listed in the table in Fig. S3a.

We also fitted the measured r_{H} vs. n data with an equation describing the diffusion of cylinders in solution: $r_{\mathrm{H}} = l\ /\ 2[\ln(\ l/2r) + \nu]$. Here $l = bn$ denotes the contour length of the molecule, b is the axial rise per basepair, r is the radius of the cylinder which may be regarded as comparable with the radius of nucleic acid double helix, and υ is a correction factor accounting for end effects. The equation above combines the equation for the diffusion coefficient of cylinders of finite length modeled as stacks of rings, $D = k_{\mathrm{B}}T[\ln(\ l/2r) + \nu]/3\pi\mu l$, with the Stokes-Einstein equation, $D = k_{\mathrm{B}}T/6\pi\mu r_{\mathrm{H}}$[5]. Equating the above two expressions effectively maps the diffusive behavior of a cylinder in solution on to the motion of a sphere of radius, r_{H}. Here, D is the nucleic acid molecule's diffusion coefficient, μ is the solvent viscosity and $k_{\mathrm{B}}T$ is the product of the Boltzmann constant, k_{B}, and the temperature, T. Performing the fitting procedure with three fit parameters, namely b, r and

v, we obtained the following values: $b = 4.4\pm8.5$ Å, $r = 9.3\pm18516$ Å, $v = 0.26\pm2001$ for B-DNA, and $b = 2.6\pm1.9$ Å, $r = 10.4\pm4042$ Å, $v = 0.06\pm389$ for A-RNA (Fig. S3a, dashed lines). Interestingly the fit value for b for A-RNA agrees well with the nominal value from crystallography, $b = 2.6$ Å. We then fixed b values for both helical forms to the nominal crystallographic values of 3.4 Å for B-DNA and 2.6 Å for A-RNA and repeated the fitting procedure with two fit parameters, r and v. We obtained the following values: $r = 9.8\pm1255$ Å, $v = -0.004\pm127$ for B-DNA, and $r = 9.7\pm315$ Å, $v = -0.02\pm32$ for A-RNA (Fig. S3a, dotted lines). The nominal mean values for r are close to ≈10 Å, typical for nucleic acid double helices, but the uncertainties are very large due to the weak, logarithmic dependence of the measured D values on r.

Supplementary Discussion

S1. Considerations influencing the choice of nucleic acid fragments for the study

Our experimental study requires precise measurement of effective charge for at least three short nucleic acid fragments under identical experimental conditions. Identical conditions refer to the same measurement device and buffer conditions with effectively identical pH and salt concentration, c, within experimental measurement error.

Based on previous experience, we chose to perform measurements on double stranded nucleic acid fragments characterized by a value of $q_{\mathrm{eff}} \approx -40\,e$, corresponding to a 60 bp dsDNA molecule[1]. Fragments that are very similar in length entail effectively redundant $Q_n(b,r)$ functions (see Section S4). Given the experimental error on measurement values, the similarity in the resulting functions would therefore not be conducive to extracting unique solutions for the unknown quantities of interest (b and r). In addition, for this study we required that all fragments satisfied the rigid rod model of DNA. Odijk-Skolnick-Fixman theory predicts that the overall persistence length, l_{p}, of a semi-flexible polymer increases with decreasing salt concentration[6]. In particular, the electrostatic contribution, $l_{\mathrm{OSF}} = l_{\mathrm{B}}/4L^2\kappa^2$, to the intrinsic persistence length increases in proportion to salt concentration, c, for a monovalent salt solution. Here l_{B} denotes the Bjerrum length and $L = b/2$ represents the linear charge spacing on the polymer, where b is the rise per basepair in this work. Further, κ^{-1} denotes the Debye length which for a monovalent electrolyte is given by $\sqrt{\varepsilon\varepsilon_0 k_{\mathrm{B}}T/2cN_{\mathrm{A}}e^2}$. Here, $\varepsilon\varepsilon_0$ is the static permittivity of the medium, N_{A} is Avogadro's number, and e is the elementary charge. Given that the polymer persistence lengths are 150 bp for dsDNA and about 430 bp for dsRNA in high salt concentration solutions (≈100 mM), our chosen fragment lengths of 30 bp, 40 bp, and 60 bp are expected to lie well within the required rigid rod limit for salt concentrations, c ≈1.2 mM, used in this study, while still providing non redundant $Q_n(b,r)$ relations conducive to the study[7].

The sequences of the dsDNA and dsRNA fragments in our study are shown in Fig. S2a. Sequences were designed such that the individual strands are expected to form no stable hairpin structures by internally complementary base-pairing. We therefore expect stoichiometric mixtures of the strands to form the expected stable double stranded structures upon annealing in solution, with the values for Gibbs free energy of the duplex formation in the range of ≈100-200 $k_{\mathrm{B}}T$ per duplex formed.

S2. Converting measured escape times, t_{esc}, to measured molecular effective charge, q_{m}

In general, the depth of the potential well , W, links t_{esc} with the molecule's effective electrical charge, q_{eff}. Simple physical insight into the relationship between t_{esc} and W is given by Kramers relation[8]:

$$t_{\mathrm{esc}} = t_{\mathrm{r}} \exp\left(\frac{W}{k_{\mathrm{B}}T}\right) \quad \text{(S2)}$$

which holds in the regime of $W > 4\ k_{\mathrm{B}}T$, and shows that the experimental measurable t_{esc} depends exponentially on W. Here, the position relaxation time of the molecule, t_{r} , is treated as a fit parameter and depends on geometric features of the potential well and is also inversely proportional to the molecule's diffusion coefficient, $D = k_{\mathrm{B}}T/6\pi\mu r_{\mathrm{H}}$ in the trap, where r_{H} denotes the hydrodynamic radius of the object and μ is the solvent viscosity.

In order to convert measured escape time, t_{esc}, to q_{eff} we first convert t_{esc} to W. W is next converted to the electrostatic free energy difference ΔF_{el} and we have also $\Delta F_{\mathrm{el}} \propto q_{\mathrm{eff}} \propto q_{\mathrm{m}}$. Here q_{m} represents a measured effective charge which may not be identical to the theoretical quantity q_{eff} due to the presence of measurement uncertainties, discussed in section S3. The process of inferring values of q_{m} from measurements of t_{esc} is described below.

S2.1 Converting measured escape time, t_{esc}, to the total well depth, W

In order to convert the average measured escape time, t_{esc}, to the depth of the potential well W, we performed Brownian Dynamics (BD) simulations of the escape process in a lattice of traps of identical geometry, reflecting the experimental situation as described in our previous work[2]. Simulations were performed for a range of input values for trap depth, W (Fig. S1b).

For various values of well depth, W, we simulated trajectories of single molecule motion through a lattice of traps. We then used these trajectories to generate stacks of optical images including all attributes of the imaging process and system, such as the optical point spread function, exposure time, lag time, average signal and background intensities, background noise, dark noise, shot noise, and laser fluctuations (Fig. S1d and e). These simulated movies corresponding to known input values of W were analysed in a manner identical to the experimental data, using the same intensity thresholds on the signal to extract average simulated escape times, $t_{\mathrm{esc,s}}$. A plot of W vs $t_{\mathrm{esc,s}}$ values was fit with a second degree polynomial and used to convert the experimentally measured t_{esc} value to the total well depth, W (Fig. S1b).

S2.2 Converting the inferred well depth, W, to q_{eff}

In our previous work, we have shown that the total well depth, W, can be written as the difference between the values of the system free energy when the molecule is outside (slit region, denoted by state 1) and inside the trap (pocket region, state 2)[9, 10]. The total free energy includes the electrostatic free energy of interaction, ΔF_{el}, and an entropic term, f, arising from spatial fluctuation of the molecule. In this work we extend the previous description to include a free energy term due to rotational motion, ΔF_{rot}, of the molecule in the system as follows:

$$W = W|_1 - W|_2 = \Delta F_{\mathrm{el}} + f = q_{\mathrm{eff}}\phi_{\mathrm{m}} + \Delta F_{\mathrm{trans}} + \Delta F_{\mathrm{rot}} \quad \text{(S3)}$$

Here ϕ_{m} is the electrical potential at the midplane in the slit region. ϕ_{m} is an accurate estimate of the electrical potential difference, $\Delta\phi$, that gives rise to the trap, since the electrical potential in the "pocket" region is zero by design. A large contribution to W in our experiments arises from the first term, $\Delta F_{\mathrm{el}} = q_{\mathrm{eff}}\phi_{\mathrm{m}}$, which denotes the electrostatic contribution to the total free energy when a charged object moves from the electrostatic energy minimum at the midplane of the slit (state 1) to midplane location along the axis of cylindrical symmetry in the pocket region (state 2). Further, $\Delta F_{\mathrm{trans}}$ and ΔF_{rot} denote contributions to W that arise from two different types of spatial fluctuations. $\Delta F_{\mathrm{trans}}$ denotes the free energy contribution from position fluctuations of the center of mass of the molecule in the depth (z) dimension of the slit, while ΔF_{rot} denotes the free energy contribution from rotational motion of a rod-shaped molecule[10]. In each case $\Delta F_{\mathrm{trans}}$ and ΔF_{rot} denote differences in

the corresponding free energies between states "1" and "2". For the translational mode, the axial fluctuation free energy term may be calculated by first writing the local molecular partition function for each state of the system:

$$Z = \int_0^{z_{\max}} e^{\frac{-q_{\text{eff}}\phi(z)}{k_{\text{B}}T}} dz \tag{S4}$$

Here $\phi(\text{z}) = \phi_{\text{m}}\cosh\left[\kappa\left(z - \frac{z_{\max}}{2}\right)\right]$ is the electrical potential at an axial location, z, in the parallel plate gap and $q_{\text{eff}}\phi(z)$ is the object's local electrical interaction energy. The limits of integration $z = 0$ and $z = z_{\max}$ denote the lower and upper wall of the parallel plate gap respectively, with $z_{\max} = 2h$ or $(2h + d)$ depending on whether the free energy calculated concerns the slit region or in the pocket region respectively. Here d is the depth of the pocket structure. The above equation holds for a point object which we have verified approximates well an object of finite size. This is because Boltzmann weighting to the midplane of the slit ensures that the molecule never approaches the walls close enough for finite size effects to make a substantial difference to the partition function. As shown previously, ΔF_{trans}, is then given by[10]:

$$\Delta F_{\text{trans}} = -k_{\text{B}}T\,\ln Z|_1 + k_{\text{B}}T\,\ln Z|_2 - q_{\text{eff}}\phi_{\text{m}} \tag{S5}$$

Next, in order to model the angular motion of a rod-shaped molecule we write a partition function that describes rotational motion of a line charge of length, l, and charge density $\sigma_l = q_{\text{eff}}/l$ located in the vicinity of the midplane of the slit. The angular potential energy landscape sampled by a rod oriented with its long axis at a polar angle θ to the z-axis of the slit (Fig. 1a) and with its midpoint located at a height, z, far away from the walls, is given by

$$\Delta F_{\text{r}}(z,\theta) = \frac{1}{\cos\theta}\int_{z-\frac{l}{2}\cos\theta}^{z+\frac{l}{2}\cos\theta} \sigma_l\phi(z)\text{d}z \tag{S6}$$

We may also write the above equation in simpler form: $\Delta F_{\text{r}}(z,\theta) = q_{\text{eff}}\langle\phi(z)\rangle$, where $\langle\phi(z)\rangle$ denotes the average electrical potential evaluated over a height in the slit ranging from $z - \frac{l}{2}\cos\theta$ to $z + \frac{l}{2}\cos\theta$. For example, for $\theta = 90°$, and $z = z_{\max}/2$, Eq. (S6) reduces to $\Delta F_{\text{r}}(z,\theta) = q_{\text{eff}}\phi_{\text{m}}$, which is the electrostatic interaction energy of a rod of charge q_{eff} lying along the mid-plane of the slit. Since the problem is azimuthally symmetric around the z-axis of the slit, the angular partition function for a rod centered on and confined to the midplane of the parallel-plate gap at $z = z_{\max}/2$ is given by

$$\Omega = 4\pi\int_0^{\pi/2} \exp\left[-\Delta F_{\text{r}}(z_{\max}/2\,,\theta)/k_{\text{B}}T\right]\sin\theta\,\text{d}\theta \tag{S7}$$

Similar to equation (S5) above, we write

$$\Delta F_{\text{rot}} = -k_{\text{B}}T\,\ln\Omega|_1 + k_{\text{B}}T\,\ln\Omega|_2 - q_{\text{eff}}\phi_{\text{m}} \tag{S8}$$

Note that equation (S8) represents the rotational free energy difference for a rod in states confined to the midplane regions of the slit and pocket. We have verified that equation (S8) is in fact an accurate estimate of the total rotational component of the free energy arising from the full translational-rotational motion of a rod that exhibits both degrees of freedom simultaneously. Once again, this is

because probabilities of occupancy are Boltzmann weighted to the midplane of the slit causing the rotational contribution to the free energy to be dominated by dynamics at the midplane.

In general in these measurements we find that for a nominal well depth of $W = 5\ k_{\mathrm{B}}T$ the translation contribution to the free energy, $\Delta F_{\mathrm{trans}} \approx 2.3\ k_{\mathrm{B}}T$, while the rotational free energy, $\Delta F_{\mathrm{rot}} \approx 0.05\text{-}0.2\ k_{\mathrm{B}}T$, leaving $\Delta F_{\mathrm{el}} = q_{\mathrm{eff}}\phi_{\mathrm{m}} \approx 2.5\ k_{\mathrm{B}}T$ which is the experimental quantity of interest (Fig. S1c). We further point out that while ΔF_{el} depends linearly on q_{eff} and ϕ_{m}, $\Delta F_{\mathrm{trans}}$ and ΔF_{rot} depend weakly (logarithmically) on q_{eff} and ϕ_{s}, and are therefore relatively insensitive to both quantities[10]. Knowing the geometry of the slit and given a nominal value of the surface potential of the wall, ϕ_s, we are able to calculate a relationship between W and q_{eff}. Once W is known from the experimental measurement we obtain a value for the measured effective charge, q_{m}, by reading it off a W vs q_{eff} plot shown in Fig. S1c. This value of q_{m} for each fragment is used in subsequent analyses.

We point out that in this work the rotational term, ΔF_{rot}, was not uniformly applied in the data analysis. The need for the small rotational contribution to the free energy was only apparent in a few datasets that involved comparatively lower magnitudes of surface electrical potential ($\phi_s \approx -2\ k_{\mathrm{B}}T/e$), with these datasets yielding no measurement outcomes for b and r otherwise (Table S1). In all remaining datasets (a dataset consists of q_{eff} measurements on three nucleic acid fragments), inclusion of the rotational free energy contribution led to no measurement outcome for b and r. The origin of this variation is currently not clear, but we emphasize that measurement outcomes were obtained in a mutually exclusive fashion, i.e., the ΔF_{rot} term had to either be included or excluded in the data analysis in each case. Measurement outcomes for b and r were never obtained in both scenarios, which precluded a situation where a given dataset yielded two potentially disparate sets of results.

We further noted that the measurement of the rise per basepair, *b,* and radius, *r,* was very sensitive to minor perturbations (1-2 %) in q_{eff} on any single fragment. The overall observation in the data analysis was that datasets frequently returned no intersection plot, as shown in Fig. S4b, which resulted in no measurement outcomes for b and r. Overall about 30% of the datasets, which were considered free of perturbations attributable to external sources, yielded results for b and r, all of which are tabulated in Table S1. This implies a 70% probability of achieving a single measurement of q_{eff} with ≈99% accuracy, which is reasonably good.

S3. Accounting for experimental inaccuracies

As follows from the equation (S3), in an ideal experiment, without any measurement uncertainties, the electrical free energy of a molecule carrying charge q_{t} may be written as: $\Delta F_{\mathrm{el}} = \phi_{\mathrm{m}} \cdot q_{\mathrm{t}} = W - \Delta F_{\mathrm{trans}} - \Delta F_{\mathrm{rot}}$. As demonstrated in previous work, the main contribution to the measurement inaccuracy in F_{el} arises from the uncertainty on the midplane potential, ϕ_{m}[1]. The midplane potential, in turn, depends on the surface potential of the wall, ϕ, and the measured slit height, $2h$, where h includes small measurement uncertainties, $h_{\mathrm{e}} \approx$1-2 nm, from AFM measurements, and is well approximated by

$$\phi_{\mathrm{m}} = 2\phi_{\mathrm{s}}\exp(-\kappa h) \tag{S9}$$

For the surface potential, we used a nominal working value of $\phi_{\mathrm{s}} = -2.8\ k_{\mathrm{B}}T/e$, estimated in previous measurements on a range of biomolecules in 1 mM NaCl, 1 mM Tris[9]. However, the true value of ϕ_{m} in any given experiment is subject to small variations on slit height (≈1 nm) and measurement error on salt concentration (<0.5%). Furthermore, a small variation in ϕ may also arise from ion-specific effects on ϕ_{s}[11]. To account for the uncertainties on both parameters, we introduced a new variable – the multiplicative correction factor, f_{M}. This factor corrects the nominal midplane potential, obtained using $\phi_{\mathrm{s}} = -2.8\ k_{\mathrm{B}}T/e$ and measured slit height, $2h$, as given by equation (S9) to the true value of midplane potential, $\phi_{\mathrm{m,t}}$:

$$\phi_{\mathrm{m,t}} = \phi_{\mathrm{m}} \cdot f_{\mathrm{M}} \tag{S10}$$

Note that f_{M} can also capture systematic departures of ϕ_{s} from the nominal value arising from ion specific effects.

The second source of error is encountered in extracting the well depth of the trap, W, using two experimental measurables: the molecule's escape time, t_{esc}, and its position relaxation time, t_{r}, as given by equation (S2). As described above, t_{r} is inversely proportional to the molecule's diffusion coefficient, D. The dominant contribution to the uncertainty in the diffusion coefficient originates from measurement uncertainties in FCS and any contribution to the altered hydrodynamic drag on the molecules arising from confinement in a parallel plate system. To correct for these uncertainties, we have introduced the hydrodynamic correction factor, f_{H}, which relates the measured hydrodynamic radius, $r_{\mathrm{H,}}$ to its true value, $r_{\mathrm{H,t}}$ as follows:

$$r_{\mathrm{H}} = r_{\mathrm{H,t}} \cdot f_{\mathrm{H}} \tag{S11}$$

Therefore, the interpreted or measured well depth, W, can differ from the true well depth, W_{t}, as given by

$$W_{\mathrm{t}} = W + k_{\mathrm{B}}T \ln f_{\mathrm{H}} \tag{S12}$$

The above relationship (S11) has been verified using Brownian Dynamics simulations. Using the equations (S3), (S10) and (S12), we obtained the following expression for the measured effective electrical charge, q_{m}, in a real experiment with measurement uncertainties:

$$q_{\mathrm{m}} = \frac{W - \Delta F_{\mathrm{trans}} - \Delta F_{\mathrm{rot}}}{\phi_{\mathrm{m}}} = f_{\mathrm{M}} \left(q_{\mathrm{t}} - k_{\mathrm{B}}T \frac{\ln f_{\mathrm{H}}}{\phi_{\mathrm{m,t}}} \right) \tag{S13}$$

Note that here we implicitly use the relation $q_{\mathrm{t}} = (W_{\mathrm{t}} - \Delta F_{\mathrm{trans}} - \Delta F_{\mathrm{rot}})/\phi_{\mathrm{m,t}}$, where q_{t} is a quantity that is free of all known experimental inaccuracies (f_{M} and f_{H}). Furthermore, the nucleic acid molecules in our experiments are labeled with two ATTO 532 dyes, each carrying a net structural charge, $q_{\mathrm{str}} = -1e$. So the measured charge of a molecular species in an ideal experiment is expected to be

$$q_{\mathrm{t}} = q_{\mathrm{eff}} + 2q_{\mathrm{dye}}. \tag{S14}$$

Here, q_{eff} denotes the effective electrical charge of the nucleic acid double helix, and q_{dye} is the effective charge of a single dye attached to each 5' terminus of the molecule. Equation (S13) can thus be rewritten as:

$$q_{\mathrm{m}} = f_{\mathrm{M}} \left(q_{\mathrm{eff}} + 2q_{\mathrm{dye}} - k_{\mathrm{B}}T \frac{\ln f_{\mathrm{H}}}{\phi_{\mathrm{m,t}}} \right) \tag{S15}$$

Hydrodynamic uncertainties, as captured by a single factor f_{H}, and the effective charge of the dye, q_{dye}, thus both enter the molecule's measured effective charge, q_{m}, in an additive fashion. For convenience, they can be combined into a single additive correction factor, $f_{\mathrm{A}} = 2q_{\mathrm{dye}} - k_{\mathrm{B}}T \frac{\ln f_{\mathrm{H}}}{\phi_{\mathrm{m,t}}}$, so that we may write

$$q_{\mathrm{m}} = f_{\mathrm{M}}(q_{\mathrm{eff}} + f_{\mathrm{A}}) \tag{S16}$$

Importantly, both quantities in the additive correction factor – q_{dye} and f_{H} – can be estimated in independent measurements as described further in sections S3.1 and S3.2.

Once the value of f_{A} is known we obtain corrected values of the measured effective charge, q_{m}, for all nucleic acid fragment lengths. We then compared these values with the corresponding calculated effective charges, q_{eff}, in order to extract values for the three unknowns of interest: b, r and f_{M}, as described in section S4.

S3.1 Measuring the hydrodynamic uncertainty, f_{H}

Using equation (S10), equation (S13) can be rewritten as:

$$q_{\mathrm{m}} = f_{\mathrm{M}} \cdot q_{\mathrm{t}} - k_{\mathrm{B}}T\frac{\ln f_{\mathrm{H}}}{\phi_{\mathrm{m}}} \tag{S17}$$

For two measurements of q_{m} of the same nucleic acid species, measured in two slightly different salt concentrations, we may write the difference in measured charges as follows:

$$q_{\mathrm{m},1} - q_{\mathrm{m},2} = q_{\mathrm{t}}\left(f_{\mathrm{M},1} - f_{\mathrm{M},2}\right) + k_{\mathrm{B}}T\ln f_{\mathrm{H}}\left(\frac{1}{\phi_{\mathrm{m},2}} - \frac{1}{\phi_{\mathrm{m},1}}\right) \tag{S18}$$

Indices 1 and 2 in the subscripts denote the values for the respective parameters in the two measurements performed.

The first term on the RHS of equation (S18) can be simplified using the equations (S9) and (S10):

$$f_{\mathrm{M}} = \frac{\phi_{\mathrm{m,t}}}{\phi_{\mathrm{m}}} = \frac{2\phi_{\mathrm{s,t}}\exp[-\kappa(h + h_{\mathrm{e}})]}{2\phi_{\mathrm{s}}\exp(-\kappa h)} = \frac{\phi_{\mathrm{s,t}}}{\phi_{\mathrm{s}}}\exp(-\kappa h_{\mathrm{e}})$$

$$\frac{f_{\mathrm{M},2}}{f_{\mathrm{M},1}} = \frac{\exp(-\kappa_2 h_{\mathrm{e}})}{\exp(-\kappa_1 h_{\mathrm{e}})} = \exp[h_{\mathrm{e}}(\kappa_1 - \kappa_2)]$$

For example, for measurements performed in salt concentrations of 1.20 mM and 1.30 mM, ${\kappa_1}^{-1} =$ 8.8 nm and ${\kappa_2}^{-1} =$8.4 nm, respectively. We further have
$|h_{\mathrm{e}}(\kappa_1 - \kappa_2)| = 1\ \mathrm{nm} \cdot |\ 0.114\ \mathrm{nm^{-1}} - 0.119\ \mathrm{nm^{-1}}\ | = 0.005 \ll 1$. Thus, we can use the following Taylor's series approximation:

$$\frac{f_{\mathrm{M},2}}{f_{\mathrm{M},1}} = \exp[h_{\mathrm{e}}(\kappa_1 - \kappa_2)] \approx 1 + h_{\mathrm{e}}(\kappa_1 - \kappa_2)$$

which gives $f_{\mathrm{M},2} \approx f_{\mathrm{M},1}[1 + h_{\mathrm{e}}(\kappa_1 - \kappa_2)]$

The first term on the RHS of equation (S18) is therefore

$$q_{\mathrm{t}}\left(f_{\mathrm{M},1} - f_{\mathrm{M},2}\right) = -q_{\mathrm{t}}f_{\mathrm{M},1}h_{\mathrm{e}}(\kappa_1 - \kappa_2)$$

We further can simplify the second term on the RHS of equation (S18):

$$k_{\mathrm{B}}T\ln f_{\mathrm{H}}\left(\frac{1}{\phi_{\mathrm{m},2}}-\frac{1}{\phi_{\mathrm{m},1}}\right)=k_{\mathrm{B}}T\ln f_{\mathrm{H}}\left(\frac{1-\phi_{\mathrm{m},2}/\phi_{\mathrm{m},1}}{\phi_{\mathrm{m},2}}\right)$$

where $\frac{\phi_{\mathrm{m},2}}{\phi_{\mathrm{m},1}}=\frac{2\phi_{\mathrm{s}}\exp(-\kappa_2 h)}{2\phi_{\mathrm{s}}\exp(-\kappa_1 h)}=\exp\left[h(\kappa_1-\kappa_2)\right]$

Here we have
$|h(\kappa_1-\kappa_2)|=36\mathrm{nm}\cdot|\,0.114\ \mathrm{nm}^{-1}-0.119\ \mathrm{nm}^{-1}\,|=0.18<1$. Thus, we use a few additional terms in the Taylor's series approximation

$$\frac{\phi_{\mathrm{m},2}}{\phi_{\mathrm{m},1}}=\exp[h(\kappa_1-\kappa_2)]\approx 1+h(\kappa_1-\kappa_2)+\frac{h^2(\kappa_1-\kappa_2)^2}{2}+\frac{h^3(\kappa_1-\kappa_2)^3}{6}$$

We can now rewrite the second term on the RHS of equation (S18) as follows:

$$k_{\mathrm{B}}T\ln f_{\mathrm{H}}\left(\frac{1}{\phi_{\mathrm{m},2}}-\frac{1}{\phi_{\mathrm{m},1}}\right)=-\frac{k_{\mathrm{B}}T\ln f_{\mathrm{H}}}{\phi_{\mathrm{m},2}}\left[h(\kappa_1-\kappa_2)+\frac{h^2(\kappa_1-\kappa_2)^2}{2}+\frac{h^3(\kappa_1-\kappa_2)^3}{6}\right]$$

Finally, equation (S18) can be rewritten as follows:

$$\frac{q_{\mathrm{m},1}-q_{\mathrm{m},2}}{\kappa_2-\kappa_1}=q_{\mathrm{t}}\cdot f_{\mathrm{M},1}\cdot h_{\mathrm{e}}+\frac{k_{\mathrm{B}}T\ln f_{\mathrm{H}}}{\phi_{\mathrm{m},2}}\left[h+\frac{h^2(\kappa_1-\kappa_2)}{2}+\frac{h^3(\kappa_1-\kappa_2)^2}{6}\right] \qquad \text{(S19)}$$

We emphasize that in an ideal experiment, without any slit height and hydrodynamic uncertainties, i.e., $h_{\mathrm{e}}=0$ and $f_{\mathrm{H}}=1$ respectively, Δq would be expected to be zero, as evident above. But in fact measurements show that the value of $q_{\mathrm{m},1}-q_{\mathrm{m},2}$ is in general around -0.5 e when $\kappa_2-\kappa_1$ is around -0.007, suggesting the presence of inaccuracies in slit height and/or hydrodynamic quantities.

Equation (S19) has two unknown parameters, $f_{\mathrm{M},1}\cdot h_{\mathrm{e}}$ and $\ln f_{\mathrm{H}}$. The quantity on the LHS, $\left(q_{\mathrm{m},1}-q_{\mathrm{m},2}\right)/(\kappa_2-\kappa_1)$, is known from measurement. Furthermore on the RHS, values for h and $\phi_{\mathrm{m},2}$ are set equal to nominal values taken from AFM measurements and equation (S9), respectively. As the true effective charge of the labeled molecule, $q_{\mathrm{t}}=q_{\mathrm{eff}}+2\,q_{\mathrm{dye}}$, also remains unknown at this point, we assume as an estimate, the calculated value of effective charge, q_{eff}, which corresponds to crystallographic structural parameters for the helical radius, r, and rise per basepair, b, describing the form of the double helix used in the particular experiment. We further assume $q_{\mathrm{dye}}\cong -0.5\,e$ (which is known from calculation). Because $\left|(q_{\mathrm{t}}\cdot f_{\mathrm{M},1}\cdot h_{\mathrm{e}})\left[(\kappa_2-\kappa_1)/\left(q_{\mathrm{m},1}-q_{\mathrm{m},2}\right)\right]\right|\approx 0.4$, the precise value of q_{t} used could be expected to impact the estimate of f_{H}, but in fact a reasonable estimate for q_{t} within 10% of the true value would suffice. For example, a 5% alteration in the assumed value of q_{t} (which implies very different helical parameters compared to the nominal helical geometry assumed) alters the value of $\ln f_{\mathrm{H}}$ by about 3% which is negligible for our purposes. In practice, in solving two equations of the form (S19), any systematic uncertainty factor multiplying q_{t} would be absorbed into the value of the first unknown ($f_{\mathrm{M},1}\cdot h_{\mathrm{e}}$), leaving the unknown quantity of interest, $\ln f_{\mathrm{H}}$, unaffected.

In order to determine f_{H} from equation (S19), we performed replicates of escape-time measurements on two nucleic acid fragment lengths, each measured in two different salt concentrations. This gives a system of two equations with two unknowns. For example, for 30 bp and 60 bp nucleic acid fragments, we obtained the following system of two equations:

$$\left.\frac{q_{\mathrm{m},1}-q_{\mathrm{m},2}}{\kappa_2-\kappa_1}\right|_{30} = q_{\mathrm{t},30}\cdot f_{\mathrm{M},1}\cdot h_{\mathrm{e}} + \frac{k_{\mathrm{B}}T\ln f_{\mathrm{H}}}{\phi_{\mathrm{m},2}}\left[h+\frac{h^2(\kappa_1-\kappa_2)}{2}+\frac{h^3(\kappa_1-\kappa_2)^2}{6}\right] \quad \text{(S19a)}$$

$$\left.\frac{q_{\mathrm{m},1}-q_{\mathrm{m},2}}{\kappa_3-\kappa_1}\right|_{60} = q_{\mathrm{t},60}\cdot f_{\mathrm{M},1}\cdot h_{\mathrm{e}} + \frac{k_{\mathrm{B}}T\ln f_{\mathrm{H}}}{\phi_{\mathrm{m},2}}\left[h+\frac{h^2(\kappa_1-\kappa_2)}{2}+\frac{h^3(\kappa_1-\kappa_2)^2}{6}\right] \quad \text{(S19b)}$$

Note that measurements for both molecular species were performed keeping at least one salt concentration the same for both species so that $f_{\mathrm{M},1}$ was identical. Due to the presence of measurement errors, we solved the equations (S19a) and (S19b) graphically as shown in Fig. S3b. For every measurement, we defined the solution space of possible $f_{\mathrm{M},1}\cdot h_{\mathrm{e}}$ and $\ln f_{\mathrm{H}}$ values, which satisfied the measured values for $(q_{\mathrm{m},1}-q_{\mathrm{m},2})/(\kappa_2-\kappa_1)$ for the first nucleic acid fragment and $(q_{\mathrm{m},1}-q_{\mathrm{m},2})/(\kappa_3-\kappa_1)$ for the second nucleic acid fragment within bounds specified by the measurement errors. We then found weighted mean values for both unknowns. We performed three sets of such an analysis which revealed average values of $\ln f_{\mathrm{H}}$ =0.007±0.025 or f_{H} =1.007±0.025 (Fig. S3b).

S3.2 Measuring the effective charge of a single dye molecule, q_{dye}

In order to determine the effective charge of a single dye molecule coupled to the end of the double helix, we performed in addition, measurements on dsDNA and dsRNA fragments labeled with a single ATTO 532 dye molecule coupled to a single 5' terminus. An isolated ATTO 532 dye molecule in solution carries a net structural charge, $q_{str}=-1e$ (Fig. S2a), which has been verified in prior measurements on single ATTO 532 molecules in solution[10]. The local electrostatic environment of the dye which arises as a result of coupling of the dye molecule into the electrostatic near field of the "parent" DNA molecule can however alter the effective charge of the dye. Therefore, despite the knowledge of the free solution effective charge of a single dye molecule, its effective charge in the molecular context, involving coupling to the end of a DNA fragment, is *a priori* not clear. We denote the effective charge of a dye molecule coupled to the terminal phosphate of a DNA fragment as q_{dye} which can not only be calculated but can also be directly determined via measurement.

In order to measure the value of q_{dye} we compared pairs of measurements of q_{m} for identical 60 bp dsDNA and dsRNA fragments carrying either one or two ATTO 532 dyes on their 5' ends. The difference between a pair of such measurements for a given molecular species permits us to directly estimate the effective charge contribution of a single ATTO532 dye molecule to the overall measurement. The measured difference is given by:

$$\Delta q = q_{\mathrm{m}} - q'_{\mathrm{m}} = f_{\mathrm{M}} q_{\mathrm{dye}} \quad \text{(S20)}$$

Here q'_{m} denotes the measured effective charge of a 60bp dsDNA or dsRNA labeled with a single dye only, while q_{m} is the measured effective charge of the same fragment labelled with two dyes.

In our experiments, a double labeled fragment n basepairs in length with fluorophores on both 5' ends carries a structural charge, $q_{\mathrm{str}}=-2ne$ (Fig. S2a). But in a singly labeled fragment one 5'-phosphate is unmodified. This terminal phosphate monoester group has two ionizable sites as opposed to a single ionizable site encountered, e.g., in the phosphodiester backbone as well as at a dye-derivatized 5' end phosphate (Fig. S2a). Nominally this would suggest that the structural charge of a dsDNA or dsRNA fragment labeled with a single fluorophore on one 5' end is $q_{\mathrm{NA}}=-(2n+1)\,e$. However, it is important to note that the two ionizable phosphate monoester sites have widely different nominal pK_{a} values of ≈2 and 7. The local electrical potential in the vicinity of the ionized phosphates is around 7-8 $k_{\mathrm{B}}T$ under our experimental conditions (≈1 mM alkali chloride, pH=9). This implies a local pH in the vicinity of the phosphate groups of around 5-6, which suggests that we can safely assume that the ionizable site in the phosphate monoester group will carry a magnitude of

structural charge less than 0.1 e (Fig. S2a). Charge renormalization will reduce the contribution of this weakly ionized group to the measured overall effective charge of the molecule to the level of around or less than 0.02 e. The latter is comparable with the standard error in the measurement of the effective charge of the dye, $\mathrm{SE}_{\mathrm{dye}}$, and we therefore neglect explicit consideration of this contribution to our working estimate value of q_{dye}. Furthermore, any possible contributions of charge uncertainties at this level to the overall measurement of molecular geometric parameters are considered in the context of the analysis presented in Fig. S5 and Fig. S6 where we examine the impact on the final results of small perturbations of the value of q_{dye} around the measured value.

Having established values for f_{H} and $f_{\mathrm{M}}q_{\mathrm{dye}}$ we proceed as described below in order to determine q_{dye}. Rearranging equation (S15) we have:

$$f_{\mathrm{M}}q_{\mathrm{eff,n}} = q_{\mathrm{m,n}} - 2f_{\mathrm{M}}q_{\mathrm{dye}} + k_{\mathrm{B}}T\frac{\ln f_{\mathrm{H}}}{\phi_{\mathrm{m}}} \tag{S21}$$

where all the quantities on the right hand side, namely, the measured effective charge of the nucleic acid molecule n basepairs in length, $q_{\mathrm{m,n}}$, the measured effective dye charge, $f_{\mathrm{M}}q_{\mathrm{dye}}$, and the final term involving the hydrodynamic correction factor, are now known.

We use the values for $f_{\mathrm{M}}q_{\mathrm{eff,n}}$ inferred from equation (S21) for fragments of different lengths, n =30, 40 and 60, in the analysis procedure invoking the calculated effective charge values $q_{\mathrm{eff},n}(b,r)$ in order to extract values for three unknowns: b, r, and f_{M}. This procedure is discussed in detail in section S4. At this point, we note that the value of f_{M} obtained from the overall analysis yields a measurement for q_{dye}, since $f_{\mathrm{M}}q_{\mathrm{dye}}$ is known from the charge difference measurement described previously.

We performed three independent measurements on singly and doubly labeled B-DNA fragments and three measurements on A-RNA. We obtained the following average value for the measurements with B-DNA: $q_{\mathrm{dye,DNA}} = -0.46\pm0.07\ e$ where the standard error on the measurement, $\mathrm{SE}_{\mathrm{dye,DNA}} = 0.04\ e$. Measurements for A-RNA reveal an average value of $q_{\mathrm{dye,RNA}} = -0.44\pm0.09\ e$, where $\mathrm{SE}_{\mathrm{dye,RNA}} = 0.05\ e$.

We point out that our measured values for q_{dye} are in good agreement with calculated values of ca. $-0.48\ e$ and $-0.43\ e$ for $q_{\mathrm{dye,DNA}}$ and $q_{\mathrm{dye.RNA}}$ respectively, assuming the charge on the dye molecule can be modeled as a sphere of radius 5 Å, and that the distance of the sphere from the 5' end of the DNA molecule is 1 nm, which is given by the effective length of the linker (Fig. S2a).

S4. Inferring the values of radius, r, rise per base pair, b, and multiplicative correction factor, f_{M}, from measurements of effective charge

In this section, we describe the procedure used to extract the molecular properties of interest from our measured values of effective charge, $f_{\mathrm{M}}q_{\mathrm{eff,n}}$.

S4.1 Relationship between the measured effective charge of the double helix, q_{m}, and rise per basepair, b and radius, r

We model an *n* basepair nucleic acid double helix of radius, r, and axial rise per basepair, b, as a cylinder of radius $r_{\mathrm{cyl}} = r$ and length *nb*, carrying a total charge of $-2ne$. Using our previously described PB framework for calculating electrostatic free energies, F_{el}, and corresponding molecular effective charges, q_{eff}, we obtain a set of q_{eff} values for charged cylinders for a range of values corresponding to 2-5 Å for b and 2-30 Å for r, with a calculated uncertainty of around 0.1%[9]. We then fit the calculated $q_{\mathrm{eff},n}(b,r)$ values with a power-law function of the form $Q_n(b,r) = a_1 + a_2(b^{\alpha}+a_3)(r^{\beta}+a_4)$ such that the maximum deviation between the fit and the calculated data was

≈0.05% (Fig. S4a). Fig. S4a lists the values of all parameters in the three fit equations for $n = 30$, 40 and 60 determined for salt concentrations ranging from 1 to 1.5 mM. Comparison of partial derivatives $(Q_n)'_b$ and $(Q_n)'_r$ reveals a much stronger dependence of $q_{\mathrm{eff,n}}$ on b than that on r:

$$(Q_n)'_b = a_2 \cdot \alpha\left(r^\beta + a_4\right) b^{\alpha-1} \quad \text{(S22a)}$$

$$(Q_n)'_r = a_2 \cdot \beta(b^\alpha + a_3) r^{\beta-1} \quad \text{(S22b)}$$

Although $r^{\beta-1}$ can be slightly larger (≈10-15%) than $b^{\alpha-1}$ for implausibly small r values ≈2-3 Å and b ≈5 Å, the $\alpha\left(r^\beta + a_4\right)$ and $\beta(b^\alpha + a_3)$ factors play a decisive role here. For any parameter set from Fig. S4a, $\alpha\left(r^\beta + a_4\right)$ is ≈3-4 times larger than $\beta(b^\alpha + a_3)$ for any r and b within the ranges considered. Thus, we find that the axial rise per basepair, b, has a stronger influence on the measured effective charge of the molecule, compared to the radius of the cylinder, whose influence is more modest. This effect is borne out clearly in the measurements where we achieve far higher precision (≈0.1 Å) in the readout of the average b value, compared to the precision on the radius, r, which is on the order of 1 Å.

We now rewrite equation (S21) to relate the measured quantity from experiment to the molecular geometrical quantities of interest, embodied in the $q_{\mathrm{eff},n}(b,r) = Q_n(b,r)$ relations:

$$q_{\mathrm{m,n}} - 2f_{\mathrm{M}} q_{\mathrm{dye}} + k_{\mathrm{B}}T \frac{\ln f_{\mathrm{H}}}{\phi_{\mathrm{m}}} = f_{\mathrm{M}} Q_n(b,r) \quad \text{(S23)}$$

The above equation has three unknown parameters: f_{M}, r and b, all on the right side of the equation. Parameters r and b describe the structure of the molecule while f_{M} describes the experimental apparatus. In order to determine these three unknowns, we require at least three measurements of $q_{\mathrm{m,n}}$ on fragments of different lengths that are described by identical values of r and b. In practice, this requires four measurements in total: three $q_{\mathrm{m,n}}$ measurements for three different fragments and occasionally (25% of all measurement sets) an additional measurement of a singly labeled fragment in order to determine $f_{\mathrm{M}} q_{\mathrm{dye}}$ as described in the previous section. To keep f_{M} constant, all the measurements needed to be performed under identical conditions. In particular, we used the same measurement device and buffer conditions with effectively identical pH and salt concentration, c. We also point out that our measurements of $q_{\mathrm{m,n}}$ include statistical uncertainties $q_{\mathrm{e,n}}$ arising primarily from the uncertainties on measured t_{esc} values.

Note that we do not explicitly consider uncertainties on the measured quantities $f_{\mathrm{M}} q_{\mathrm{dye}}$ and f_{H} at this stage. Since these two quantities appear in an additive fashion in the final $q_{\mathrm{m},n}$ value of interest, we consider their uncertainties in a consolidated fashion. In particular, we explore the impact of small perturbations on the overall additive quantity, $f_{\mathrm{A}} = 2q_{\mathrm{dye}} - k_{\mathrm{B}}T \cdot \ln f_{\mathrm{H}}/\phi_{\mathrm{m,t}}$, on the final results for r and b. Fig. S5 and Fig. S6 illustrate the results of this study. We find that perturbations $\leq \pm 2\mathrm{SE}_{\mathrm{dye}}$ on the value of q_{dye} preserve the qualitative measured trends for the radius, r, in most of the cases (Fig. S5a and Fig. S6a). The results for the rise per basepair, b, on the other hand, remain robust to such perturbation (Fig. S5b and Fig. S6b).

For convenience, we introduce variable names q_{30}, q_{40} and q_{60} in place of $q_{\mathrm{m,n}} - 2f_{\mathrm{M}} q_{\mathrm{dye}} + k_{\mathrm{B}}T \cdot \ln f_{\mathrm{H}}/\phi_{\mathrm{m,t}}$ for n=30, 40 and 60 respectively. In order to simplify the problem and eliminate f_{M}, which is a common multiplicative factor in all the measurements in a given experiment, we perform pairwise division of three equations denoted by equation (S23). Thus, we obtain two equations with two unknowns, r and b:

$$\frac{q_{30}}{q_{60}} \pm 3\sqrt{q_{e,30}^2 + q_{e,60}^2} = \frac{Q_{30}\,(b,r)}{Q_{60}\,(b,r)} \quad \text{(S24a)}$$

$$\frac{q_{40}}{q_{60}} \pm 3\sqrt{q_{e,40}^2 + q_{e,60}^2} = \frac{Q_{40}\,(b,r)}{Q_{60}\,(b,r)} \quad \text{(S24b)}$$

Once r and b are known, using the simulation based approach described in the following section S4.2, we determine f_{M} by substitution in one of the original equations.

The value of f_{M} obtained for data sets that include singly labeled nucleic acid fragments enables us to estimate values for q_{dye} as described in section S3.2. Knowing the values for $q_{\mathrm{dye,DNA}}$ and $q_{\mathrm{dye,RNA}}$ permits us to simplify all further measurements and analysis by rearranging equation (S23) as follows:

$$q_{\mathrm{m,n}} + k_{\mathrm{B}}T\frac{\ln f_{\mathrm{H}}}{\phi_{\mathrm{m}}} = f_{\mathrm{M}}[Q_n(b,r) + 2q_{\mathrm{dye}}] \quad \text{(S25)}$$

We now have:

$$\frac{q_{30}{}^*}{q_{60}{}^*} \pm 3\sqrt{q_{e,30}^2 + q_{e,60}^2} = \frac{Q_{30}\,(b,r)^*}{Q_{60}\,(b,r)^*} \quad \text{(S26a)}$$

$$\frac{q_{40}{}^*}{q_{60}{}^*} \pm 3\sqrt{q_{e,40}^2 + q_{e,60}^2} = \frac{Q_{40}\,(b,r)^*}{Q_{60}\,(b,r)^*} \quad \text{(S26b)}$$

where $q_{30}{}^*$, $q_{40}{}^*$ and $q_{60}{}^*$ denote $q_{\mathrm{m,n}} + k_{\mathrm{B}}T \cdot \ln f_{\mathrm{H}}/\phi_{\mathrm{m,t}}$ where n=30, 40 and 60 respectively. Furthermore, $Q_{30}\,(b,r)^*$, $Q_{40}\,(b,r)^*$ and $Q_{60}\,(b,r)^*$ represent $Q_n(b,r) + 2q_{\mathrm{dye}}$ for n =30, 40, 60. We solve the system of two equations (S26a) and (S26b) using the same algorithm as for equations (S24a) and (S24b) as described in the next section S4.2.

S4.2 Algorithm for determining rise per base pair, b and radius, r of the double helix

In this section we describe the procedure we use to extract the values of the unknowns of interest using equations (24a) and (24b) (or equations (26a) and (26b)). The algorithm was developed and validated using simulated values of measured molecular effective charge, $q_{\mathrm{s,n}}$, where the subscript 's' emphasizes the fact that these values are calculated or simulated for the purpose of developing the algorithm, and not measured in experiment. In order to do so, we begin with $q_{\mathrm{s,n}}$ values calculated for any set of input parameters, $r = r_{\mathrm{in}}$, $b = b_{\mathrm{in}}$, $f_{\mathrm{M}} = f_{\mathrm{M,in}}$, as given by the equations $q_{\mathrm{s,n}} = f_{\mathrm{M}}Q_n(b,r)$, where $Q_n(b,r) = a_1 + a_2(b^{\alpha} + a_3)\left(r^{\beta} + a_4\right)$ for each fragment. We then superimpose an amount of charge corresponding to ±0.2% relative error on the value for each fragment, so that an input value of the form $q_{\mathrm{s,n}} \pm 0.006q_{\mathrm{s,n}}$ represents a measured mean value, $q_{\mathrm{s,n}}$, with Gaussian distributed uncertainty characterized by a standard deviation of $0.002q_{\mathrm{s,n}}$. Such values are analogous to experimental measurements of the form $q_{\mathrm{m,n}} \pm 3q_{\mathrm{m,e}}$, where $q_{\mathrm{m,e}}$ is about 0.2% of $q_{\mathrm{m,n}}$. We applied these simulated input values to our analysis routine and sought to establish an algorithm that returned the known inputs for b, r and f_{M}.

Initially, we determined all possible combinations of b and r values that satisfied each of the two equations separately, as follows. Each effective charge ratio, i.e., $q_{\mathrm{s,30}}/q_{\mathrm{s,60}}$ and $q_{\mathrm{s,40}}/\,q_{\mathrm{s,60}}$, excluding errors can be thought of a 2D surface parallel to both r and b axes. But in practice, these mean values are broadened by errors, such that the standard deviations on each of the input ratios can be written as $q_{e,1} = \sqrt{\left(0.002q_{s,30}\right)^2 + \left(0.002q_{s,40}\right)^2}$ and $q_{e,2} = \sqrt{\left(0.002q_{s,40}\right)^2 + \left(0.002q_{s,60}\right)^2}$ respectively. Including uncertainties corresponding to three standard deviations yields a probability weighted input written as $q_{\mathrm{s,30}}/q_{\mathrm{s,60}} \pm 3q_{e,1}$ and $q_{\mathrm{s,40}}/q_{\mathrm{s,60}} \pm 3q_{e,2}$. Intersection of the ranges of the two simulated input values with the calculated quantities given by $Q_{30}\,(b,r)/Q_{60}\,(b,r)$ and

$Q_{40}\ (b,r)/Q_{60}\ (b,r)$ (right hand sides of equations S24a and S24b) gives two independent manifolds of solutions in b-r space as illustrated in Fig. S4b. The analyses were performed using calculated surfaces plotted using a grid resolution of 0.01 Å in b and r.

The intersection of the above two manifolds yields a final probability weighted space of solutions in b and r which are common to the system of three input simulated measurement values. Each member of the final "b-r manifold" solution space (Fig. S4b lower panel) is associated with a probability tag that reflects the product of individual probabilities of the "overlapping" values. Because the uncertainties in the measurement resulted in relatively broad b-r manifolds, we found that an unrestricted direct weighted average determination of inferred output values for the rise per basepair and helical radius (b_{out} and r_{out} respectively) did not accurately and consistently recover the known inputs b_{in} and r_{in}.

We therefore developed and validated the following procedure to recover the known inputs, b_{in} and r_{in}. We first focus on estimating the rise per basepair, b. Using the final b-r manifold for a given input pair ($b_{\mathrm{in}}, r_{\mathrm{in}}$), we calculated a weighted average of b (which we term b_{out}) over a range in r corresponding to r =6 to 30 Å. This procedure was carried out for various sets of b_{in} and r_{in} ranging from 2-4 Å for b, and 8-18 Å for r, with a step size of 0.1 Å for b and 0.4 Å for r. We rounded the obtained b_{out} values to the nearest 0.1 Å. We found that this procedure consistently yielded b_{out} values that accurately reflected the specific b_{in} input value, departing from the inputs by 0.2 Å at the most (Fig. S4c.I). Fig. S4c illustrates the overall accuracy of the method for different sets of tested b_{in} and r_{in} parameters. For nominal values of b=3.4 Å for DNA and 2.6 Å for RNA, the accuracy of the procedure, as assessed by the ratio $b_{\mathrm{out}}/b_{\mathrm{in}}$, is 1.0 if the corresponding r_{in} values are within the ranges of 10.5-17.0 Å and 11.3-16.5 Å respectively. Outside these optimal ranges, we note that b_{out} can exceed b_{in} by 0.1-0.2 Å when r_{in} lies below the optimal range. On the other hand, we find that b_{out} is smaller than b_{in} by about 0.1 Å when the corresponding r_{in} value lies above the optimal range (Fig. S4c.I).

The goal of the next analysis step is to establish a procedure to infer the helical radius, r. Here we use the b-r manifolds obtained for various input pairs ($b_{\mathrm{in}}, r_{\mathrm{in}}$), and construct a probability distribution in r, restricting the value of b to b_{in}. We then determined the value of r_{out} by fitting a Gaussian function to the region of the first peak in the probability distribution of r values, similar to that shown in Fig. S4b (bottom panel). This value was consistently found to lie within 1 Å of r_{in} over a wide range of r_{in}, e.g., 6-20 Å. This implies that as long as we can accurately determine b_{out}, such that $b_{\mathrm{out}}/b_{\mathrm{in}} = 1.0$, we can determine r_{out} with <1 Å accuracy. In practice, when dealing with experimental data we do not have access to b_{in}, but rather only to b_{out}, obtained by the approach described above.

The analysis clearly indicates that the accuracy in the determination of r depends on the accuracy in the determination of b. Fig. S4c.II demonstrates that when $b_{\mathrm{out}}/b_{\mathrm{in}}$ =1.0 the obtained r_{out} values lie within ±10% of the input r_{in}. However when b_{out} is either under- or overestimated by ≈4% (≥0.1 Å) we find that r_{out} is correspondingly under- or overestimated by ≈40% compared to the known input value (Fig. S4c.II). For instance, for small r_{in} values <10 Å the method entails an overestimation of b_{out} by at least 0.1 Å which in turn implies overestimated values for $r_{\mathrm{out}} \approx 1.4\, r_{\mathrm{in}}$. Thus, our simulation procedure is not capable of accurately recovering r_{out} values for r_{in} <10 Å. We comment on the implications of this observation for our results, particularly in the context of A-RNA, at the end of Section 4.3. Furthermore, when the simulation-vetting procedure on occasion yields a value of r_{out} <10 Å, we find that b_{out} has been underestimated, i.e., $b_{\mathrm{out}} = b_{\mathrm{in}} - 0.1$ Å. In these cases, we also find that correcting the b_{out} value upwards by 0.1 Å yields an r_{out} value that is within 1 Å of r_{in}.

Once r_{out} and b_{out} have been determined using the above procedure, the multiplicative correction factor, $f_{\mathrm{M,out}}$, is then determined by substituting the obtained values for b_{out} and r_{out} in

any of the three equations $q_{\mathrm{s,n}} = f_{\mathrm{M}} Q_n(b, r)$. Performing the above data analysis procedure using measured inputs q_n or q_n^* in equations (S24a) and (S24b) or (S26a) and (S26b) respectively, we obtain all our measurables b_{m}, r_{m} and f_{M}. Note that equations (S24a) and (S24b) are used for datasets where q_{dye} is also a measurable, and equations (S26a) and (S26b) are used in cases where q_{dye} is known from a previous measurements.

We found that the results for r_{m} and the trends of r_{m} vs a_{H} depended sensitively on the exact value of the additive correction factor, $f_{\mathrm{A}} = 2q_{\mathrm{dye}} - k_{\mathrm{B}}T \ln f_{\mathrm{H}}/\phi_{\mathrm{m,t}}$. Since the uncertainty on q_{dye} can be estimated more accurately than that on $\ln f_{\mathrm{H}}$, we first focus on the impact of the measurement uncertainty on q_{dye} given by $\mathrm{SE}_{\mathrm{dye}}$. We therefore varied the value of q_{dye} in the range of $q_{\mathrm{dye,m}} \pm 2\mathrm{SE}_{\mathrm{dye}}$ in increments of $\mathrm{SE}_{\mathrm{dye}}$. We repeated the *b-r* analysis described above with these perturbed values of q_{dye} and determined the corresponding r_{m} and b_{m} values for each dataset using our simulation-vetted procedure described above. The results are shown in Fig. S5. Clearly measurements of the rise per basepair, b_{m}, are relatively insensitive to value of q_{dye} (Fig. S5b). The measured values for r_{m} in turn are more sensitive to the particular choice of q_{dye} (Fig. S5a). We found that while most cases display a direct dependence of r_{m} on a_{H}, the results corresponding to $q_{\mathrm{dye}} = q_{\mathrm{dye,m}} + \mathrm{SE}_{\mathrm{dye}}$ show the clearest trends for both A-RNA and B-DNA. It is therefore likely that $q_{\mathrm{dye}} = q_{\mathrm{dye,m}} + \mathrm{SE}_{\mathrm{dye}}$ approximates closest the true value of q_{dye}, and we focus on the results corresponding to $q_{\mathrm{dye}} = q_{\mathrm{dye,m}} + \mathrm{SE}_{\mathrm{dye}}$ for all analyses and discussions in the study.

In addition, we further examined the impact of an altered value of $\ln f_{\mathrm{H}}$ on the measured b_{m} and r_{m} results keeping the value of q_{dye} constant (Fig. S6). For example, in place on the value $\ln f_{\mathrm{H}}$=0.007 used in the analysis in Fig. S5 we used a value nearly a factor 2 larger corresponding to $\ln f_{\mathrm{H}}$=0.013. Again we found that the values obtained for b_{m} remained effectively unchanged. We also observed a robust linear dependence of r_{m} on a_{H}, with a small difference however in the $r_{0,\mathrm{A}}$ and $r_{0,\mathrm{B}}$ intercept values in each case with respect to the previous results. The intercept values in this analysis turned out to be overall about 1 Å smaller than in the previous analysis procedure. The values however lie within each other's estimated bands of uncertainty (compare tables in Fig. S5 and Fig. S6).

All the measured r_{m} and b_{m} values obtained with the method described in this section for A-RNA and B-DNA fragments in CsCl, RbCl, NaCl and LiCl salt solutions are listed in Table S1 along with the corresponding experimental details for all measurements. Fig. S7 presents the results for representative datasets in each salt species for both B-DNA and A-RNA fragments.

S4.3 Simulation based studies of the role of the multiplicative correction factor, f_{M}, in the measurement of b and r

Assuming particular values of $f_{\mathrm{M,in}}$, b_{in} and r_{in} as known inputs we obtain simulated effective charge values for all three fragments $q_n = f_{\mathrm{M,in}} Q_n(b_{\mathrm{in}}, r_{\mathrm{in}})$. We ran the data analysis procedure described in the sections above using these values in equations (S24a) and (S24b) for a range of values b_{in}(2-4 Å), r_{in}(8-18 Å) and f_{M} chosen as a random positive value. As indicated above, the vetting of the analysis procedure in this fashion revealed that there is an optimal range for r_{in} over which the analysis delivers output values $f_{\mathrm{M,out}}$, b_{out} and r_{out} within 4%, <1% and 10% of the inputs respectively. For example, for nominal values of b_{in}=3.4 Å and 2.6 Å (typical for B-DNA and A-RNA) the optimal range in r_{in} that yields <10% error in determining r_{out} (i.e., $|(r_{\mathrm{out}} - r_{\mathrm{in}})/r_{\mathrm{in}}| < 0.1$) lies between r_{in} =10.5-17.0 Å and 11.3-16.5 Å respectively. In this range, we obtain high accuracy in the determination of b_{out} where we find that $b_{\mathrm{out}}/b_{\mathrm{in}}$ =1 (Fig. S4c.I), and the accuracy in the determination of f_{M} is better than 4% ($|(f_{\mathrm{M,out}} - f_{\mathrm{M,in}})/f_{\mathrm{M,in}}| < 0.04$) (Fig.S4c.III). For r_{in} less than 10.4 Å we note that 1.1< $\frac{r_{\mathrm{out}}}{r_{\mathrm{in}}}$ <1.8 (Fig. S4c.II). However, it is worth noting that even when the accuracy of the analysis in r is poor, as reflected in the ratio $r_{\mathrm{out}}/r_{\mathrm{in}}$ ≈1.8, we obtain

$f_{\mathrm{M,out}}/f_{\mathrm{M,in}} \approx 0.8$ and $b_{\mathrm{out}}/b_{\mathrm{in}} \approx 1.08$ (Fig. S4c). The accuracy in determining b stems from the higher sensitivity of q_{eff} to b compared to r as discussed earlier.

We point out that the value for f_{M} serves as an important diagnostic purpose in our ability to distinguish between model-IA and model-IIA of A-RNA. In principle, for a true value of r=5 Å our data analysis procedure would naturally provide an overestimate of $r_{\mathrm{m}} \approx$15 Å, which is larger by a factor three than the true value. However, the analysis procedure also shows that this overestimate of r is coupled with a large underestimate of f_{M} of the order of 30% relative to any input value of $f_{\mathrm{M,in}}$. In practice, $q_{\mathrm{m,n}}$ measurements performed for B-DNA and A-RNA fragments under effectively identical conditions, using the same measurement device, pH and salt concentration, c, reveal very close f_{M} values for both helical forms. E.g., for RbCl measurements, $f_{\mathrm{M,DNA}}$ =0.902, corresponding to r_{m} =12.4 Å and b_{m} =3.2 Å, is very close to $f_{\mathrm{M,RNA}}$ =0.919, where r_{m} =13.3 Å and b_{m} =2.6 Å. Assuming that the true radius of B-DNA is not much smaller than 10 Å and that the B-DNA measurement therefore reflects an accurate result, such close agreement in the f_{M} values implies that the obtained r_{m} values for A-RNA lie in the range where we expect about 10% uncertainty in the inferred r values, as is typical of the method (Fig. S4c.II and Fig. S4c.III). Were the true value rather r=5 Å, this would be immediately reflected in the value of $f_{\mathrm{M,RNA}}$ which, according to our analysis vetting procedure, would be at least 30% smaller than $f_{\mathrm{M,DNA}}$. Clearly this is not the case, permitting us to infer comparable accuracy for r measurements for both A-RNA and B-DNA.

S4.4 The influence of ionic species on f_{M}

In practice, although we can determine f_{M} reasonably accurately for every single measurement, unrestricted comparison of f_{M} across all measurements is not very meaningful as the major determinant of f_{M} stems from experimental variations such slit height uncertainty, h_{e}. But measurements performed under identical conditions given by salt concentration and slit height (same measurement device) may be directly compared to test for relative departures of f_{M}. We expect such a comparison to carry information on any variation in surface electrical potential that may arise solely on account of a single known variable factor in the experiments in question, say the cationic species in solution.

In order to compare the effect of different counterion species on f_{M}, we performed f_{M} measurements for the same nucleic acid species in different alkali metal chloride solutions, keeping all other experimental conditions identical, including salt concentration. Comparing f_{M} values, averaged over all measurements performed under identical conditions, we indeed noted slightly different f_{M} values as a function of cationic species. We found that the values for f_{M} increased in the order Cs≈Rb<Na<Li. We also found that our values for the quantity $f_{\mathrm{M}}\phi_{\mathrm{s}} = \phi_{\mathrm{s,t}}$, the true effective surface potential in our experiments, are in good agreement with zeta (ζ) potentials reported for silica surfaces in alkali metal chloride solutions, as shown in Fig. S8[12]. Our $\phi_{\mathrm{s,t}}$ values are of course higher in magnitude than the corresponding ζ potential values in each case, but this is to be expected since: (1) the ζ potential reflects the value of the electrical potential at the shear surface near a particle, which can be distinct and further away than its geometric surface, and (2) samples of silica may vary greatly in their surface electrical properties depending on preparation and treatment procedures[13].

S5. Dependence of the inferred r_{m} vs. a_{H} relationship on the assumed values of the hydrated cationic radii, a_{H}

Fig. 4 demonstrates that r_{m} values for both DNA and RNA vary linearly with hydrated radii of the cationic species, a_{H}, in solution. We assumed values for a_{H} taken from Ref. 18. These values were determined from limiting ionic conductance values using both slip and stick hydrodynamic conditions at the surfaces of spheres of radii, a_{H}, that represent a migrating ionic entity which is

assumed to be spherical in solution. The Stokes drag (friction coefficient) on an ion in solution is given by $\gamma_s \pi \mu a_H$, where $\gamma_s = 6$ for the stick boundary condition and $\gamma_s = 4$ for the slip case. For stick boundary conditions the reported Stokes radii were smaller than the crystal ionic radii for Rb^+ and Cs^+ (e.g., r_{Cs} =1.65 Å and $a_{H,Cs}$ =1.19 Å; r_{Rb} =1.49 Å and $a_{H,Rb}$ =1.18 Å). In contrast, for slip boundary conditions the reported a_H values for Rb^+ and Cs^+ are comparable to the crystal ionic radii ($a_{H,Cs} = 1.79$ Å and $a_{H,Rb} = 1.78$ Å), and are therefore considered more plausible than the former case. Fig. S9a illustrates the r_m vs. a_H dependence for hydrated ionic radii obtained using slip boundary conditions from Ref. 18, as shown in Fig. 4a. Linear extrapolation of the measured r_m values to $a_H = 0$ yields $r_{0,A}$ =10.5±0.6 Å and $r_{0,B}$ =11.8±0.6 Å for A-RNA and B-DNA respectively (Fig. S9a), as presented in the main text.

As an independent verification of the a_H values in Ref. 18, we analyzed our electrical conductivity measurements as a function of salt concentration (Fig. S2d), which were used to monitor the salt concentration in each measurement. We fitted the data with the equation $c = A + B\gamma$, where A and B are fit coefficients and γ (in $\mu S/cm$) is the measured conductivity of a solution with salt concentration, c (in mM). In order to determine the values for hydrated cationic radii we used the fitted values for slopes, $B = 4\pi\mu R_i / 10^4 e_0^2 N_A$, since

$$c = \frac{4\pi\mu R_i}{e_0^2 N_A}(\gamma - \gamma_{sol}), \text{ with } \frac{1}{R_i} = \frac{1}{a_{Cl^-}} + \frac{1}{a_H} \quad (S27)$$

Here, a_H is the hydrated radius of the cationic species, a_{Cl^-} is the hydrated radius of Cl^-, γ_{sol} denotes the conductivity of pure solvent, and γ (in $\frac{S}{m}$) is the measured conductivity of the solution with salt concentration, c (in mM). The value for a_{Cl^-}=1.81 Å was taken from McMillan's study[14]. Fig. S2d lists our measured values for hydrated cationic radii, a_m, which lie between 8-12% of the values in Ref. 18.

Furthermore, we explored the dependence of r_m on a_H values from two other literature sources. Nightingale used a calibration curve to convert Stokes radii from conductance measurements to hydrated radii of ions in solution[15]. This was done by taking Stokes radii measurements using stick boundary conditions (γ_s=6) for four cations in the series from tetraethyl- to tetrapentylammonium. These values were related to the corresponding values of hydrated radii that were in turn simply taken to be their crystal radii. These large cations were considered to be non-hydrated, so that their crystal radii were assumed to reflect their true hydrated radii in aqueous solutions. The calibration curves thus obtained was extrapolated to the regime of small Stokes radii and the a_H values for smaller ions, e.g., alkali metal ions with Stokes radii <2.82 Å (Stokes radius for tetraethylammonium cation) were read off from this curve. Nightingale's a_H values vary from 3.29 to 3.82 Å for cations in the order $Rb^+ \rightarrow Li^+$, while the values in Ref. 18 lie in the range 1.78-3.58 Å. Fig. S9b displays the r_m vs. a_H dependence for Nightingale's a_H values and the corresponding linear fit functions with a shared value of slope for both helical forms. Extrapolation of the fit to $a_H = 0$ leads to very small values for both $r_{0,B}$ and $r_{0,A}$ (2.8 and 4.1 Å respectively). Furthermore, the slope of the fit function is significantly larger than 1.

We performed a similar analysis using a_H values obtained by Marcus[16]. Values for a_H in this study were calculated using a model which links the ionic radius, the width of the hydration shell and the number of molecules in this shell with the values for standard molar Gibbs free energies of hydration. Marcus' values for hydrated ionic radii are smaller than Nightingale's and again lie within a fairly narrow range: 2.13-2.42 Å. Linear fits of the r_m vs a_H data once again lead to very small values for $r_{0,B}$ and $r_{0,A}$ (1.2 and 2.5 Å) and the slope of the r_m vs. a_H fit line is around 5 (Fig. S9c).

S6. Comparing the radii of two forms of the double helix: analysis of model structures of B-DNA and A-RNA

The 3DNA web server 2.0 was used to generate generic fiber model structures (derived from a database of published experimental crystallographic data) of B-DNA and A-RNA of the desired sequence (Fig. S2a)[17]. The B-DNA and A-RNA models we use have a helical rise per basepair of 3.4 and 2.6 Å respectively. These atomic structures were used to generate molecular surface structures which were then imported into the mesh generation package GMSH. Finite element numerical calculations were then performed as described in the following section.

The 'main backbone' atoms in the molecular visualization software packages used for the structural analysis are the C3' and C4' atoms for DNA and RNA respectively[18, 19]. The ribbon structures trace out these atomic positions (Fig. S10a). The average distance of these main backbone atoms was calculated to be around 7.9 Å for B-DNA and 9.5 Å for A-RNA. Considering all backbone carbon atoms, namely, C3', C4', C5', the corresponding values are 7.9±0.3 Å for B-DNA and 9.3±0.7 Å for A-RNA. Taking all possible backbone atoms (P, O1P, O2P, O3', O5', C3', C4', C5'), however, we find that the mean atomic distances from the principal axes of the structures are 8.7±0.9 Å for B-DNA and 8.9±0.9 Å for A-RNA. All the above cases provide estimates of a helical radius where the value for A-RNA is systematically larger than for B-DNA. However, considering only the spatial distributions of the P atoms, we obtain values for the average distance from the helical axis that are more similar for the two structures; we note a value of 9.23±0.01 Å for B-DNA that is in fact slightly larger than the average distance of 8.6±0.6 Å obtained for A-RNA. Next we consider the axial radius of gyration which in turn provides a measure of the average displacement of all atoms from the principal axis. The radius of gyration of A-RNA is approximately 7.8 Å and is around 1 Å larger than the value of 6.7 Å characterizing B-DNA. Overall we find that the backbone carbon atoms and the axial radius of gyration point to values that indicate that the helical radius of A-RNA is about 1 Å larger than B-DNA. Furthermore, we point out that the axial radii of gyration of the molecular surfaces generated by a probe of radius of 1 Å, using default van der Waals (vdW) atomic radii ($w = 0$), are 6.5 Å and 7.8 Å for B-DNA and A-RNA, respectively (model-IB and model-IA of Fig. 2). These values are in fact very similar to the all-atom axial radii of gyration values above. Clearly, an enlargement of all atomic radii of all atoms ($w > 0$) would lead to a further increase in these values. E.g., Figure 2A further displays two additional molecular surfaces for B-DNA (w=1.4) and A-RNA (w=3 Å). The radii of gyration of these surfaces are 7.7 Å and 9.6 Å, respectively.

S7. Electrostatic modeling and free energy calculations for B-DNA and A-RNA

S7.1.1 Governing Equations

We first solved the non-linear Poisson-Boltzmann (PB) equation in the experimental geometry for two states of the molecule in the system: the "slit" state (#1) and the "pocket" state (#2) as shown in Fig. 1a and Fig. S10c. The PB equation is given by

$$-\nabla \cdot (\varepsilon\varepsilon_0 \nabla\phi) = \rho_{\mathrm{e}} \tag{S28}$$

where ϕ is the local electrical potential in the system, ρ_e is the charge density, and $\varepsilon\varepsilon_0$ is the permittivity of the medium. The charge density, ρ_{e}, in the aqueous solution is described by the Boltzmann distribution for ionic species:

$$\rho_{\mathrm{e}} = \sum_i c_i N_{\mathrm{A}} e z_i \exp\left(\frac{-z_i e\phi}{k_{\mathrm{B}}T}\right) \tag{S29}$$

where N_A is Avogadro's number, and c_i and z_i are the bulk concentration and the valences of the ith ionic species, respectively. Here $z_+ = -z_- = 1$ holds for a binary, symmetric and monovalent electrolyte.

Fig. 1a schematically represents a nucleic acid molecule in a nanofluidic device consisting of a nanoslit and a pocket region which serves as an electrostatic trap. Thermodynamically, the direction of the trapping process is determined by the difference in the free energy of the system between two different configurations, namely a "slit-state" (Fig. S10c, panel 1) and "pocket-state" (Fig. S10c, panel 2). Neglecting the orientational and spatial degrees of the freedom of the molecule, the problem can be simplified to the calculation of the free energy for two molecular configurations at the locations of minimum axial free energy showed in Fig. S10c. The free energy functional for our problem for any fixed state of the molecule is given by[20, 21]:

$$F_{\mathrm{el}} = \int_{\mathrm{V}} \left[\frac{\varepsilon\varepsilon_0}{2} \boldsymbol{E} \cdot \boldsymbol{E} - 2cN_{\mathrm{A}}k_{\mathrm{B}}T(\cosh\psi - \psi\sinh\psi - 1) \right] dV \tag{S30}$$

where $\boldsymbol{E} = -\nabla\phi$ is the electric field, and $\psi = e\phi/k_{\mathrm{B}}T$ is the nondimensional electrical potential.

In this study, we use the finite element (FE) approach to solve equation (S28) for DNA and RNA structures. We consider macroscopic molecular representations based on solvent excluded and solvent accessible surfaces (SES and SAS) deduced from atomic structures. Subsequently, we calculate free energy differences between the two states of the molecule. Note, that in these calculations the molecule is placed at the midplane of the parallel plate gap in the slit and pocket regions (i.e., $z = z_{\max}/2$), with its long axis parallel to the midplane of the slit (i.e., $\theta = 90°$). We then deduce the effective charge of the molecule from the relationship $\Delta F_{\mathrm{el}} = q_{\mathrm{eff}}\phi_{\mathrm{m}}$. Here $\Delta F_{\mathrm{el}} = F_1 - F_2$ is the difference in electrostatic free energy between the two states of the system, as calculated using equation (S30), and ϕ_{m} is the electrical potential at the midplane of the slit region in the absence of the molecule[21].

We then compare the effective charge values obtained for the molecular models with those of charged cylinders in order to deduce the equivalent radius, r_{cyl}, of a cylindrical object which leads to the same value of effective charge, q_{eff}, as described in sections S7.3 and S7.4. Further discussion on equivalent cylinders is provided in section S7.5.

S7.1.2 Boundary Conditions for the solution of the PB equation

We solve equation (S28) using Neumann boundary conditions that specify constant charge densities at the surfaces of the cylinder or charged atoms in the molecular structure. Note that constant charge on DNA is an excellent approximation given the highly acidic nature of the phosphate groups ($pK_a \approx 2$) under the conditions of our experiment (pH≈9). The effect of charge regulation of the silica walls due to the proximity of the charged molecule has a negligible impact on the calculated electrostatic free energy (F_{el}) which turns out to be essentially identical to the value obtained for constant charge boundary conditions. We therefore treat the silica walls with constant charge boundary conditions in both states involving the molecule in either the slit or the pocket region. For the silica surfaces of the device we have $-\varepsilon\varepsilon_0\nabla\phi \cdot \mathbf{n} = \sigma_{\mathrm{w}}$ at the boundary, where $\sigma_{\mathrm{w}} = -0.1\ e/\mathrm{nm}^2$ (giving $\psi_{\mathrm{m}} \approx -0.1$, similar to experiments) is a nominal surface charge density, and $\mathbf{n}$ is the normal vector pointing into the electrolyte.

While the application of this boundary condition is straightforward for cylinders and for the solid surfaces of the device, the process of defining a molecular surface is more challenging owing to the complicated, corrugated nature of a molecular surface constructed from atoms. Traditionally, there are 3 methods to define a molecular surface: (i) van der Waals (vdW) surface, (ii) Solvent Accessible Surface (SAS), and (iii) Solvent Excluded Surface (SES)[22]. The vdW surface of the molecular structure is simply the surface of the volume obtained by the union of all atoms in the molecule which are treated as spheres of radii given by each atom's respective vdW radius. The SAS in turn is a

continuous surface generated by the center of a spherical probe of radius r_p rolled over the vdW surface. It can be readily demonstrated that the SAS is equivalent to a vdW surface where the vdW radii of all atoms are increased uniformly by an amount equal to r_p. The SES, however, is defined by tracking the contact points of the rolling probe as shown in Fig. S10f. Accordingly, the SES can be regarded as a smooth manifold which approximates the true vdW surface as $r_p \to 0$. One of the advantages of the SES is that it produces a smooth geometry which is favorable for mesh generation and finite-element analysis. For the above reasons, we use a SES created by a probe size of $r_p = 1$ Å in order to generate the effective vdW surface of the molecular structures (Fig. 2). In our work we regard the vdWS and SES as synonymous. In order to create the SAS, we simply generate a SES of a molecular structure where the default vdW radii values of all atoms are increased by a constant value, w.

MSMS[23] is a molecular surface rendering software package which generates a SES by rolling a spherical probe of radius r_p over the surfaces of spheres representing atoms in the molecular structure. The radii of these spheres are taken to be equal to the corresponding vdW radius of each atom. MSMS is embedded as a third-party package into UCSF Chimera[24] which is a molecular visualization software. We point out that Chimera has different algorithms to determine the vdW radii of atoms based on whether the structure contains explicit H-atoms or not. In our case, since the atomic structures generated by 3DNA[25] do not contain explicit hydrogen atoms, "united atom radii" based on protein organic set (ProtOr) are used[26]. For more detail, we refer the reader to the Chimera User's Guide: https://www.cgl.ucsf.edu/chimera/docs/UsersGuide/midas/vdwrad.html.

In the present study, we consider 30 bp DNA and RNA molecules carrying a total structural charge of $q_{str} = -60e$. Since the structural charge of the molecule is localized at the negatively charged O atoms in the backbone phosphate groups, we distribute the total charge over the spheres corresponding to the O1P and O2P atoms using the following procedure. We identify all surface patches in the molecular surface that are made up of points lying at a minimum distance from the nearest "O1P" and "O2P". This essentially distinguishes the surfaces of the charge carrying O backbone atoms from all other atoms in the structure. We then apply a Neumann boundary condition of the form $-\varepsilon\varepsilon_0 \nabla\phi \cdot \mathbf{n} = \sigma_p$ to the "O1P-O2P" patches, where $\sigma_p = q_{str}/A_p$ is a charge density, and A_p represents the total surface area of all patches. We utilized GMSH[27] for the subsequent mesh generation and solved the governing equations using FEniCS[28] which is an open-source FE software package.

S7.3 Domain decomposition of the electrostatic free energy, and relating the double helix to an equivalent cylinder model

We solved equation (S28), and calculated the difference in free energy, ΔF_{el}, discussed above (Fig. S10c) for molecular helices and charged cylinders. These free energies were used to obtain values for $q_{eff} = \Delta F_{el}/\phi_m$ and $\eta = q_{eff}/q_{str}$ which represent the effective charge and charge renormalization factor, respectively[9]. We are interested in mapping the molecular electrostatic problem onto a simpler case given by a cylindrical object of radius, r_{cyl}, and length, l. For a rise per base pair, b, the length of the corresponding cylinder is given by $l = nb$, where n represents the number of basepairs. In our model, the total structural charge is uniformly distributed over the curved surface of the cylinder; i.e. $\sigma_p = q_{str}/2\pi r_{cyl} l$. According to our definition, r_{cyl} is the radius of an equivalent cylinder whose effective charge is equal to that of the double helical molecular structure.

Fig. 2a presents calculations of the electrostatic potential distribution for B-DNA and A-RNA for $r_p = 1$ Å and two different values of $w = 0$ and $w = 1.4$ Å for B-DNA, and $w = 0$ and $w = 3$ Å for A-RNA. As shown in Fig. 2a, the equivalent radius for the case of a B-DNA with $w = 0$ is approximately r_{cyl}=8.8 Å. The surface potential distributions for the various models are

considerably different from one another which arises from the non-uniform charge distribution and the topography of the molecular surface. To further compare the molecular models with charged cylinders, we considered the electrical potential distribution on a plane perpendicular to the plane of the slit containing the axis of the molecule/cylinder (Fig. S10c). We determined the average potential on this plane as a function of radial distance from the molecular axis, ρ (Fig. S10d). Comparing the cylinder model and the molecular structure, we find that, as expected, due to differences in geometry and surface charge distributions, there is indeed a disparity in the average potentials in "near fields" (NF) of the two objects ($\rho \lessapprox 2$ nm). This difference in average potential, however, decays monotonically with distance vanishes in the "bulk" (B) and "far field" (FF) regions ($\rho > 2$ nm). Fig. S10e depicts the contributions of these regions to F_{el} by evaluation of the integral in equation (S30) over subdomains representing NF, bulk (B), and FF regions. In this analysis, a capsule of radius 20 Å measured from the molecular axis, enclosing the molecule/cylinder is considered as the NF region, and a sheet of thickness of 40 Å near the walls represents the FF region. Although the definition of these subdomains is empirical, the analysis qualitatively shows that the contribution of "bulk" region to the free energies, and therefore the effective charge, is not significant in comparison to those of the FF and NF, which in turn we find are comparable in magnitude. Thus the regions in the vicinity of both molecule and walls contribute in approximately equal measure to the overall experimental effect. Note that while in this picture the FF region is designated as the electrostatic far-field of the molecule it may equally well be thought of as the electrostatic near-field of the wall regions. Thus the interaction free energy stems almost entirely from the near-field regions of the interacting objects.

S7.4 The role of probe radius, r_{p}, and its impact on the calculated effective charge, q_{eff}

In the calculation of molecular free energies, the geometric properties of the molecular surface used depend on the choice of radius of the rolling probe. Therefore the probe radius, r_{p}, is another parameter that merits investigation. Free energy calculations for various molecular models show that, generally, the probe radius has a negligible impact on the calculated effective charge as long as the global features of the molecular surface are unaffected by the change of probe size. We examined this effect by considering a larger probe radius of r_{p} =5 Å. For B-DNA we find that this increase in probe radius (from 1 to 5 Å) increases the magnitude of the effective charge by approximately 2%. Interestingly the impact on the calculated q_{eff} of A-RNA is much larger (≈25%). Figure S10B displays the influence of probe radius on the surface potentials of the two helical species. A comparison reveals that increasing the probe radius only slightly modifies the B-DNA surface by smoothing out small details (such as crevices) of the molecular surface, and therefore, as noted above has a relatively minor impact on the calculated effective charge. Contrary to B-DNA, the A-RNA structure undergoes a significant change, losing its narrow and deep major groove, which effectively reflects the fact that the molecular interior becomes progressively impenetrable to rolling probes of larger radii, as shown in Fig. S10b (top view).

In general, the effective charge values calculated for A-RNA with $r_{\mathrm{p}} < 5$ suggest equivalent cylinder radii values, $r_{\mathrm{cyl}} < r_{\mathrm{c}}$, which turn out to be much smaller than the experimentally measured $r_{0,\mathrm{A}}$ value. While there is no requirement *a priori* for the radius of the equivalent cylinder to be comparable to that of the outer helical envelope, the indication of $r_{\mathrm{cyl}} < r_{\mathrm{c}}$ from these computational molecular models may in fact reflect an unphysical result for the following reasons. One consideration is likely to be the continuum character of the PB equation which also treats ions as point-like particles. It is known that at high magnitudes of electrical potential the finite size of ions causes the point-ion assumption to break down. This is because the close packing condition - which specifies an upper bound on ionic concentrations - is violated. The maximum magnitude of surface potentials for A-RNA models under our experimental conditions ($|\psi|_{\mathrm{max}} \approx 11.5$) indicates local concentrations of

around ≈100 M >> 9 M which represents the close packing concentration given by $(2a_{\mathrm{H}})^{-3}$ for Na^+ ions ($a_{\mathrm{H}} \approx 2.8$ Å). This strongly suggests that a departure from the PB regime is highly likely for an A-RNA molecule. Another feature distinguishing the A-RNA structure from that of B-DNA is the deep major groove, which creates the impression of a "hollow spine" along the molecular axis when viewed from the top (Fig. 2a and Fig. S10b). The point-ion PB model predicts high counterion concentrations in the major groove under our experimental conditions, and yet again it is not clear that the PB calculations point to physically plausible local concentrations under experimental conditions where ionic species have finite sizes and the maximum attainable concentrations would be bounded by an upper limit[29]. We point that within the PB model the experimental measurements require the presence of a hydration sheath of thickness *w*, whose main structural effect is to entirely occlude ions from within an outer molecular surface envelope.

S7.5 Accounting for finite ion size in the point-ion PB model

We now discuss the role of finite ion size in the molecular electrostatics problem. We focus in particular on explicit corrections to the PB model that account for finite ion size. In particular we show that the simple PB model is in fact able to account for finite ion size in a direct fashion involving an increase in the radius of the corresponding equivalent cylinder.

Using a lattice gas approach, Borukhov *et al.* proposed a modified PB (MPB) model which uses the close packing limit to define an upper bound for local ionic concentrations[30]. Use of this MPB model and the related free energy functionals in our calculations gives results that are effectively identical to the point-ion model for B-DNA as expected. For A-RNA however, the MPB model yields larger calculated r_{cyl} values, in good agreement with the experimental measurements. This is expected on the grounds that the average surface electrical potentials for A-RNA tend to be higher than for B-DNA. However, we point out that the close packing limit is a purely geometric condition which prohibits unphysical overlapping of ions in a lattice model. This particular MPB model does not take into account short-range interactions between ions and surfaces due to which steric effects can manifest at ion concentrations much lower than the close packing limit, as demonstrated in more recently described MPB models such as the Poisson-Helmholtz-Boltzmann (PHB) model[11]. The ability to capture the role of finite ion size in the limit of low ion densities could be important in modeling B-DNA self consistently and may be possible using the PHB model. Thus while the simple PB model does permit us to effectively deduce aspects of the interfacial structural detail of the double helix required to capture the experimental measurement (see below), a more general model incorporating finite ion size will enhance the robustness of the parameter values and molecular structural detail inferred in this work.

Despite the fact that the simple point-ion PB model does not explicitly incorporate finite ion size, we have found that the point-ion approach can indeed lend itself to accounting for finite ion size at the molecule/electrolyte interface. The basis of the underlying argument is illustrated in Fig. S10f. Essentially, the existence of a hydration layer around the molecule and finite size of counterions implies the presence of a low-dielectric "shell" region in the vicinity of the molecular structure, whose thickness may be expected to be well approximated by the radius of a hydrated counterion. For illustrative purposes we compare two cylinder models of the same length, carrying identical amounts of total charge. The first model (model (a)) has the charge distributed on the "interior" molecular ("vdW") surface but is surrounded by a dielectric shell of dielectric constant ε_{s}, representing the charge free (c=0), ion-excluded zone (Fig. S10f model (a)). The exterior surface of this shell region may be regarded as equivalent to an "ion accessible surface" (IAS) beyond which the point-ion description should hold provided the local electrical potential ψ <9 for $c \approx 1$ mM. This condition may be expected to apply for B-DNA in our experiments. The second model (model (b)) considers a simpler hollow object consisting of a single cylindrical surface of radius equal to the IAS in model (a). Model (b) ignores interior dielectric detail entirely. Figure S10F(ii) compares the calculated q_{eff}

values for the two models by plotting the ratio of effective charges for the two cases. We find that neglecting the dielectric region and distributing the same amount of charge on the outer (IAS) surface in model (b) has negligible impact on the effective charge. For example, for $\varepsilon_s = 2$ and $t = 3$ Å we expect the discrepancy in q_{eff} for the two models to lie at around 0.7% for a 30 bp fragment and 0.3% for 60 bp fragment of B-DNA (Fig. S10f). These percentage differences are of the the same order as the broadening of the experimental data due to statistical uncertainty and may be regarded as effectively negligible for our purposes. Furthermore we find that the similarity in q_{eff} between the dielectric shell and simple cylinder models holds for a range of shell thicknesses, t, and shell dielectric constants, ε_s, relevant to the problem (Fig. S10f). We therefore expect the effective cylindrical radius parameter, r_{cyl}, to successfully capture the effect of finite ion size in the determination of q_{eff}. Thus, based on the above results, we have neglected the dielectric shell region, that could more accurately reflect an ion excluded zone, for all q_{eff} calculations for molecular structures and cylinders. Significantly, the above result provides a physical basis for why we observe a dependence of the measured effective cylinder radius, r_{m}, of the double helix on the radius of the cationic species in solution (Fig. 4a).

List of important variables and parameters

Symbol	Variable or parameter name
b	Helical rise per basepair
b_{m}	Experimentally measured helical rise per basepair
c	Salt concentration
d	Depth of the pocket structure
D	Diffusion coefficient
e	Elementary unit charge
f_{A}	Additive correction factor
f_{H}	Hydrodynamic correction factor
f_{M}	Multiplicative correction factor
F_{el}	Electrostatic free energy
ΔF_{el}	Electrostatic contribution to the total free energy
ΔF_{rot}	Free energy contribution to W arising from rotational motion of a rod-shaped molecule
$\Delta F_{\mathrm{trans}}$	Free energy contribution to W arising from position fluctuations of the center of mass
$2h$	Measured slit height
κ^{-1}	Debye length
k_{B}	Boltzmann's constant
l	Contour length of the nucleic acid molecule
n	Number of basepairs
μ	Solvent viscosity
T	Temperature
t_{cycle}	Cycle time in fluorescence imaging
t_{esc}	Average escape time of the molecule
t_{exp}	Exposure time in fluorescence imaging
t_{lag}	Lag time in fluorescence imaging
t_{r}	Position relaxation time of the trapped molecule
r	Helical radius
r_{m}	Measured radius of the nucleic acid molecule
r_{H}	Hydrodynamic radius measured using FCS
q_{dye}	Effective charge of a single dye attached to each 5' terminus of a nucleic acid
q_{eff}	Calculated effective electrical charge
q_{m}	Measured electrical charge in a real experiment
q_{NA}	Number of fully ionized backbone phosphate groups
q_{str}	Net structural charge
W	Depth of the trap or potential well
x_{e}	Error on parameter x
x_{in}	Input test value for parameter x used in a simulation
x_{out}	Output value for parameter x obtained in a simulation with input value x_{in}
x_{t}	True value for parameter x
ϕ_{m}	Electrical potential at the slit mid-plane
ϕ_{s}	Electrical potential at the surface of the slit wall

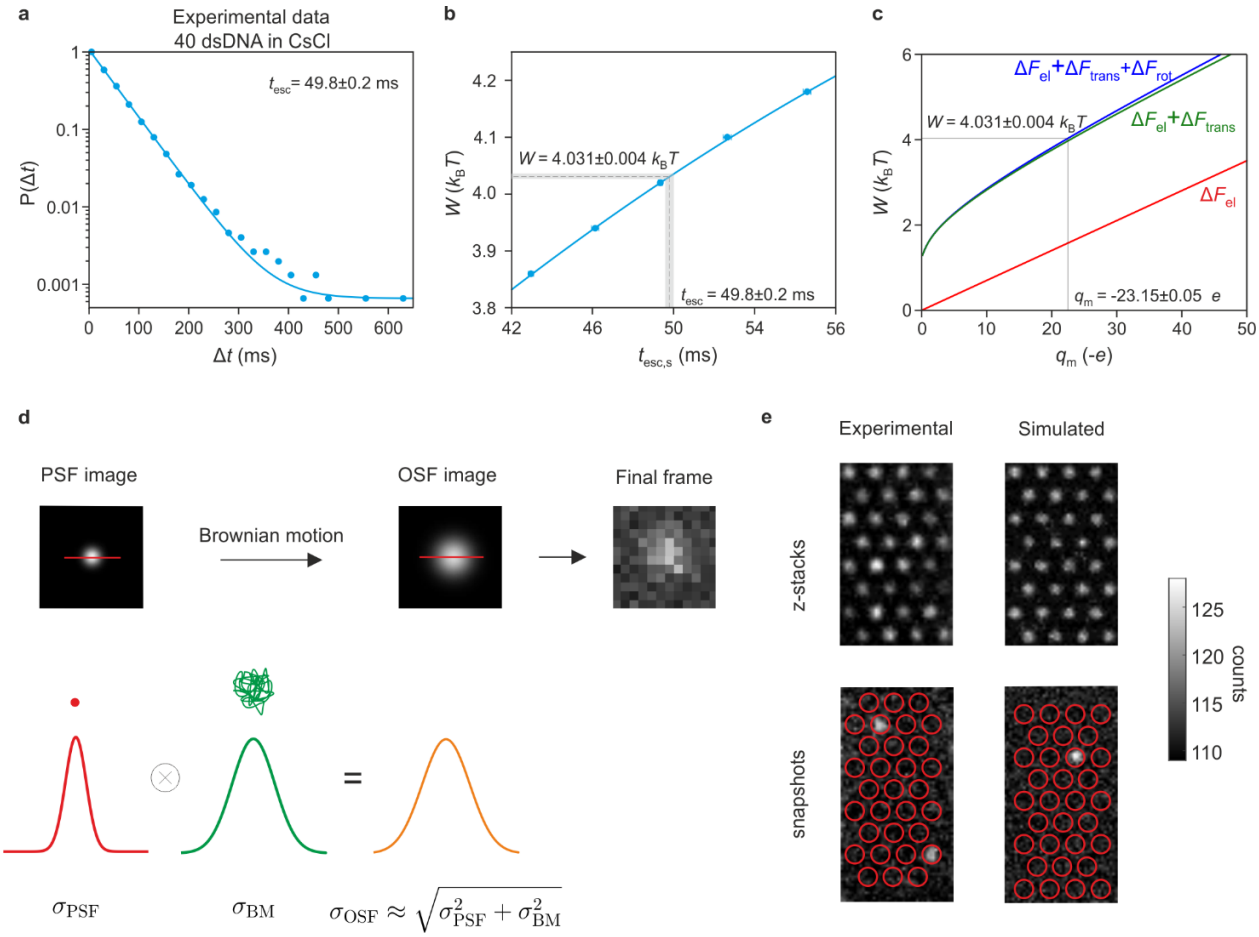
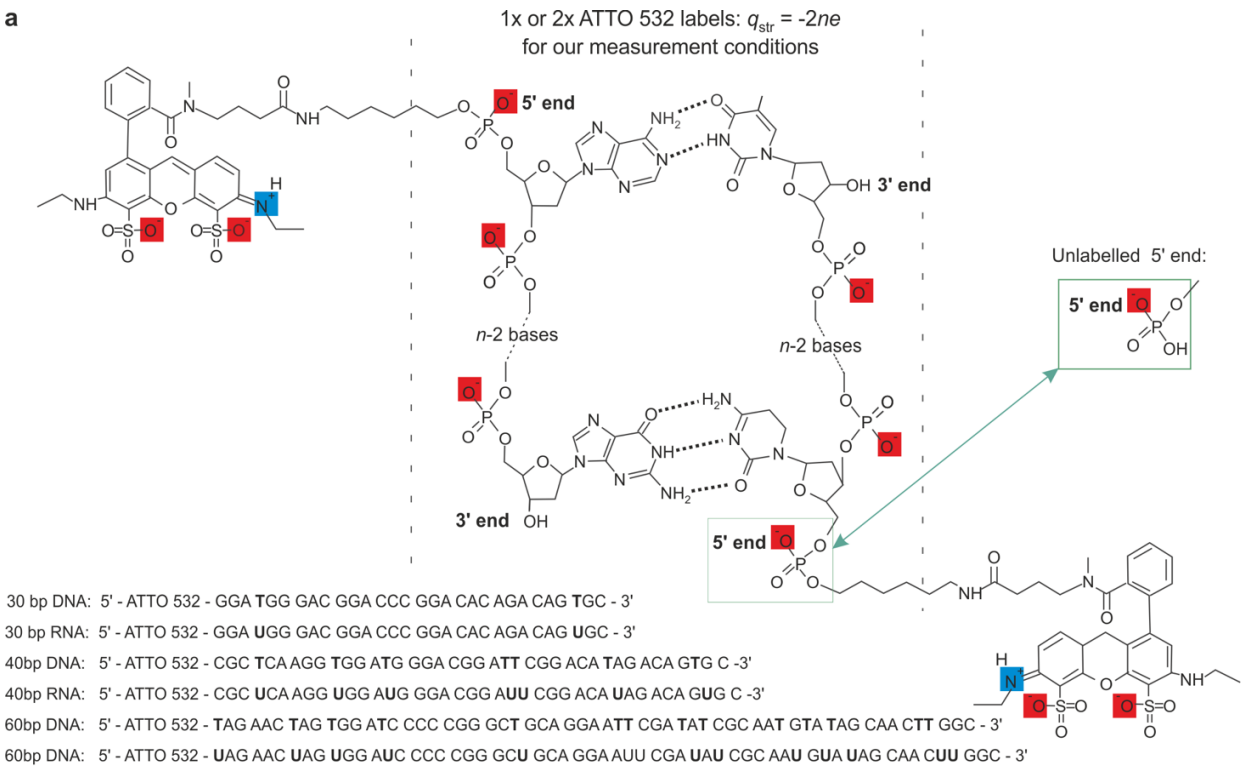
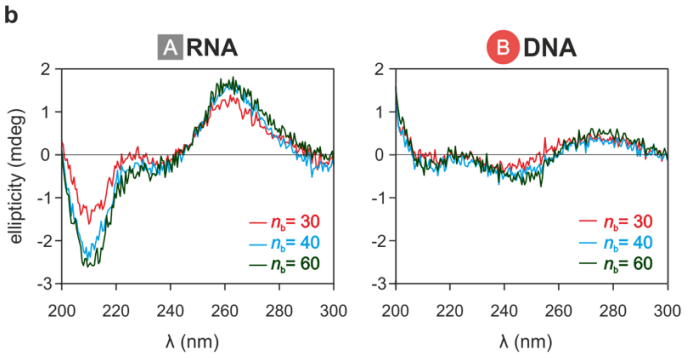
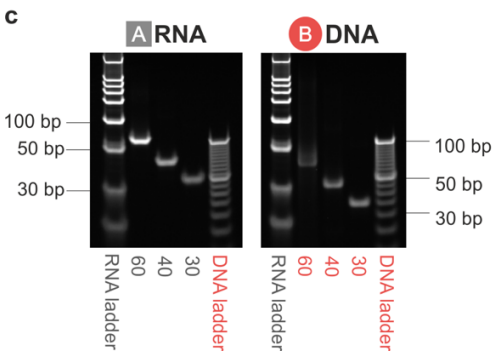


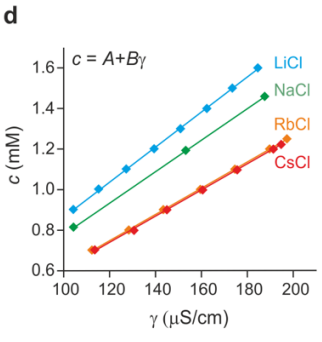
Figure S1. Converting measured escape times, t_{esc}, to measured molecular effective charge, q_m. **(a)** A sample histogram of measured escape times fitted with a single exponential, $P(\Delta t) \propto \exp(-\Delta t/t_{esc})/t_{esc}$, for 40 dsDNA measured in 1.21 mM CsCl, 1 mM TRIS, pH=8.9. **(b)** Brownian Dynamics (BD) simulations of molecular motion in a free energy landscape yield a relationship for potential well depth W vs. average escape time, $t_{esc,s}$, fitted with a second degree polynomial. Values for $t_{esc,s}$ were obtained from image analysis of simulated movies (procedure described below). The t_{esc} value from experimental measurements was converted to a measurement of W using this fit relation. **(c)** Plot of W as a function of q_m, for $\phi_s = -2.8\ k_BT/e$, displaying the various contributions to W, namely ΔF_{el}, ΔF_{trans} and ΔF_{rot}. **(d)** A series of images depicting from left to right: the optical point spread function (PSF) for a single stationary molecule, a representative optical image for a molecule exhibiting thermal motion, which we call the object spread function (OSF) image, and a final pixelated image superimposing the OSF on the background intensity, including shot noise, mimicking the actual experiment. The OSF image is a convolution of the PSF image of a stationary emitter with a probability density representative of the molecule's spatial fluctuations due to Brownian motion within a time period $t_{exp} = 5$ ms, obtained from a BD simulation, as described in Ref. 2. **(e)** Top: Maximum intensity projection of experimental (left) and simulated (right) widefield fluorescence images of an array of 32 traps. Bottom: typical experimental (left) and simulated (right) snapshot camera images. Locations of traps are indicated by red circles. The simulation contains a single molecule sampling the array, while the experiment can involve more than one molecule simultaneously in the same field of view. Photobleaching is not expected to pose an issue as established in previous work[1].





Nucleic acid	λ_{min} (-) (nm)	$\lambda_{crossover}$ (nm)	λ_{max} (+) (nm)
A-RNA	210	243	263
B-DNA	247	260	275

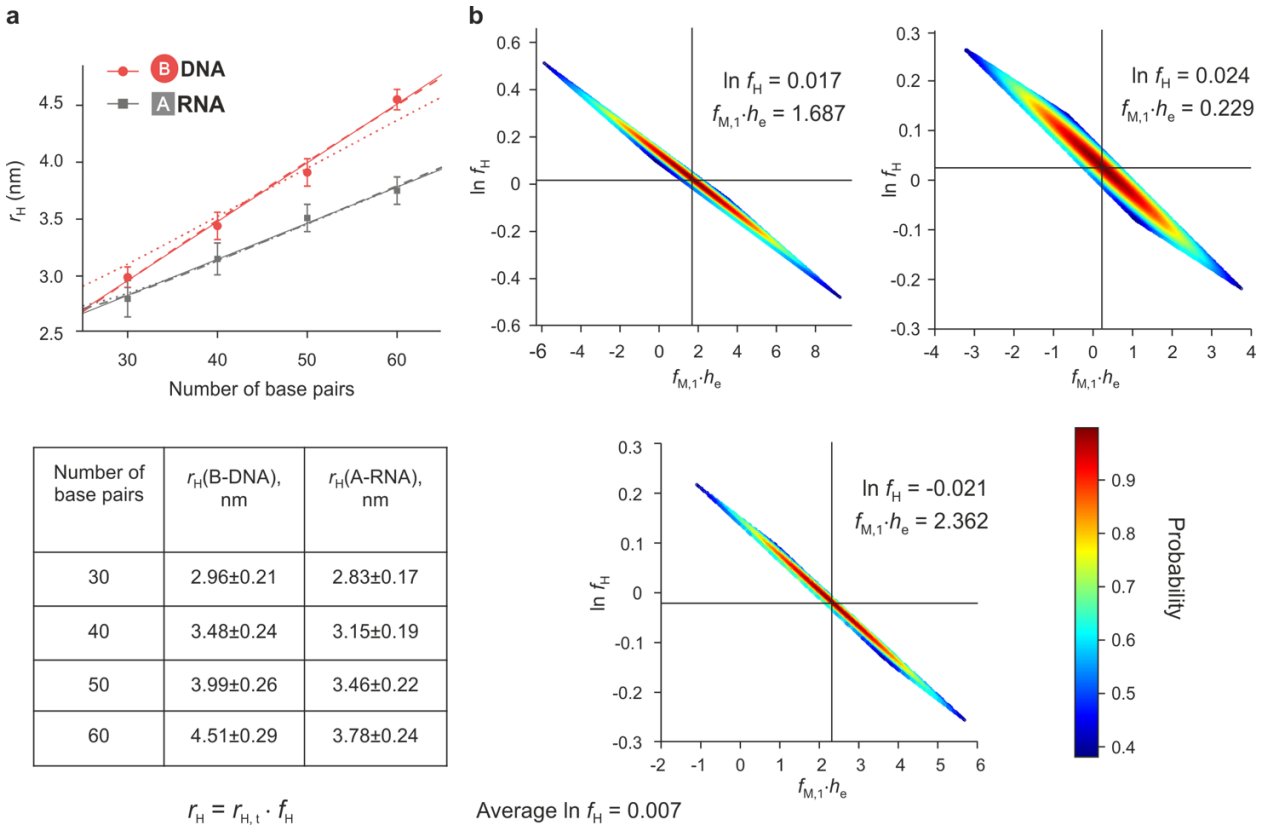




Salt	*A*	*B*	a_m, Å	a_H, Å
LiCl	-0.00397	0.00869	3.14	3.58
NaCl	-0.00185	0.00781	2.40	2.76
RbCl	-0.03148	0.00651	1.64	1.78
CsCl	-0.04213	0.00652	1.65	1.79

Figure S2. Characterization of B-DNA and A-RNA samples. (a) Chemical structure of dsDNA with two ATTO 532 modifications on both 5'-ends. Charge carrying atoms, ionized under our conditions, are highlighted in blue (positive) and red (negative). In singly labeled nucleic acid fragments only one 5'-phosphate end carries the dye modification; the other remains underivatized, as shown. A ds nucleic acid, *n* basepairs in length, labeled with either one or two ATTO 532 dyes on

its 5'-ends respectively, carries a structural charge $q_{\mathrm{str}} = q_{\mathrm{NA}} = -2ne$. This value is the charge of the nucleic acid alone and excludes the contribution of the dye. dsDNA and dsRNA sequences used in the measurements have effectively identical sequences with uracil (U) replacing thymine (T) in dsRNA (bottom). **(b)** CD spectra of 30 bp, 40 bp, 60 bp dsDNA and dsRNA fragments measured in an electrolyte solution containing 1 mM NaCl, 1-1.3 mM Tris. The table presents average peak and crossover bands for dsDNA and dsRNA structures, corresponding to B- and A-helices respectively. **(c)** 20% native polyacrylamide gel for A-RNA (left) and B-DNA (right) fragments stained with GelRed dye. dsRNA gel (left): Lane 1 – dsRNA ladder, 2 – 60 bp dsRNA, 3 – 40 bp dsRNA, 4 – 30 bp dsRNA, 5 – 5 bp dsDNA ladder. dsDNA gel (right): Lane 1 – dsRNA ladder, 2 – 60 bp dsDNA, 3 – 40 bp dsDNA, 4 – 30 bp dsDNA, 5 – 5 bp dsDNA ladder. All fragments display slightly lower mobilities than the corresponding fragments in the ladders, likely due to the presence of the charged fluorescent dye labels. **(d)** Converting measured solution conductivity, γ (in $\mu\mathrm{S/cm}$) to salt concentration, c (in mM). Solid lines denote the linear calibration function $c = A + B\gamma$ used to convert γ to c. Fit A and B coefficients are individual for every salt: CsCl (red), RbCl (orange), NaCl (green), and LiCl (blue). The table lists values for hydrated cationic radii, a_{m}, that we obtained using the equation (S27), $a_{\mathrm{Cl^-}} = 1.81$ Å and the fit relation. Values of a_{H} from Ref. 18 are also listed.

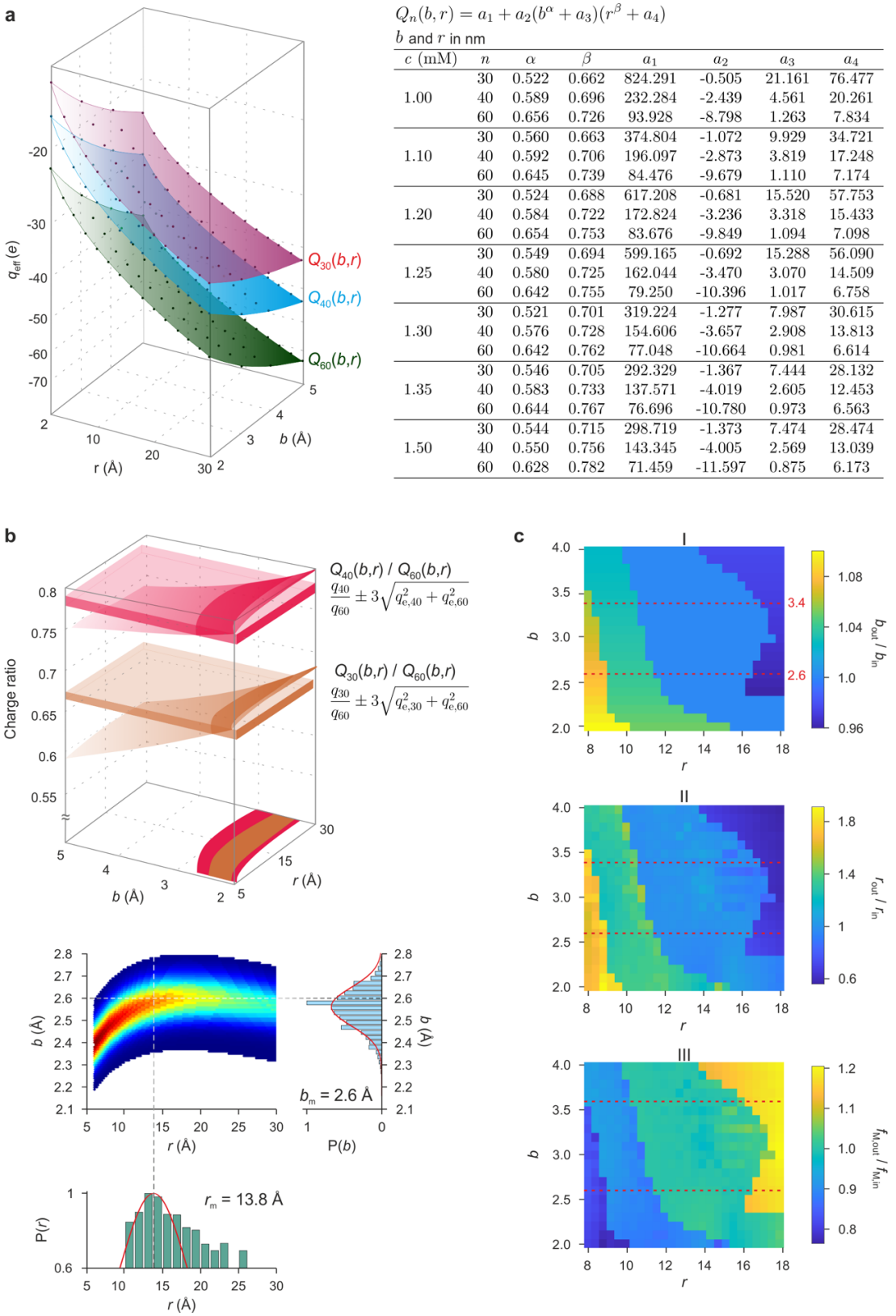


Number of base pairs	r_H(B-DNA), nm	r_H(A-RNA), nm
30	2.96±0.21	2.83±0.17
40	3.48±0.24	3.15±0.19
50	3.99±0.26	3.46±0.22
60	4.51±0.29	3.78±0.24

$r_H = r_{H,t} \cdot f_H$

Average ln f_H = 0.007

Figure S3. Measuring the hydrodynamic uncertainty, f_H. (a) Hydrodynamic radii, r_H of dsDNA (red circles) and dsRNA (grey squares) for fragments of length n basepairs measured using FCS. Independent linear fits of r_H vs n were performed for both dsDNA (red solid line) and dsRNA (grey solid line) fragments. r_H values for each fragment from the linear fit relations were used in BD simulations and are listed in the table below. Furthermore, the measured r_H vs n data were also fitted with an equation of the form $r_H = l / 2[\ln(l/2r) + v]$ as described in the text. Performing the fitting procedure with three fit parameters, b, r v, we obtained: $b = 4.4\pm8.5$ Å, $r = 9.3\pm18516$ Å, $v = 0.26\pm2001$ for B-DNA (red dashed line), and $b = 2.6\pm1.9$ Å, $r = 10.4\pm4042$ Å, $v = 0.06\pm389$ for A-RNA (grey dashed line). Dotted lines (red for B-DNA, grey for A-RNA) illustrate the fits performed with b values fixed to the nominal crystallographic values, 3.4 Å for B-DNA and 2.6 Å for A-RNA. In this case we obtained: $r = 9.8\pm1255$ Å, $v = -0.004\pm127$ for B-DNA, and $r = 9.7\pm315$ Å, $v = -0.02\pm32$ for A-RNA. **(b)** Measuring the hydrodynamic correction factor, f_H. Solving the system of two linear equations of the form equation (S18) graphically, we first obtained the space of possible $f_{M,1} \cdot h_e$ and $\ln f_H$ values, and then determined the weighted mean values (black solid lines) for both unknowns. Three sets of measurements revealed average value of $\ln f_H = 0.007\pm0.025$ or $f_H = 1.007\pm0.025$.



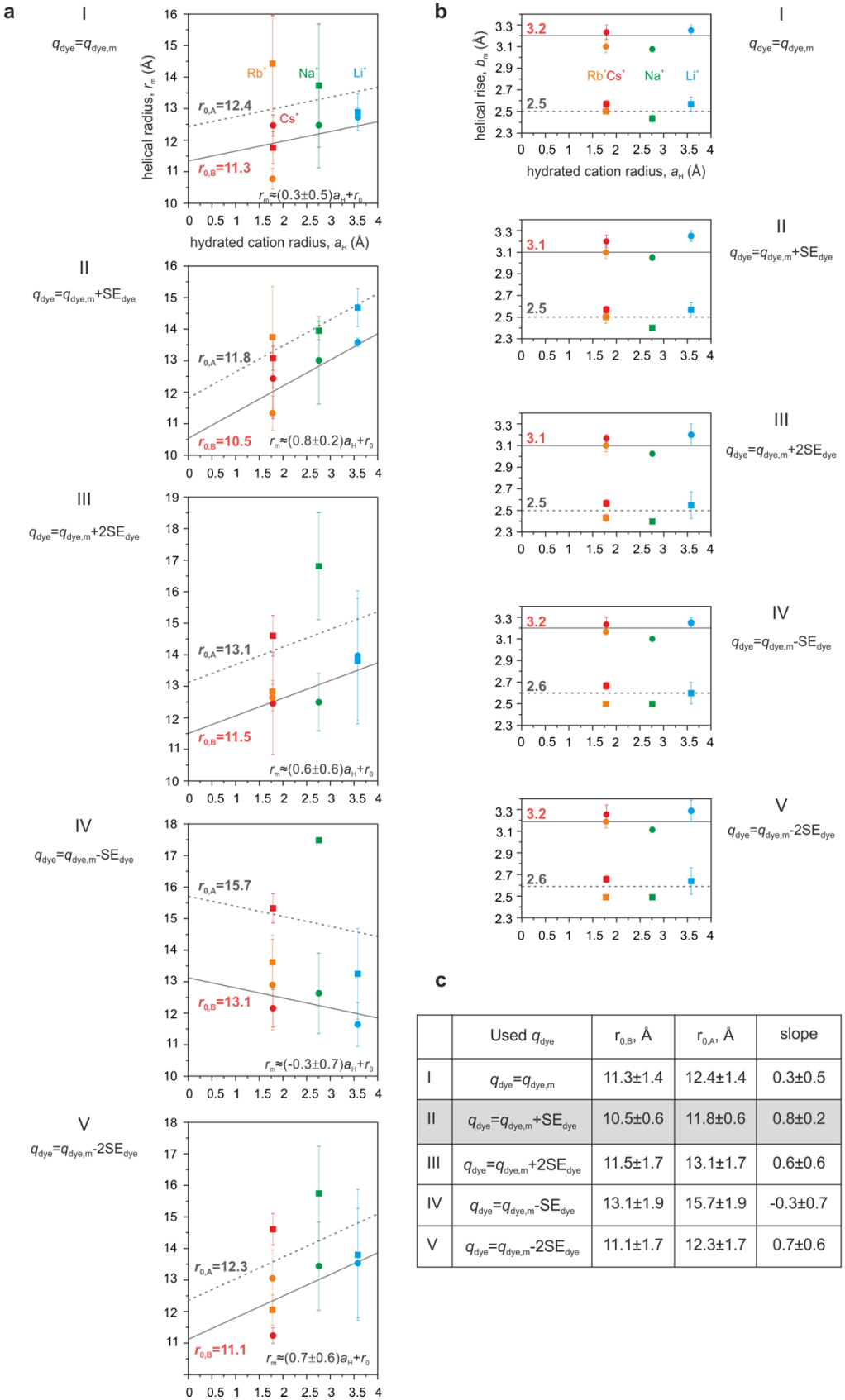
$Q_n(b,r) = a_1 + a_2(b^\alpha + a_3)(r^\beta + a_4)$

b and r in nm

c (mM)	n	α	β	a_1	a_2	a_3	a_4
1.00	30	0.522	0.662	824.291	-0.505	21.161	76.477
	40	0.589	0.696	232.284	-2.439	4.561	20.261
	60	0.656	0.726	93.928	-8.798	1.263	7.834
1.10	30	0.560	0.663	374.804	-1.072	9.929	34.721
	40	0.592	0.706	196.097	-2.873	3.819	17.248
	60	0.645	0.739	84.476	-9.679	1.110	7.174
1.20	30	0.524	0.688	617.208	-0.681	15.520	57.753
	40	0.584	0.722	172.824	-3.236	3.318	15.433
	60	0.654	0.753	83.676	-9.849	1.094	7.098
1.25	30	0.549	0.694	599.165	-0.692	15.288	56.090
	40	0.580	0.725	162.044	-3.470	3.070	14.509
	60	0.642	0.755	79.250	-10.396	1.017	6.758
1.30	30	0.521	0.701	319.224	-1.277	7.987	30.615
	40	0.576	0.728	154.606	-3.657	2.908	13.813
	60	0.642	0.762	77.048	-10.664	0.981	6.614
1.35	30	0.546	0.705	292.329	-1.367	7.444	28.132
	40	0.583	0.733	137.571	-4.019	2.605	12.453
	60	0.644	0.767	76.696	-10.780	0.973	6.563
1.50	30	0.544	0.715	298.719	-1.373	7.474	28.474
	40	0.550	0.756	143.345	-4.005	2.569	13.039
	60	0.628	0.782	71.459	-11.597	0.875	6.173

Figure S4. Principle behind the measurement of rise per base pair, b and radius, r, of the double helix, in a real experiment (i.e., $f_M \neq 1$). (a) 2D surfaces for the effective charge values obtained by fitting the calculated effective charge values (shown with points), $q_{\text{eff},n}(b,r)$, with a power-law function. The table lists the fit values of all parameters in the power-law fit equations for $n = 30$, 40

and 60 basepairs determined for salt concentrations ranging from 1 to 1.5 mM. **(b)** Measured values for effective charge ratios, e.g. $\frac{q_{30}}{q_{60}} \pm 3\sqrt{q_{e,30}^2 + q_{e,60}^2}$ and $\frac{q_{40}}{q_{60}} \pm 3\sqrt{q_{e,40}^2 + q_{e,60}^2}$, superimposed as planes of finite thickness in charge on the corresponding 2D surfaces, e.g. $Q_{30}\ (b,r)/Q_{60}\ (b,r)$ and $Q_{40}\ (b,r)/Q_{60}\ (b,r)$. This yields two domains of possible solutions in b and r. Intersection of these domains yields a probability weighted manifold of solutions from which measured values of helical rise per base pair, b_{m} and radius, r_{m}, are extracted. The lower panel illustrates the results for one measurement of A-RNA in CsCl measurements. **(c)** Results of a simulation based study of the overall accuracy in the determination of r (panel I), b (panel II), and f_{M} (panel III) for various combinations of input parameters b_{in} and r_{in} . The level of accuracy expected is plotted as a ratio $x_{\mathrm{out}}/x_{\mathrm{in}}$, where x denotes either b, r or f_{M}. Dotted red lines indicate $b = 3.4$ Å or 2.6 Å and are provided as visual guides. Maximum accuracy in determination of r, b and f_{M} is obtained within the ranges of r_{in}= 10.5-17.0 Å for $b = 3.4$ Å and $r_{\mathrm{in}} = 11.3$-16.5 Å for $b = 2.6$ Å.

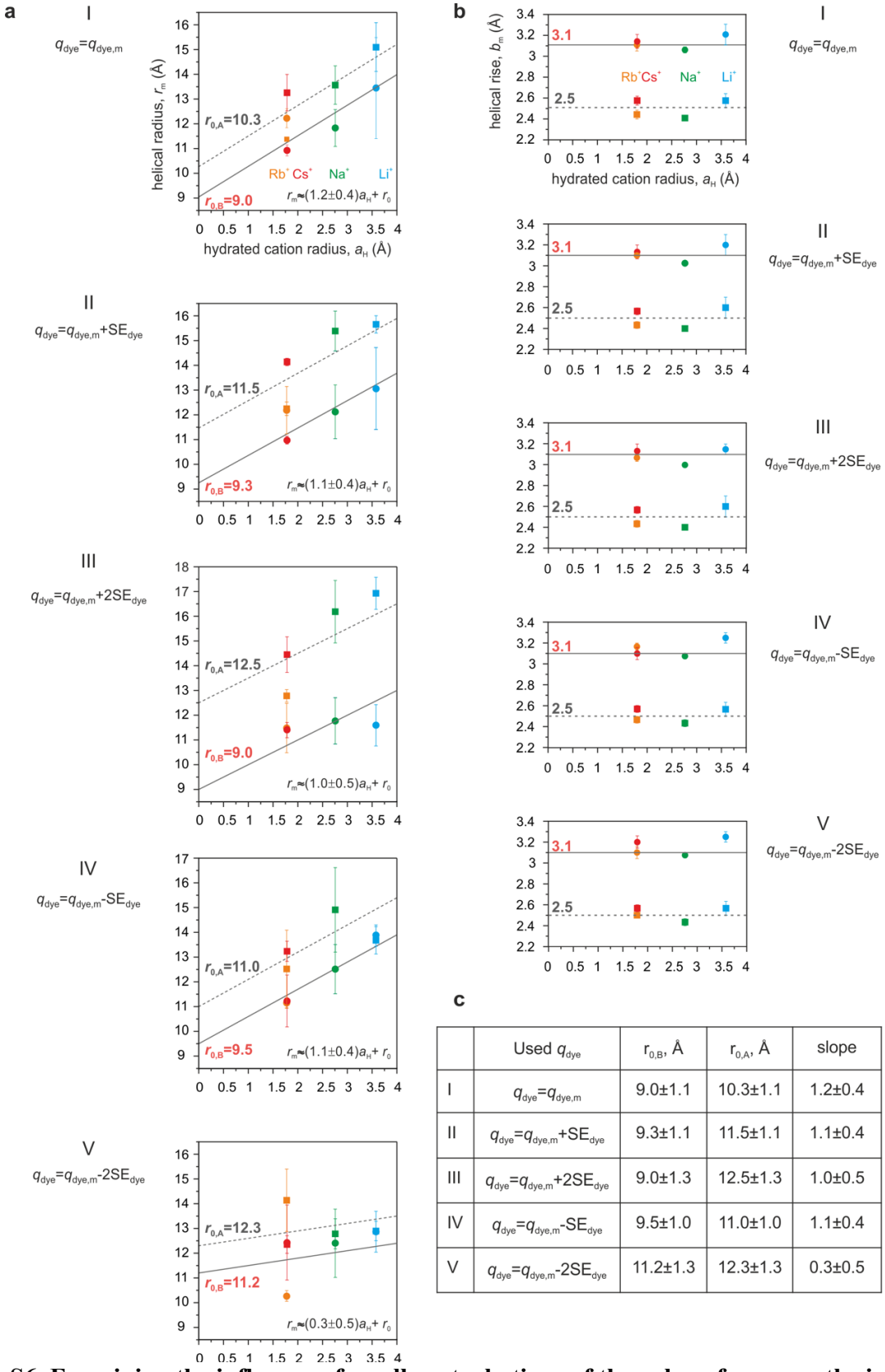


c

	Used q_{dye}	$r_{0,B}$, Å	$r_{0,A}$, Å	slope
I	$q_{dye}=q_{dye,m}$	11.3±1.4	12.4±1.4	0.3±0.5
II	$q_{dye}=q_{dye,m}+SE_{dye}$	10.5±0.6	11.8±0.6	0.8±0.2
III	$q_{dye}=q_{dye,m}+2SE_{dye}$	11.5±1.7	13.1±1.7	0.6±0.6
IV	$q_{dye}=q_{dye,m}-SE_{dye}$	13.1±1.9	15.7±1.9	-0.3±0.7
V	$q_{dye}=q_{dye,m}-2SE_{dye}$	11.1±1.7	12.3±1.7	0.7±0.6

Figure S5. Examining the influence of small perturbations of the value of q_{dye} on the inferred average values for helical radius, r_m, and rise per base pair, b_m. The analysis is performed for $\ln f_H = 0.007$ and corresponding measured q_{dye} values: $q_{dye,DNA} = -0.46\,e$ with $SE_{dye,DNA} =$

$0.04\,e$, $q_{\mathrm{dye,RNA}} = -0.44\,e$ with $\mathrm{SE}_{\mathrm{dye,RNA}} = 0.05\,e$. The analysis procedure is repeated by introducing systematic offsets on the average q_{dye} value given by $\pm\mathrm{SE}_{\mathrm{dye}}$ and $\pm 2\mathrm{SE}_{\mathrm{dye}}$. **(a)** Influence of the value of q_{dye} on the measured average r_{m} values for B-DNA (circles) and A-RNA (squares). The r_{m} vs a_{H} data were fitted with a linear expression of the form $r_{\mathrm{m}} = a_{\mathrm{H}} \cdot k + r_0$ with a shared value of slope, k, for both helical forms (solid line for B-DNA and dashed line for A-RNA). **(b)** Influence of the value of q_{dye} on the measured average b_{m} values for B-DNA (circles) and A-RNA (squares). Black lines (solid for B-DNA and dashed for A-RNA) denote the average values for b_{m} over all the measurements for a given q_{dye} value. **(c)** List of fitted values for $r_{0,\mathrm{A}}$, $r_{0,\mathrm{B}}$ and slope, k, obtained by linear extrapolation of the measured r_{m} vs a_{H} data to a_{H} =0. The result corresponding to $q_{\mathrm{dye}} = q_{\mathrm{dye,m}} + \mathrm{SE}_{\mathrm{dye}}$ (highlighted in the table) is used for all the further analysis and discussions in the study.



	Used q_{dye}	$r_{0,B}$, Å	$r_{0,A}$, Å	slope
I	$q_{dye}=q_{dye,m}$	9.0±1.1	10.3±1.1	1.2±0.4
II	$q_{dye}=q_{dye,m}+SE_{dye}$	9.3±1.1	11.5±1.1	1.1±0.4
III	$q_{dye}=q_{dye,m}+2SE_{dye}$	9.0±1.3	12.5±1.3	1.0±0.5
IV	$q_{dye}=q_{dye,m}-SE_{dye}$	9.5±1.0	11.0±1.0	1.1±0.4
V	$q_{dye}=q_{dye,m}-2SE_{dye}$	11.2±1.3	12.3±1.3	0.3±0.5

Figure S6. Examining the influence of small perturbations of the value of q_{dye} on the inferred average values for helical radius, r_m, and rise per base pair, b_m. The analysis is performed for $\ln f_H = 0.013$ and corresponding measured q_{dye} values: $q_{dye,DNA} = -0.45\,e$ with $SE_{dye,DNA} =$

$0.03\,e$, $q_{\mathrm{dye,RNA}} = -0.42\,e$ with $\mathrm{SE}_{\mathrm{dye,RNA}} = 0.03\,e$. The analysis procedure is repeated by introducing systematic offsets on the average q_{dye} value given by $\pm\mathrm{SE}_{\mathrm{dye}}$ and $\pm 2\mathrm{SE}_{\mathrm{dye}}$. **(a)** Influence of the value of q_{dye} on the measured average r_{m} values for B-DNA (circles) and A-RNA (squares). The r_{m} vs a_{H} data were fitted with a linear expression of the form $r_{\mathrm{m}} = a_{\mathrm{H}} \cdot k + r_0$ with a shared value of slope, *k*, for both helical forms (solid line for B-DNA and dashed line for A-RNA).
(b) Influence of the value of q_{dye} on the measured average b_{m} values for B-DNA (circles) and A-RNA (squares). Black lines (solid for B-DNA and dashed for A-RNA) denote the average values for b_{m} over all the measurements for a given q_{dye} value. (**c)** List of fitted values for $r_{0,\mathrm{A}}$, $r_{0,\mathrm{B}}$ and slope, *k*, obtained by linear extrapolation of the measured r_{m} vs a_{H} data to $a_{\mathrm{H}} = 0$.

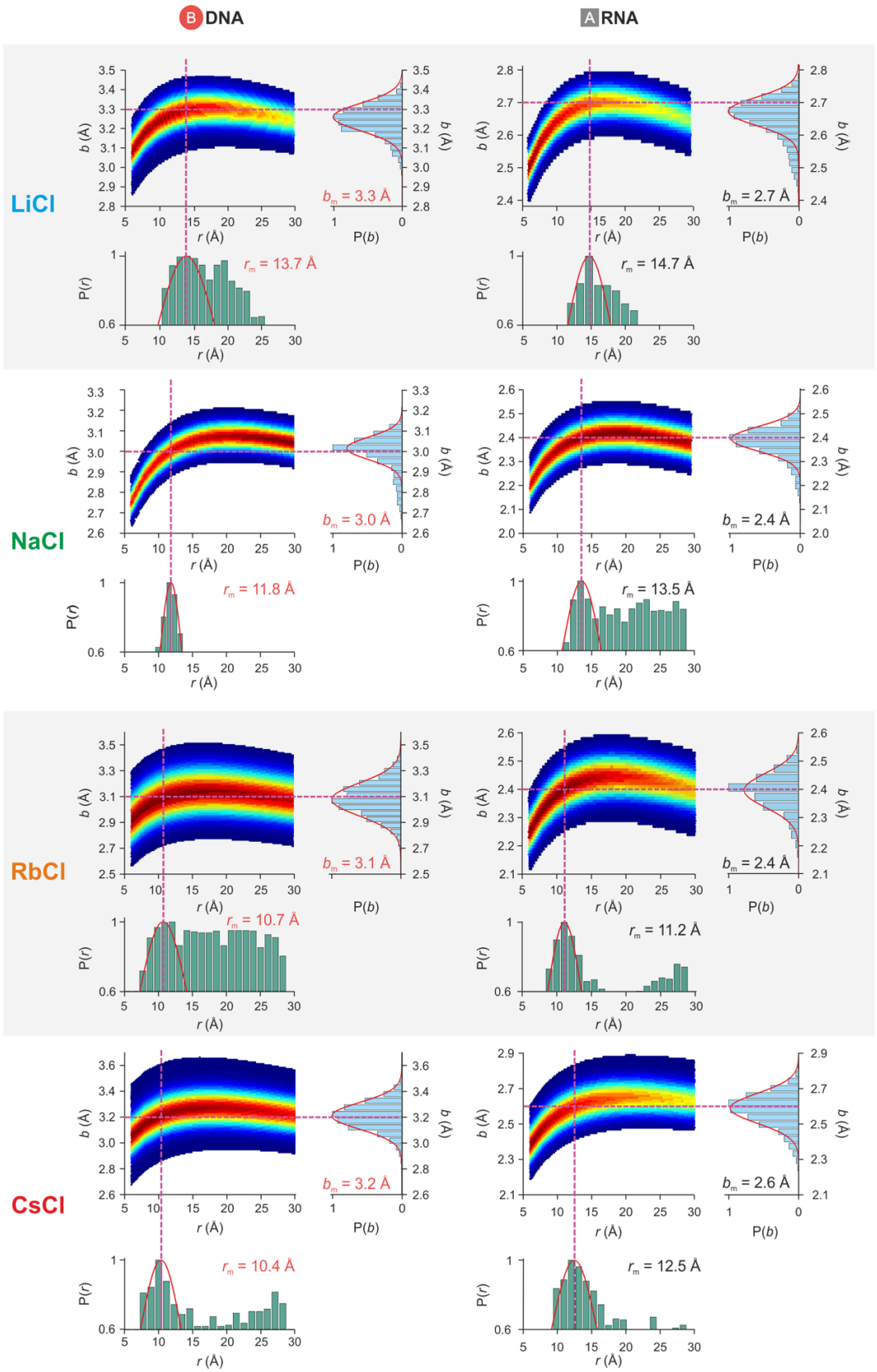


Figure S7. Example measured *b-r* probability manifolds for B-DNA (left) and A-RNA (right) for experiments performed in solutions containing LiCl, NaCl, RbCl or CsCl (from top to bottom). Experimental details on these data sets are denoted in boldface in Table S1.

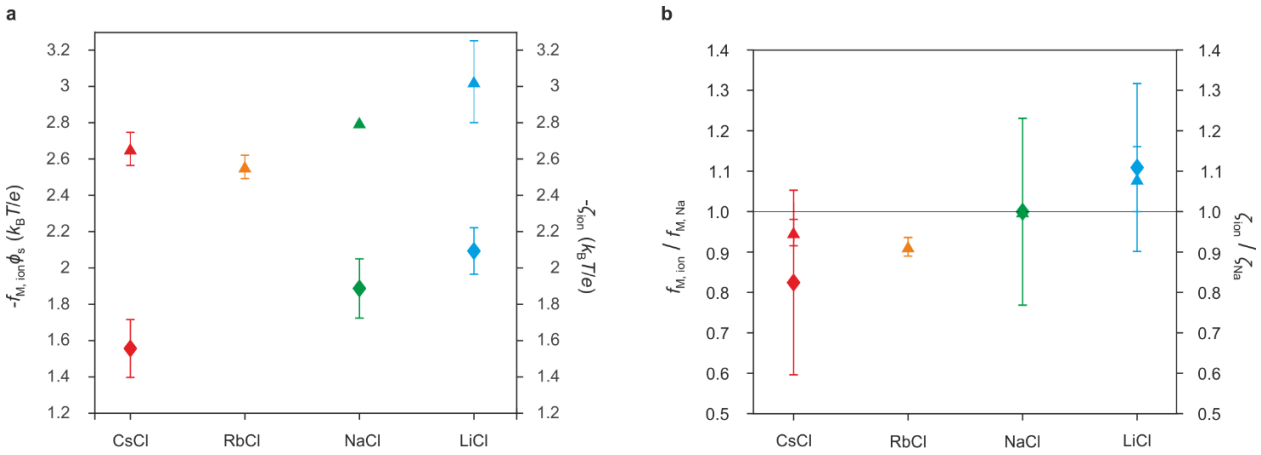


Figure S8. The influence of ionic species on the value of the multiplicative correction factor, f_{M}. **(a)** Comparison of measured $f_{\mathrm{M}}\phi_{\mathrm{s}}$ values (triangles), reflecting the true effective surface potential, $\phi_{\mathrm{s,t}}$, in our experiments, with zeta (ζ) potential values (diamonds) for CsCl (red), RbCl (orange), NaCl (green) and LiCl (blue) aqueous solutions obtained from Ref. 15. **(b)** Comparison of measured $f_{\mathrm{M,ion}}/\, f_{\mathrm{M,Na}}$ values (triangles) with the values for $\zeta_{\mathrm{ion}}/\zeta_{\mathrm{Na}}$ (diamonds) for CsCl (red), RbCl (orange), NaCl (greean) and LiCl (blue) aqueos solutions reveal good mutual agreement in the trends.

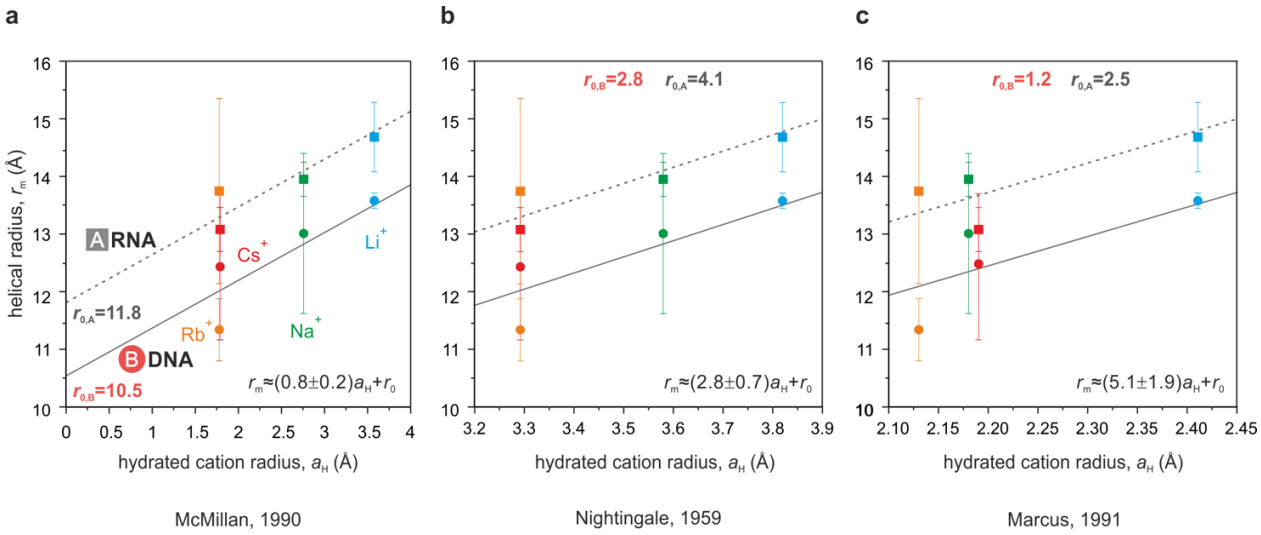


Figure S9. Dependence of the inferred r_m vs a_H relationship on the assumed values of the hydrated cationic radii, a_H. Values for a_H are taken from various sources: **(a)** Ref. 18. **(b)** Ref. 19. **(c)** Ref. 20

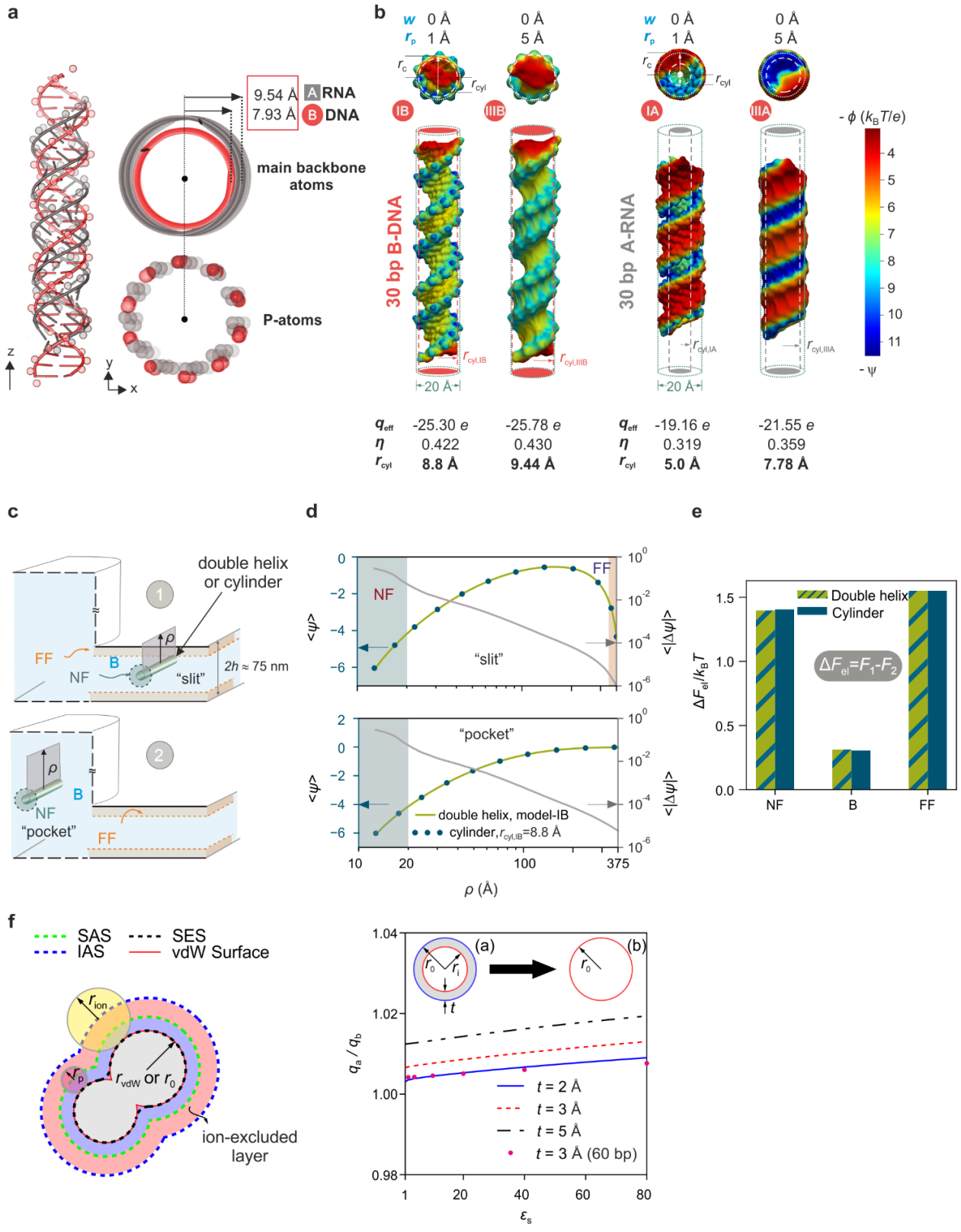


Figure S10. (a) Model structures of A-RNA (grey) and B-DNA (red) generated with the 3DNA platform[17] and visualized with Protein Imager[18] (left) and nglview[19] (right). Side view of the superimposed helices (left) and axial (top)-view down the principle axis of the model structures (right). 'Main backbone' atoms presented in ribbon form (top right) and phosphorous atoms as

spheres (bottom right). Mean backbone atom radii for A-RNA and B-DNA are 9.54 Å and 7.93 Å respectively, while the P atoms suggest a comparable average axial distance in both cases. **(b)** Impact of probe size, r_{p}, on the calculated effective charge, q_{eff}. For B-DNA, a larger probe smooths out the corrugations of the molecular surface but preserves its global structure resulting in a small change in the calculated effective charge (<2%). For A-RNA, an increase in probe radius can lead to the loss of the major groove which affects the effective charge substantially (>10%). **(c)** Analysis of calculated electrostatic free energies in a single electrostatic fluidic trap where state (1) represents the molecule in the slit and state (2) depicts a trapped molecule. NF denotes the electrostatic "near-field" in the vicinity of the molecule while FF defines a thin layer near the walls. The plane containing the axis of the molecule and perpendicular to the wall is used to calculate the average potentials in panel **d**. **(d)** Variations of the average potential, $\langle\psi\rangle$, vs axial distance, ρ, for a B-DNA (model-IB) and its corresponding cylindrical model (r_{cyl}=8.8 Å). The difference in average potential,$\langle|\Delta\psi|\rangle$, monotonically decreases with distance leading to almost identical average potential distributions for B-DNA and the cylinder in the "bulk" and in the "far-field" (ρ >2 nm). **(e)** Contributions of different regions to the total free energy difference for B-DNA (model-IB) and its equivalent cylindrical model ($r_{\mathrm{cyl}} = 8.8$ Å). The total free energy differences, and therefore magnitude of the effective charges, are mostly determined by the contributions from the NF and FF regions which make roughly equal contributions. **(f)** Left: Schematic representation of molecular surfaces. The grey region denotes the interior of the molecule, while the van der Waals surface (vdWS - red lines) and ion accessible surface (IAS - blue lines) display low dielectric regions inaccessible to water molecules and ions, respectively. The solvent accessible surface (SAS - green line) denotes the surface of closest approach of water molecules to the vdWS. The charge distribution outside the IAS is governed by the Boltzmann distribution. Right: Influence of a dielectric shell surrounding a charged cylinder on the calculated effective charge. We compare a cylinder of radius r_{i} =10 Å shielded by a dielectric layer of thickness, t, with a uniform dielectric constant, ε_{s}, yielding a calculated effective charge q_{a} (model (a)), with a hollow cylinder of radius, $r_0 = r_{\mathrm{i}} + t$, with no dielectric layer, described by a calculated effective charge q_{b} (model (b)). Cylinder lengths of 102 Å and 204 Å correspond to those for 30 bp and 60 bp B-DNA, respectively. Calculations were performed for c = 1 mM with the total charge $q_{\mathrm{str}} = -2\,ne$ uniformly distributed on the lateral surface of the cylinders (red) for 30 bp B-DNA (lines) and 60 bp B-DNA (pink circles). The ratio $q_{\mathrm{a}}/q_{\mathrm{b}}$ is of order 1% over a wide range of ε_{s} and t values suggesting that in the electrometry measurement, a hollow cylinder of radius $r_0 = r_{\mathrm{i}} + t$ is an excellent approximation to a charged cylinder of radius r_{i} surrounded by a dielectric shell of thickness t. Panels **(b)**, and **(d)-(f)** are reproduced from Ref. 31, with the permission of AIP Publishing.

	Molecule	Device	Buffer 1 mM Tris +	T (°C)	W (k_BT)	t_{esc} (s)	q_m (-e)	f_M	Structural parameters b_m (Å)	r_m (Å)
LiCl	**30bp DNA**	**2*h*=75.2 nm**	**1.23 mM LiCl, pH=9.0**	**22.8**	**4.226**	**52.3±0.3**	**25.28±0.07**			
	40bp DNA	**2*h*=75.2 nm**	**1.23 mM LiCl, pH=9.1**	**22.9**	**4.655**	**93.9±0.4**	**30.46±0.06**	0.86	3.3	13.7
	60bp DNA	***d*=167 nm**	**1.25 mM LiCl, pH=9.1**	**22.8**	**5.374**	**242.5±1.1**	**40.71±0.07**			
	30bp DNA		1.32 mM LiCl, pH=9.0	21.9	3.863	41.0±0.4	25.60±0.16			
	40bp DNA	2*h*=74.7 nm	1.32 mM LiCl, pH=9.0	22.2	4.312	69.2±1.0	31.08±0.22	0.89	3.2	13.4
	60bp DNA	*d*=146 nm	1.29 mM LiCl, pH=9.1	22.0	5.197	209.7±0.6	41.20±0.04			
	60bp DNA (1 dye)		1.29 mM LiCl, pH=9.1	22.0	5.151	203.4±2.1	40.79±0.15			
	30bp RNA	**2*h*=75.2 nm**	**1.23 mM LiCl, pH=8.9**	**22.5**	**4.099**	**46.3±0.2**	**23.86±0.04**			
	40bp RNA	**2*h*=75.2 nm**	**1.25 mM LiCl, pH=8.9**	**23.2**	**4.408**	**70.4±0.8**	**28.35±0.13**	0.87	2.7	14.7
	60bp RNA	***d*=167 nm**	**1.22 mM LiCl, pH=8.9**	**22.7**	**5.316**	**192.5±0.6**	**37.26±0.04**			
	30bp RNA		1.21 mM LiCl, pH=9.0	22.7	4.244	53.7±0.4	24.74±0.08			
	40bp RNA	2*h*=75.2 nm	1.20 mM LiCl, pH=9.1	22.8	4.645	82.6±0.1	29.08±0.02	0.95	2.5	13.6
	60bp RNA	*d*=167 nm	1.20 mM LiCl, pH=9.1	22.8	5.422	210.6±0.9	37.96±0.06			
	60bp RNA (1 dye)		1.20 mM LiCl, pH=9.0	22.8	5.277	185.1±1.7	37.60±0.13			
	30bp RNA		1.25 mM LiCl, pH=9.0	22.5	4.183	50.2±0.1	25.63±0.03			
	40bp RNA	2*h*=75.2 nm	1.25 mM LiCl, pH=9.0	22.3	4.569	80.0±0.2	30.33±0.03	0.93	2.5	15.7
	60bp RNA	*d*=167 nm	1.24 mM LiCl, pH=9.1	21.9	5.367	207.2±1.0	39.60±0.06			
	60bp RNA (1 dye)		1.25 mM LiCl, pH=9.1	22.6	5.311	187.1±2.1	39.20±0.15			
NaCl	**30bp DNA**	**2*h*=74.7 nm**	**1.25 mM NaCl, pH=9.1**	**22.0**	**4.104**	**50.2±0.2**	**25.77±0.05**			
	40bp DNA	**2*h*=74.7 nm**	**1.24 mM NaCl, pH=9.2**	**22.0**	**4.602**	**94.0±1.0**	**31.06±0.14**	0.96	3.0	11.8
	60bp DNA	***d*=146 nm**	**1.25 mM NaCl, pH=9.2**	**22.3**	**5.396**	**256.4±0.9**	**41.09±0.04**			
	60bp DNA (1 dye)		**1.25 mM NaCl, pH=9.2**	**22.5**	**5.364**	**247.1±1.9**	**40.69±0.10**			
	30bp DNA	2*h*=74.7 nm	1.24 mM NaCl, pH=9.0	22.1	4.324	61.2±0.5	27.57±0.12			
	40bp DNA	*d*=146 nm	1.22 mM NaCl, pH=9.0	21.8	4.863	116.6±0.4	33.11±0.04	0.98	3.1	13.0
	60bp DNA		1.22 mM NaCl, pH=9.1	21.7	5.790	357.8±0.9	43.91±0.03			
	30bp DNA		1.10 mM NaCl, pH=9.1	21.7	4.800	93.2±1.1	26.61±0.12			
	40bp DNA	2*h*=74.7 nm	1.12 mM NaCl, pH=9.1	21.7	5.276	173.4±0.8	32.08±0.05	1.03	3.0	10.4
	60bp DNA	*d*=146 nm	1.28 mM NaCl, pH=9.1	21.9	5.350	250.1±0.7	42.54±0.04			
	60bp DNA (1 dye)		1.29 mM NaCl, pH=9.0	22.0	5.309	229.4±1.7	42.01±0.10			
	30bp DNA	2*h*=73.8 nm	1.30 mM NaCl, pH=9.1	22.7	4.154	31.9±0.1	26.19±0.02			
	40bp DNA	*d*=157 nm	1.30 mM NaCl, pH=9.2	23.0	4.589	54.1±0.2	31.49±0.07	0.85	3.1	16.9
	60bp DNA		1.31 mM NaCl, pH=9.1	22.9	5.358	141.2±0.9	41.81±0.09			
	30bp RNA	**2*h*=71.5 nm**	**1.26 mM NaCl, pH=9.1**	**22.2**	**4.622**	**45.6±0.2**	**26.46±0.06**			
	40bp RNA	**2*h*=71.5 nm**	**1.27 mM NaCl, pH=9.1**	**22.2**	**5.057**	**77.9±0.9**	**31.34±0.14**	1.04	2.4	13.5
	60bp RNA	***d*=150 nm**	**1.29 mM NaCl, pH=9.2**	**22.2**	**5.800**	**183.3±1.0**	**40.69±0.07**			
	30bp RNA		1.17 mM NaCl, pH=9.1	22.5	4.230	50.3±0.8	23.85±0.17			
	40bp RNA	2*h*=74.7 nm	1.17 mM NaCl, pH=9.1	22.6	4.657	86.3±0.9	28.48±0.12	0.93	2.4	13.9
	60bp RNA	*d*=146 nm	1.23 mM NaCl, pH=9.1	22.5	5.137	163.7±0.4	36.79±0.04			
	60bp RNA (1 dye)		1.23 mM NaCl, pH=9.1	22.7	5.077	152.1±1.2	36.34±0.10			
	30bp RNA	2*h*=73.8 nm	1.29 mM NaCl, pH=9.1	24.1	4.039	25.2±0.1	24.31±0.06			
	40bp RNA	*d*=157 nm	1.28 mM NaCl, pH=9.2	23.9	4.438	42.8±0.3	28.83±0.07	0.93	2.4	14.5
	60bp RNA		1.28 mM NaCl, pH=9.2	23.6	5.150	98.7±0.2	37.40±0.03			
RbCl	**30bp DNA**	**2*h*=76.6 nm**	**1.26 mM RbCl, pH=9.0**	**22.6**	**4.162**	**48.2±0.6**	**26.67±0.16**			
	40bp DNA	**2*h*=76.6 nm**	**1.26 mM RbCl, pH=8.9**	**22.6**	**4.549**	**83.2±1.7**	**31.94±0.34**	1.01	3.1	10.7
	60bp DNA	***d*=186 nm**	**1.26 mM RbCl, pH=8.9**	**22.8**	**5.369**	**240.1±1.0**	**42.65±0.06**			
	30bp DNA	2*h*=76.6 nm	1.21 mM RbCl, pH=8.8	22.9	4.210	50.6±0.7	25.30±0.21			
	40bp DNA	*d*=186 nm	1.22 mM RbCl, pH=8.9	22.8	4.613	89.8±0.8	30.41±0.10	0.90	3.2	12.4
	60bp DNA		1.20 mM RbCl, pH=8.9	22.9	5.500	271.3±1.7	40.45±0.08			
	* 30bp DNA	2*h*=76.6 nm	1.25 mM RbCl, pH=8.9	23.1	3.705	32.1±0.2	20.30±0.08			
	40bp DNA	*d*=186 nm	1.25 mM RbCl, pH=9.0	22.9	4.072	54.8±0.1	24.19±0.02	0.77	3.0	10.9
	60bp DNA		1.25 mM RbCl, pH=9.0	22.7	4.789	133.2±0.7	32.17±0.07			
	* **30bp RNA**	**2*h*=76.6 nm**	**1.19 mM RbCl, pH=8.9**	**22.1**	**3.897**	**36.1±0.6**	**20.67±0.05**			
	40bp RNA	**2*h*=76.6 nm**	**1.20 mM RbCl, pH=8.9**	**22.1**	**4.212**	**55.0±0.5**	**24.44±0.10**	0.86	2.4	11.2
	60bp RNA	***d*=186 nm**	**1.21 mM RbCl, pH=8.9**	**22.5**	**4.853**	**120.9±0.4**	**31.78±0.06**			
	30bp RNA	2*h*=76.6 nm	1.23 mM RbCl, pH=8.9	22.8	4.068	43.3±1.9	24.37±0.54			
	40bp RNA	*d*=186 nm	1.22 mM RbCl, pH=9.0	22.2	4.477	70.9±2.9	28.84±0.53	0.92	2.6	13.3
	60bp RNA		1.22 mM RbCl, pH=9.0	22.5	5.132	165.0±0.5	37.46±0.04			
	* 30bp RNA	2*h*=76.6 nm	1.22 mM RbCl, pH=8.9	22.4	3.711	30.3±0.6	19.87±0.05			
	40bp RNA	*d*=186 nm	1.21 mM RbCl, pH=9.0	22.7	4.105	40.9±0.5	23.44±0.12	0.71	2.5	16.7
	60bp RNA		1.21 mM RbCl, pH=8.9	22.4	4.697	111.5±0.2	30.57±0.04			

Table continued from previous page

	Molecule	Device	Buffer 1 mM Tris +	T (°C)	W (k_BT)	t_{esc} (s)	q_m (-e)	f_M	Structural parameters b_m (Å)	r_m (Å)
CsCl	*** 30bp DNA**	**2*h*=73.4 nm *d*=144 nm**	**1.22 mM CsCl, pH=9.0**	**23.7**	**4.006**	**45.2±0.6**	**21.52±0.13**			
	40bp DNA		**1.22 mM CsCl, pH=9.0**	**23.7**	**4.477**	**78.8±0.6**	**25.94±0.08**	0.81	**3.2**	**10.4**
	60bp DNA		**1.22 mM CsCl, pH=9.0**	**23.7**	**5.433**	**267.3±1.1**	**34.55±0.05**			
	* 30bp DNA	2*h*=76.6 nm *d*=186 nm	1.20 mM CsCl, pH=8.9	22.8	3.414	25.2±0.1	15.53±0.06			
	40bp DNA		1.20 mM CsCl, pH=8.9	22.8	3.707	40.1±0.1	18.43±0.01	0.55	3.3	12.2
	60bp DNA		1.19 mM CsCl, pH=8.9	22.4	4.386	96.6±0.9	24.82±0.11			
	* 30bp DNA	2*h*=76.6 nm *d*=186 nm	1.21 mM CsCl, pH=8.9	23.0	3.664	29.5±0.4	18.62±0.20			
	40bp DNA		1.21 mM CsCl, pH=8.8	22.9	4.031	49.8±0.2	22.48±0.05	0.64	3.1	14.7
	60bp DNA		1.21 mM CsCl, pH=8.9	22.5	4.755	129.1±0.6	29.78±0.05			
	*** 30bp RNA**	**2*h*=76.6 nm *d*=186 nm**	**1.20 mM CsCl, pH=9.0**	**22.8**	**3.538**	**26.7±0.3**	**16.95±0.15**			
	40bp RNA		**1.20 mM CsCl, pH=9.0**	**22.6**	**3.839**	**39.9±0.1**	**20.08±0.04**	0.66	**2.6**	**12.5**
	60bp RNA		**1.18 mM CsCl, pH=9.1**	**23.0**	**4.486**	**89.3±0.2**	**26.26±0.04**			
	* 30bp RNA	2*h*=76.6 nm *d*=186 nm	1.20 mM CsCl, pH=8.9	22.7	3.442	24.9±0.1	16.09±0.05			
	40bp RNA		1.20 mM CsCl, pH=9.0	22.9	3.749	36.7±0.2	19.15±0.08	0.63	2.5	13.0
	60bp RNA		1.19 mM CsCl, pH=9.0	22.9	4.333	80.8±0.6	24.90±0.10			
	* 30bp RNA	2*h*=75.2 nm *d*=167 nm	1.11 mM CsCl, pH=9.0	23.1	4.377	56.8±0.5	22.17±0.09			
	40bp RNA		1.12 mM CsCl, pH=9.0	22.8	4.782	95.1±1.4	26.17±0.15	0.83	2.6	13.8
	60bp RNA		1.12 mM CsCl, pH=9.0	22.8	5.687	266.7±0.9	34.24±0.04			

Table S1. Experimental details on all r and b measurements. DNA datasets are highlighted in red. The measured b-r probability manifolds and inferred b_m and r_m values for datasets denoted in boldface are shown in Fig. S7. Datasets labeled with * were analyzed including the rotational free energy term, ΔF_{rot} (see section S2.2).

References

(1) Ruggeri, F.; Zosel, F.; Mutter, N.; Rozycka, M.; Wojtas, M.; Ozyhar, A.; Schuler, B.; Krishnan, M. Single-molecule electrometry. *Nature Nanotechnology* **2017**, *12* (5), 488-495. DOI: 10.1038/nnano.2017.26.
(2) Ruggeri, F.; Krishnan, M. Lattice diffusion of a single molecule in solution. *Physical Review E* **2017**, *96* (6), 062406. DOI: 10.1103/PhysRevE.96.062406.
(3) Demarest, S. J.; Martinez-Yamout, M.; Chung, J.; Chen, H. W.; Xu, W.; Dyson, H. J.; Evans, R. M.; Wright, P. E. Mutual synergistic folding in recruitment of CBP/p300 by p160 nuclear receptor coactivators. *Nature* **2002**, *415* (6871), 549-553. DOI: 10.1038/415549a.
(4) Borgia, A.; Zheng, W. W.; Buholzer, K.; Borgia, M. B.; Schuler, A.; Hofmann, H.; Soranno, A.; Nettels, D.; Gast, K.; Grishaev, A.; et al. Consistent View of Polypeptide Chain Expansion in Chemical Denaturants from Multiple Experimental Methods. *Journal of the American Chemical Society* **2016**, *138* (36), 11714-11726. DOI: 10.1021/jacs.6b05917.
(5) Tirado, M. M.; Garciadelatorre, J. Translational friction coefficients of rigid, symmetric top macromolecules. Application to circular cylinders. *Journal of Chemical Physics* **1979**, *71* (6), 2581-2587. DOI: 10.1063/1.438613. Tirado, M. M.; Martinez, C. L.; Delatorre, J. G. Comparison of theories for the translational and rotational diffusion coefficients of rod-like macromolecules. Application to short DNA fragments. *Journal of Chemical Physics* **1984**, *81* (4), 2047-2052. DOI: 10.1063/1.447827.
(6) Odijk, T. Polyelectrolytes near the rod limit. *Journal of Polymer Science Part B-Polymer Physics* **1977**, *15* (3), 477-483. DOI: 10.1002/pol.1977.180150307. Skolnick, J.; Fixman, M. Electrostatic Persistence Length of a Wormlike Polyelectrolyte. *Macromolecules* **1977**, *10* (5), 944-948. DOI: 10.1021/ma60059a011.
(7) Kovacic, R. T.; Vanholde, K. E. Sedimentation of Homogeneous Double-Strand DNA Molecules. *Biochemistry* **1977**, *16* (7), 1490-1498. DOI: 10.1021/bi00626a038. Kapahnke, R.; Rappold, W.; Desselberger, U.; Riesner, D. The stiffness of dsRNA: hydrodynamic studies on fluorescence-labelled RNA segments of bovine rotavirus. *Nucleic Acids Research* **1986**, *14* (8), 3215-3228. DOI: 10.1093/nar/14.8.3215.
(8) Kramers, H. A. Brownian motion in a field of force and the diffusion model of chemical reactions. *Physica* **1940**, *7*, 284-304. DOI: 10.1016/s0031-8914(40)90098-2.
(9) Krishnan, M. A simple model for electrical charge in globular macromolecules and linear polyelectrolytes in solution. *Journal of Chemical Physics* **2017**, *146* (20), 205101. DOI: 10.1063/1.4983485.
(10) Ruggeri, F.; Krishnan, M. Entropic Trapping of a Singly Charged Molecule in Solution. *Nano Letters* **2018**, *18* (6), 3773-3779. DOI: 10.1021/acs.nanolett.8b01011.
(11) Brown, M. A.; Bossa, G. V.; May, S. Emergence of a Stern Layer from the Incorporation of Hydration Interactions into the Gouy-Chapman Model of the Electrical Double Layer. *Langmuir* **2015**, *31* (42), 11477-11483. DOI: 10.1021/acs.langmuir.5b02389.
(12) Franks, G. V. Zeta potentials and yield stresses of silica suspensions in concentrated monovalent electrolytes: Isoelectric point shift and additional attraction. *Journal of Colloid and Interface Science* **2002**, *249* (1), 44-51. DOI: 10.1006/jcis.2002.8250. Redondo, A. B.; Jordan, I.; Ziazadeh, I.; Kleibert, A.; Giorgi, J. B.; Worner, H. J.; May, S.; Abbas, Z.; Brown, M. A. Nanoparticle-Induced Charge Redistribution of the Air-Water Interface. *Journal of Physical Chemistry C* **2015**, *119* (5), 2661-2668. DOI: 10.1021/jp511915b.
(13) Darlington, A. M.; Gibbs-Davis, J. M. Bimodal or Trimodal? The Influence of Starting pH on Site Identity and Distribution at the Low Salt Aqueous/Silica Interface. *Journal of Physical Chemistry C* **2015**, *119* (29), 16560-16567. DOI: 10.1021/acs.jpcc.5b02480.
(14) Pau, P. C. F.; Berg, J. O.; McMillan, W. G. Application of Stokes' law to ions in aqueous solution. *Journal of Physical Chemistry* **1990**, *94* (6), 2671-2679. DOI: 10.1021/j100369a080.
(15) Nightingale, E. R. Phenomenological Theory of Ion Solvation. Effective Radii of Hydrated Ions. *Journal of Physical Chemistry* **1959**, *63* (9), 1381-1387. DOI: 10.1021/j150579a011.
(16) Marcus, Y. Thermodynamics of solvation of ions. Part 5.—Gibbs free energy of hydration at 298.15 K. *Journal of the Chemical Society-Faraday Transactions* **1991**, *87* (18), 2995-2999. DOI: 10.1039/ft9918702995.
(17) Li, S. X.; Olson, W. K.; Lu, X. J. Web 3DNA 2.0 for the analysis, visualization, and modeling of 3D nucleic acid structures. *Nucleic Acids Research* **2019**, *47* (W1), W26-W34. DOI: 10.1093/nar/gkz394.
(18) Tomasello, G.; Armenia, I.; Molla, G. The Protein Imager: a full-featured online molecular viewer interface with server-side HQ-rendering capabilities. *Bioinformatics* **2020**, *36* (9), 2909-2911. DOI: 10.1093/bioinformatics/btaa009.
(19) Nguyen, H.; Case, D. A.; Rose, A. S. NGLview-interactive molecular graphics for Jupyter notebooks. *Bioinformatics* **2018**, *34* (7), 1241-1242. DOI: 10.1093/bioinformatics/btx789.
(20) Overbeek, J. T. G. The role of energy and entropy in the electrical double layer. *Colloids and Surfaces* **1990**, *51*, 61-75.
(21) Krishnan, M. Electrostatic free energy for a confined nanoscale object in a fluid. *Journal of Chemical Physics* **2013**, *138* (11), 114906. DOI: 10.1063/1.4795087.
(22) Lee, B.; Richards, F. M. The interpretation of protein structures: estimation of static accessibility. *Journal of Molecular Biology* **1971**, *55* (3), 379-400. DOI: 10.1016/0022-2836(71)90324-x. Richards, F. M. Areas, volumes,

packing, and protein structure. *Annual Review of Biophysics and Bioengineering* **1977**, *6*, 151-176. DOI: 10.1146/annurev.bb.06.060177.001055. Connolly, M. L. Analytical molecular surface calculation. *Journal of Applied Crystallography* **1983**, *16* (OCT), 548-558. DOI: 10.1107/s0021889883010985. Richmond, T. J. Solvent accessible surface area and excluded volume in proteins: Analytical equations for overlapping spheres and implications for the hydrophobic effect. *Journal of Molecular Biology* **1984**, *178* (1), 63-89. DOI: 10.1016/0022-2836(84)90231-6.
(23) Sanner, M. F.; Olson, A. J.; Spehner, J. C. Reduced surface: An efficient way to compute molecular surfaces. *Biopolymers* **1996**, *38* (3), 305-320. DOI: 10.1002/(sici)1097-0282(199603)38:3<305::aid-bip4>3.0.co;2-y.
(24) Pettersen, E. F.; Goddard, T. D.; Huang, C. C.; Couch, G. S.; Greenblatt, D. M.; Meng, E. C.; Ferrin, T. E. UCSF chimera - A visualization system for exploratory research and analysis. *Journal of Computational Chemistry* **2004**, *25* (13), 1605-1612. DOI: 10.1002/jcc.20084.
(25) Lu, X. J.; Olson, W. K. 3DNA: a software package for the analysis, rebuilding and visualization of three-dimensional nucleic acid structures. *Nucleic Acids Research* **2003**, *31* (17), 5108-5121. DOI: 10.1093/nar/gkg680.
(26) Tsai, J.; Taylor, R.; Chothia, C.; Gerstein, M. The packing density in proteins: Standard radii and volumes. *Journal of Molecular Biology* **1999**, *290* (1), 253-266. DOI: 10.1006/jmbi.1999.2829.
(27) Geuzaine, C.; Remacle, J. F. Gmsh: A 3-D finite element mesh generator with built-in pre- and post-processing facilities. *International Journal for Numerical Methods in Engineering* **2009**, *79* (11), 1309-1331. DOI: 10.1002/nme.2579.
(28) Martin S. Alnæs, J. B., Johan Hake, August Johansson, Benjamin Kehlet, Anders Logg, Chris Richardson, Johannes Ring, Marie E. Rognes, and Garth N. Wells. The FEniCS Project Version 1.5. *Archive of Numerical Software* **2015**, *3* (100), 9-23.
(29) Kirmizialtin, S.; Silalahi, A. R. J.; Elber, R.; Fenley, M. O. The Ionic Atmosphere around A-RNA: Poisson-Boltzmann and Molecular Dynamics Simulations. *Biophysical Journal* **2012**, *102* (4), 829-838. DOI: 10.1016/j.bpj.2011.12.055.
(30) Borukhov, I.; Andelman, D.; Orland, H. Steric effects in electrolytes: A modified Poisson-Boltzmann equation. *Physical Review Letters* **1997**, *79* (3), 435-438. DOI: 10.1103/PhysRevLett.79.435.
(31) Behjatian, A.; Krishnan, M. Electrostatic free energies carry structural information on nucleic acid molecules in solution. *Journal of Chemical Physics* **2022**, *156* (13). DOI: 10.1063/5.0080008.

6
Conclusions

In this Thesis, we have demonstrated how an electrostatic fluidic trap can serve as a powerful tool for various applications: from probing the electrical properties of particles, molecules, and nanoslit surfaces to solving the problems of structural biology and looking into the structure of molecular interface in solution. We have also discussed the current limitations of the technique and described the steps taken to address the challenge of extending the capabilities of the method. Below we briefly describe the main achievements of this work and outline the possible trends for further development and applicability of the electrostatic fluidic trapping approach.

In Chapter 3, we have demonstrated the applicability of an electrostatic fluidic trap for confining objects in solvents of different polarities. Our measurements clearly show the presence of significant repulsive forces enough for electrostatic trapping even in low-polar and apolar media. Though in this work we have focused on trapping particles, the same principles may be applied for single-molecule trapping and measuring in low-polar and/or apolar organic solvents. Although organic media is not a native environment for biological macromolecules, the ability to explore the properties of biomolecules in pure organic solvents or solvent mixtures is of great interest and use for fundamental biochemical studies and biotechnological applications [119][120][121][122]. In conjunction with molecular and interfacial structural measurements described in Chapter 5, single-molecule

trapping in organic solvents or solvent mixtures provides a prospective platform for research in non-aqueous enzymology or protein bioengineering. Examples of prospective studies include but are not limited to studying the correlation between enzyme stability/activity and the nature of solvent, investigating the solvent effect on protein (un-)folding, or exploring the effect of water/alcohol mixtures mimicking membrane environment on proteins or peptides [123][124][125].

Besides that, Chapter 3 presents a new approach for measuring the net surface charge density of ionizable surfaces based on electrostatic fluidic trapping. This method is highly versatile, does not require the use of any external electric fields, and can be applied to any solvent and solvent mixture if they are compatible with our system, i.e., compatible with glass and silicon dioxide, and can be loaded into nanoslits.

In Chapter 4, we have explored the applicability of nanostructured charged lipid bilayer systems for single-molecule electrostatic trapping. We have shown that passivation of glass/SiO_2 nanoslits of trapping devices with lipid bilayer coatings makes it possible to trap and measure single molecules in non-buffered aqueous solutions (pH 5-6). In contrast to standard glass/SiO_2 devices, lipid bilayer-coated devices enable experiments with molecules that are not resistant to alkaline conditions. Moreover, trapping of positively charged molecules in a system of positively charged lipid bilayers can be the next step in expanding the capabilities of an electrostatic fluidic trap.

Nevertheless, despite all the advantages provided by charged lipid bilayers, we found it difficult to control the charge composition, and consequently the surface electrical potential, of formed SLBs in the nanoslits. Hence, the applicability of other materials for trapping devices is worth exploring. For trapping of negatively charged molecules, anionic polymers, e.g., polyethylene glycol (PEG), or oxides with the points of zero charge, pzc$\approx$1-1.5, e.g., WO_3 and V_2O_5, can probably provide a good alternative to SiO_2 [126]. For positively charged molecules, the applicability of cationic polymers, e.g., polyethyleneimine (PEI) or poly-L-lysine (PLL), or oxides with pzc$\geqslant$9, e.g., Al_2O_3, PbO, ZnO, CdO, can be explored [126].

Finally, in Chapter 5, which is the culmination of this work, we demonstrated the ability of precise measurements of electrostatic interactions to reveal both the structure and the interface of a molecular species in solution. Working with A- and B-form nucleic acid double helices we determined the values for the helical rise per basepair and the helical radius with ~ 0.1Å and ~ 1Å precision respectively. Such precision is comparable with that of well-established structural biology techniques, such as Nuclear Magnetic Resonance (NMR) or crystallography. However, in contrast to NMR or crystallography, our approach does not require any laborious sample preparation, such as crystallisation or isotope labelling. Furthermore, the combination of ET*e* with molecular structural modelling sheds light on the contact region between a molecule and an electrolyte, providing insights into the structure of the Stern layer. While there are prior studies devoted to probing the structure of solid-liquid interface for macroscopic surfaces, our approach can probe the interface of a *molecule* in solution [49][65]. These experiments serve as proof-of-principle that high-precision q_{eff} measurements can yield information on the structural features of a biomolecule and its interface in solution.

The results of this work carry broad implications for the use of ET*e* in structural biology providing a new tool for rapid and non-destructive solution-phase characterisation of biomolecular structures. Furthermore, we hope that in the future, by analysing the trajectory of an individual molecule in a lattice of electrostatic traps, we can track its structural fluctuations over time. That provides a great platform for studying, for example, protein (un-)folding or enzyme catalysis. Another perspective application of the ET*e* approach is a *charge spectrometry* technique for studying the mixtures of chemically similar yet structurally/conformationally distinct states of a molecular species, as described in Section 5.2.

References

[1] M. Krishnan, N. Mojarad, P. Kukura, V. Sandoghdar, *Nature* **2010**, *467*, 692–695.

[2] N. Mojarad, M. Krishnan, *Nature Nanotechnology* **2012**, *7*, 448–452.

[3] F. Ruggeri, F. Zosel, N. Mutter, M. Rozycka, M. Wojtas, A. Ozyhar, B. Schuler, M. Krishnan, *Nature Nanotechnology* **2017**, *12*, 488–495.

[4] F. Ruggeri, M. Krishnan, *Physical Review E* **2017**, *96*, 062406.

[5] F. Ruggeri, M. Krishnan, *Nano Letters* **2018**, *18*, 3773–3779.

[6] F. Ruggeri, M. Krishnan, *Journal of Chemical Physics* **2018**, *148*, 123307.

[7] G. Kokot, M. I. Bespalova, M. Krishnan, *Journal of Chemical Physics* **2016**, *145*, 194701.

[8] M. Bespalova, R. Öz, F. Westerlund, M. Krishnan, *Langmuir* **2022**, *Advance online publication.*

[9] M. Krishnan, *Journal of Chemical Physics* **2017**, *146*, 205101.

[10] M. Bespalova, A. Behjatian, N. Karedla, R. Walker-Gibbons, M. Krishnan, *Macromolecules* **2022**, *55*, 6200–6210.

[11] J. P. Taylor, J. Hardy, K. H. Fischbeck, *Science* **2002**, *296*, 1991–1995.

[12] P. Guptasarma, *Bioessays* **1995**, *17*, 987–997.

[13] M. Bon, S. J. McGowan, P. R. Cook, *Faseb Journal* **2006**, *20*, 1721–1723.

[14] F. Kulzer, T. Xia, M. Orrit, *Angewandte Chemie-International Edition* **2010**, *49*, 854–866.

[15] F. Secundo, *Chemical Society Reviews* **2013**, *42*, 6250–6261.

[16] S. H. Behrens, D. G. Grier, *Journal of Chemical Physics* **2001**, *115*, 6716–6721.

[17] B. W. Ninham, V. A. Parsegian, *Journal of Theoretical Biology* **1971**, *31*, 405–428.

[18] F. Rossotti, H. Rossotti, *The Determination of Stability Constants and Other Equilibrium Constants in Solution*, McGraw-Hill Book Compony, Inc., **1961**.

[19] M. Lund, B. Jonsson, *Quarterly Reviews of Biophysics* **2013**, *46*, 265–281.

[20] G. S. Manning, *Journal of Chemical Physics* **1969**, *51*, 924–933.

[21] G. S. Manning, *Quarterly Reviews of Biophysics* **1978**, *11*, 179–246.

[22] R. R. Netz, H. Orland, *European Physical Journal E* **2003**, *11*, 301–311.

[23] G. S. Manning, *Macromolecules* **2007**, *40*, 8071–8081.

[24] H. A. Kramers, *Physica* **1940**, *7*, 284–304.

[25] M. Krishnan, *Journal of Chemical Physics* **2013**, *138*, 114906.

[26] M. I. Bespalova, S. Mahanta, M. Krishnan, *Current Opinion in Chemical Biology* **2019**, *51*, 113–121.

[27] D. Li, *Electrokinetics in Microfluidics*, Academic Press, **2004**.

[28] J. N. Israelachvili, *Intermolecular and Surface Forces*, 3rd, Academic Press, **2011**.

[29] E. Verwey, J. Overbeek, *Theory of the Stability of Lyophobic Colloids*, Elsevier, Amsterdam, **1948**.

[30] B. Derjaguin, L. Landau, *Acta Physicochimica U.R.S.S.* **1941**, *14*, 633–662.

[31] G. Ledet, T. Mandal, *US Pharm.* **2012**, *37*, 7–11.

[32] I. D. Morrison, *Colloids and Surfaces a-Physicochemical and Engineering Aspects* **1993**, *71*, 1–37.

[33] M. M. Gacek, J. C. Berg, *Electrophoresis* **2014**, *35*, 1766–1772.

[34] S. A. Jones, G. P. Martin, M. B. Brown, *Journal of Pharmaceutical Sciences* **2006**, *95*, 1060–1074.

[35] B. Comiskey, J. D. Albert, H. Yoshizawa, J. Jacobson, *Nature* **1998**, *394*, 253–255.

[36] D. C. Grahame, *Chemical Reviews* **1947**, *41*, 441–501.

[37] H. Ohshima, T. W. Healy, L. R. White, *Journal of Colloid and Interface Science* **1982**, *90*, 17–26.

[38] A. V. Delgado, F. Gonzalez-Caballero, R. J. Hunter, L. K. Koopal, J. Lyklema, *Journal of Colloid and Interface Science* **2007**, *309*, 194–224.

[39] S. Mohammadi-Jam, K. Waters, R. Greenwood, *Advances in Colloid and Interface Science* **2022**, *309*, 102778.

[40] F. H. J. van der Heyden, D. Stein, C. Dekker, *Physical Review Letters* **2005**, *95*, 116104.

[41] J. Lyklema, *Colloids and Surfaces a-Physicochemical and Engineering Aspects* **2011**, *376*, 2–8.

[42] D. Stein, M. Kruithof, C. Dekker, *Physical Review Letters* **2004**, *93*, 035901.

[43] D. C. Martins, V. Chu, J. P. Conde, *Biomicrofluidics* **2013**, *7*, 034111.

[44] R. B. Schoch, H. van Lintel, P. Renaud, *Physics of Fluids* **2005**, *17*, 100604.

[45] Y. Ma, Y. S. Su, S. Z. Qian, L. H. Yeh, *Sensors and Actuators B-Chemical* **2017**, *247*, 697–705.

[46] Y. Green, *Physical Review Fluids* **2022**, *7*, 013702.

[47] J. Lutzenkirchen, T. Preocanin, D. Kovacevic, V. Tomisic, L. Lovgren, N. Kallay, *Croatica Chemica Acta* **2012**, *85*, 391–417.

[48] W. A. Ducker, T. J. Senden, R. M. Pashley, *Nature* **1991**, *353*, 239–241.

[49] I. Siretanu, D. Ebeling, M. P. Andersson, S. L. S. Stipp, A. Philipse, M. C. Stuart, D. van den Ende, F. Mugele, *Scientific Reports* **2014**, *4*, 4956.

[50] K. Kurihara, *Pure and Applied Chemistry* **2019**, *91*, 707–716.

[51] P. A. Covert, D. K. Hore, *Annual Review of Physical Chemistry Vol 67* **2016**, *67*, 233–257.

[52] J. Schaefer, G. Gonella, M. Bonn, E. H. G. Backus, *Physical Chemistry Chemical Physics* **2017**, *19*, 16875–16880.

[53] C. S. Tian, Y. R. Shen, *Surface Science Reports* **2014**, *69*, 105–131.

[54] K. A. Lovering, A. K. Bertram, K. C. Chou, *Journal of Physical Chemistry C* **2016**, *120*, 18099–18104.

[55] S. W. Ong, X. L. Zhao, K. B. Eisenthal, *Chemical Physics Letters* **1992**, *191*, 327–335.

[56] E. C. Y. Yan, Y. Liu, K. B. Eisenthal, *Journal of Physical Chemistry B* **1998**, *102*, 6331–6336.

[57] C. Lutgebaucks, G. Gonella, S. Roke, *Physical Review B* **2016**, *94*, 195410.

[58] A. M. Darlington, J. M. Gibbs-Davis, *Journal of Physical Chemistry C* **2015**, *119*, 16560–16567.

[59] H. G. Steinruck, C. T. Cao, Y. Tsao, C. J. Takacs, O. Konovalov, J. Vatamanu, O. Borodin, M. F. Toney, *Energy Environmental Science* **2018**, *11*, 996–996.

[60] P. Fenter, C. Park, K. L. Nagy, N. C. Sturchio, *Thin Solid Films* **2007**, *515*, 5654–5659.

[61] S. ben Jabrallah, F. Malloggi, L. Belloni, L. Girard, D. Novikov, C. Mocuta, D. Thiaudiere, J. Daillant, *Physical Chemistry Chemical Physics* **2017**, *19*, 167–174.

[62] M. Brucher, P. Jacob, A. von Bohlen, J. Franzke, C. Sternemann, M. Paulus, R. Hergenroder, *Langmuir* **2010**, *26*, 959–966.

[63] S. S. Lee, F. Heberling, N. C. Sturchio, P. J. Eng, P. Fenter, *Journal of Physical Chemistry C* **2016**, *120*, 15216–15223.

[64] M. A. Brown, A. B. Redondo, M. Sterrer, B. Winter, G. Pacchioni, Z. Abbas, J. A. van Bokhoven, *Nano Letters* **2013**, *13*, 5403–5407.

[65] M. A. Brown, Z. Abbas, A. Kleibert, R. G. Green, A. Goel, S. May, T. M. Squires, *Physical Review X* **2016**, *6*, 011007.

[66] M. Oivanen, S. Kuusela, H. Lonnberg, *Chemical Reviews* **1998**, *98*, 961–990.

[67] K. Talley, E. Alexov, *Proteins-Structure Function and Bioinformatics* **2010**, *78*, 2699–2706.

[68] P. Jonsson, M. P. Jonsson, F. Hook, *Nano Letters* **2010**, *10*, 1900–1906.

[69] F. Persson, J. Fritzsche, K. U. Mir, M. Modesti, F. Westerlund, J. O. Tegenfeldt, *Nano Letters* **2012**, *12*, 2260–2265.

[70] A. A. Brian, H. M. McConnell, *PNAS* **1984**, *81*, 6159–6163.

[71] Y. H. M. Chan, S. G. Boxer, *Current Opinion in Chemical Biology* **2007**, *11*, 581–587.

[72] E. Reimhult, M. K. Baumann, S. Kaufmann, K. Kumar, P. R. Spycher, *Biotechnology and Genetic Engineering Reviews* **2010**, *27*, 185–216.

[73] S. Mashaghi, T. Jadidi, G. Koenderink, A. Mashaghi, *International Journal of Molecular Sciences* **2013**, *14*, 4242–4282.

[74] L. K. Tamm, H. M. McConnell, *Biophysical Journal* **1985**, *47*, 105–113.

[75] E. Sackmann, *Science* **1996**, *271*, 43–48.

[76] W. Romer, Y. H. Lam, D. Fischer, A. Watts, W. B. Fischer, P. Goring, R. B. Wehrspohn, U. Gosele, C. Steinem, *Journal of the American Chemical Society* **2004**, *126*, 16267–16274.

[77] E. Sackmann, M. Tanaka, *Trends in Biotechnology* **2000**, *18*, 58–64.

[78] E. K. Sinner, W. Knoll, *Current Opinion in Chemical Biology* **2001**, *5*, 705–711.

[79] J. Bompard, O. Maniti, R. Aboukhachfe, D. Ausserre, A. Girard-Egrot, *Langmuir* **2021**, *37*, 9457–9471.

[80] B. Raguse, V. Braach-Maksvytis, B. A. Cornell, L. G. King, P. D. J. Osman, R. J. Pace, L. Wieczorek, *Langmuir* **1998**, *14*, 648–659.

[81] J. Kurniawan, J. F. V. de Souza, A. T. Dang, G. Y. Liu, T. L. Kuhl, *Langmuir* **2018**, *34*, 15622–15639.

[82] U. Mennicke, T. Salditt, *Langmuir* **2002**, *18*, 8172–8177.

[83] A. C. Simonsen, L. A. Bagatolli, *Langmuir* **2004**, *20*, 9720–9728.

[84] P. S. Cremer, S. G. Boxer, *Journal of Physical Chemistry B* **1999**, *103*, 2554–2559.

[85] S. Garcia-Manyes, F. Sanz, *Biochimica Et Biophysica Acta-Biomembranes* **2010**, *1798*, 741–749.

[86] A. Alessandrini, P. Facci, *Micron* **2012**, *43*, 1212–1223.

[87] H. A. Rinia, B. de Kruijff, *Febs Letters* **2001**, *504*, 194–199.

[88] J. A. Goodchild, D. L. Walsh, S. D. Connell, *Langmuir* **2019**, *35*, 15352–15363.

[89] A. Alessandrini, P. Facci, *Soft Matter* **2014**, *10*, 7145–7164.

[90] J. X. Mou, J. Yang, Z. F. Shao, *Journal of Molecular Biology* **1995**, *248*, 507–512.

[91] C. A. Keller, B. Kasemo, *Biophysical Journal* **1998**, *75*, 1397–1402.

[92] R. Richter, A. Mukhopadhyay, A. Brisson, *Biophysical Journal* **2003**, *85*, 3035–3047.

[93] E. Reimhult, F. Hook, B. Kasemo, *Langmuir* **2003**, *19*, 1681–1691.

[94] H. P. Wacklin, *Current Opinion in Colloid & Interface Science* **2010**, *15*, 445–454.

[95] G. Pabst, N. Kucerka, M. P. Nieh, M. C. Rheinstadter, J. Katsaras, *Chemistry and Physics of Lipids* **2010**, *163*, 460–479.

[96] G. Fragneto, *European Physical Journal-Special Topics* **2012**, *213*, 327–342.

[97] M. C. Howland, A. W. Szmodis, B. Sanii, A. N. Parikh, *Biophysical Journal* **2007**, *92*, 1306–1317.

[98] S. Kamble, S. Patil, M. Kulkarni, A. V. R. Murthy, *Colloids and Surfaces B-Biointerfaces* **2019**, *176*, 55–61.

[99] J. Andrecka, K. M. Spillane, J. Ortega-Arroyo, P. Kukura, *Acs Nano* **2013**, *7*, 10662–10670.

[100] J. Larsen, N. S. Hatzakis, D. Stamou, *Journal of the American Chemical Society* **2011**, *133*, 10685–10687.

[101] W. Kunz, J. Henle, B. W. Ninham, *Current Opinion in Colloid & Interface Science* **2004**, *9*, 19–37.

[102] K. D. Collins, *Methods* **2004**, *34*, 300–311.

[103] R. Perez-Jimenez, R. Godoy-Ruiz, B. Ibarra-Molero, J. M. Sanchez-Ruiz, *Biophysical Journal* **2004**, *86*, 2414–2429.

[104] M. C. Pinna, A. Salis, M. Monduzzi, B. W. Ninham, *Journal of Physical Chemistry B* **2005**, *109*, 5406–5408.

[105] P. Bauduin, F. Nohmie, D. Touraud, R. Neueder, W. Kunz, B. W. Ninham, *Journal of Molecular Liquids* **2006**, *123*, 14–19.

[106] J. M. Broering, A. S. Bommarius, *Journal of Physical Chemistry B* **2005**, *109*, 20612–20619.

[107] P. Lo Nostro, B. W. Ninham, A. Lo Nostro, G. Pesavento, L. Fratoni, P. Baglioni, *Physical Biology* **2005**, *2*, 1–7.

[108] S. Bae, H. Son, Y. G. Kim, S. Hohng, *Physical Chemistry Chemical Physics* **2013**, *15*, 15829–15832.

[109] N. Schwierz, D. Horinek, U. Sivan, R. R. Netz, *Current Opinion in Colloid & Interface Science* **2016**, *23*, 10–18.

[110] W. Kunz, *Specific Ion Effects*, World Scientific Publishing, **2009**.

[111] K. D. Collins, M. W. Washabaugh, *Quarterly Reviews of Biophysics* **1985**, *18*, 323–422.

[112] A. W. Omta, M. F. Kropman, S. Woutersen, H. J. Bakker, *Science* **2003**, *301*, 347–349.

[113] J. D. Smith, R. J. Saykally, P. L. Geissler, *Journal of the American Chemical Society* **2007**, *129*, 13847–13856.

[114] Y. J. Zhang, S. Furyk, D. E. Bergbreiter, P. S. Cremer, *Journal of the American Chemical Society* **2005**, *127*, 14505–14510.

[115] Y. J. Zhang, P. S. Cremer, *Current Opinion in Chemical Biology* **2006**, *10*, 658–663.

[116] L. M. Pegram, M. T. Record, *Journal of Physical Chemistry B* **2008**, *112*, 9428–9436.

[117] Y. J. Zhang, P. S. Cremer, *Annual Review of Physical Chemistry Vol 61* **2010**, *61*, 63–83.

[118] W. Kunz, *Current Opinion in Colloid & Interface Science* **2010**, *15*, 34–39.

[119] A. M. Klibanov, *Nature* **2001**, *409*, 241–246.

[120] G. Carrea, S. Riva, *Angewandte Chemie-International Edition* **2000**, *39*, 2226–2254.

[121] R. M. Ionescu, C. R. Matthews, *Nature Structural Biology* **1999**, *6*, 304–307.

[122] A. L. Serdakowski, J. S. Dordick, *Trends in Biotechnology* **2008**, *26*, 48–54.

[123] N. Doukyu, H. Ogino, *Biochemical Engineering Journal* **2010**, *48*, 270–282.

[124] A. Giugliarelli, M. Paolantoni, A. Morresi, P. Sassi, *Journal of Physical Chemistry B* **2012**, *116*, 13361–13367.

[125] L. A. Munishkina, C. Phelan, V. N. Uversky, A. L. Fink, *Biochemistry* **2003**, *42*, 2720–2730.

[126] M. Kosmulski, *Advances in Colloid and Interface Science* **2016**, *238*, 1–61.